SEISMIC REHABILITATION OF CONCRETE FRAME BEAM-COLUMN JOINTS

By

TAREK ABBAS EL-AMOURY

B.Sc., M.Sc.

A Thesis

Submitted to the School of Graduate Studies

in Partial Fulfilment of the Requirement

for the Degree

Doctor of Philosophy

McMaster University

© Copyright by Tarek A. El-Amoury, April 2004

DOCTOR OF PHILOSOPHY (2003)
(Civil Engineering)

McMaster University
Hamilton, Ontario

TITLE: Seismic rehabilitation of concrete frame beam-column joints

AUTHOR: Tarek Abbas El-Amoury, B.Sc. (Cairo University)

M.Sc. (Cairo University)

SUPERVISOR: Professor A. Ghobarah

NUMBER OF PAGES: xxx, 351 pages

ABSTRACT

Many reinforced concrete frame structures were designed and constructed before the development of seismic codes or according to earlier versions of seismic codes. Thus, these structures were designed only for gravity loads or for much lower lateral loads than the loads specified by the current seismic codes. Non-ductile reinforcement details in the form of insufficient shear reinforcement in the joint zone or inadequate anchorage length of beam bars are some of the main characteristics of these structures. Post-earthquake investigations confirmed the vulnerability of these structures to severe earthquakes. Poorly designed joints, especially the exterior ones have been identified as critical structural elements that could fail prematurely. Many failure cases were recorded as a result of joint shear failure or anchorage failure of beam bars.

The objectives of this study were to investigate the seismic behaviour of existing concrete frames under simulated seismic loads as well as to develop effective rehabilitation schemes for strengthening concrete frames with non-ductile reinforcement details. The experimental part of this study was conducted to investigate the effect of non-ductile reinforcement details on the behaviour of the joint. Several rehabilitation schemes were proposed to mitigate the hazards caused by such poorly detailed concrete joints. These strengthening schemes included using of externally bonded fibre reinforced polymer (FRP) sheets and steel elements. Twelve exterior full-scale beam-column joints were tested under quasi-static cyclic loading. The specimens were divided into three groups, the first group has no transverse reinforcement in the joint zone, the second group

has inadequate embedment length of beam bars and the last group has both no ties in the joint and inadequate anchorage length of beam bars. The joint shear resistance was improved using FRP jacket, whereas the inadequate anchorage conditions of beam bars were improved using FRP sheets or steel elements. The analytical part of this study was conducted to study the effect of FRP wraps on the compression behaviour of axially-loaded concrete elements and to develop analytical models to predict the shear response of concrete joints without transverse reinforcement, with transverse reinforcement or with FRP sheets. The proposed models were introduced into a non-linear dynamic analysis program and then used to simulate existing and rehabilitated beam-column subassemblies.

From the test results, several rehabilitation systems to improve the performance of non-ductile concrete joints were proposed and successfully evaluated. FRP jacket proved to be effective in upgrading the joint shear resistance. FRP sheets and steel elements were effective in upgrading the anchorage conditions of beam bars. The proposed shear and materials models, which were introduced into a macro model to represent beam-column joints, were capable of representing the cyclic behaviour of existing and rehabilitated beam-column subassemblies. These models would help the design engineers to assess existing structures and propose practical rehabilitation schemes for these structures.

ACKNOWLEDGEMENTS

I wish to express my sincere appreciation to my research supervisor, Dr. A. Ghobarah, for his guidance, advice, encouragement and time spent throughout the course of this study. Sincere gratitude is due to my Supervisory Committee members, Dr. R. Kianoush and Dr. D. Metzger for their valuable comments and suggestions on this research and their time spent in reviewing this thesis.

The help of the Applied Dynamic Laboratory technicians, in particular David Perrett who assisted me during the course of the experimental program, is appreciated.

Financial support from McMaster University, Intelligent Sensing for Innovative Structures Research Network (ISIS Canada), and Ontario Ministry of Training, Colleges and Universities are gratefully appreciated.

Finally, much appreciation is extended to my family, my mother, sisters and my wife for their support, patience and sincere supplication.

In the name of God, the most gracious, the most merciful

This work is dedicated to my family, my country and

my entire Muslim nation

TABLE OF CONTENT

		Page
ABSTRACT		iii
ACKNOWLEDGEMENTS		v
TABLE OF CONTENTS		vii
LIST OF FIGURES		xii
LIST OF TABLES		xxi
LIST OF SYMBOLS		xxiii
CHAPTER 1	**INTRODUCTION**	1
	1.1 BACKGROUND	1
	1.2 BEHAVIOUR OF BEAM-COLUMN JOINTS	3
	1.2.1 Rehabilitation of joints	6
	1.2.2 Modeling of beam-column joints	11
	1.3 MOTIVATION	14
	1.4 OBJECTIVES	15
	1.5 SCOPE	16
	1.6 ORGANIZATION	17
CHAPTER 2	**EXPERIMENTAL PROGRAM**	27
	2.1 INTRODUCTION	27
	2.2 JOINTS DESIGN AND DETAILS	27
	2.2.1 Shear-deficient joints "T-S"	28
	2.2.2 Bond-deficient joints "T-B"	29
	2.2.3 Shear/bond-deficient joints "T-SB"	30
	2.3 MATERIAL PROPERTIES	30
	2.3.1 Concrete	30
	2.3.2 Steel	31
	2.3.3 Fibre reinforced polymer sheets	31
	2.3.3.1 Tensile tests of FRP coupons	33
	2.3.3.2 FRP anchors	33
	2.4 JOINT CONSTRUCTION	34
	2.5 REHABILITATION SYSTEMS	36

2.6 APPLICATION OF FRP SHEETS 36
2.7 TEST SET-UP 38
2.8 LOADING ROUTINE 39
2.8.1 Load control 39
2.8.2 Displacement control 40
2.9 INSTRUMENTATION 40
2.9.1 Load measurements 40
2.9.2 Displacement measurements 41
2.9.3 Measurement of beam section rotation at the column face 41
2.9.4 Measurement of joint shear distortion 42
2.9.5 Measurement of strains 43
2.10 ANALYSIS OF EXPERIMENTAL DATA 43
2.10.1 Hysteretic loops 44
2.10.2 Displacement ductility factor and storey drift 44
2.10.3 Cracking moment 45
2.10.4 Yield and ultimate moments 46
2.10.5 Storey shear 46
2.10.6 Shear deformation of beam-column joints 47
2.10.7 Stresses in steel reinforcement and FRP sheets 48
2.10.8 Shear in beams 49
2.10.9 Shear in beam-column joints 50
2.10.10 Joint contribution to drift angle 51
2.10.11 Stiffness 52
2.10.12 Energy dissipation 53

CHAPTER 3 BEHAVIOUR OF SHEAR STRENGTH-DEFICIENT JOINTS 73

3.1 INTRODUCTION 73
3.2 JOINT T-S1 73
3.3 JOINT T-S1RR 75
3.4 JOINT T-S5 77
3.5 JOINT T-S4R 79
3.6 ANALYSIS OF EXPERIMENTAL RESULTS 80
3.6.1 Beam-tip load-displacement relationships 81
3.6.2 Storey shear- drift angle relationships 83
3.6.3 Cracking, yield and ultimate moments 84
3.6.4 Shear deformation of beam-column joints 85
3.6.5 Moment-rotation relationships 86
3.6.6 Shear in beam 87
3.6.7 Shear in beam-column joints 88
3.6.8 Joint contribution to storey drift 89
3.6.9 Stiffness 90

3.6.10 Energy dissipation 90
3.6.11 Strain in FRP jacket 91
3.7 SUMMARY 91

CHAPTER 4 BEHAVIOUR OF BOND-DEFICIENT JOINTS 121

4.1 INTRODUCTION 121
4.2 JOINT T-B10 121
4.3 JOINT T-B12 123
4.4 JOINT T-B11 125
4.5 ANALYSIS OF EXPERIMENTAL RESULTS 127
4.5.1 Bond behaviour in joints 127
4.5.2 Beam-tip load-displacement relationships 129
4.5.3 Storey shear-storey drift angle relationships 130
4.5.4 Moment-rotation relationships 131
4.5.5 Cracking, yield and ultimate moments 133
4.5.6 Response of beam-column joints 134
4.5.7 Shear in beam 135
4.5.8 Stiffness 136
4.5.9 Energy dissipation 137
4.5.10 Strains in beam reinforcement bars and CFRP sheets 137
4.6 SUMMARY 138

CHAPTER 5 BEHAVIOUR OF SHEAR/BOND-DEFICIENT JOINTS 155

5.1 INTRODUCTION 155
5.2 JOINT T-SB3 155
5.3 JOINT T-SB3R 157
5.4 JOINT T-SB6 159
5.5 JOINT T-SB8 161
5.6 JOINT T-SB7 163
5.7 ANALYSIS OF EXPERIMENTAL RESULTS 165
5.7.1 Beam-tip load-displacement relationships 165
5.7.2 Storey shear-storey drift angle relationships 167
5.7.3 Cracking, yield and ultimate moments 168
5.7.4 Shear deformation of beam-column joints 169
5.7.5 Moment-rotation relationships 170
5.7.6 Shear in beam 172
5.7.7 Stiffness 172
5.7.8 Energy dissipation 173
5.7.9 Behaviour of rehabilitation schemes 173
5.7.9.1 Joint T-SB6 173
5.7.9.2 Joint T-SB7 175

5.8 SUMMARY 176

CHAPTER 6 MATERIAL MODELS 205

6.1 INTRODUCTION 205
6.2 CONCRETE MODEL 206
6.2.1 Compression envelope of unconfined concrete 206
6.2.2 Compression envelope for concrete confined with steel ties 207
6.2.3 Compression envelope of concrete confined with FRP sheets 208
6.2.3.1 Introduction 208
6.2.3.2 Model development 209
6.2.3.3 Model Verification 213
6.2.4 Concrete tension envelope 214
6.3 MODELING OF EXTERNALLY BONDED FRP SHEETS 216
6.3.1 FRP tension envelope 217
6.3.2 FRP compression envelope 218
6.4 STEEL MODEL 220
6.4.1 Background 220
6.4.2 Material constitutive relationships 221
6.4.3 Proposed model 225
6.4.4 Model verification 227
6.5 SUMMARY 228

CHAPTER 7 JOINT SHEAR MODELS 241

7.1 INTRODUCTION 241
7.2 SHEAR MECHANISMS IN BEAM-COLUMN JOINTS 241
7.3 MODELING OF BEAM-COLUMN JOINTS with shear reinforcement 242
7.3.1 Model derivation 243
7.3.2 Model verification 248
7.4 MODELING OF BEAM-COLUMN JOINTS WITH NO SHEAR REINFORCEMENT 249
7.4.1 Uncracked joint 249
7.4.2 Cracked joint 250
7.4.3 Model verification 252
7.5 MODELING OF FRP-STRENGTHENED JOINTS 253
7.5.1 FRP-shear strengthened concrete model 253
7.5.2 Model verification 255
7.6 SUMMARY 256

CHAPTER 8 BEAM-COLUMN JOINT MODEL 267

8.1 INTRODUCTION 267
8.2 COMPUTATIONAL TOOL 269
8.3 KINEMATIC MODELS 270
8.3.1 Flexural elements 270
8.3.2 Beam-column joints 273
8.4 APPLICATIONS 274
8.4.1 Current-code designed joint 275
8.4.2 Pre-seismic code designed joints 276
8.4.2.1 Joint T-B10 277
8.4.2.2 Joint T-S1 278
8.4.2.3 Joint T-SB3 278
8.4.2.4 Specimen J1 279
8.4.3 FRP-rehabilitated specimens 280
8.4.3.1 Joint T-S4R 281
8.4.3.2 Joint T-2R 282
8.4.3.3 Joint T-SB7 282
8.4.3.4 Specimen # 3 283
8.5 SUMMARY 285

CHAPTER 9 CONCLUSIONS AND RECOMMENDATIONS 321

9.1 SUMMARY 321
9.2 CONCLUSIONS 322
9.3 RECOMMENDATIONS FOR FUTURE RESEARCH 325

APPENDIX A DESIGN OF REHABILITATION SCHEMES 327
A.1 DESIGN OF FRP-SHEAR JACKET 327
A.2 DESIGN OF FLEXURAL STRENGTHENING SCHEMES 329
A.2.1 FRP sheets 329
A.2.2 Design of steel bridle 331
A.2.3 Design of additional flexural reinforcement 332

APPENDIX B BOND-SLIP COMPUTER PROGRAM 335

REFERENCES 341

LIST OF FIGURES

		Page
Figure 1-1	Structural collapse due to beam-column joint failure	19
Figure 1-2	Applied load and crack pattern of an exterior beam-column joint	19
Figure 1-3	Details of external steel reinforcement of concrete jacket (Corazao and Durrani, 1989)	20
Figure 1-4	Beam-column joint confinement cage (Alcocer and Jirsa, 1993)	20
Figure 1-5	Confinement of the joint zone with flat steel plates (Beres et al., 1992a and b)	21
Figure 1-6	Corrugated steel sheet jacket for the beam and columns (Ghobarah et al., 1996)	21
Figure 1-7	Strengthening the anchorage of beam bars (Estrada, 1990)	22
Figure 1-8	Crack pattern of GFRP-rehabilitated joints (Ghobarah and Said, 2001 and 2002)	22
Figure 1-9	Application of CFRP sheets to bridge bent (Pantelides et al., 1997)	23
Figure 1-10	CFRP jacket for exterior joint (Gergely et al., 2000)	23
Figure 1-11	Modeling of beam-column joint (Biddah and Ghobarah, 1998)	24
Figure 1-12	High order 12-noded beam-column element (Elmorsi, 1998)	25
Figure 1-13	Macro-modeling of beam-column joint (Youssef, 2000)	25
Figure 1-14	Finite element modeling of beam-column joint (Balgin and Scott, 2000)	25
Figure 1-15	Crack pattern and stresses path in beam-column joint (Shiohara, 2001)	26
Figure 1-16	Components of beam-column joint model (Lowes and Altoontash, 2002)	26
Figure 2-1	Deformation of a typical moment resisting frame under lateral load effect	57
Figure 2-2	Specimen groups layout	57
Figure 2-3	Concrete dimensions and reinforcement details of shear-deficient joints	58

Figure 2-4	Concrete dimensions and reinforcement details of bond-deficient joints	59
Figure 2-5	Concrete dimensions and reinforcement details of shear/bond-deficient joints	60
Figure 2-6	FRP coupons	61
Figure 2-7	Force/unit width versus strain of the tested GFRP coupons	61
Figure 2-8	Force/unit width versus strain of the tested CFRP coupons	62
Figure 2-9	Failure patterns of FRP coupons	62
Figure 2-10	Proposed rehabilitation schemes	63
Figure 2-11	Schematic diagram of the test set-up	66
Figure 2-12	Test set-up	67
Figure 2-13	Loading routine	68
Figure 2-14	Measurement of beam section rotation	68
Figure 2-15	Measurement of joint shear distortion	68
Figure 2-16	Strain gauges location	69
Figure 2-17	The drift angle definition (Uzumeri and Seckin, 1974)	70
Figure 2-18	Stress-strain curve for the steel bars under cyclic loads (Chen, 1982)	71
Figure 2-19	Specimen peak-to-peak stiffness	71
Figure 3-1	Failure pattern of joint T-S1	96
Figure 3-2	Strengthening scheme of joint T-S1RR	96
Figure 3-3	Debonding of FRP sheets wrapped around joint T-S1RR	97
Figure 3-4	Cracking of joint T-S1RR after removing the GFRP jacket	98
Figure 3-5	Buckling of column reinforcement bars of joint T-S1RR	98
Figure 3-6	Strengthening scheme of joint T-S5	99
Figure 3-7	Debonding of GFRP sheets from the column sides of joint T-S5	100

Figure 3-8	Cracking and spalling of concrete after removing the GFRP sheets of joint T-S5	100
Figure 3-9	Strengthening scheme of joint T-S4R	101
Figure 3-10	Cracking pattern of joint T-S4R at displacement ductility level of 3	102
Figure 3-11	Flexural hinging of joint T-S4R	102
Figure 3-12a	Beam-tip load-displacement relationship of joint T-S1	103
Figure 3-12b	Beam-tip load-displacement relationship of joint T-S1RR	103
Figure 3-12c	Beam-tip load-displacement relationship of joint T-S5	104
Figure 3-12d	Beam-tip load-displacement relationship of joint T-S4R	104
Figure 3-13	Envelopes of the loading loops for the tested joints	105
Figure 3-14a	Storey shear force-drift angle relationship of joint T-S1	105
Figure 3-14b	Storey shear force-drift angle relationship of joint T-S1RR	106
Figure 3-14c	Storey shear force-drift angle relationship of joint T-S5	106
Figure 3-14d	Storey shear force-drift angle relationship of joint T-S4R	107
Figure 3-15	Envelopes of storey shear-drift angle relationships of the tested joints	107
Figure 3-16a	Joint shear deformation-storey shear force relationship of joint T-S1	108
Figure 3-16b	Joint shear deformation-storey shear force relationship of joint T-S1RR	108
Figure 3-16c	Joint shear deformation-storey shear force relationship of joint T-S5	109
Figure 3-16d	Joint shear deformation-storey shear force relationship of joint T-S4R	109
Figure 3-17	Envelopes of joint shear force-deformation of the tested joints	110
Figure 3-18a	Beam moment-rotation at 175 mm from column face of joint T-S1	110
Figure 3-18b	Beam moment-rotation at 175 mm from column face of joint T-S1RR	111
Figure 3-18c	Beam moment-rotation at 175 mm from column face of joint T-S5	111
Figure 3-18d	Beam moment-rotation at 175 mm from column face of joint T-S4R	112

Figure 3-19a	Beam shear force resisted by concrete and stirrups of joint T-S1	112
Figure 3-19b	Beam shear force resisted by concrete and stirrups of joint T-S1RR	113
Figure 3-19c	Beam shear force resisted by concrete and stirrups of joint T-S5	113
Figure 3-19d	Beam shear force resisted by concrete and stirrups of joint T-S4R	114
Figure 3-20a	Joint shear force resisted by concrete of joint T-S1	114
Figure 3-20b	Joint shear force resisted by concrete and composite sheets of joint T-S1RR	115
Figure 3-20c	Joint shear force resisted by concrete and composite sheets of joint T-S5	115
Figure 3-20d	Joint shear force resisted by concrete and composite sheets of joint T-S4R	116
Figure 3-21a	Contribution of joint shear deformation to positive storey drift	116
Figure 3-21b	Contribution of joint shear deformation to negative storey drift	117
Figure 3-22	Stiffness degradation with storey drift	117
Figure 3-23	Cumulative energy dissipated by tested joints	118
Figure 3-24	Strain in FRP jacket	118
Figure 4-1	Bond-slip cracks of joint T-B10	141
Figure 4-2	Strengthening of joint T-B12	141
Figure 4-3	Cracking of joint T-B12 at a DDF of 3.0	142
Figure 4-4	Fracture of the CFRP sheets of joint T-B12	142
Figure 4-5	Strengthening of joint T-B11	143
Figure 4-6	Weld failure of plate-supporting bolts of joint T-B11	143
Figure 4-7	Cracking and spalling of concrete of joint T-B11	144
Figure 4-8a	Beam-tip load-displacement relationship of joint T-B10	145
Figure 4-8b	Beam-tip load-displacement relationship of joint T-B12	145
Figure 4-8c	Beam-tip load-displacement relationship of joint T-B11	146
Figure 4-9	Hysteretic loops envelopes of the tested joints	146

Figure 4-10a	Storey shear-drift angle relationship of joint T-B10	147
Figure 4-10b	Storey shear-drift angle relationship of joint T-B12	147
Figure 4-10c	Storey shear-drift angle relationship of joint T-B11	148
Figure 4-11a	Beam rotation at 175 mm from column face-beam moment at column face of joint T-B10	148
Figure 4-11b	Beam rotation at 175 mm from column face-beam moment at column face of joint T-B12	149
Figure 4-11c	Beam rotation at 175 mm from column face-beam moment at column face of joint T-B11	149
Figure 4-12	Joint shear deformation-storey shear force of joint T-B11	150
Figure 4-13	Contribution of concrete shear strength and steel ties in carrying the joint shear force of joint T-B10	150
Figure 4-14a	Beam shear force resisted by concrete and stirrups of joint T-B10	151
Figure 4-14b	Beam shear force resisted by concrete and stirrups of joint T-B12	151
Figure 4-14c	Beam shear force resisted by concrete and stirrups of joint T-B11	152
Figure 4-15	Stiffness degradation with storey drift	152
Figure 4-16	Cumulative energy dissipated by joint group T-B	153
Figure 4-17	Steel bars strain-beam-tip load relationship of joint T-B10	153
Figure 4-18	Distribution of strains along the length of CFRP sheets of joint T-B11	154
Figure 5-1	Failure pattern of joint T-SB3	179
Figure 5-2	Strengthening of joint T-SB3R	180
Figure 5-3	Buckling of the composite sheets of joint T-SB3R	181
Figure 5-4	Debonding of the GFRP sheets of joint T-SB3R	181
Figure 5-5	Strengthening of joint T-SB6	182
Figure 5-6	Steel angle attached to joint T-SB6	183
Figure 5-7	Deforming of the steel angle of joint T-SB6	183

Figure 5-8	Failure pattern of joint T-SB6	184
Figure 5-9	Steel rods installed to joint T-SB8	185
Figure 5-10	Strengthening of joint T-SB8	185
Figure 5-11	Failure pattern of joint T-SB8	186
Figure 5-12	Anchoring of the beam bottom reinforcement of joint T-SB7	186
Figure 5-13	Bending of the tie rods in positive loading direction of joint T-SB7	187
Figure 5-14	Failure of the external tie rods of joint T-SB7	187
Figure 5-15a	Beam-tip load-displacement relationship of joint T-SB3	188
Figure 5-15b	Beam-tip load-displacement relationship of joint T-SB3R	188
Figure 5-15c	Beam-tip load-displacement relationship of joint T-SB6	189
Figure 5-15d	Beam-tip load-displacement relationship of joint T-SB8	189
Figure 5-15e	Beam-tip load-displacement relationship of joint T-SB7	190
Figure 5-16	Envelopes of the hysteretic loops of the joint group T-SB	190
Figure 5-17a	Storey shear-drift angle relationship of joint T-SB3	191
Figure 5-17b	Storey shear-drift angle relationship of joint T-SB3R	191
Figure 5-17c	Storey shear-drift angle relationship of joint T-SB6	192
Figure 5-17d	Storey shear-drift angle relationship of joint T-SB8	192
Figure 5-17e	Storey shear-drift angle relationship of joint T-SB7	193
Figure 5-18	Envelopes of storey shear-drift angle relationships of joint group T-SB	193
Figure 5-19a	Joint shear deformation-storey shear of joint T-SB3	194
Figure 5-19b	Joint shear deformation-storey shear of joint T-SB3R	194
Figure 5-19c	Joint shear deformation-storey shear of joint T-SB6	195
Figure 5-19d	Joint shear deformation-storey shear of joint T-SB8	195
Figure 5-19e	Joint shear deformation-storey shear of joint T-SB7	196

Figure 5-20a	Beam moment-rotation at 175 mm from column face of joint T-SB3	196
Figure 5-20b	Beam moment-rotation at 175 mm from column face of joint T-SB3R	197
Figure 5-20c	Beam moment-rotation at 175 mm from column face of joint T-SB6	197
Figure 5-20d	Beam moment-rotation at 175 mm from column face of joint T-SB8	198
Figure 5-20e	Beam moment-rotation at 175 mm from column face of joint T-SB7	198
Figure 5-21a	Beam shear force resisted by concrete and stirrups of joint T-SB3	199
Figure 5-21b	Beam shear force resisted by concrete and stirrups of joint T-SB6	199
Figure 5-21c	Beam shear force resisted by concrete and stirrups of joint T-SB8	200
Figure 5-21d	Beam shear force resisted by concrete and stirrups of joint T-SB7	200
Figure 5-22	Stiffness degradation with storey drift	201
Figure 5-23	Cumulative energy dissipated with storey drift	201
Figure 5-24	Strain in rehabilitation scheme elements of joint T-SB6	202
Figure 5-25	Strain in external tie rods of joint T-SB7	203
Figure 6-1	Stress-strain behaviour of unconfined and steel-confined concrete members	230
Figure 6-2	Confinement of rectangular concrete sections with FRP sheets	231
Figure 6-3	Experimental (Hosotani et al., 1997) and analytical stress-strain relationship	232
Figure 6-4	Experimental (Cole and Belarbi, 2001) and analytical stress-strain relationship	232
Figure 6-5	Concrete tension envelope (Stevens et al., 1987)	233
Figure 6-6	Behaviour of the FRP spring: (a) Deformation of FRP sheet in tension (b) FRP and steel angle model in tension (c) modeling of the retrofit steel angle	234
Figure 6-7	Response of FRP spring: (a) modeling of FRP in compression (b) Response of FRP spring in tension and compression	235
Figure 6-8	Different stages in developing the bond stress-slip relationship (Eligehausen et al., 1983)	236

Figure 6-9	Bond stress-slip relationships: (a) Actual (b) Idealized for straight bars (Eligehausen et al., 1983) (c) Idealized for hooks (Soroushian et al., 1988)	237
Figure 6-10	Reinforcing bars with straight or hooked end embedded in concrete	238
Figure 6-11	Solution algorithm of bond-slip model	239
Figure 6-12	Force-displacement relationship for embedded steel bars tested under monotonic loads	240
Figure 7-1	Shear transfer mechanisms in concrete frame joints	257
Figure 7-2	Compatibility conditions for cracked concrete element (Vecchio and Collins, 1986)	257
Figure 7-3	Equilibrium conditions for cracked concrete element (Vecchio and Collins, 1986)	258
Figure 7-4	Solution algorithm for determining the shear force-strain relationship	259
Figure 7-5	Experimental behaviour of beam-column joints (Fuji and Morita, 1991) compared to the analytical predicted behaviour	260
Figure 7-6	Diagonal compression strut oriented between the compression zones in the beams and the columns	261
Figure 7-7	Solution strategy for the Fixed Angle Softened Strut Model	262
Figure 7-8	Joint shear force-deformation of a frame joint without ties	263
Figure 7-9	Comparison between the behaviour of a frame joint with and without ties	263
Figure 7-10	Predicted behaviour of joint T-S1	264
Figure 7-11	Predicted behaviour of joint T-S1 after strengthening with two CFRP sheets	264
Figure 7-12	Predicted behaviour of joint T-S1 after strengthening with three GFRP sheets	265
Figure 8-1	Displacement-control loading scheme	295
Figure 8-2	Multi-spring model to represent flexural members (Lai et al., 1984)	295
Figure 8-3	Hysteretic model for steel spring (Youssef and Ghobarah, 1999)	296
Figure 8-4	Hysteretic response for concrete spring (Youssef, 2000)	296
Figure 8-5	Hysteretic model for shear spring (Youssef and Ghobarah, 2001)	297

Figure 8-6	Kinematic beam-column model	298
Figure 8-7	Reinforcement details of specimen J2 (Ghobarah et al., 1997)	299
Figure 8-8	Analytical prediction of model elements of specimen J2	300
Figure 8-9	Experimental measurements and analytical response of specimen J2	301
Figure 8-10	Analytical prediction of model elements of joint T-B10	302
Figure 8-11	Experimental measurements and analytical response of joint T-B10	303
Figure 8-12	Analytical prediction of model elements of joint T-S1	304
Figure 8-13	Experimental measurements and analytical response of joint T-S1	305
Figure 8-14	Analytical prediction of model elements of joint T-SB3	306
Figure 8-15	Experimental measurements and analytical response of joint T-SB3	307
Figure 8-16	Reinforcement details of specimen J1 (Ghobarah et al, 1996)	308
Figure 8-17	Analytical prediction of model elements of specimen J1	309
Figure 8-18	Experimental measurements and analytical response of specimen J1	310
Figure 8-19	Analytical prediction of model elements of joint T-S4R	311
Figure 8-20	Experimental measurements and analytical response of joint T-S4R	312
Figure 8-21	Analytical prediction of model elements of specimen T2R	313
Figure 8-22	Experimental measurements and analytical response of specimen T2R	314
Figure 8-23	Analytical prediction of model elements of joint T-SB7	315
Figure 8-24	Experimental measurements and analytical response of joint T-SB7	316
Figure 8-25	Dimensions and reinforcement details of specimen # 3 (Clyde and Pantelides, 2002)	317
Figure 8-26	Rehabilitation scheme of specimen # 3 (Clyde and Pantelides, 2002)	317
Figure 8-27	Analytical prediction of model elements of specimen # 3	318
Figure 8-28	Experimental measurements and analytical response of specimen # 3	319

LIST OF TABLES

Page

Table 2-1 Concrete properties 54

Table 2-2 Properties of the reinforcement bars 54

Table 2-3 Tensile properties of the Unified Inch Coarse Screw Threads (UNC) steel rods 55

Table 2-4 FRP sheet properties as provided by the manufacturer 55

Table 2-5 Adhesives properties as provided by the manufacturer 56

Table 2-6 Properties of the composite sheets as tested against the provided manufacturer data 56

Table 3-1 Comparison of Shear-deficient joints behaviour 93

Table 3-2 Beam concrete shear resistance as a fraction of $\sqrt{f_c^{'}}$ 94

Table 3-3 Joint concrete shear resistance as a fraction of $\sqrt{f_c^{'}}$ 94

Table 4-1 Behaviour of Bond-deficient joints 140

Table 4-2 Concrete shear resistance as a fraction of $\sqrt{f_c^{'}}$ for beams 140

Table 5-1 Comparison of Shear/Bond joints behaviour 177

Table 5-2 Shear resistance of concrete as a fraction of $\sqrt{f_c^{'}}$ for beams 178

Table 6-1 Parameters of the bond stress–slip relationship (Filippou et al., 1983; and Eligehausen et al., 1983) 229

Table 8-1 Model parameters of specimen J2 286

Table 8-2a Parameters of steel springs in beam and columns of specimen T-B10 287

Table 8-2b Parameters of concrete springs in beam and columns of specimen T-B10 287

Table 8-3 Model parameters of joint T-S1 288

Table 8-4 Model parameter of specimen T-SB3 289

Table 8-5 Model parameters of specimen J1 290

Table 8-6 Model parameters of specimen T-S4R 291

Table 8-7 Model parameters of Specimen T2R 292

Table 8-8 Model parameters of specimen T-SB7 293

Table 8-9 Model parameters of specimen # 3 294

LIST OF SYMBOLS

A	Aggregate size
a_b	Depth of compression zone in the beam
a_c	Depth of compression zone in the column
A_c	Area of exterior or central concrete spring
A_{ce}	Area of external concrete spring
A_{ci}	Area of central concrete spring
A_{frp}	Cross sectional area of FRP flexural sheets
A_g	Gross cross sectional area of concrete element
A_s	Cross sectional area of tensile beam reinforcement
$A_{s'}$	Cross sectional area of compressive beam reinforcement
a_{stu}	Depth of diagonal joint compression strut
A_{stu}	Cross sectional area of diagonal compression strut in shear element
A_{sx}	Longitudinal reinforcement in shear element
A_v	Cross sectional area of shear reinforcement in shear element
b_a	Width of steel angle leg
b_j	Effective width of beam-column joint
b_{stu}	Width of diagonal joint compression strut
b_v	Effective width of shear element
b_x	Dimension of concrete section in x-direction
b_y	Dimension of concrete section in y-direction

c	Concrete cover of the concrete section
d	Effective depth of beam section
d_b	Diameter of longitudinal steel bar of the concrete section
d_{cy}	Yield displacement of concrete spring
d_j	Effective depth of beam-column joint
d_s	Deformation of steel spring
d_{sp}	Spacing of exterior springs
d_{su}	Deformation of steel spring that corresponds to P_{su}
d_v	Effective depth of shear element
E_c	Initial concrete stiffness
E_{frp}	Modulus of elasticity of FRP flexural sheets
E_g	Tangent stiffness of the FRP-confined concrete stress-strain relationship
E_j	Modulus of elasticity of FRP jacket
E_s	Steel modulus of elasticity
E_{sec}	Secant concrete stiffness
F	Force in shear springs
f_1	Principal tensile concrete stress
f_{1max}	Maximum concrete tensile stress transmitted across a crack
f_2	Principal compressive concrete stress
f_{2max}	Maximum concrete strength in compression that corresponds to tensile strain ε_1
f_c	Concrete compressive stress

f_{cr}	Concrete cracking strength
f_{ct}	Concrete tensile stress
$f_c^{'}$	Concrete compressive strength
$f_{cc}^{'}$	Confined concrete strength
f_{frp}	Tensile stress in shear-strengthening jacket
$f_l^{'}$	Lateral confining pressure produced by steel ties
f_{sx}	Axial stress of longitudinal reinforcement in shear element
f_v	Stress in shear reinforcement
f_y	Steel yield strength
f_{yh}	Yield strength of confining hoops
h_c	Depth of column section in loading plane
h_j	Depth of FRP shear-strengthening jacket
I_{frp}	Second moment of inertia of FRP flexural sheets
k_1	Initial stiffness of FRP spring
k_2	Post-yield stiffness of FRP spring
k_e	Confinement effectiveness coefficient
k_{frp}	Elastic stiffness of FRP flexural sheets
k_h	Confinement coefficient of concrete section
k_p	Tensile stiffness of epoxy springs
k_{s1}	Initial stiffness of steel spring representing the retrofit steel angle
k_{s2}	Post-yield stiffness of steel spring representing the retrofit steel angle

K_s	Initial stiffness of steel spring
L	Length of FRP flexural sheets
l_1	Unsupported length of the retrofit steel angle leg
l_d	Development length of the steel bar as required by code provisions
L_e	Length of the steel bar at which average bond stress u_e exists
N	Axial load capacity of the shear element
P_f	Compression force applied to FRP sheets
P	Axial load applied on column
P_1	Ultimate strength of bar hook
P_3	Residual strength of bar hook
P_{cr}	Critical buckling load of FRP sheets under compression load
P_{cy}	Yield force of concrete spring
P_h	Force developed in the bar hook
P_s	Force in steel spring
P_{spy}	Yield force of the steel spring representing the anchoring steel angle
P_{sy}	Yield force of steel spring representing the flexural reinforcement
P_{su}	Ultimate strength of steel spring
r	Post-yield stiffness parameter of steel spring
r_c	Chamfer radius of concrete section
R_{so}	Ratio of the residual strength to the ultimate strength of steel spring
s	Slip of steel bar

S	Spacing of shear reinforcement
s_1	Steel bar slip corresponding to bond stress of τ_1
s_3	Steel bar slip corresponding to bond stress of τ_3
s_h	Slip of the bar hook
s_{h1}	Slip of the bar hook corresponding to the ultimate hook force
s_{h3}	Slip of the bar hook corresponding to the residual hook force
S_{mx}	Crack spacing in x-direction
S_{my}	Crack spacing in y-direction
S_x	Spacing of the reinforcement in x-direction
S_y	Spacing of the reinforcement in y-direction
t_a	Thickness of steel angle leg
t_j	FRP jacket thickness
u_e	Average bond stress along the embedded length of the steel bar
u_{xf}	Unrestrained displacement of concrete section in x-direction
u_{xj}	Lateral deformation of the FRP jacket in x-direction
u_{xr}	Lateral displacement of concrete section in x-direction due to lateral confining pressure
u_{yf}	Unrestrained displacement of concrete section in y-direction
u_{yr}	Lateral displacement of concrete section in y-direction due to lateral confining pressure
v	Shear stress that could be resisted by the shear element
v_c	Concrete Poisson's ratio

v_{ci}	Shear stress that could be transmitted across a crack
V_j	Shear strength of concrete shear element
w_f	Lateral deflection of FRP sheets under compression force
w	Crack width of concrete element
w_i	The ith length of unconfined concrete region in a concrete section
Z	Post-yield slope of concrete spring
ΣA_{st}	Sum of steel cross-sectional area in a concrete section
γ	Shear strain
θ	Crack inclination to the horizontal and inclination of the principal axes
ρ_s	Transverse reinforcement ratio
ρ_x	Reinforcement ratio of longitudinal reinforcement
σ_x	Lateral confining pressure in x- direction imposed by FRP jacket on concrete section
σ_y	Lateral confining pressure in y- direction imposed by FRP jacket on concrete section
σ_j	FRP jacket tensile stress
σ_r	Lateral confining pressure in radial direction imposed by FRP jacket on concrete section
ε_1	Principal tensile concrete strain
ε_2	Principal compressive concrete strain
ε_j	Tensile strain in FRP jacket
ε_c	Concrete strain

ε_{cc}	Compressive concrete strain corresponding to $f_{cc}^{'}$
ε_{cr}	Concrete cracking strain
ε_{o}	Compressive concrete strain corresponding to $f_{c}^{'}$
ε_{x}	Strain in x-direction of the concrete element
ε_{v}	Strain in y-direction of the shear element
ε_{x}	Lateral concrete strain in x-direction
α	Inclination of the diagonal compression strut
α_{s}	Softening parameter of steel spring
α_{t}	Factor that defines the residual concrete tensile strength
α_{tx} *and* α_{ty}	Factors that define the residual concrete tensile strength in x and y directions, respectively.
τ	Steel-to-concrete bond stress
τ_{1}	Ultimate steel-to-concrete bond strength
τ_{3}	Residual steel-to-concrete bond strength
λ_{t}	Factor defines the decay rate of concrete post-cracking tensile strength
β	Post-yield slope of steel stress-strain relationship
δ_{sy}	Yield displacement of steel spring representing the retrofit steel angle

This page is intentionally left blank

Chapter 1

INTRODUCTION

1.1 BACKGROUND

Building codes are frequently updated as a result of the advances in engineering knowledge and experience. Buildings constructed before the development of seismic codes, prior to 1970, were designed for gravity loads only. Over the past thirty years, major changes in the zoning maps and design philosophies occurred. Changes in seismic zoning maps may move buildings to more vulnerable seismic zones. Changes in the function of the building may increase the seismic loads due to increased importance factor or gravity loads. Therefore, many of the existing concrete buildings may not comply with the recent code provisions, and therefore these buildings represent significant hazard to the life of occupants and their investment. When assessing these buildings, deficiencies such as weak column-strong beam, inadequate lap splice of column bars, absence of joint shear reinforcement and insufficient anchorage of beam bars are observed.

Recent earthquakes such as the 1989 Loma Prieta, 1994 Northridge, 1995 Hanshin-Awaji (Kobe) and the 1999 Kocaeli (Turkey) tested the vulnerability of existing reinforced concrete buildings to strong ground motions. Failure of beam–column joints was identified as one of the leading causes of collapse of such structures. Concrete joints designed and built according to the pre-seismic code provisions (before 1970) had non-

ductile reinforcement detailing. As a consequence, non-ductile failure modes, such as joint shear failure, anchorage-slip of beam bars or failure of column bars lap splice, occurred. Figure 1-1 shows a complete collapse of a reinforced concrete building during the 1999 Kocaeli (Turkey) earthquake as a result of beam-column joint failure.

Brittle failure modes in the joint zone would significantly reduce the overall ductility of the structure. Rehabilitation of the beam-column joints represents a feasible approach to mitigate the hazard in existing structures and to provide safety to the occupants. Recent studies on the effect of shear and anchorage-slip rehabilitation on the behaviour of reinforced concrete moment resisting frame have shown that significant improvement in the overall frame ductility can be achieved (Ghobarah and Biddah, 1999; and Ghobarah and Youssef, 1999).

Several rehabilitation techniques were proposed during the last two decades. These techniques include the use of concrete jackets, flat and corrugated steel plates. However, these retrofit techniques are labour intensive and involve artful reinforcement detailing. Recently, fibre reinforced polymer (FRP) materials were used to strengthen various structural elements. The advanced composite materials have the advantage of ease of installation, corrosion resistance and high strength to weight ratio.

To evaluate a specific existing structure and propose a suitable rehabilitation technique, the structure behaviour under seismic load, before and after retrofit, needs to be assessed. The most comprehensive approach is the non-linear dynamic time history analysis of the structure. However, most of the available non-linear structural analysis software packages assume rigid beam-column joint regardless of the joint reinforcement

detailing, and therefore ignore the joint shear deformation and the bond behaviour of beam and column bars anchored into the joint. For pre-seismic code designed and constructed joints, the contributions of shear and anchorage-slip deformations to the total storey drift are significant. Thus, the validity of non-linear structural analysis packages that assume rigid joints for modeling pre-seismic codes constructed buildings is questionable.

1.2 BEHAVIOUR OF BEAM-COLUMN JOINTS

The behaviour of reinforced concrete frames when subjected to seismic loads received considerable attention during the last three decades. Field surveys performed following major seismic events investigated the causes of damage and collapse of moment resisting frames. Several experimental and analytical studies were performed to improve the design guidelines of the critical zones in concrete frames. Few studies were focused on the behaviour of the existing frames and the strengthening techniques that could be proposed to improve their seismic response.

Blume et al. (1961) tested an interior concrete beam-column joint under cyclic loads. The crack patterns at different loading stages were monitored. Hanson and Connor (1967) studied an isolated exterior beam-column joint. The study concluded that a joint without transverse reinforcement could sustain limited load because of concrete shear failure and column bars buckling.

The first comprehensive investigation of the behaviour of concrete frame joints under seismic loads was proposed by Park and Paulay (1975). Inadequate or no

transverse reinforcement in the joint zone would significantly reduce the joint shear strength and lead to joint shear failure. The forces acting on an exterior joint are shown in Figure 1-2. Diagonal tensile stresses in the joint zone would result in diagonal cracks. Consequently, concrete compressive strength decreases due to the principal tensile strain normal to principal compressive strain. As shear stresses are mainly resisted by concrete compression strut, degradation of the strut strength would result in a corresponding reduction of joint shear strength and eventually joint shear failure would occur.

ACI-ASCE (1976) presented the first detailed design guidelines for the concrete beam-column joints. The joint shear capacity is a function of the concrete shear strength and the steel ties in the joint zone. The amount of required transverse reinforcement is based on the traditional 45° truss model. These steel ties must be continued into the column for 1/6 of the column height to prevent distress in the column adjacent to the joint core. The bottom beam reinforcement should be hooked up for the exterior joints or continued through the joint for the interior joints. According to the current ACI-ASCE (1997) provisions, the joint shear capacity should be provided by the concrete section alone (Clause 4.3.1). Steel ties must be provided within the joint zone to provide adequate confinement to the joint core and improve the joint ductility.

Anchorage-slip of the beam bars embedded in the joint zone is another source of non-ductile structural response. The anchorage-slip can be defined as the sum of the reinforcement extension and slip in the embedment zone (Alsiwat and Saatcioglu, 1992). According to the pre-seismic code provisions, bottom beam reinforcement was assumed in compression at the negative moment zone and therefore the bars were anchored a short

distance into the joint zone (normally 150 mm). Under reversible lateral seismic loads, the beam at the beam-column joint is subjected to alternating positive and negative moments. A tension force will be developed in the beam bottom bars due to the positive beam moment. In this case, the short anchorage length is inadequate and bond-slip of the bars occurs. In addition, concrete-to-steel bond strength would significantly degrade under cyclic load. The tensile force developed in a steel bar is evaluated as the integration of the bond stress along the embedded length of the bar. Therefore, degradation of bond strength would result in severe reduction of bottom reinforcement strength and corresponding deterioration of structural lateral load strength. Slippage of the bars causes a fixed end rotation at the beam-column interface with significant reduction in the stiffness of the structure.

A recent study of the behaviour of beam-column joints reinforced with plain bars was conducted (Liu and Park, 2001a and b). Although the beam longitudinal bars were bent into the joint core, deterioration of bond stress along the anchorage length of these bars was recorded. The tensile forces of the bars had to be transmitted to the joint core through a compression concrete strut rather than a truss mechanism. It was concluded that, the exterior beam-column joint assembly could only be fully activated if the premature failure associated with the opening of the beam bar hook can be prevented. This emphasizes the importance of providing the joint core with adequate transverse reinforcement. Strengthening the anchorage of these bars is a feasible way to improve the joint response when subjected to seismic loads.

1.2.1 Rehabilitation of joints

Rehabilitation of existing structures has received much attention during the last two decades. Several rehabilitation schemes for structural members, such as concrete jacket, steel jacket and, more recently, composite material jacket, were proposed.

Concrete jacketing of structural frame elements is a viable retrofitting technique. Eleven single and multiple beam-column subassemblies were tested under cyclic load (Corazao and Durrani, 1989). New steel cages were added to the columns, beams and the joint. Concrete was poured to enlarge the joint zone as shown in Figure 1-3. Beam Flexural hinging failure mode occurred instead of joint shear failure mode.

Four interior beam-column subassemblies, including a part of the slab, were constructed (Alcocer and Jirsa, 1993). No transverse reinforcement was installed in the joint region to represent the 1950 construction practice. To strengthen the specimens, concrete jacket was used for the columns only or for the columns and the beams. A steel cage consisting of four steel angles connected together with flat steel plates, was installed around the joint to confine the new concrete, as shown in Figure 1-4. As a result of the strengthening system, the behaviour of the rehabilitated specimens was improved.

Reinforced concrete jacket was used to strengthen three interior beam-column subassemblies (Hakuto, 1995). The joints were designed according to the 1950 New Zealand building code with no shear reinforcement in the joint zone. The retrofitted specimens showed enhancement in strength, ductility and stiffness. It was concluded that joint shear failure could be avoided as long as the diagonal tensile stress in the joint core was kept less than the concrete tensile strength. In spite of the improvement in specimens

behaviour, the proposed rehabilitation procedures using concrete jackets are complex and labour intensive. Therefore, field applications of these systems are not widespread.

Steel jackets were also proposed for strengthening beam-column joints. A comprehensive research program was conducted by the National Center for Earthquake Engineering Research (NCEER), to study the behaviour of interior and exterior, as-built and rehabilitated, beam-column joints. As a part of the program, 34 specimens were tested. Flat steel plates were used to confine the joint in an attempt to prevent the spalling of concrete and to maintain the concrete integrity (Beres et al., 1992a and b), as shown in Figure 1-5. Slight increase in the column shear resistance and storey drift, as compared to the as-built specimen, was recorded. Steel channels were attached to the beam bottom face to prevent the slip of the bars. When testing the retrofitted specimens, an increase of 10% of the specimens stiffness was recorded, the specimens strength was maintained to higher storey drift whereas no increase in the energy dissipated by the specimen occurred. The rehabilitation schemes could not significantly improve the specimens response.

Corrugated steel sheet jacket was used for joint confinement (Ghobarah et al., 1996), as shown in Figure 1-6. A gap was left between the concrete and the jacket to be filled with grout. The joint shear resistance of the rehabilitated specimens was significantly improved and instead of the joint shear failure mode, flexural hinging of the beam took place.

A ¾ scale model of a typical interior beam-column subassembly of a 14-storey reinforced concrete residential building was rehabilitated and tested (Estrada, 1990). Steel plates were anchored to the beam bottom face at each side of the joint and connected

together using threaded steel rods driven through the column, as shown in Figure 1-7. The idea was to transmit the force of the inadequately anchored steel reinforcement using equivalent steel plates. Steel-plate jacket was used to enhance the shear strength of the column and the joint. The strengthening scheme improved the development conditions of the beam bottom bars so that the bars reached the yield strength even though they had inadequate anchorage length inside the joint. Satisfactory performance of the column steel jacket was recorded despite the slippage of the jacket on the interior face of the joint. The specimen reached a drift of 4% without significant deterioration in strength.

To strengthen the anchorage of beam bars; two steel plates were attached to the beam sides, extended to the joint zone and anchored to the concrete beam using 20 mm diameter expansion anchors (Biddah, 1997). Progressive shear failure of the anchors caused a sudden drop of the specimen strength without much increase in ductility.

Fibre reinforced polymer (FRP) composites were recently used for strengthening concrete frame joints. Rehabilitation of beam-column joints using glass fibre reinforced polymers (GFRP) was investigated (Ghobarah and Said, 2001 and 2002). The test specimens were designed with deficient shear strength but with adequate positive beam reinforcement anchoring in the joint. In other words, Anchorage-slip failure was not included in the study. In one rehabilitation scheme, the joint zone was wrapped with U-shaped GFRP sheets. The ends of the composite sheets were tied together using two steel plates and four steel tie rods through the joint. The behaviour of the rehabilitated specimen was significantly improved. The brittle shear failure of the beam-column joint was eliminated and instead a ductile flexural hinging of the beam occurred. Another

rehabilitation scheme was developed by wrapping the joint zone with three unidirectional GFRP straps, mounted at the direction of diagonal tension forces in the joint at ± 45°. The sheets delaminated and bulged at a displacement ductility level of 4.0, which triggered the shear failure of the joint, as shown in Figure 1-8. Although the final failure pattern was a joint shear failure, the rehabilitation scheme improved the joint shear strength, delayed the shear failure and gave the opportunity for creating a flexural hinge in the beam.

Carbon fibre reinforced polymer (CFRP) sheets, were used to strengthen an external beam-column joint in shear (Pantelides et al., 2000; and Clyde and Pantelides, 2002). The retrofitted specimen was wrapped with multiple layers of CFRP sheets. The joint shear capacity was increased by 25% and the specimens reached a storey drift of 5%.

The use of CFRP jacket to strengthen a bridge bent was studied (Pantelides at al., 1997). The cab beam-column joints of a full-scale bridge bent were wrapped using CFRP before demolishing, as shown in Figure 1-9. The bent was tested under lateral load to failure. Satisfactory improvement in the bent ductility and strength was recorded.

Fourteen specimens that represented 1/3-scale model of an exterior beam-column joint were tested under simulated seismic loads (Gergely et al., 2000). Of these, ten specimens were rehabilitated with CFRP sheets, as shown in Figure 1-10. The variables considered were the composite system configuration, fibre orientation, and the concrete surface preparation. Whereas the control specimens showed a joint shear failure, the rehabilitated joints showed more ductile failure mode with significant improvement of

specimens strength, ductility and energy dissipation.

Eighteen specimens that represented 2/3-scale model of exterior beam-column joint were tested (Antonopoulos and Triantafillou, 2003). The specimens were deficient in joint shear strength. The main objective of this study was to evaluate the contribution of FRP to the joint shear strength and hence all specimens, even the rehabilitated specimens, were designed such that joint shear failure occurs. The contribution of FRP composites to the joint shear strength was assessed by comparing the specimen strength with the strength of the control joints. Thirteen specimens were strengthened using different configuration of CFRP sheets or strips whereas only one specimen was strengthened using GFRP sheets. The tests demonstrated the importance of anchoring the FRP sheets to prevent debonding of the sheets from the concrete surface. The composite sheets were found to be more effective if mounted in the beam direction rather than in the column direction.

The use of near surface mounted (NSM) composite bars with composite laminates for rehabilitation of columns and beam-column joints was investigated (Prota et al., 2002). The NSM bars were installed parallel to the column axis to enhance the flexural capacity of the columns, and parallel to the beam axis as a shear reinforcement in the joint. To prevent the debonding of these bars from the concrete surface, composite laminates were wrapped around the columns and the joint perpendicular to the NSM bars. Considerable improvement in strength and ductility of the specimens was recorded. However, further investigations are needed to study the debonding of NSM bars under compressive stresses and the possible practical field applications.

1.2.2 Modeling of beam-column joints

Experimental evidence showed that the deformation of beam-column joint has substantial influence on the structural response under ground excitations. The joint deformation is governed by shear deformation and bond behaviour of the beam bars. Satisfactory joint behaviour is characterized by minimal contribution of joint distortion to storey drift. Ideally, for well-designed and detailed joint, the joint contribution to storey drift decreases with increasing storey drift as a result of hinging of the adjacent beams. For inadequately designed joint, the contribution of joint distortion to storey drift increases with increasing storey drift due to the cracking of the joint which may consequently lead to joint failure.

Only a limited number of analytical models that consider the shear and bond-slip deformations in beam-column joints are available. Pessiki et al. (1990) proposed a simple kinematic model for the joint zone. The beams and columns frame into rigid members, which were pin-connected to form a box at the joint location. The stability of the box was maintained using a diagonal spring. Flexibility was introduced to the structure as the box deforms. However, this model was not developed into a working model.

Biddah and Ghobarah (1998) developed a model that simulates the behaviour of beam-column joints under cyclic loads. The model was composed of two rotational springs in series, one represented the joint shear deformation and the other represented the beam bars bond-slip, as shown in Figure 1-11. The shear deformation was estimated as the difference between the rotations at the beam and column ends, which equals to the rotation of the shear rotational spring. The beam bars bond-slip was represented as

another rotational spring that has a bilinear M-θ relationship. The model was capable of predicting the strength degradation and pinching effect in a satisfactory manner.

Elmorsi (1998) avoided the need for using refined meshes of simple finite elements, e.g. quadrilateral plane stress elements, by using high power elements in the critical regions of the joint panel and plastic hinge zones in the beams and the columns. To model the shear strain inside the element, which has a quadratic distribution, a cubic displacement field was used. Therefore, twelve-node inelastic plane stress element, with nodes displacement as degrees of freedom, was developed. The beams and the columns were modeled using beam-column elastic element. Ten-node inelastic plane stress element was used as a transition element to connect the joint element to the beam-column element, as shown in Figure 1-12. The transition element was used to provide gradual transition between the cubic displacement field to the linear displacement field. In addition, it would model the inelastic behaviour of beams and columns that is usually concentrated at the member ends. The reinforcement bars were modeled as inelastic truss element. The shear reinforcement was represented as smeared reinforcement in the element. The model was verified using well-designed and detailed joints tested by Kaku and Asakusa (1991) and satisfactory results were obtained. However, the capability of the model to predict the shear behaviour of existing deficient joints was not demonstrated.

Youssef (2000) modeled the joint shear behaviour using two diagonal springs, as shown in Figure 1-13. The modified compression field theory (Vecchio and Collins, 1986) was used to define the backbone response of the shear force-deformation relationship. Inelastic zero-length concrete and steel springs were developed to represent

the nonlinear beam and column flexural behaviour. Bond-slip of the steel bars was implemented in the material model of the bars. Therefore, the constitutive relation of the steel bars represented not only the stress-strain relation of steel but also the interaction between the steel and the concrete.

Finite element modeling of the beam-column connections was carried out by several researchers. Baglin and Scott (2000) used non-linear finite element analysis software package, SBETA (Cervenka, 1992), to analyze a beam-column subassembly under monotonic loads. First-order quadrilateral plane stress elements were used for meshing the specimen, as shown in Figure 1-14. Mesh refinement was carried out at critical regions such as concrete compression zone and joint shear diagonal strut. The specimen was subjected to monotonic loads applied at the beam tip. The model showed good correlation with the experimental results. The intention of this study was to validate the capability of SBETA package to model the non-linear structural behaviour. Using detailed models with a refined mesh at each joint in analyzing a complete structure is time consuming and impractical.

Shiohara (2001) proposed a new technique for modeling the interior beam-column joints. In this model, the joint shear capacity was assumed to be preserved and maintained. Therefore, the degradation of storey shear was related to the anchorage deterioration of the beam bars passing through the joint not to the degradation of the joint shear strength. The joint was divided into four segments, connected together using a horizontal spring, which represented the joint shear reinforcement with the beam bars, and a vertical spring, which represented the column bars passing through the joint as

shown in Figure 1-15. The equilibrium equations of the internal forces in the four segments resulted in five equations to be solved simultaneously. By solving these equations the storey shear is evaluated, assuming the tensile forces of beam bars and joint ties are known. The model was mainly used for predicting the storey shear at joint shear failure. It was assumed that the storey shear is only function of the tensile forces in the beam bars, which are dependent on the anchorage capacity, and not affected by joint shear reinforcement. Therefore, a robust model is required to predict the anchorage capacity, which is not currently available.

A macro model was proposed to model the inelastic response of reinforced concrete (RC) buildings (Lowes and Altoontash, 2002). The model accounts for the shear failure in the joint, the anchorage failure of the beam and column bars and the interface-shear failure at the joint perimeter. A shear panel component, as shown in Figure 1-16, was developed to model the inelastic behaviour associated with joint shear failure. Bar-slip spring was developed to represent the inelastic behaviour associated with the anchorage failure. The model can be implemented in two-dimensional non-linear structural analysis software packages.

1.3 MOTIVATION

When subjected to strong ground excitation, existing structures may suffer severe cracking in the joint zone. This would result in a degradation of joint strength which would significantly contribute to storey drift and may lead to overall structural collapse. Several schemes were proposed for rehabilitation of joint shear strength using concrete

jacket, flat steel plates and corrugated steel sheets jacket. However, these retrofit schemes are difficult, labour intensive and disruptive to the function of the structure. Limited experimental investigation of retrofitting the anchorage-slip of beam bars was conducted. Therefore, there is a persistent need to develop economical, effective and non-disruptive rehabilitation techniques for strengthening the shear resistance and preventing the anchorage-slip in beam-column joints.

Most of the available structural software packages ignore the deformation in the joint zone, and assume a rigid beam-column joint. This assumption is reasonable for well-designed and detailed joints. However, for many of the existing buildings this assumption is not valid. A non-linear dynamic analysis program to assess the existing structures before rehabilitation is needed. The effective design and development of various rehabilitation techniques is only possible if representative modeling of the rehabilitation scheme and analytical tools for predicting the structural behaviour before and after rehabilitation is available.

1.4 OBJECTIVES

The objectives of the present research are:

1. To develop several rehabilitation techniques to enhance the beam-column joint shear resistance and to account for the anchorage failure of the beam reinforcement bars, and hence to improve the ductility of existing concrete frames when subjected to seismic loads.
2. To develop a joint model that is capable of evaluating the behaviour of existing

concrete frames when subjected to seismic loads. The joint model should also be capable of evaluating the response of the rehabilitated concrete frames.

1.5 SCOPE

The present research is focusing on the rehabilitation of exterior joints, as it is believed that the shear strength of exterior joints are more vulnerable than interior joints which are partially confined by beams attached to the four sides of the joint and contribute to the core confinement. On the contrary, the anchorage-slip failure mode of exterior and interior joints is similar. To achieve the research objectives, the scope of this research includes:

1. Developing an experimental program to examine the behaviour of concrete frame joints with no shear reinforcement in the joint zone and/or with inadequate anchorage length of beam bottom bars. The experimental program includes testing of twelve exterior beam-column subassemblies. Three joints were constructed and tested to represent deficient existing joints. The other joints were rehabilitated then tested.
2. Proposing jacketing schemes using GFRP or CFRP sheets to upgrade the joint shear resistance.
3. Evaluating rehabilitation techniques to account for the anchorage failure of inadequately anchored beam bars.
4. Proposing simple guidelines for designing the proposed rehabilitation systems that could be used for preliminary design purpose.

5. Developing concrete material model to predict the monotonic compression behaviour of FRP-confined concrete elements.
6. Developing steel model to predict the anchorage-slip behaviour of embedded steel bars.
7. Developing shear models to predict the behaviour of concrete joints without shear reinforcement, or with externally bonded FRP sheets.
8. Incorporating the developed models into a structural analysis computer program to verify the validity of these models to predict the behaviour of existing concrete frame joints before and after rehabilitation.

1.6 ORGANIZATION

This thesis is organized into nine chapters. Chapter 2 describes the proposed experimental program. Detailed description of the test beam-column specimens, test set-up and loading routine is presented. The proposed rehabilitation techniques are described. The parameters that will be used to evaluate the joint response are also presented.

Chapter 3 describes the response of four beam-column joints with deficient joint shear strength. Three joints are jacketed using GFRP or CFRP sheets. Chapter 4 describes the experimental response of three beam-column joints with deficient anchorage length of beam bars. Two joints are strengthened using CFRP sheets. The behaviour of five beam-column joints with deficient joint shear strength and beam bars anchorage length is presented in Chapter 5. Four of these joints are strengthened using composite sheets or steel elements.

In Chapter 6 the material models for concrete, FRP sheet and steel reinforcement are presented. Detailed description of the new FRP-confined concrete model is outlined. The FRP model that represents the response of composite sheets under tension and compression is described. The steel-to-concrete bond laws, and a simple but sufficiently accurate steel model that considers the anchorage conditions in concrete joint are discussed.

Three shear models are described in Chapter 7. The first model uses the strut and tie model to predict the response of concrete joints without shear reinforcement. The two other models use the modified compression field theory to predict the shear behaviour of concrete joints with steel ties or externally bonded FRP sheets.

Kinematic models for beams, columns and beam-column joints are described in Chapter 8. The analytical response of nine existing and strengthened beam-column joints is predicted and compared to the experimental behaviour to assess the proposed shear and material models.

In Chapter 9, conclusions of the study and recommendations for future research are presented.

Simple guidelines for designing the proposed rehabilitation techniques are presented in Appendix A. In Appendix B, Fortran program BOND1, that predicts the monotonic response of steel bars under pull-out force, is listed.

Figure 1-1 Structural collapse due to beam-column joint failure

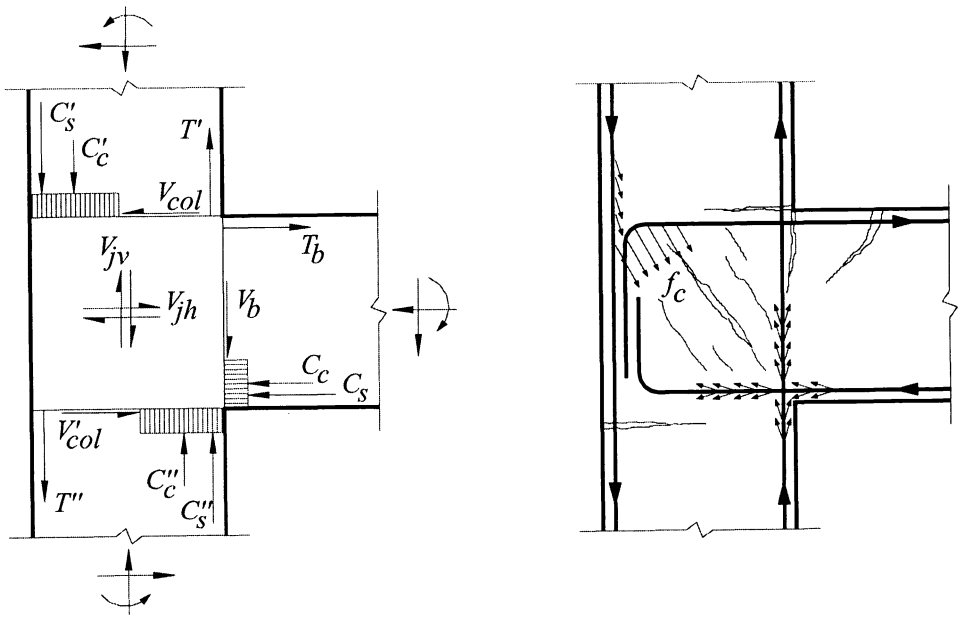

(a) Stress resultant (b) Crack pattern

Figure 1-2 Applied load and crack pattern of an exterior beam-column joint

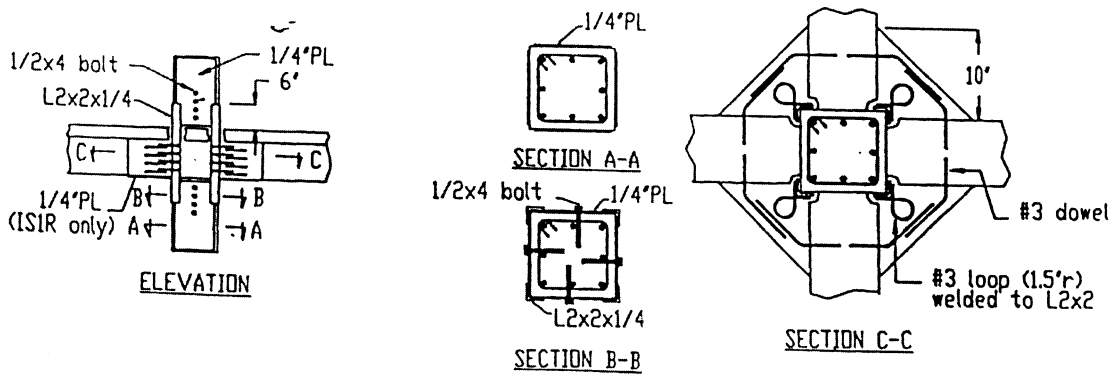

Figure 1-3 Details of external steel reinforcement of concrete jacket (Corazao and Durrani, 1989)

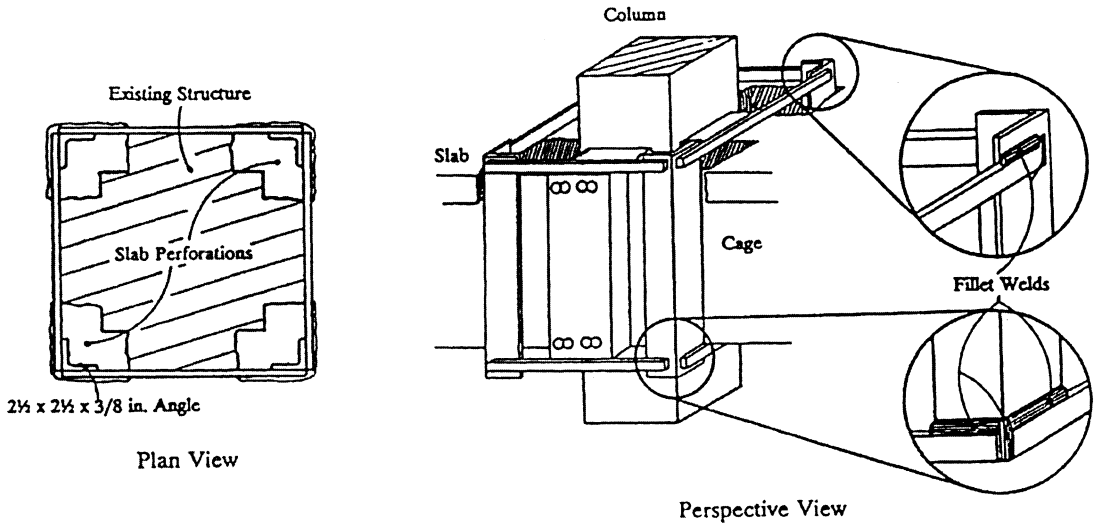

Figure 1-4 Beam-column joint confinement cage (Alcocer and Jirsa, 1993)

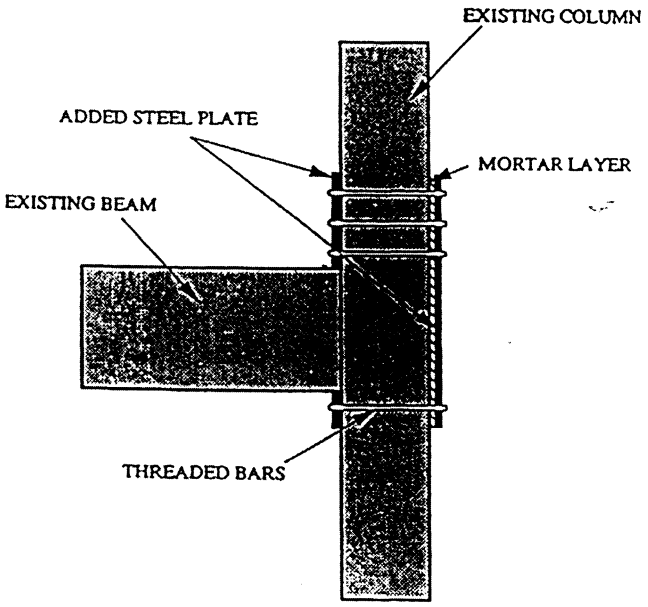

Figure 1-5 Confinement of the joint zone with flat steel plates (Beres et al., 1992a and b)

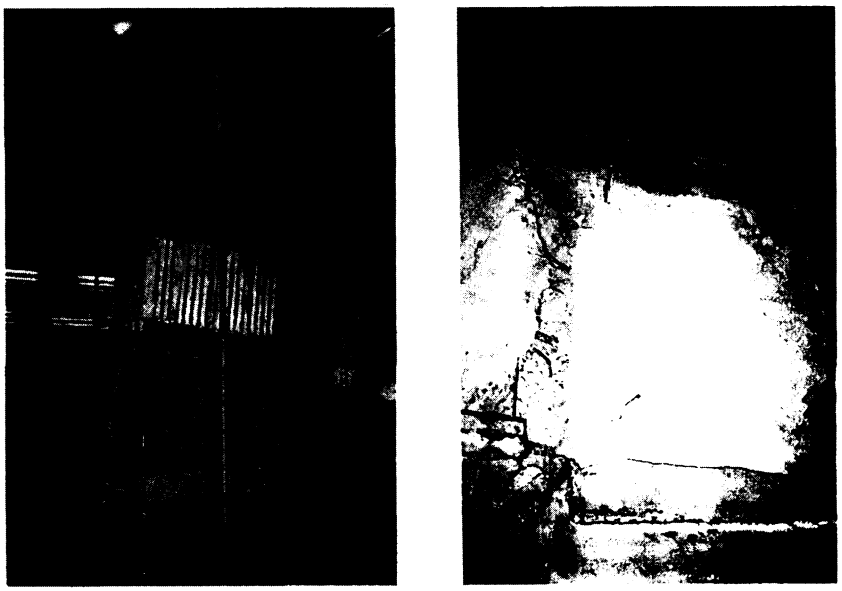

(a) At end of the test (b) After removing the steel jacket

Figure 1-6 Corrugated steel sheet jacket for the beam and columns (Ghobarah et al., 1996)

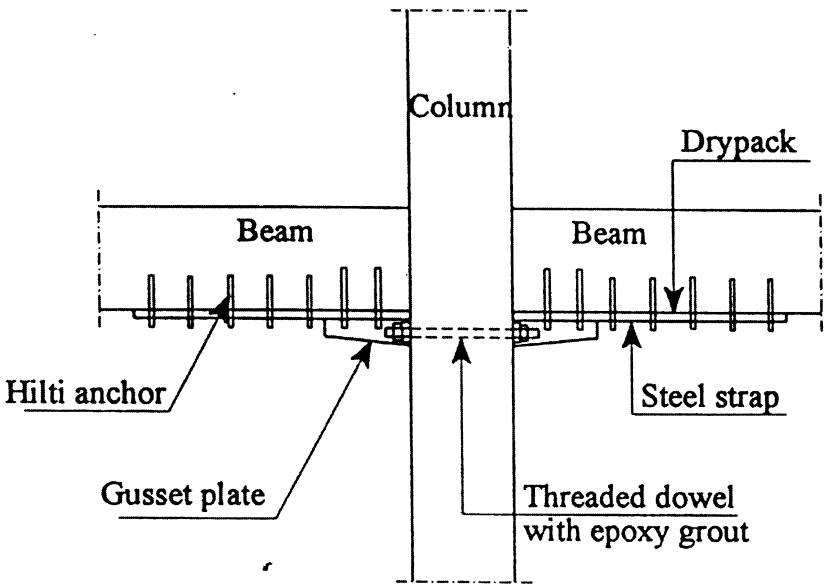

Figure 1-7 Strengthening the anchorage of beam bars (Estrada, 1990)

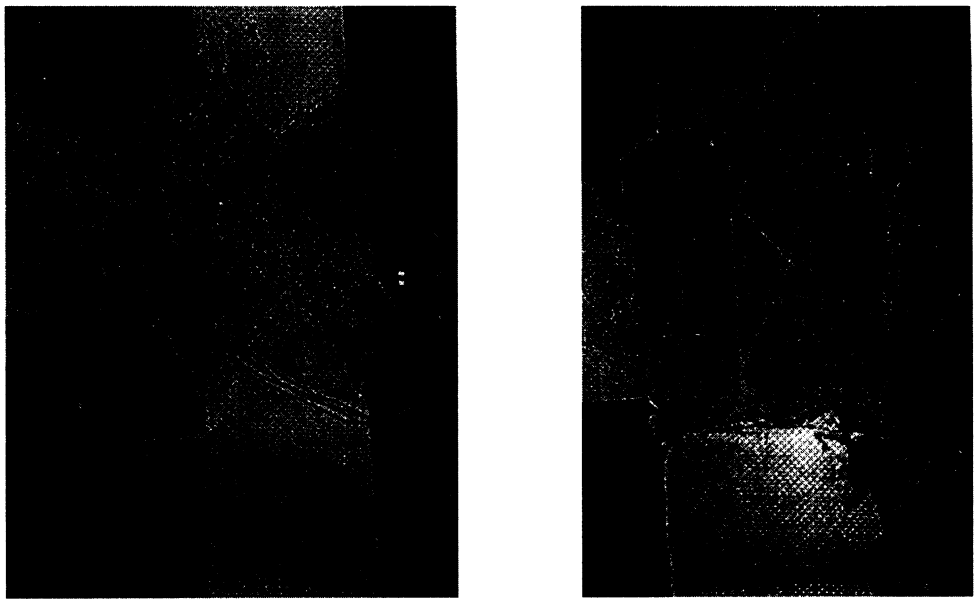

Figure 1-8 Crack pattern of GFRP-rehabilitated joints (Ghobarah and Said, 2001 and 2002)

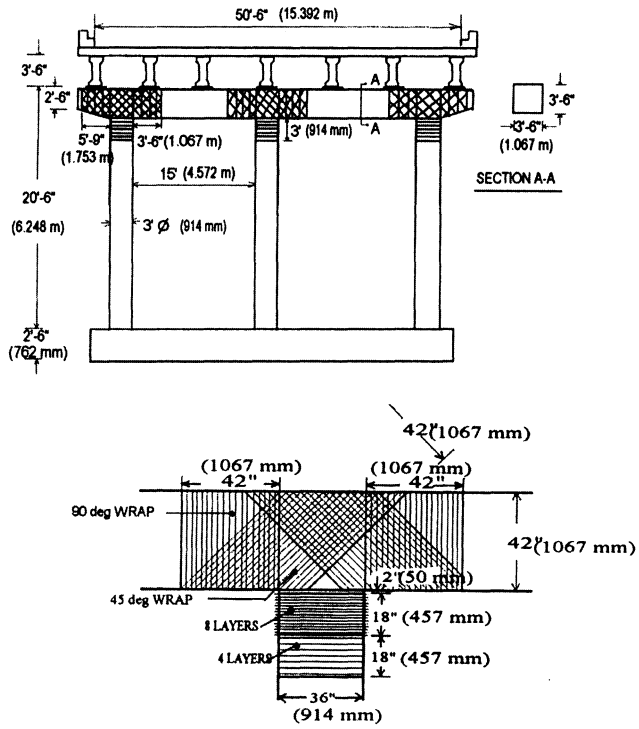

Figure 1-9 Application of CFRP sheets to bridge bent (Pantelides et al., 1997)

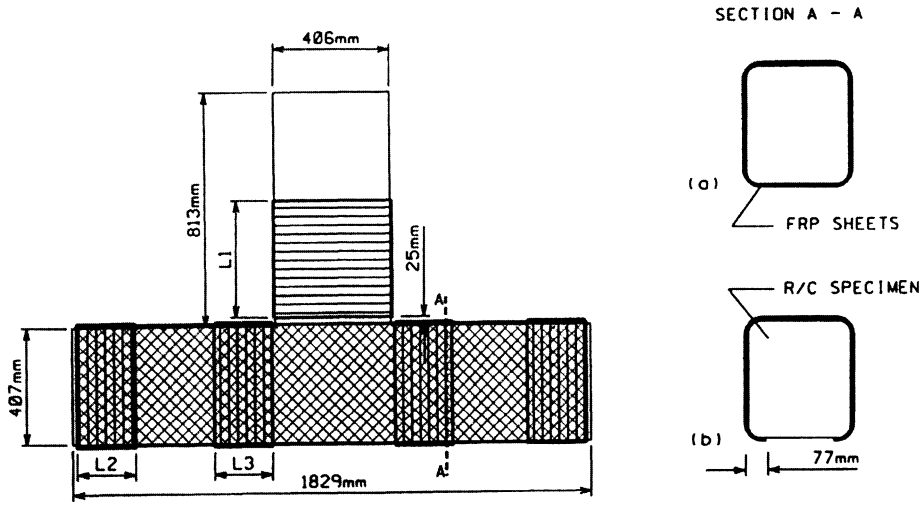

Figure 1-10 CFRP jacket for exterior joint (Gergely et al., 2000)

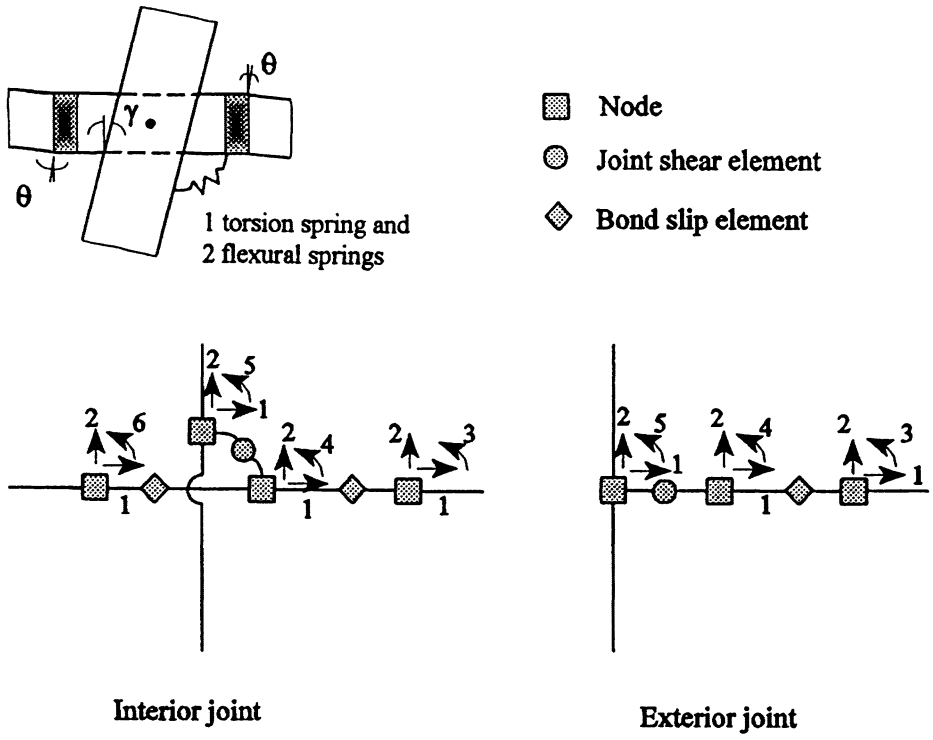

Figure 1-11 Modeling of beam-column joint (Biddah and Ghobarah, 1998)

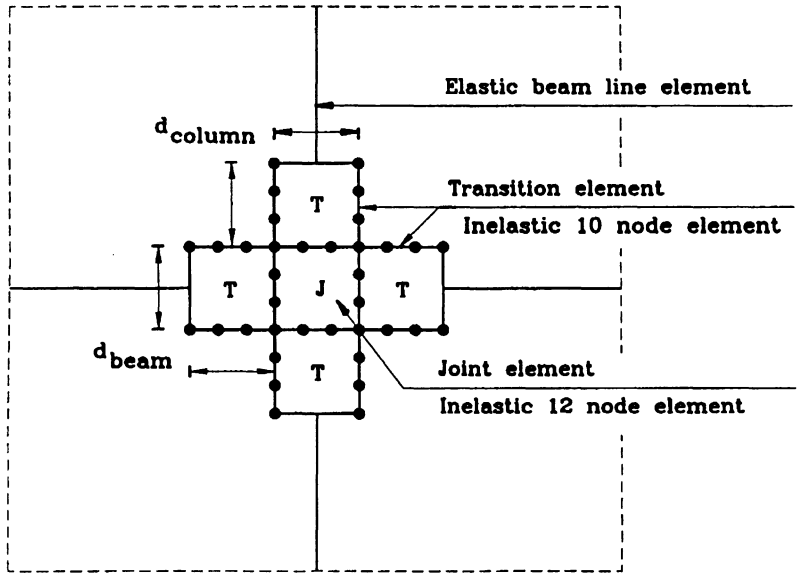

Figure 1-12 High order 12-noded beam-column element (Elmorsi, 1998)

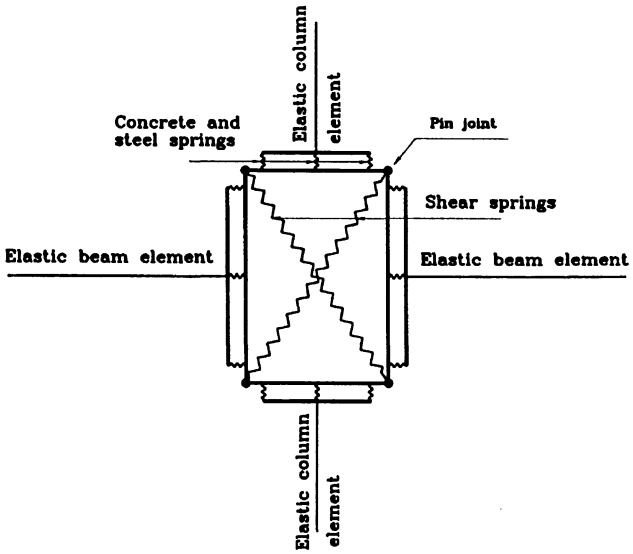

Figure 1-13 Macro-modeling of beam-column joint (Youssef, 2000)

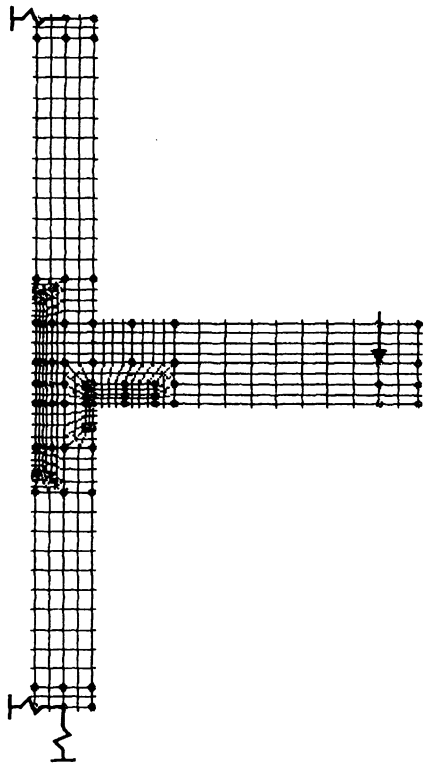

Figure 1-14 Finite element modeling of beam-column joint (Baglin and Scott, 2000)

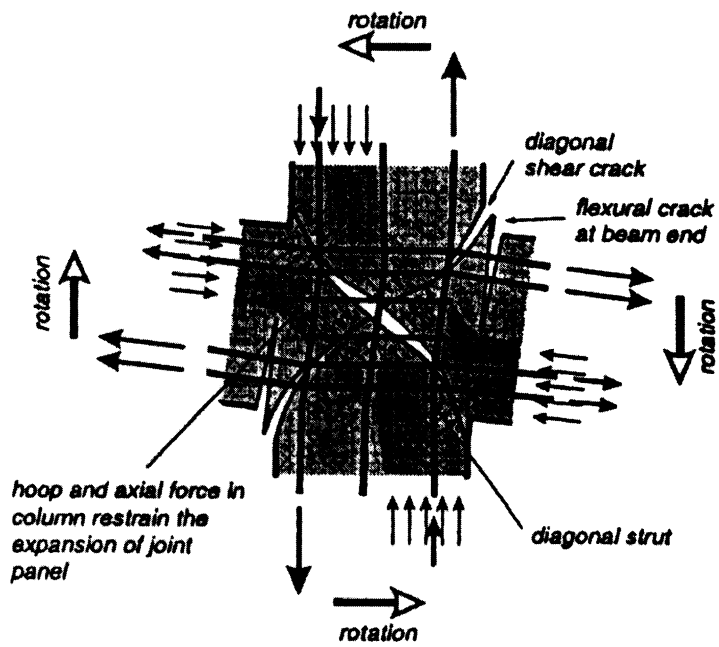

Figure 1-15 Crack pattern and stresses path in beam-column joint (Shiohara, 2001)

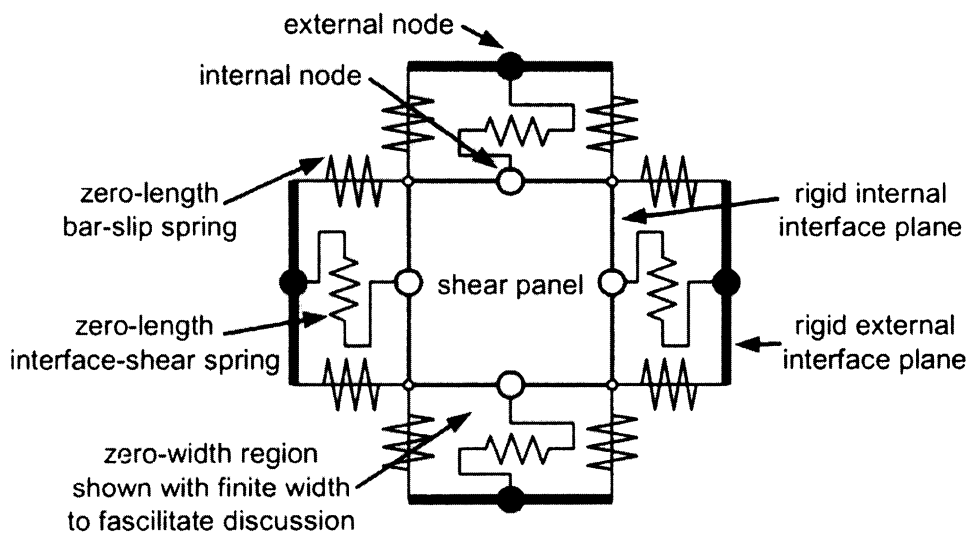

Figure 1-16 Components of beam-column joint model (Lowes and Altoontash, 2002)

Chapter 2

EXPERIMENTAL PROGRAM

2.1 INTRODUCTION

Twelve full-scale beam-column joints were tested. The joints represented exterior concrete frame joint that was built in accordance to the pre-1970 code provisions (ACI 318-63, 1968). Three control joints and nine rehabilitated joints were tested under a cyclic load applied at the beam tip. The joints represented a component of a reinforced concrete frame with floor-to-floor height of 3.00 m and 3.74 m bays. The joints were categorized into 3 groups, *shear-deficient joints*, *bond-deficient joints*, and *shear/bond-deficient joints*. The first group represented the beam-column joints with shear strength deficiency, the second group represented the joints with beam bars anchorage deficiency and the last group represented the joints with combined joint shear and beam bars anchorage deficiencies. A detailed description of the experimental program is presented in this chapter.

2.2 JOINTS DESIGN AND DETAILS

The selected joints were part of an exterior lateral load resisting concrete frame as shown in Figure 2-1. They were designed and detailed according to the pre-1970 code provisions. The beam and column cross sections were selected to be 250 mm wide and 400 mm deep. The joints were designed assuming that points of contra-flexure occur at

mid-height of columns and mid-span of beams. The frame bay was 3.74 m wide and the floor height was 3.00 m, which represent a typical residential building frame. The test specimen included the beam-column joint and the adjacent beams and columns to the points of contra-flexure. The nominal concrete compression strength and steel yield strength used in the design were 25 and 400 MPa, respectively. The joints were divided into three groups, as shown in Figure 2-2. In order to identify the specimens, letter T was used to describe the shape of the specimens, letter S was used to indicate to shear deficiency and letter B was used to indicate to bond-slip deficiency.

2.2.1 Shear-deficient joints "T-S"

Four joints were constructed to represent the joint shear strength deficiency. A control joint T-S1 and three rehabilitated joints T-S1RR, T-S4R and T-S5 were tested. The beam was reinforced with 4#20 bars as top and bottom flexural reinforcement. Both beam top and bottom bars were hooked into the joint zone to enhance the bars anchorage condition and eliminate the bond-slip failure mode. The bars were extended for a distance of 12 times the bar diameter beyond the 90° hook. The beam was reinforced using #10 stirrups. The first stirrup was placed at a distance of 75 mm from the column face, then the stirrups were spaced at 150 mm for the following 600 mm of the beam length, and then spaced at 200 mm for the rest of the beam span. The column was reinforced using 3#20 bars at each side, and 2#15 intermediate bars as longitudinal reinforcement and using #10 ties spaced at 200 mm. No ties were placed inside the joint to represent the pre-1970 construction. Some characteristics of typical reinforcement details, such as column bars lap splice, were suppressed to avoid undesirable failure modes which are not of

interest in this study. The specimen dimensions and reinforcement details are shown in Figure 2-3. The beam flexural capacity was estimated to be 198.3 kN.m, in both the positive and negative moment directions, whereas the column flexural capacity was estimated to be 205.2 kN.m under axial load of 600 kN. The column strength is higher than the beam strength to avoid the *"strong beam-weak column"* condition. After testing joints T-S1 and T-S4, the spalled concrete was removed, new strain gauges were installed and new concrete was poured in the joint area, then the joints were prepared for retesting. These joints were renamed as T-S1RR and T-S4R.

2.2.2 Bond-deficient joints "T-B"

Three joints T-B10, T-B11, and T-B12, were constructed to represent beam bars anchorage deficiency. The joint T-B10 represented the control joint whereas joints T-B11 and T-B12 were strengthened with carbon fibre reinforced polymer (CFRP) sheets. The beam was reinforced with 2#20 as top and bottom flexural steel. The top bars were anchored into the column with a 90° hook whereas the bottom bars were anchored 150 mm into the beam-column joint. This length represents 26% of the bars development length required to reach their yield strength according to CSA A23.3 (1994) Clause 12.2.2. The beam was reinforced using #10 stirrups with the same spacing as joints T-S. The column was reinforced using 3#20 bars at each side, and 2#15 intermediate bars as longitudinal reinforcement and using #10 as transverse reinforcement. To eliminate the possibility of joint shear failure mode, the beam-column joint was reinforced with 4#10 ties. The specimen dimensions and reinforcement details are shown in Figure 2-4. The theoretical beam flexural capacity was estimated to be 103.9 kN.m, in both the positive

and negative moment directions, whereas the column flexural capacity was estimated to be 205.2 kN.m under axial load of 600.0 kN. This ensures that column failure is avoided.

2.2.3 Shear/bond-deficient joints "T-SB"

Five joints were constructed to represent the existing concrete joints that suffer from both the joint shear strength and beam bars anchorage strength deficiencies. Joint T-SB3 represented the control specimen whereas joints T-SB3R, T-SB6, T-SB7 and T-SB8 were strengthened then tested. The beam was reinforced with 4#20 as top and bottom reinforcement bars. The beam top bars were anchored into the column with a 90° hook whereas the beam bottom bars were anchored 150 mm into the beam-column joint. The beam was reinforced using #10 stirrups spaced as in joints T-S. The column was reinforced using 3#20 bars at each side, 2#15 intermediate bars as longitudinal reinforcement and using #10 bars spaced at 200 mm as transverse reinforcement. No ties were installed in the beam-column joint. The specimen dimensions and reinforcement details are shown in Figure 2-5.

2.3 MATERIAL PROPERTIES

2.3.1 Concrete

The specified concrete compressive strength $f_c^{'}$ was selected to be 25 MPa. Concrete test cylinders were cast with the joints. Three cylinders were tested after 7 days, 28 days and on the joint test day, to determine the concrete compressive strength, in accordance to the ASTM-C39-96 (2002) specifications. Three cylinders of each batch

were tested after 28 days, to determine the concrete splitting tensile strength, in accordance to the ASTM C496-96 (2002) specifications. For some batches, the concrete modulus of elasticity was determined in accordance to the ASTM C469-94 (2002) specification. The modulus of elasticity is assumed to be equal to the secant modulus at stress of 40% of the ultimate strength. The measured modulus of elasticity was marginally higher than that given by the CSA A23.3 (1994) Clause 8.6.2 by 6.6%. The measured concrete properties are summarized in Table 2-1.

2.3.2 Steel

Grade 400 MPa steel reinforcement deformed bars were used as principal and transverse reinforcement. The yield and ultimate tensile strengths of these bars are summarized in Table 2-2. For rehabilitated joints, Unified Inch Coarse Screw Threads (UNC) steel rods of diameters 12, 16, 20, 25 and 32 mm were used. Samples of these rods were tested to determine their yield and ultimate strengths. The threads were removed from the middle part of the rod sample then the sample was machined to reduce its diameter and ensure that the failure occurred away from the machine grips. Two strain gauges were attached to each sample to measure the longitudinal strain. The rod yield strength was estimated to be the strength at an offset strain of 0.1% (ASTM-A370-02, 2003). The effective cross sectional area of the rods were provided by the manufacturer. The test results of the rod samples are summarized in Table 2-3.

2.3.3 Fibre reinforced polymer sheets

Fibre reinforced polymer (FRP) sheets are composed of continuous fibres embedded in a resin matrix that allows the fibres to work together as a single element.

Carbon fibre reinforced polymer (CFRP) and glass fibre reinforced polymer (GFRP) sheets were used in this study for joint rehabilitation. MBrace composite strengthening system, provided by Master Builders Technologies (2000), was used with uni-directional CFRP and GFRP sheets. Tyfo composite sheets, provided by Fyfe Co. (2000), were used with uni-directional and bi-directional GFRP sheets. The properties of these sheets as provided by the manufacturers, are presented in Table 2-4.

To attach the composite sheets to the concrete surface, adjoining types of epoxy were used as recommended by the manufacturers. For the MBrace sheets, MBrace™ Primer was used to improve the concrete-surface tensile and bond strengths. The Primer is composed of two parts, Part A which is a resin and Part B which is a hardener. The two parts were mixed at a ratio of 3:1 by volume. A paint roller was used to cover the concrete surface with a thin layer of the Primer. MBrace™ Saturant LTC was used to apply the sheets to the concrete surface. The Saturant, like the Primer, is composed of two parts, Part A which is a resin and Part B which is a hardener. Part A was stirred separately then the hardener was added with a ratio of 3:1 by volume and mixed together for three minutes. The concrete surface was then coated with the Saturant. The composite sheets were saturated with the Saturant before being applied to the concrete surface. Tyfo S epoxy was used with the Fyfe Co. composite sheets. The two parts of the epoxy were premixed with a ratio of 100:42 by volume and thoroughly mixed for five minutes with 400-600 RPM mixer until uniformly blended, then applied in the same way as the MBrace Saturant. Table 2-5 presents the properties of the adhesives used in this study.

2.3.3.1 Tensile tests of FRP coupons

To verify the given properties of the composite sheets, samples were tested in tension in accordance to the ASTM D3039-95 (2002) specifications. CFRP and GFRP coupons were prepared. Each coupon was 500 mm long. To avoid the rupture of the coupon at the machine grips, the coupon ends were thickened with six 150 mm long sheets, as shown in Figure 2-6. The coupons were loaded in tension and the strain was measured using an electric strain gauge. The force/unit width is plotted versus the strain, as shown in Figure 2-7 and Figure 2-8. In cases where the strain gauges were damaged before the coupon rupture, a dashed line was extended to the rupture point. The properties provided by the manufacturer are also plotted in the figures. The common failure mode was splitting of the coupon at the middle part. Some coupons ruptured at the machine grips and so their results were excluded. The test results are summarized in Table 2-6, and some of the failure patterns are shown in Figure 2-9.

2.3.3.2 FRP anchors

In joints T-S4R and T-S5, FRP anchors were installed right through the beam-column joint to anchor the wrapped sheets on both sides of the joint. For joint T-S4R, four CFRP anchors were used; each was made of 30 tows, 500 mm long, and bundled together to form a rod. The anchors were saturated with the Saturant, inserted inside pre-drilled holes right through the joint then the anchor ends were well spread on the composite sheets. For joint T-S5, four GFRP anchors were used, each was composed of 50 tows, 500 mm long, and bundled together to form a rod. They were installed in the

same way as the CFRP anchors. The number of tows in each anchor was chosen to transmit a tensile force that is higher than the tensile strength of the composite sheets between two successive anchors and higher than the tensile strength of 1/2 in. (12.2 mm) diameter steel rod used to anchor the composite sheets in a previous study (Said, 2000).

2.4 JOINT CONSTRUCTION

The joints were constructed in a horizontal position. Three sets of wooden forms were designed for easy assembly and disassembly after casting. The bottom and the sides of the forms consisted of 5/8 in. plywood with the sides stiffened with 2 in. square border. The gaps between the plywood sheets were sealed with tape to prevent bleeding of the concrete that may occur during casting. Prior to assembling the reinforcement cage, some of the steel bars were instrumented with strain gauges. The ribs on the bars were removed and the bars were smoothed at the strain gauge locations. For assembling the reinforcement steel, the column longitudinal bars were positioned using the two end ties after sliding all the column ties inside. The beam longitudinal bars were then positioned perpendicular to the column longitudinal bars using the beam two end stirrups after sliding all the beam stirrups from the far beam end. The column and beam transverse reinforcement were then positioned and tied to the longitudinal bars with a flexible steel wire. The wooden forms were coated with a thin film of oil to facilitate stripping of the forms without damage. Steel chairs were used to maintain the proper cover distance between the form and the reinforcement bars. The sides of the forms were

tied together using threaded steel tie rods to prevent bulging of the form under the lateral pressure of wet concrete. The concrete was delivered to the laboratory by concrete truck. The concrete consists of Portland cement (#10) with content of 238 Kg/m^3; coarse aggregates of maximum size 20 mm, fine aggregate (sand) and water. The target slump was 75 mm. The concrete was mechanically vibrated to eliminate voids. Several hours after casting, the joints were covered with wet burlap to provide a moist curing environment. Polyethylene sheets were used over the burlap sheets to retain the moisture. After three days, the forms were stripped then the specimens were cured for another seven days. Concrete cylinders were poured with each batch and cured in the same manner as the joints. Before testing, the joints were painted with a flat white paint to aid in locating the cracks.

After testing once, some joints were repaired for retesting. These joints were distinguished by the letter "R" beside its label, e.g. T-SB3R. The joints were laid horizontally and the disintegrated and spalled concrete was removed using air hammer. New strain gauges were installed on the reinforcement bars then the joints were put into the wooden forms again and washed with water to remove the dust and any small particles before casting the concrete. The concrete mix was designed and prepared in the laboratory. It consists of Portland cement (#10); coarse aggregates of maximum size 10 mm, fine aggregate (sand) and water. The repaired joints were cured in the same manner as the original joints.

2.5 REHABILITATION SYSTEMS

Several rehabilitation schemes were proposed to enhance the joint shear strength and to account for the anchorage failure of beam bars. For joint shear strengthening, composite sheet jackets were applied to the joint zone. To confine the concrete in the joint zone, steel or FRP anchors were installed right through the joint at the free ends of the sheets. In some joints, the plastic hinge regions in the beam and columns were also wrapped with FRP sheets.

To account for the anchorage failure of beam bottom bars, three rehabilitation schemes were proposed. CFRP or GFRP sheets were attached to the beam bottom face and extended to the column inner face. A steel angle was installed at the beam-column corner to prevent the sheets debonding from concrete surface. In another scheme, new steel rods were installed below the existing beam bottom bars as additional flexural reinforcement. In the last scheme, a steel bridle was welded to the beam reinforcement bars and anchored to the column backside, in order to prevent the slip of the beam bars.

Simple design guidelines for estimating the components of each rehabilitation system are presented in Appendix A. Detailed sketches of the proposed rehabilitation schemes are shown in Figure 2-10. A detailed description of the strengthening scheme of each joint is described in Chapters 3 to 5.

2.6 APPLICATION OF FRP SHEETS

Special care was given to the application process of composite sheets to the

concrete surface, as the quality of the bond between the sheets and the concrete surface is crucial in the efficiency of the strengthening technique. In general, application of FRP composite systems are divided into two categories:

(a) Contact-critical, e.g. column jacketing.

(b) Bond-critical, e.g. FRP sheets bonded to the beam bottom face.

In both cases, as recommended by several specifications such as ICBO-AC178 (2001), the concrete surface must be smooth, clean from protrusions, free of sharp edges and protrusions that may cause voids behind the sheets or may damage the fibres. In case of uneven surfaces, a special epoxy paste, such as MBrace™ Putty, could be used to level the surface. In a recent study (Chajes et al., 1996), the effect of surface preparation was investigated. The investigated types of surface preparation techniques were:

(1) No surface preparation

(2) Grinding with a stone wheel to give a smooth finish

(3) Mechanical abrading with a wire wheel to slightly expose the aggregate.

Single-lap shear tests were conducted on specimens in which one-inch wide epoxy/graphite plates were bonded to concrete. Whereas the grinding technique gave fair results, the mechanical abrasion of the concrete surface gave the highest bond stress between the concrete and the FRP sheets.

In the current study, the concrete surface was mechanically ground before applying the composite sheets. Any bumps or protrusions were removed and the sharp corners were rounded to a radius of about 12 mm. The uneven concrete surface was levelled using the epoxy mortar Sikadur 31-Hi-Mod-GEL. Finally, the concrete surface

was brushed using a wire brush and compressed air.

Application of the different types of FRP sheets on the concrete surface was similar regardless of the type of the sheet. The two parts of the Primer were mixed using an electric mixer then the Primer was used to cover the concrete surface with a thin layer. The Primer was left for an hour to harden. The two parts of the Saturant were mixed then the FRP sheets were impregnated with the Saturant and the concrete surface was covered with thin layer of the Saturant. The FRP sheets were laid down on the concrete surface, adjusted and pressed against the surface using a steel roller to remove the excess adhesive and the entrapped air between the sheets. The sheets were allowed to cure at least 7 days at room temperature before testing.

2.7 TEST SET-UP

The specimens were tested in the column vertical position, hinged at the top and bottom column ends and subjected to a cyclic load applied at the beam tip using a hydraulic actuator of stroke ± 254 mm. Two 20 mm thick steel plates were connected together by four 20 mm diameter threaded rods to form a collar. The collar connected the loading ram to the beam tip. The bottom column hinge consisted of two identical 38 mm thick steel plates with semi-spherical groove and were separated by a steel ball. The top column hinge consisted of a semi-spherical steel plate rested against a reaction beam. The top and bottom column ends are supported laterally against a reaction frame. Figure 2-11 shows a schematic diagram of the test set-up and Figure 2-12 shows a photograph of a

joint in the test set-up before testing.

A constant axial load of 600 kN was applied to the column. The load was applied using a hydraulic jack and measured using a load cell. This load represents the gravity load that acts on the column, and was approximately equal to $0.2A_g f_c^{'}$, where A_g is the column cross-sectional area and $f_c^{'}$ is the concrete compressive strength. However the column load was continuously adjusted to remain constant during the test, slight variations of column load, as a result of the vertical reaction of the applied cyclic load at the beam tip, was unavoidable.

2.8 LOADING ROUTINE

A quasi-static cyclic load was applied at the beam tip of the test joints. The load was selected to cause forces that simulate high levels of inelastic deformations that may be experienced by the structure during severe earthquake shaking. Quasi-static cyclic loading gives a conservative estimate of the real strength of the structural element because earthquake forces are dynamic and increase the strain rate which generally increases the structural strength and stiffness (Mander et al., 1988; and Park, 1994). The loading routine, as shown in Figure 2-13, consisted of two phases, load control phase followed by displacement control phase.

2.8.1 Load control

The first phase was a load control where the beam was subjected to an increasing cyclic load. During the first cycle, the beam was loaded up to 3.0 kN up and down to

verify that the instruments were working properly. During the second cycle, the beam was loaded to cracking. The cycle was repeated again to the same cracking load. During the next cycle, the beam was loaded until yielding of the top and bottom bars was reached. The beam-tip displacement corresponding to the yielding load, Δ_y was recorded. The second loading phase, displacement control, was initiated at this point.

2.8.2 Displacement control

The beam was loaded to reach multiples of the recorded yield displacement which represent the displacement ductility level. Two cycles were applied at each ductility level to verify the stability of the hysteretic joint behaviour. In order to capture the post-peak strength behaviour of the joint, the test continued until the beam load degraded to less than 25% of the recorded ultimate strength.

2.9 INSTRUMENTATION

Three types of instruments were used; load cells to measure the applied beam and column loads, displacement transducers to measure the displacement at specific location on the beam, column and the joint and electric strain gauges to record the behaviour of steel bars and FRP sheets during the test. Data from these instruments was recorded using computer-controlled data acquisition system.

2.9.1 Load measurements

A 300 kN capacity load cell was used to measure the cyclic beam-tip load. The cell was attached to the shaft of the hydraulic actuator. The load cell consisted of eight electric strain gauges connected together to form a full bridge. The column vertical load

was measured using another load cell that was attached to a solid steel cylinder and was placed between the reaction beam and the hydraulic jack. Each load cell was calibrated, before the beginning and at the mid of the experimental program, in compression using a calibrated Tinius-Olsen Universal Testing machine. To represent the beam load directions, the upward beam load, push-up direction, was designated with a positive sign whereas the downward beam load, pull-down direction, was designated with a negative sign.

2.9.2 Displacement measurements

Two linear potentiometers were used to measure the beam-tip vertical displacement and the column-top lateral displacement. Each one of these potentiometers has a stroke of 500 mm, with an initial position at mid way to give a stroke of ± 250 mm. The beam potentiometer was fixed to a pipe frame which is independent of the loading frame whereas the column potentiometer was attached to a fixed laboratory wall. The two devices were calibrated before the beginning and at the mid of the experimental program.

2.9.3 Measurement of beam section rotation at 175 mm from the column face

Two linear variable differential transformers, LVDT's, of 1.5 in. (38.1 mm) travel, were attached to the beam bottom and top surfaces at 175 mm from the column face as shown in Figure 2-14. The angle of rotation, θ was estimated to be:

$$\theta = \frac{\Delta_1 - \Delta_2}{h_b} \tag{2-1}$$

where h_b is the beam depth, Δ_1 and Δ_2 are the bottom and top displacement measured on the tension and compression beam faces, respectively. The signs of these displacements

must be included when substituting in the previous equation. A clockwise rotation was distinguished by positive sign.

The beam-section rotation versus the beam end moment will be plotted for each joint. This rotation is caused by the tensile strains of the beam longitudinal bars and by the bars slip from the joint region. The beam deformation due to this end rotation, $\delta_{b,\theta}$ could be obtained as:

$$\delta_{b,\theta} = \theta \,.\, L_c / 2 \tag{2-2}$$

where L_c is the clear beam span.

2.9.4 Measurement of joint shear distortion

Two diagonal, ½ in. (12.7 mm) stroke, LVDT's were placed on the joint region. The data from these instruments enabled the average shear distortions to be estimated as given by Beckingsale et al. (1980) and Hakuto (1995). The assumed deformed shape of the joint core concrete due to shear stresses is illustrated in Figure 2-15. It should be noted that the contribution of compressive diagonal deformation in joint shear deformation is much smaller than the contribution of diagonal tensile deformation (Shiohara, 2001). The joint shear distortion can be calculated as:

$$\gamma_1 = \frac{\delta_j - \delta_j^{'}}{2D} \tan \alpha_j \tag{2-3}$$

$$\gamma_2 = \frac{\delta_j - \delta_j^{'}}{2D \tan \alpha_j} \tag{2-4}$$

$$\gamma_j = \gamma_1 + \gamma_2 \tag{2-5}$$

where δ_j and $\delta_j^{'}$ are the changes in the length of the diagonals, where a compression displacement was given a negative sign, D is the initial length of the diagonal in the joint core and α_j is the angle of the diagonal to the horizontal.

2.9.5 Measurement of strains

The local strains in the reinforcement bars in the beam, column and the joint were measured using electric resistance wire strain gauges. At the location of the gauges, the ribs on the steel bar were removed and the bar was smoothed then the gauges were attached to the bar. The gauges were wired, labelled and kept away from the fresh concrete during casting. Figure 2-16 shows the location of the gauges on the three test groups. When repairing a joint, the strain gauges were replaced with new ones. Strain gauges were installed on various components of the rehabilitation scheme at selected positions. Epoxy filler was applied on the surface of the composite sheets to obtain a smooth levelled surface before sticking the gauges on the sheets. For threaded steel rods, the threads were removed and the surface was smoothed with sand grinding blades. Figure 2-16d shows an example of the strain gauges of the rehabilitation scheme of joint T-SB6.

2.10 ANALYSIS OF EXPERIMENTAL DATA

The recorded experimental data was analyzed to evaluate the response of the rehabilitation schemes. Analysis of the recorded data includes calculating the displacement ductility factor, storey drift, cracking moment, yield moment, shear in

beam, shear in joint, joint shear deformation, storey shear force, specimen stiffness and energy dissipation capacity of the tested joints.

2.10.1 Hysteretic loops

For all joints, the beam-tip load versus the beam-tip displacement relationships were plotted. The maximum load carrying capacity with the maximum beam displacement were recorded and used for comparison between the joints. The loops pinching were observed in each cycle. Pinching is characterized by the narrow width of the hysteretic loops near mid-cycle, resulting in less energy dissipation per cycle. Pinching is mainly caused by slippage of the longitudinal beam bars and closing of flexural cracks in the plastic hinge zones. The envelopes of the hysteretic loops were determined for each joint and plotted. The development of slow strength degradation of the joint is one of the rehabilitation objectives.

2.10.2 Displacement ductility factor and storey drift

Structural ductility is an essential property for those structures responding inelastically during severe earthquakes. The term *ductility* defines the ability of a structure or structural components to deform beyond the elastic limit without excessive strength deterioration. In this study, the displacement ductility, μ_Δ was used to evaluate the inelastic deformation capacity of the joints. The displacement ductility factor (DDF) was evaluated as:

$$\mu_\Delta = \Delta / \Delta_y \tag{2-6}$$

where, Δ and Δ_y are the structural displacement and the displacement corresponding to

the first yield of the steel reinforcement, respectively.

The lateral displacement, or Drift (R), of a structural system under lateral load effect is important from many different perspectives, such as structural stability or P-Δ effect, performance-based design and damage to various non-structural components. In reality, the lateral drift of the structure is calculated as:

$$R = \frac{\delta_{col}}{H} \tag{2-7}$$

In this study, due to the support conditions at the top and the bottom column ends, the storey drift was evaluated as:

$$R = \frac{\delta}{L/2} \tag{2-8}$$

where δ_{col} is the column-lateral displacement, δ is the beam-tip displacement, H is the floor height and L is the beam span between the centrelines of the supporting columns.

2.10.3 Cracking moment

The cracking moment was calculated by multiplying the cracking load, the load that induces the first crack in the beam, by the moment arm to the critical section at the column face. The cracking tensile stress is given by:

$$f_{ct} = \frac{M_{cr}\, h_b / 2}{I_g} \tag{2-9}$$

where, f_{ct} is the tensile cracking stress, M_{cr} is the cracking moment, h_b is the beam depth and I_g is the gross sectional moment of inertia taking into account the existing steel bars. The obtained cracking stress is compared to the theoretical concrete modulus of rupture

given by CSA A23.3 (1994) Clause 8.6.4, which equals $0.6\sqrt{f_c'}$.

2.10.4 Yield and ultimate moments

Yield and ultimate moments were calculated by multiplying the yield and ultimate loads by the moment arm to the critical section at the column face. The yield load was taken as the load corresponding to the first yield of the top or bottom beam longitudinal bars. The theoretical moment values were calculated assuming a linear strain distribution in the concrete and based on the measured steel and concrete strengths. The concrete block factors given by the CSA A23.3 (1994) provisions were used to simplify the concrete stress distribution. A computer program "Response2000" (Bentz, 2000) was also used to verify the theoretical calculations of these moments.

2.10.5 Storey shear

In frame structures, the inertia forces during an earthquake are transferred from one floor to another by horizontal shear forces through the floor columns. The deflected shape of a frame subjected to a lateral load is shown in Figure 2-1. The points of contra-flexure are assumed to occur at the mid column height and beam span. The free body diagram of the joint and the connecting beam and columns is shown in Figure 2-17b. A lateral deflection δ_{col} is expected to occur. However, in the test set-up, the hinged column ends were prevented from lateral motion but left free to rotate and axially. Thus, the storey shear was estimated, as shown in Figure 2-17a, to be:

$$V\,H = F(L/2) \tag{2-10}$$

where V is the storey shear, H is the floor height, F is the beam-tip load and L is the beam

span.

By considering the equilibrium of the free body diagram, as shown in Figure 2-17b, and taking the summation of moments about point A, then:

$$P\delta_{col} + V_{actual} H = F(L/2 - \delta_{col}/2) \tag{2-11}$$

where P is the column vertical load and δ_{col} is the column lateral displacement.

By expanding the two previous equations, the actual storey shear could be evaluated to be:

$$V_{actual} = V - R(F/2 + P) \tag{2-12}$$

The significant parameter for the designer is the actual storey shear. Using Equation (2-10) and Equation (2-12), it is possible to convert the measured column shear to the actual storey shear (Uzumeri and Seckin, 1974).

2.10.6 Shear deformation of beam-column joints

Joint shear deformation gives a measure of the joint stiffness. It is recommended by the current codes, e.g. ACI-ASCE (1997), to keep the behaviour of the joint in the elastic range. This is because the joint response is mainly controlled by shear and bond mechanisms, which exhibit poor hysteretic behaviour. It is also essential to ensure that joint deformation does not contribute excessively to the overall storey drift. In the analysis of the experimental data, the joint deformations were plotted against the storey shear force. The joint deformations were estimated using Equations (2-3) to (2-5) and the storey shear was evaluated as described in the previous section. Reducing the joint deformations is one of the objectives of joint rehabilitation.

2.10.7 Stresses in steel reinforcement and FRP sheets

The strain measured in the various steel elements need to be converted into steel stresses and hence the force in these elements can be evaluated. Due to the reversing nature of the loading, the stress computation must be based on the complete loading history. When calculating the stresses, two stages are defined. The first is the pre-yielding stage where the steel bars did not reach its yield strain. In this case the steel stress was evaluated as:

$$f_s = E_s(\varepsilon_s - \varepsilon_i) \tag{2-13}$$

where f_s is the steel stress, E_s is the steel modulus of elasticity, ε_s is the steel strain and ε_i is the initial steel strain at the beginning of the loading cycle.

The second stage is the post-yield stage where non-linearity of the behaviour due to the Bauschinger effect (Chen, 1982) occurs at much lower strain than the initial yield strain, as shown in Figure 2-18. To include this effect in the steel stress calculations, the model presented by Kent and Park (1971) was adopted in this study. The model was based on the Ramberg-Osgood function to represent the steel stress which is:

$$\varepsilon_s E_s = f_s[1 + (f_s / f_{ch})^{r-1}] \tag{2-14}$$

where f_{ch} is the characteristic stress and it was found to be dependent on the plastic strain of the last loading cycle, and r is Ramberg-Osgood parameter and it depends on the number of cycles past yield. The previous two factors are evaluated bas:

$$r = \frac{4.49}{\ln(1+N)} - \frac{6.03}{EXP(N)-1} + 0.297 \qquad \text{for } N \text{ odd} \tag{2-15}$$

$$r = \frac{2.20}{\ln(1+N)} - \frac{0.469}{EXP(N)-1} + 3.04 \qquad \text{for } N \text{ even} \tag{2-16}$$

where N is the cycle number past yield, e.g. for the yield cycle $N = 0$

$$f_{ch} = f_y\left(\frac{0.744}{\ln(1+1000\varepsilon_{pl})} + \frac{0.071}{1-EXP(1000\varepsilon_{pl})} + 0.241\right) \tag{2-17}$$

where ε_{pl} is the plastic strain at the end of the previous cycle.

Due to the elastic response of the composite sheets, the strains measured in the FRP sheets were converted into stresses using a simple linear model for the FRP sheets. The stress in the FRP sheets, f_{frp} that corresponds to strain ε_{frp} is evaluated as:

$$f_{frp} = E_{frp}(\varepsilon_{frp} - \varepsilon^i_{frp}) \tag{2-18}$$

where E_{frp} is the modulus of elasticity of the composite sheets, ε^i_{frp} is the initial FRP sheet strain at the beginning of the loading cycle.

The force developed in the composite sheets was then evaluated as:

$$F_{frp} = f_{frp} A_{frp} \tag{2-19}$$

where A_{frp} is the cross sectional area of the composite sheets

2.10.8 Shear in beams

To estimate the effect of beam shear force, it is convenient to express this in terms of the nominal shear stress. The nominal beam shear stress is defined as:

$$v_b = \frac{V_b}{b\,d} \tag{2-20}$$

where, V_b is the beam shear force, b and d are the beam width and effective depth, respectively.

The shear in the beam was resisted by the concrete and the transverse reinforcement, such that:

$$V_b = V_c + V_s \tag{2-21}$$

where V_c is the shear force resisted by the concrete and V_s is the shear force resisted by the transverse steel.

Using the traditional truss model, the contribution of the shear reinforcement equals:

$$V_s = \frac{A_v f_s jd \cot\theta}{s} \tag{2-22}$$

where A_v is the area of the transverse reinforcement, f_s is the stress of the transverse reinforcement, which is assumed constant along each stirrup leg, jd is the concrete-section moment arm, θ is the crack inclination to the horizontal and s is the spacing between transverse reinforcement.

To simplify the previous equation, although this overestimates the transverse reinforcement shear force, jd was taken to be $0.9d$ and θ was taken 45°. The concrete and steel contributions in carrying the beam shear force was plotted against the specimen displacement ductility factor for each joint.

2.10.9 Shear in beam-column joints

The shear force developed in the joint was evaluated using the expression provided by Park and Paulay (1975), which is:

$$V_j = A_s f_s - V_{col} \tag{2-23}$$

where V_j is the joint shear force, A_s is the area of the beam tensile reinforcement, f_s is the

beam bars steel stress, and V_{col} is the column shear force.

The joint shear stress, v_j is written as:

$$v_j = \frac{V_j}{b_j d_j} \tag{2-24}$$

where b_j is the joint effective width and d_j is the joint effective depth.

The joint shear force is carried by the concrete, steel ties and FRP sheets according to the expression:

$$V_j = V_c + V_s + V_{frp} \tag{2-25}$$

where V_c is the concrete contribution, V_s is the steel ties contribution and V_{frp} is the composite sheets contribution.

Using the conventional 45° truss model, the steel ties and the FRP sheet contributions are evaluated as:

$$V_s = \frac{A_v f_y d_j}{s} \tag{2-26}$$

$$V_{frp} = A_{frp} f_{frp} \tag{2-27}$$

where A_v are the area of the steel ties, s ties spacing in the joint zone, f_y is the steel yield stress, and A_{frp} and f_{frp} are the cross sectional area and the stress of FRP sheets, respectively.

2.10.10 Joint contribution to drift angle

Joint contribution to specimen deformation gives a good indication of the joint behaviour under lateral earthquake loads. In poor detailed beam-column joint, the joint contributes significantly to the structure drift. The joint contribution to storey drift, R_j, is

estimated as (Alcocer and Jirsa, 1991):

$$R_j = \gamma_j (1 - \frac{h_b}{H} - \frac{h_c}{L}) \tag{2-28}$$

Where H is the column height, h_c is the column depth, h_b is the beam depth and L is the beam span. The contribution of joint shear deformation to drift angle for each joint will be plotted versus the storey drift.

2.10.11 Stiffness

Structural stiffness is a measure of the structure deformability. Under seismic loads, stiffness must be large enough to control the drift and limit the damage of the non-structural elements. Concrete buildings suffer from stiffness degradation under cyclic loads. This is due to concrete cracking, opening and closing of residual cracks, concrete spalling, bond degradation, and Bauschinger effect in the reinforcing bars. Analytical studies (Gupta and Krawinkler, 1998; and Humar, 1980) were carried out on the effect of stiffness degradation on the dynamic response of structures subjected to severe ground motions. Stiffness degradation would reduce the amount of hysteretic damping of the structure, increase the storey drift and consequently increase the ductility demand.

In this study, the stiffness of the specimens was evaluated using the peak-to-peak stiffness (secant stiffness) of the beam-tip load–displacement relationship. It is calculated as the slope relative to the abscissa of a line that joins load peaks in the same cycle as shown in Figure 2-19. The degradation in the peak-to-peak stiffness was plotted versus the storey drift for each joint. Reducing the stiffness degradation is one of the rehabilitation objectives.

2.10.12 Energy dissipation

During an earthquake event, a large amount of energy is released. If the structure is to survive without collapse, it must be capable of absorbing and dissipating energy through kinematic energy, viscous damping energy, recoverable elastic strain energy and irrecoverable inelastic energy. In a well-designed structure, the energy supply must be larger than the energy demand. The total energy dissipated by a structure consists of (a) energy dissipated by the steel reinforcement; (b) energy dissipated by friction along existing cracks in concrete; and (c) energy dissipated during the formation of new cracks.

For each joint, the energy dissipated during a cycle was calculated to be the area enclosed by the load-displacement hysteretic loop. The cumulative energy dissipated was obtained by summing the energy dissipated in consecutive loops throughout the test, and was plotted versus the storey drift for each joint.

Table 2-1 Concrete properties

	Specimen	Compressive Concrete strength (MPa)		28-day tensile strength (MPa)	28-day modulus of elasticity (MPa)
		28- day	Test-day		
Shear-deficient joints	T-S1	23.25	30.8	2.48	NA
	T-S1RR*	32.19	31.94	NA	NA
	T-S4R*	36.98	43.24	NA	NA
	T-S5	32.59	36.66	1.94	NA
Bond-deficient joints	T-B10	33.73	34.14	3.07	28304.735
	T-B11	33.73	34.91	3.07	28304.735
	T-B12	33.73	37.02	3.07	28304.735
Shear/bond-deficient joints	T-SB3	23.25	30.60	2.48	NA
	T-SB3R*	NA	43.52	NA	NA
	T-SB6	32.59	39.54	1.94	NA
	T-SB7	26.78	22.51	2.32	NA
	T-SB8	26.78	22.51	2.32	NA

* Repair concrete compressive strength

Table 2-2 Properties of the reinforcement bars

Bar number	Diameter (mm)	Cross sectional area (mm^2)	Yield strength (MPa)	Ultimate strength (MPa)
10	11.3	100.29	477.0	720.0
15	16.0	201.06	409.5	617.5
20	19.5	298.65	477.0	764.0

Table 2-3 Tensile properties of the Unified Inch Coarse Screw Threads (UNC) steel rods

Nominal diameter (mm)	Effective cross-sectional area (mm^2)	Yield strength (MPa)	Ultimate strength (MPa)
12 (1/2 in.)	91.548	400.128	602.483
16 (5/8 in.)	145.806	414.863	471.999
20 (3/4 in.)	215.483	566.499	1022.845
25 (1.0 in.)	390.967	324.844	472.9057
32 (1 ¼ in.)	625.160	328.64	436.305

Table 2-4 FRP sheet properties as provided by the manufacturer

Fibre type	Ultimate tensile strength (MPa)	Ultimate strain (%)	Modulus of elasticity (GPa)	Design thickness (mm)
MBrace CF 130 uni-directional CFRP sheets	3550	1.5	235	0.165
MBrace EG 900 uni-directional GFRP sheets	1700	2.0	71	0.353
Tyfo SEH-51A uni-directional GFRP sheets	575	2.2	26.1	1.3
Tyfo BC* bi-directional (±45°) GFRP sheets	279	1.5	19	0.864

* Properties are in the 0° direction.

Table 2-5 Adhesives properties as provided by the manufacturer

Property	MBrace™ Primer	MBrace Saturant LTC	Tyfo S Epoxy
Tensile strength (MPa)	12	14	72.4
Tensile modulus (GPa)	0.717	1.138	3.18
Ultimate elongation (%)	3.0	5.3	5.0
Flexural strength (MPa)	24.0	25	123.4
Flexural modulus (GPa)	0.593	0.552	3.18

Table 2-6 Properties of the composite sheets as tested against the provided manufacturer data

Fibre type	Ultimate tensile strength (N / mm-sheet width)	Ultimate strain (%)	Modulus of elasticity (kN / cm-sheet width)
MBrace CF 130* uni-directional CFRP sheets	709.6 (585.8)	1.63 (1.5)	4156.4 (3877.5)
MBrace EG 900* uni-directional GFRP sheets	465.0 (610)	1.472 (2.0)	3128.0 (3050.0)

* Values between parentheses are provided by the manufacturer

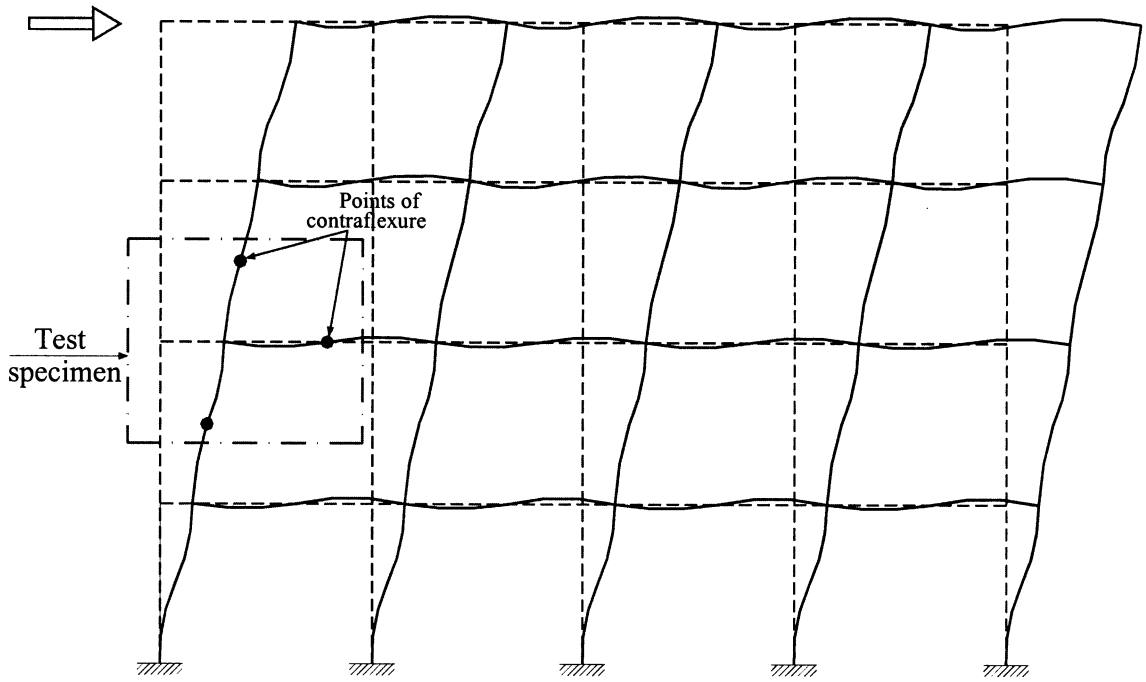

Figure 2-1 Deformation of a typical moment resisting frame under lateral load effect

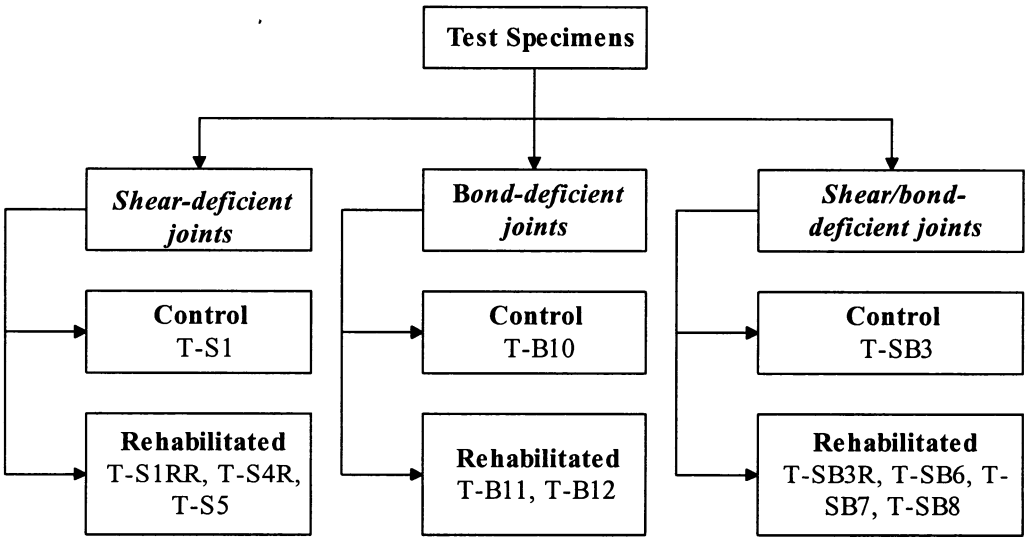

Figure 2-2 Specimen groups layout

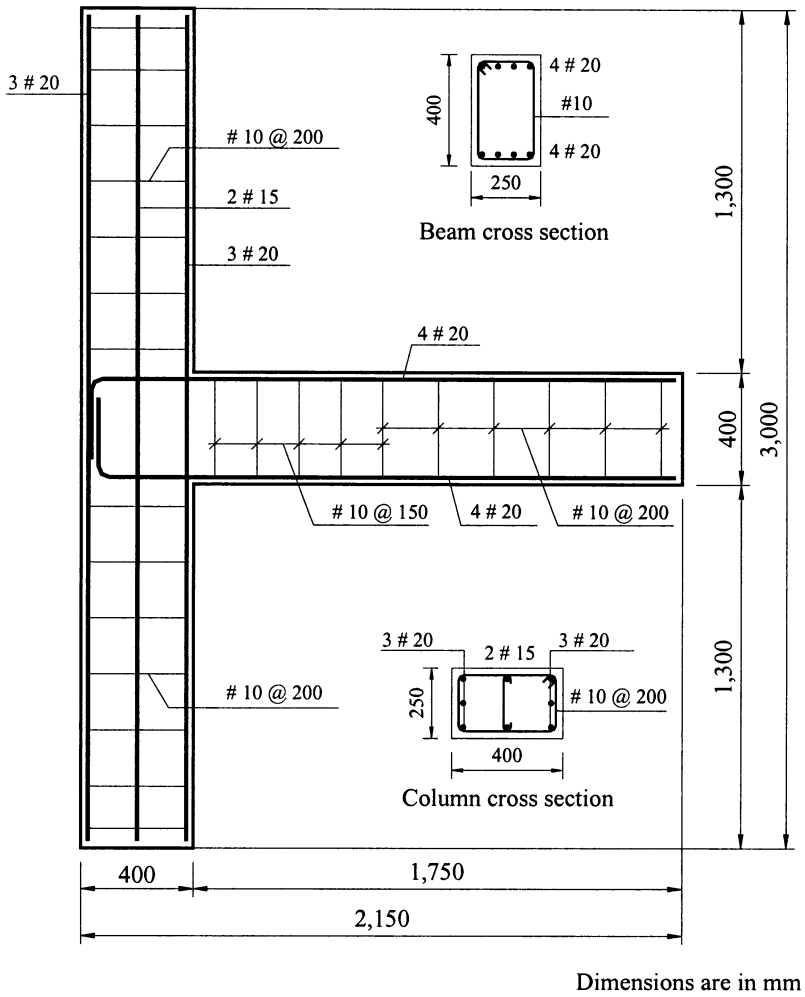

Figure 2-3 Concrete dimensions and reinforcement details of shear-deficient joints

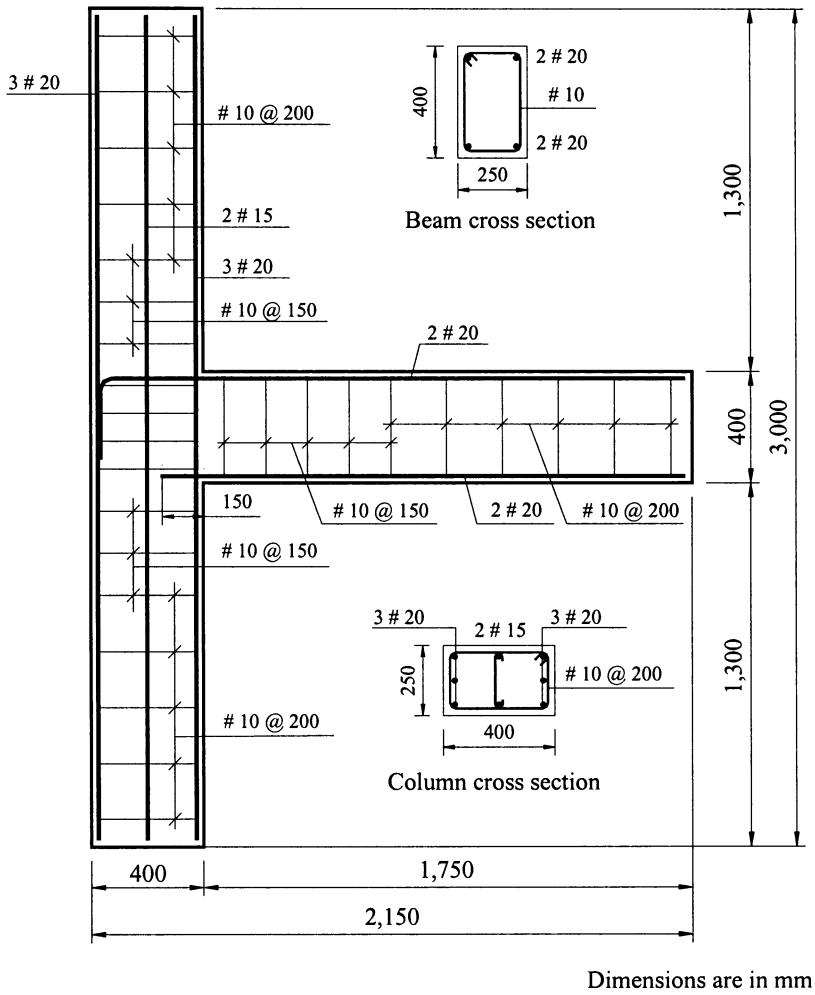

Dimensions are in mm

Figure 2-4 Concrete dimensions and reinforcement details of bond-deficient joints

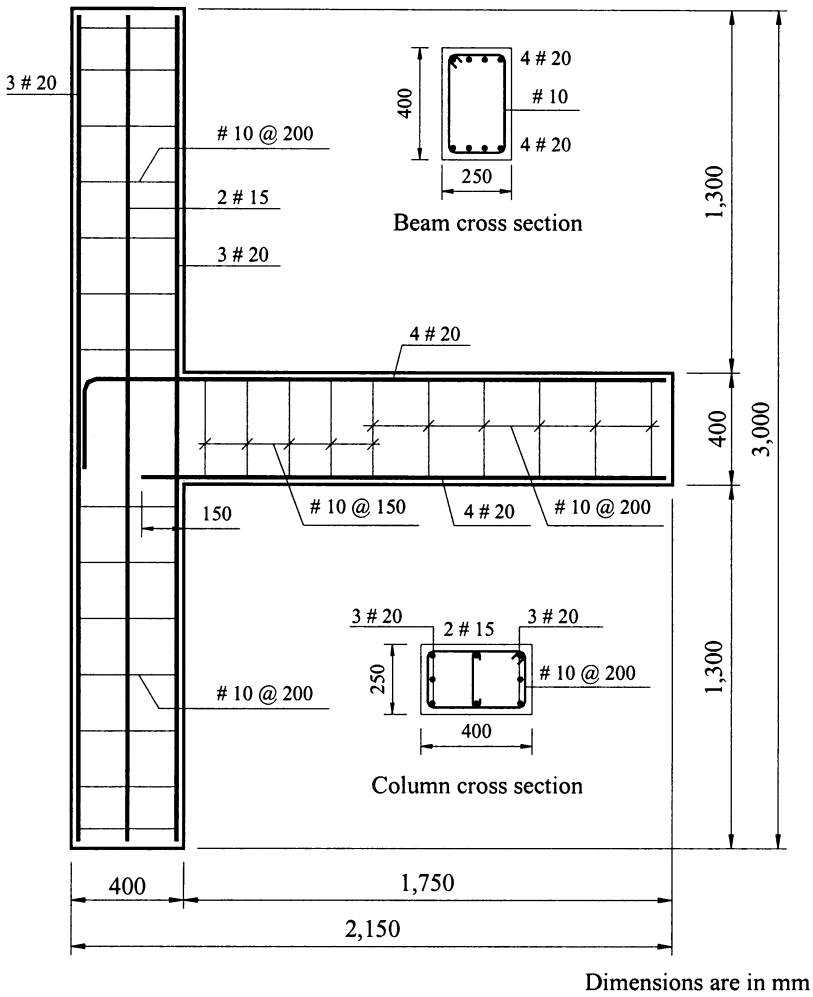

Figure 2-5 Concrete dimensions and reinforcement details of shear/bond-deficient joints

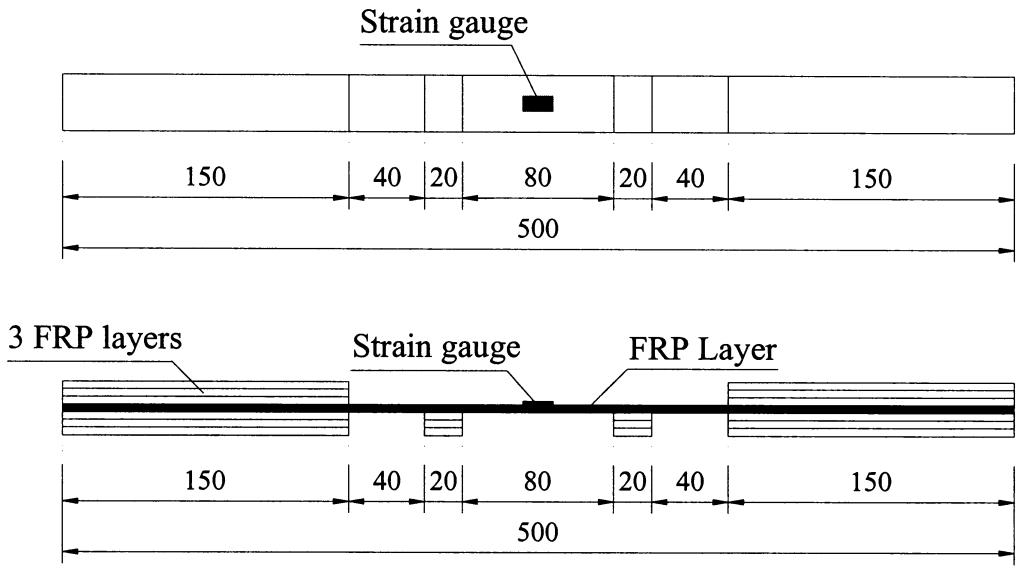

Figure 2-6 FRP coupons

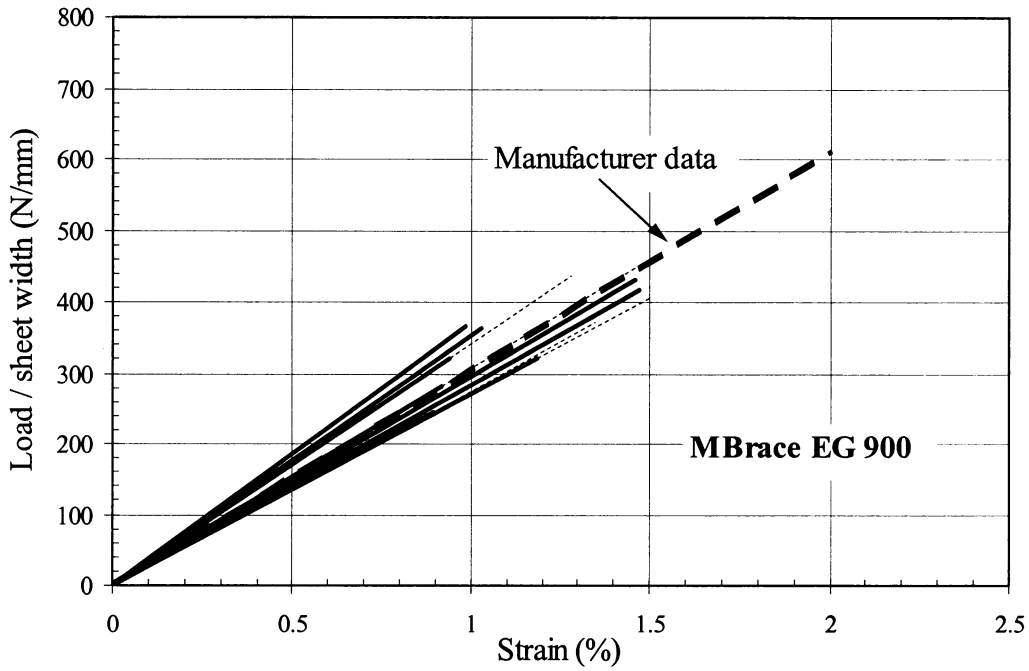

Figure 2-7 Force/unit width versus strain of the tested GFRP coupons

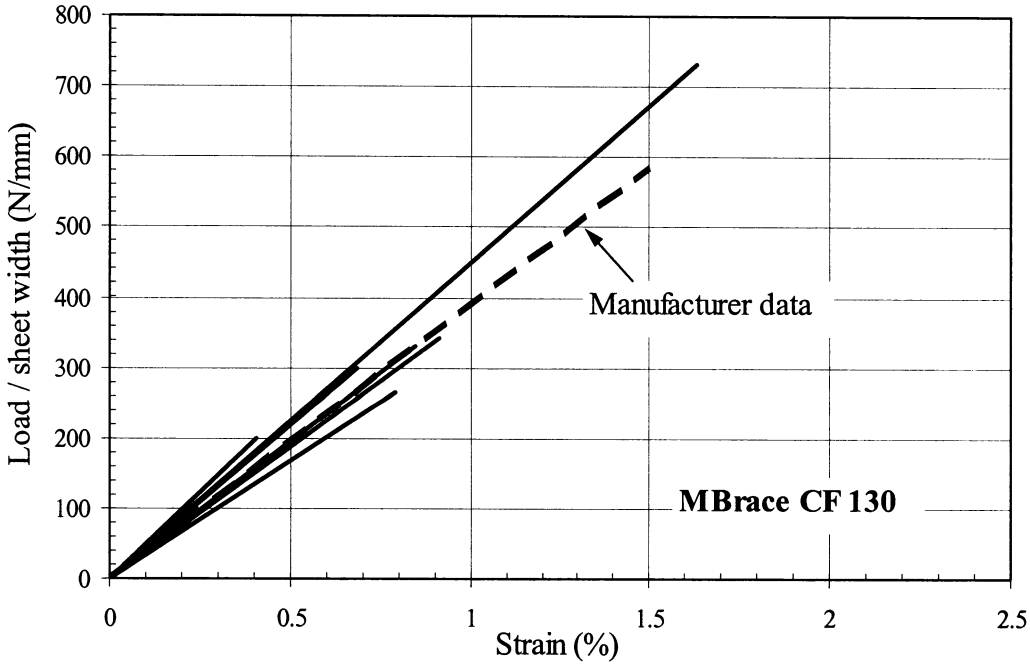

Figure 2-8 Force/unit width versus strain of the tested CFRP coupons

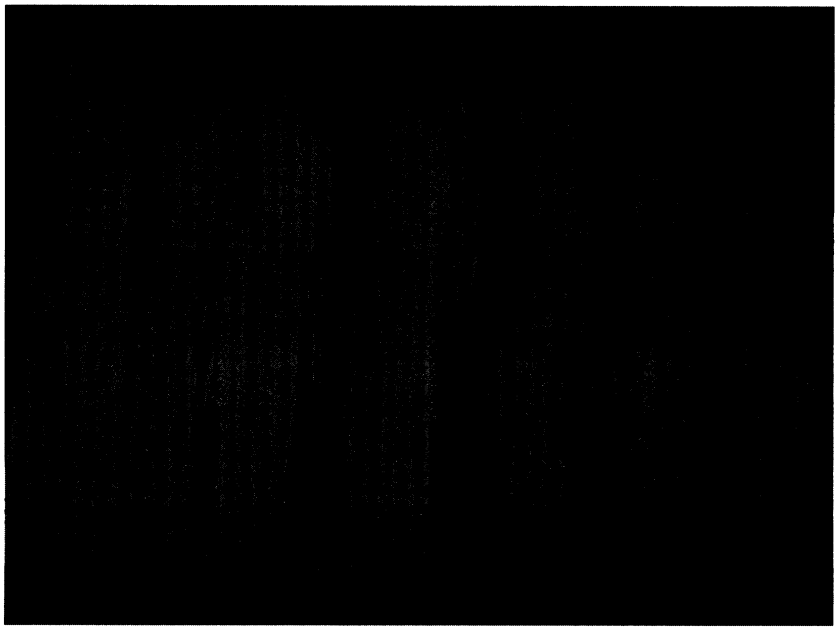

Figure 2-9 Failure patterns of FRP coupons

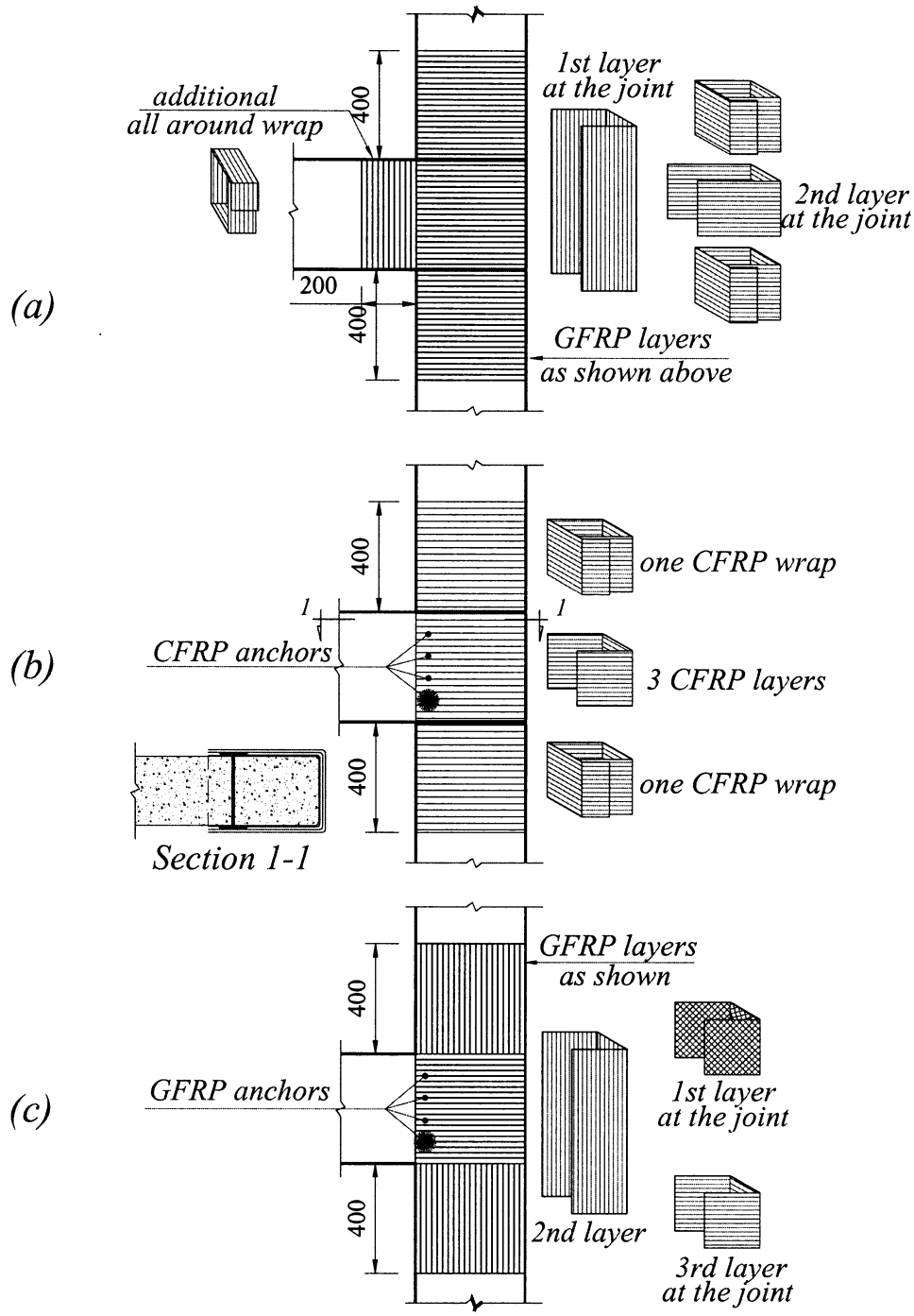

Figure 2-10 Proposed rehabilitation schemes

(*a*) Joint T-S1RR (*b*) Joint T-S4R (*c*) Joint T-S5

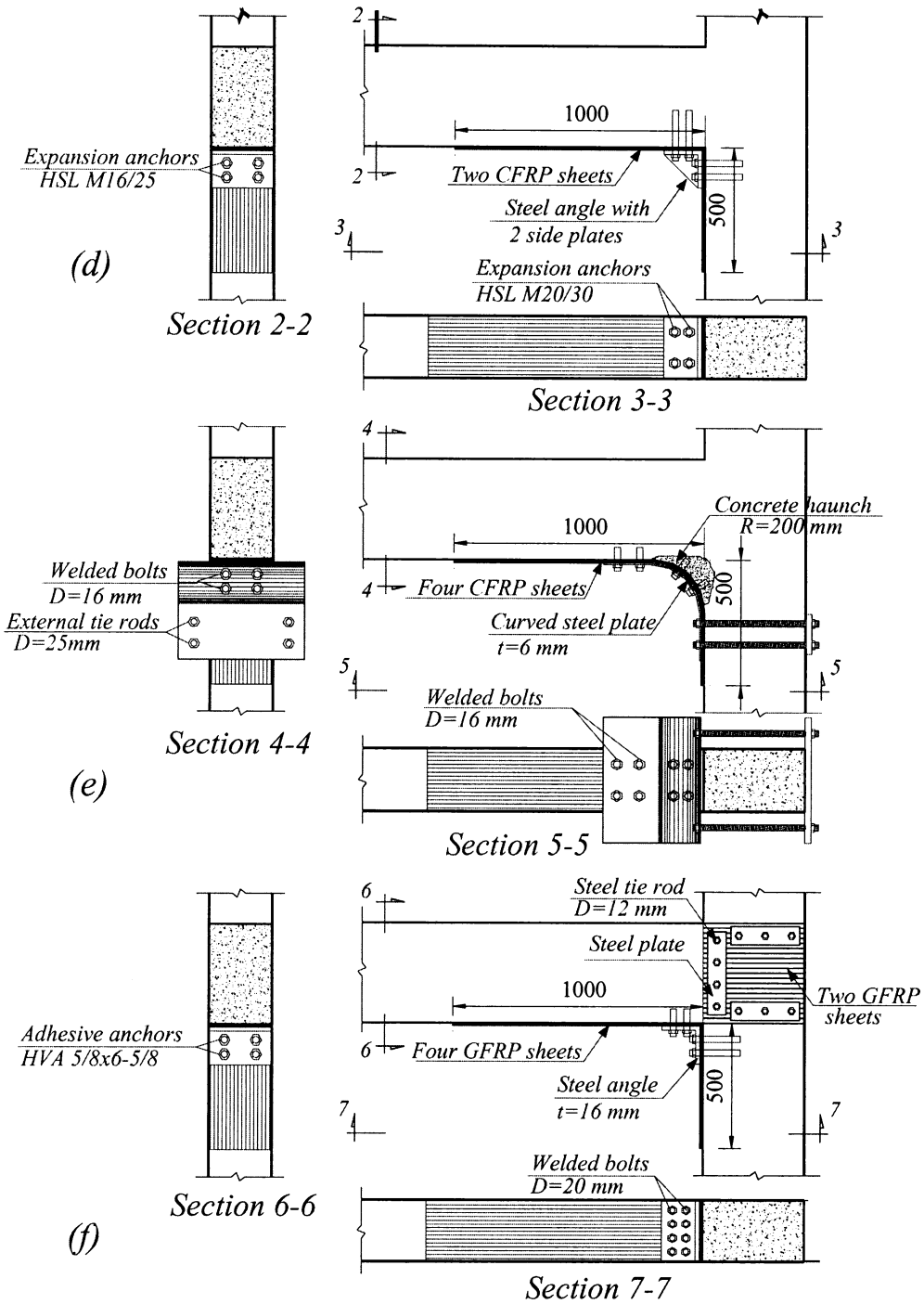

Figure 2-10 Proposed rehabilitation schemes (cont.)

(*d*) Joint T-B12 (*e*) Joint T-B11 (*f*) Joint T-SB3

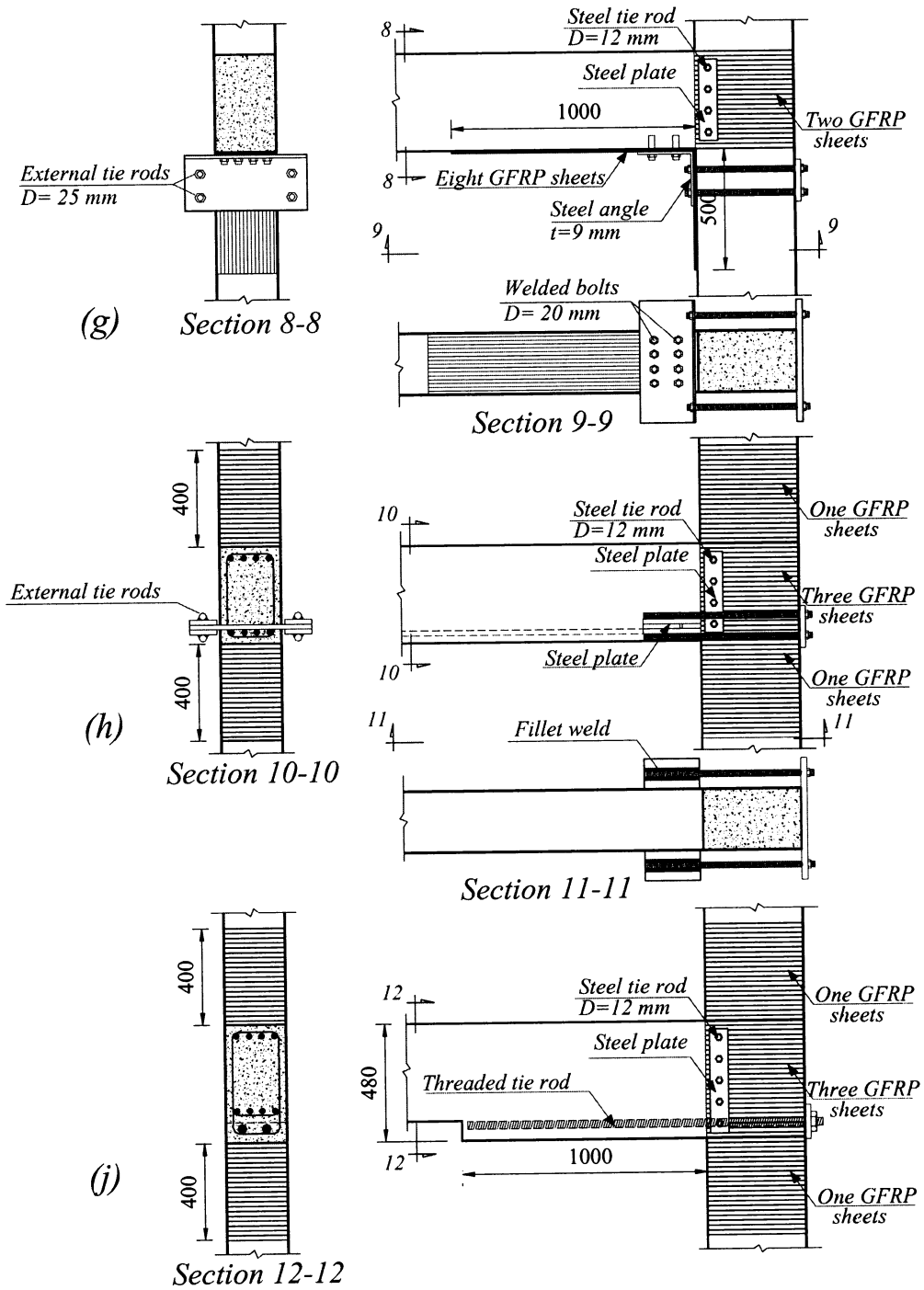

Figure 2-10 Proposed rehabilitation schemes (cont.)

(*g*) Joint T-SB6 (*h*) Joint T-SB7 (*j*) Joint T-SB8

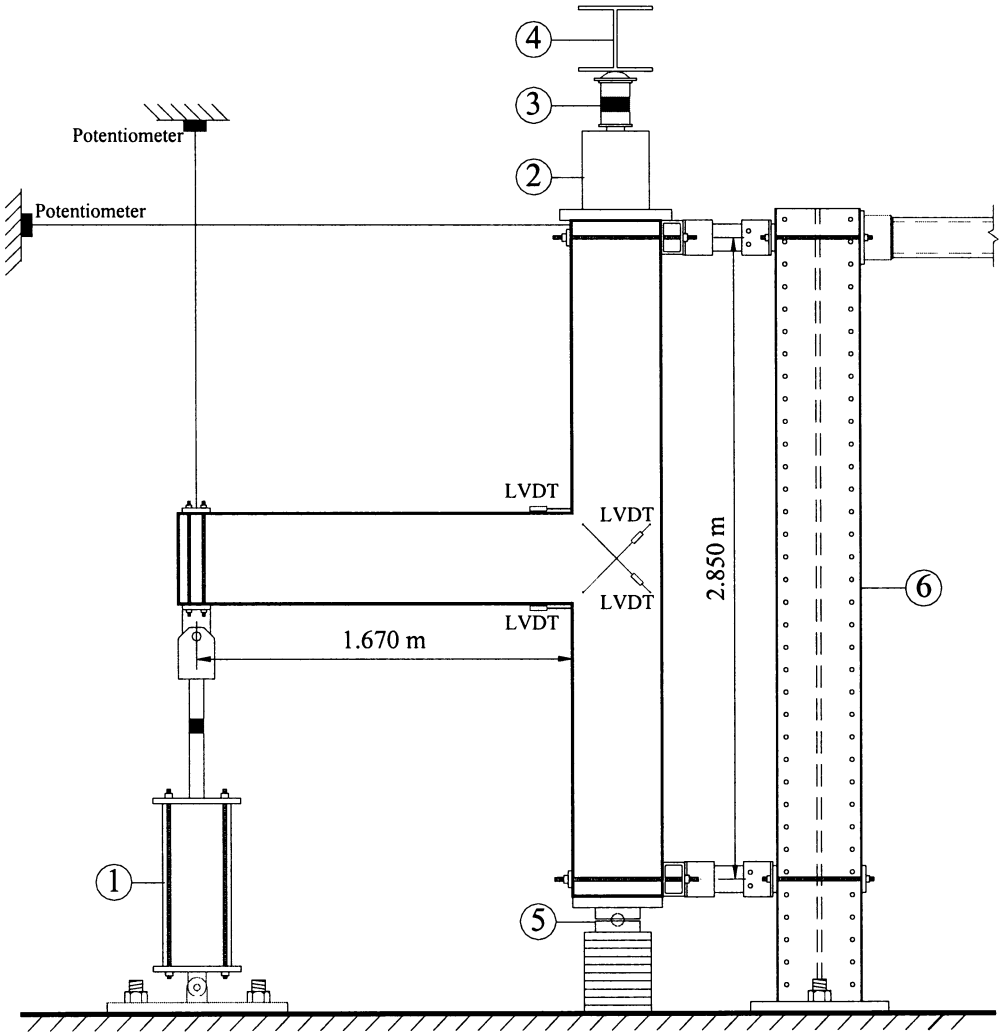

(1) Loading actuator
(2) Hydraulic jack
(3) Loading cell with the top column hinge
(4) Reaction beam
(5) Bottom column hinge
(6) Reaction frame

Figure 2-11 Schematic diagram of the test set-up

Figure 2-12 Test set-up

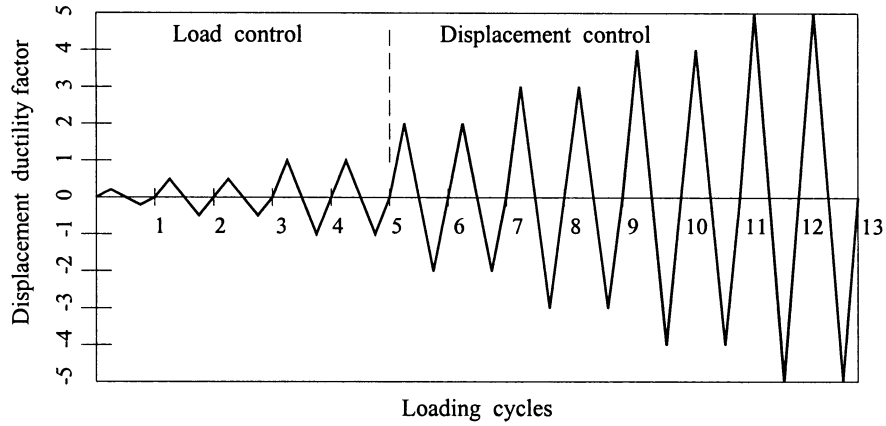

Figure 2-13 Loading routine

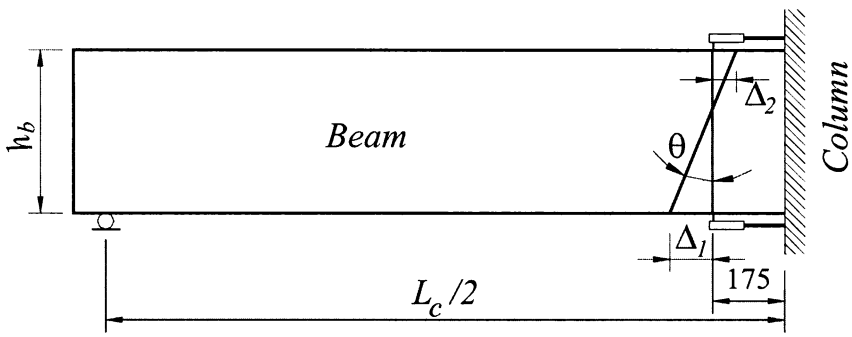

Figure 2-14 Measurement of beam section rotation

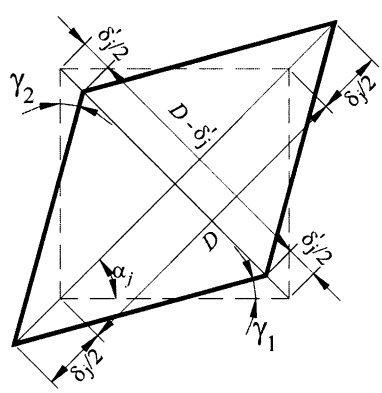

$$\gamma_j = \gamma_1 + \gamma_2 = \frac{\delta_j - \delta_j'}{2D}(\tan\alpha_j + \frac{1}{\tan\alpha_j})$$

Figure 2-15 Measurement of joint shear distortion and expansion

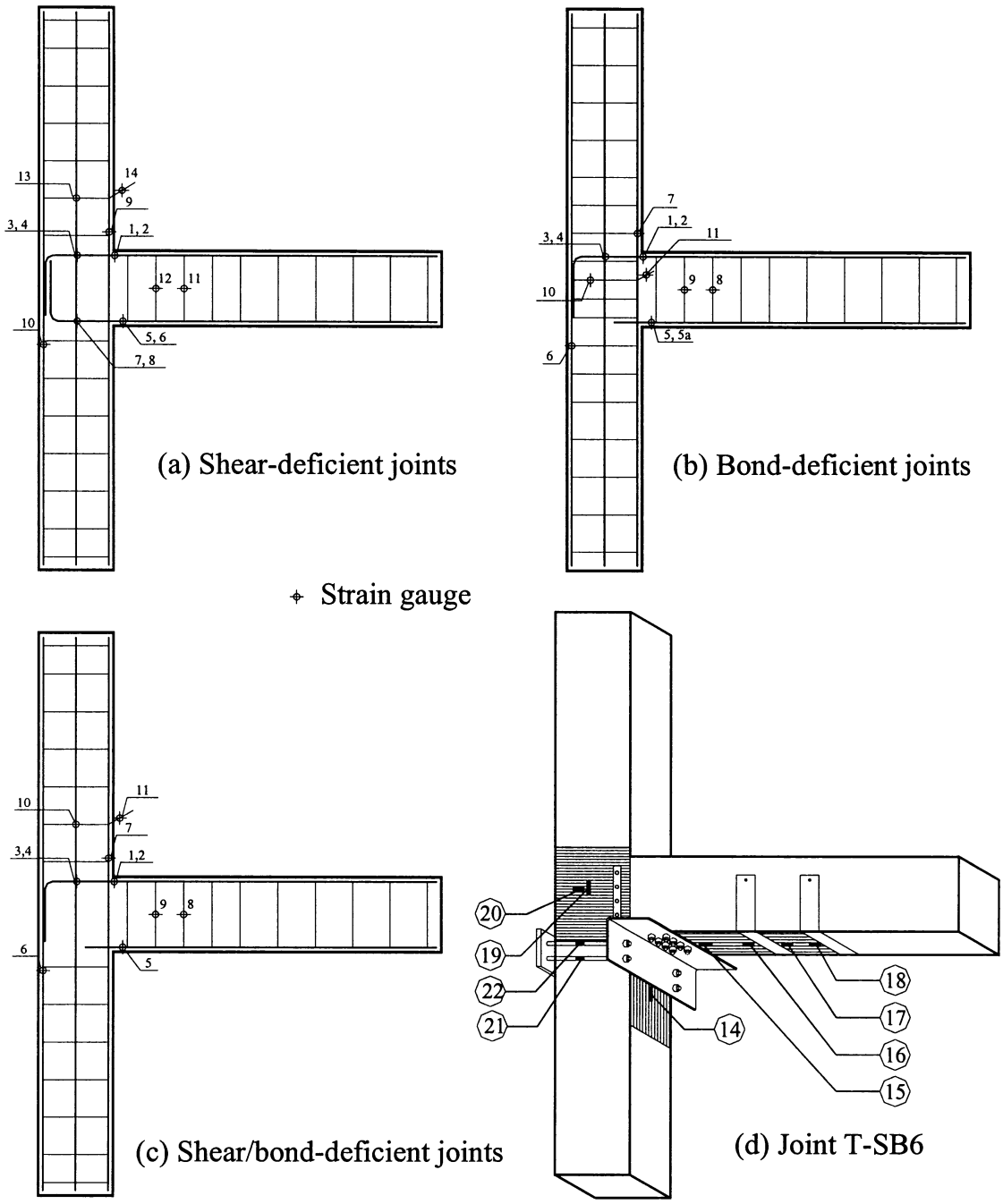

Figure 2-16 Strain gauges location

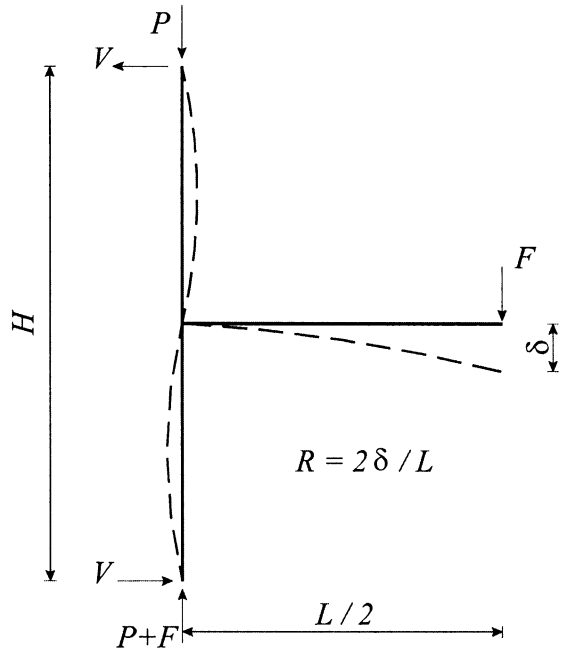

(a) Free body diagram of the test joint

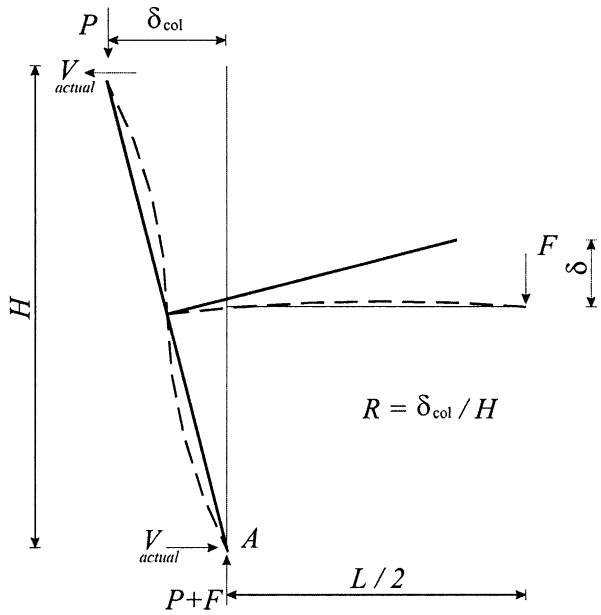

(b) Free body diagram of real structure

Figure 2-17 The drift angle definition (Uzumeri and Seckin, 1974)

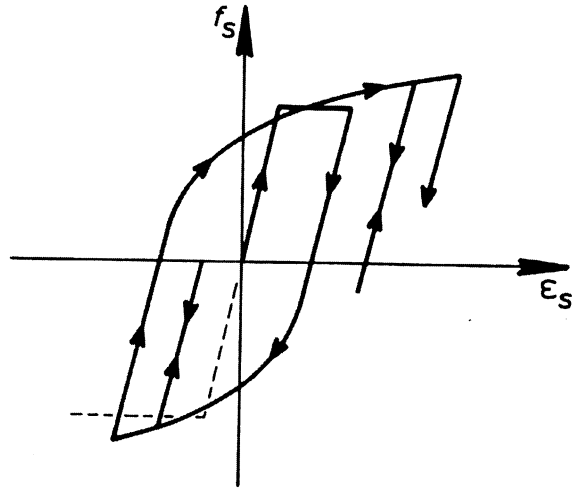

Figure 2-18 Stress-strain curve of steel bars under cyclic loads (Chen, 1982)

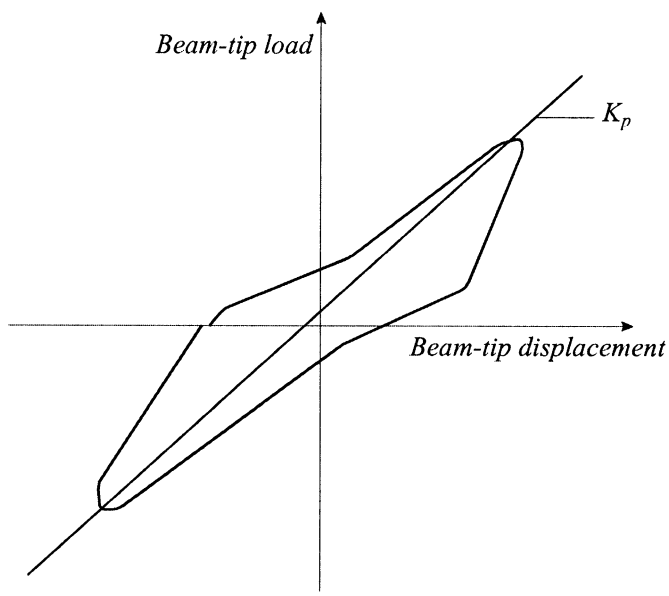

Figure 2-19 Specimen peak-to-peak stiffness

This page is intentionally left blank

Chapter 3

BEHAVIOUR OF SHEAR-DEFICIENT JOINTS

3.1 INTRODUCTION

The overall behaviour of the Shear-deficient joints, T-S1, T-S1RR, T-S5, and T-S4R, is discussed in this chapter. Joint T-S1 represented the control joint with no transverse reinforcement in the joint zone. The other joints were strengthened using fibre reinforced polymer (FRP) sheets then tested. The cracks were mapped during the test as they may give insight into the failure mechanism of each joint. The beam-tip load-displacement, storey shear-drift angle, storey shear-joint deformation, beam moment-rotation relationships are presented. The effectiveness of the strengthening schemes in improving the joint behaviour is assessed based on the joint load carrying capacity, joint ductility, energy absorption ability, rate of stiffness degradation and the joint failure mode.

3.2 JOINT T-S1

This joint represented a typical beam-column joint that was built before developing the 1970 seismic code. It was designated as the control joint. Due to the high moment capacity of the beam and the lack of shear reinforcement in the joint, a joint shear failure was expected to occur.

During the first loading cycle, the beam was loaded until first beam crack

occurred at 10.0 kN. When loading the joint to ±40.0 kN, new flexural and flexural-shear cracks formed along the beam. During the fourth cycle, inclined shear cracks occurred in the beam-column joint zone at a load of 60.0 kN. The bottom steel bars yielded at a load of 110.0 kN and a corresponding beam-tip displacement of 28.0 mm. The beam top bars yielded at a load of 99.1 kN and at the same displacement of 28.0 mm. This displacement was designated as the yield displacement, Δ_y.

In the displacement-control loading phase, the beam was loaded to reach a displacement ductility factor (DDF) of 2 (±56.0 mm). The joint reached its ultimate strength of 116.0 kN. During this cycle, the joint shear cracks widened and extended to the rear of the column. During the pushing-up part (positive part) of the loading cycle, severe degradation of the joint stiffness occurred when the yield displacement was exceeded. When repeating the same cycle, the load carrying capacity was degraded to about 60% of the ultimate capacity and severe pinching of the load-deflection loop was observed. During the next cycle, a DDF of 2.5 (±70.0 mm) was achieved. The load carrying capacity degraded to less than 50% of the ultimate capacity. When repeating this cycle, the joint strength degraded to +33.6 kN and -18.2 kN, and the test was terminated.

At the end of the test, the joint panel suffered diagonal shear cracks, as shown in Figure 3-1. The joint diagonal cracks extended to the column. Longitudinal cracks at the column backside were recorded due to the opening of beam bars 90° hooks. When removing the cracked and spalled concrete, buckling of column longitudinal bars was revealed. The overall behaviour of the joint was brittle with severe strength deterioration.

3.3 JOINT T-S1RR

After testing joint T-S1, the disintegrated and spalled concrete was removed from the beam-column joint zone and the adjacent beam and column parts. New concrete was poured and the joint was re-named as T-S1RR. MBrace EG 900 GFRP sheets were used to strengthen the joint shear resistance. A U-shaped sheet was wrapped around the beam-column joint and extended for 400 mm above and below the joint with the reinforcing fibres parallel to the column longitudinal axis. A second U-shaped sheet was wrapped around the joint and extended for 200 mm onto the beam with the fibres parallel to the beam longitudinal axis. The possible regions of plastic hinge in column above and below the joint, and in beam at beam-column interface, were wrapped using closed composite sheet with the fibres parallel to the hoop direction, as shown in Figure 3-2.

The joint was loaded up to 3.0 kN up and down in the first cycle to verify that the instrumentations were working properly. During the next cycle, the specimen was loaded to cracking. The old cracks in the beam opened up and new cracks formed in the new concrete at a load of 22.0 kN up and 16.0 kN down. When the joint was loaded to the first yielding of the steel bars, the bottom and top bars yielded at a load of 135.0 and 129.3 kN, respectively. The corresponding displacement of 30.0 mm was used in the following cycles as the yield displacement, Δ_y.

During the sixth cycle, a DDF of 2 (±60.0 mm) was achieved. The joint reached its ultimate load of 143.0 kN which was higher than the ultimate load of the other joints. The increased applied shear was because the GFRP sheets extended onto the beam.

Debonding of the wrapped sheets around the beam was initiated as a result of the developed cracks underneath the composite sheets, as shown in Figure 3-3. During the eighth cycle, the beam was loaded to a DDF of 3 (±90.0 mm). When pushing up, the joint reached a load of 105.0 kN at a displacement of 63.0 mm followed by a gradual deterioration in the load carrying capacity to 83.7 kN at a displacement of 3 Δ_y. When unloading the joint, 10% drop of the column load was recorded as a result of the joint strength deterioration. When pulling down, the joint reached a maximum load of 63.0 kN followed by a gradual drop in the load. At the end of the cycle, the column lost 16% of its load and the composite sheet extending onto the beam was torn at the beam-column interface. Repeating this cycle, the joint strength degraded to about 50% of the ultimate load. During the next cycle, the joint reached a DDF of 4 (±120.0 mm). The joint strength degraded to about 25% of its ultimate load, and the composite sheets wrapped around the joint completely debonded especially at the top and bottom edges, as shown in Figure 3-3. The column lost 1/3 of its load and decreased to less than 400.0 kN. The test was halted, and the composite sheets were removed from the joint. Diamond shape shear cracks were revealed with buckling of the column steel bars, as shown in Figure 3-4 and Figure 3-5.

The overall joint behaviour was improved as compared to joint T-S1. Although, the load carrying capacity of the joint was increased, shear failure still occurred due to the high shear force resulting from the unintentional strengthening of the beam. This load increase caused cracking of the beam-column joint and accelerated the joint failure.

3.4 JOINT T-S5

The joint was wrapped with a bi-directional Tyfo BC GFRP sheet with the fibre direction at ±45°. Four 12 mm diameter holes were drilled right through the joint near the beam-column interface where GFRP anchors were installed and their ends were spread on this sheet. Each anchor was composed of 50 tows extracted from a Tyfo SEH-51A sheet of length 500 mm. The number of tows in each anchor was selected to provide a tensile strength more than the strength provided by the ½ in. (12.7 mm) diameter steel rod that was used to confine the joint in a recent study (Ghobarah and Said, 2001). The tows were bundled together before being impregnated with the epoxy adhesive and inserted into the holes through the joint. A Tyfo SEH-51A GFRP sheet was wrapped around the joint and extended above and below the joint for 400 mm with the reinforcing fibres parallel to the column longitudinal axis. Another Tyfo SEH-51A GFRP sheet was wrapped around the joint with the fibres parallel to the beam longitudinal axis, as shown in Figure 3-6.

The first beam crack occurred during the second cycle at a load of 16.8 kN up and 12.0 kN down. During the fourth cycle, the beam bottom and top bars reached their yield load of 108.0 kN and 99.3 kN, respectively. A corresponding beam-tip displacement of 30.0 mm was recorded and designated as the yield displacement, Δ_y.

During the eighth cycle, the joint was loaded to a DDF of 2 (±60 mm). The joint reached its ultimate capacity of 112.5 kN when pushing-up. During this cycle, tapping test indicated initiation of composite sheets debonding at the lower column. During the

tenth cycle, the specimen was loaded to a DDF of 3 (±90 mm). The composite sheets wrapped around the upper and lower columns fractured at the column corners, and debonded from the concrete surface, as shown in Figure 3-7. A degradation of column axial load of 10% was recorded. When repeating the same cycle, the composite sheets around the joint debonded, however, the GFRP anchors held the sheets around the joint. The sheets reached a maximum strain of 0.48% during this cycle. Severe deterioration of the specimen strength accompanied with considerable pinching of the load-deflection loop occurred. While reaching a DDF of 4 (±120 mm) in the following cycle, the load carrying capacity was reduced to about 32.0 kN. The GFRP anchors sheared off and fractured, thus eliminating the confinement effect of the composite sheets and the column axial load dropped significantly. The test was terminated in the middle of the cycle.

When the composite jacket was removed from the joint region, a combined adhesive and cohesive failure modes of the fibre were observed. The adhesive failure mode refers to the bond failure of the epoxy adhesive between the concrete and the composite sheets, and the cohesive failure refers to the delamination of the concrete cover with the composite sheets. Whereas the adhesive failure mode is a brittle and progressive failure, the cohesive failure mode is more desirable. Cracking of the joint region and buckling of the column bars are shown in Figure 3-8. The failure was initiated at the column plastic hinge regions due to the lack of confinement. The GFRP anchors proved to be effective in tying the composite sheets however, they could not sustain large shear deformations.

3.5 JOINT T-S4R

Uni-directional MBrace CF 130 CFRP sheets were used to strengthen the joint. Three U-shaped sheets were wrapped around the beam-column joint with the fibres parallel to the beam longitudinal axis. To provide confinement and to prevent the debonding of the sheets from concrete surface, four CFRP anchors were used to anchor the sheets end near the beam on both sides of the joint. Each anchor was made of 30 tows of 500 mm long bundled together to form a rod. The joint was wrapped with the first CFRP sheet then the anchors were inserted into the 12 mm diameter holes that were driven right through the joint. The ends of the tows were spread on the sheet and followed by wrapping the joint with the two other sheets. The idea was to transfer the forces developed in these sheets through the anchors and form closed hoops. 400 mm of the column above and below the joint was wrapped with a closed CFRP sheet with the fibres parallel to the hoop direction, as shown in Figure 3-9.

During the fourth loading cycle, yielding of the beam bars was reached. A yield load of 107 kN with a corresponding displacement of 26.0 mm were recoded in the push-up and pull-down loading directions. A major crack at the beam-column interface occurred, initiating the beam hinging. Flexural and shear-flexural cracks formed along the beam span.

During the eighth cycle, the joint was loaded to a DDF of 2 (±52.0 mm). The cracks at the beam-column interface opened up and widened. No debonding of the composite sheets was observed. The joint reached its ultimate strength of 128.4 kN when

it was pushed up to a DDF of 3 (±78.0 mm). When pulling the beam down, the joint reached a load of 120.0 kN. During this loading cycle the top beam corner steel bar fractured. This was caused by low cyclic fatigue as a result of the large number of repeated loading cycles. When repeating the same cycle, the joint reached a load level of 122.4 and 96.9 kN up and down, respectively. Severe diagonal cracks of the beam occurred, as shown in Figure 3-10. After loading the joint to a DDF of 4, a large residual displacement of more than 65.0 mm was recorded. When repeating the cycle, the beam bars buckled between the stirrups and the load carrying capacity dropped to about 30.0 kN and a beam flexural hinge formed, as shown in Figure 3-11.

To the end of the test, no significant reduction of the column axial load was recorded. The composite jacket performed well to the end of the test. The CFRP anchors proved effective in tying the free ends of the composite sheets together. No debonding of the jacket from the concrete surface occurred and the failure mode changed from the brittle joint shear failure to the desired beam flexural hinging.

3.6 ANALYSIS OF EXPERIMENTAL RESULTS

In this section, the behaviour of the tested joints and the effectiveness of the strengthening schemes are evaluated. The hysteretic behaviour of the joints, joint displacement ductility factor, beam-column joint shear deformations, cracking and yielding moments, contribution of concrete shear strength and beam stirrups in carrying the beam shear force, contribution of beam-column joint to storey drift, shear resistance

mechanisms of the beam-column joint, energy dissipation ability and degradation of joint stiffness are discussed. For the following analysis, a positive sign is given for the upward beam-tip load and the corresponding beam tip-displacement, displacement ductility factor, drift angle, storey shear, beam moment, beam rotation and joint deformation.

3.6.1 Beam-tip load-displacement relationships

The beam-tip load-displacement relationships of the joints are shown in Figure 3-12a to Figure 3-12d. The displacement corresponding to yielding of the beam bars was used to determine the displacement ductility level of each joint. The corresponding yield load was recorded and compared to the theoretical load obtained from the beam theory. The theoretical yield and ultimate loads are presented in Table 3-1. Each displacement ductility level was repeated to ensure the stability of joint behaviour. In order to capture the post ultimate behaviour, the test was continued until the joint strength degraded to less than 25% of its ultimate strength.

Pinching of the hysteretic loops was noted after exceeding the yield. Pinching is characterized by the narrow width of the hysteretic loops near mid-cycle, resulting in less energy dissipation per cycle. It is mainly caused by the slippage of the longitudinal beam bars, penetration of yield along the bars, and closing of flexural cracks in the plastic hinge zones. Each load cycle can be divided into several regions. The first region is at small displacement level which is highly affected by pinching. In this region, the joint exhibits large displacement values at small load levels. The second region is up to the displacement level of the last cycle, where the joint behaves almost elastically with high stiffness, the old cracks open and no new damaged areas formed. The third region is

when the displacement level of last cycle is exceeded. This region is characterized by softening behaviour with low joint stiffness. New cracks, damage areas and bars yielding form. When unloading the joint, non-linear behaviour is observed followed with a linear region until reaching the pinching zone. The non-linear region is characterized by small recovered displacement as a result of the concrete strain in the newly damaged areas. The elastic part has almost the same slope of the loading part following the pinching zone. When repeating this cycle, the same behaviour occurs except for the softening part.

The hysteretic behaviour of joint T-S1 was almost symmetric in both loading directions (positive and negative) up to onset of yielding. Strength softening with severe pinching occurred at a DDF of 2.0. Deterioration of joint strength occurred as a result of the joint shear failure and degradation of the bond conditions of the beam reinforcement bars. After the joint deterioration, the bond forces diminished along the embedded length of the beam bars and therefore the 90° bars hook carried most of the bar tensile force. This caused the spalling of the concrete cover at the column backside and hence buckling of the column longitudinal bars.

Joint T-S1RR exceeded the theoretical yield and ultimate strengths as a result of the tensile stresses developed into the composite sheets extended onto the beam. The joint had stable loops with minimal pinching until reaching DDF of 3. Strength degradation occurred after exceeding a DDF of 2, due to debonding of the composite sheets around the joint. After the jacket debonding, severe strength degradation with high pinching occurred.

Joint T-S5 reached almost the same strength values of the control joint T-S1.

Stable behaviour was recorded up to a DDF of 2. The GFRP sheet wrapped around the column with the reinforcing fibres normal to the hoop direction was ineffective in confining these regions. At a DDF of 3, the composite sheets debonded from the concrete surface, left the joint unconfined and permitted the shear cracks to propagate underneath the sheets. As a result, the joint strength deteriorated to less than 50% of the ultimate load. However, pinching of the hysteretic loops was less than the control joint. At a DDF of 4, the cracks extended underneath the composite sheets around the beam-column joint thus reducing their effectiveness to confine the joint. As a result, the GFRP anchors could not resist the shear deformation due to debonding of the GFRP sheets and failed in shear. After the anchors failed, the jacket completely debonded from the joint and a joint shear failure occurred.

Joint T-S4R showed the most stable behaviour. Although the joint reached lower strength than joint T-S1RR, it preserved its strength up to DDF of 3. The fractured corner steel bar caused torsional moment in the beam due to the shift in the centre of the resisting forces. While reaching DDF of 4, this torsional moment caused wide diagonal cracks in the beam and opening of the beam stirrups. Although this accelerated the joint failure, the failure mode was still a ductile beam hinging.

Figure 3-13 shows the envelopes of the hysteretic loops of the joints. Joint T-S4R gave the most stable behaviour up to a DDF of 3. Beyond this ductility level, strength deterioration occurred due to the torsional moment developed into the beam.

3.6.2 Storey shear- drift angle relationships

The storey shear was estimated as described before in Section 2.10.5, taking into

consideration the P-Δ effect. The beam-tip displacement was converted to drift angle using Equation (2-8). Storey shear-drift angle relationships are shown in Figure 3-14a to Figure 3-14d, and the envelopes of these relationships are shown in Figure 3-15. Strength deterioration of joint T-S1 occurred when storey drift of 0.02 radians was exceeded, whereas joint T-S4R showed stable behaviour up to drift of 0.04 radians.

3.6.3 Cracking, yield and ultimate moments

The cracking moment was obtained by multiplying the cracking beam load; the load corresponds to onset of the first beam crack, by the moment arm; the distance from the applied load centre to the column face. The concrete tensile stress was then evaluated using Equation (2-9). The concrete tensile stress was compared with the modulus of rupture given by CSA A23.3 (1994) Clause 8.6.4, which equals $0.6\sqrt{f_c'}$. The results are shown in Table 3-1. Joint T-S1RR and T-S5 were in good agreement with the code provisions. The cracking load of joint T-S4R could not be recorded due to the pre-cracking of the joint in a previous test.

The yield and ultimate moments "M_y, M_u" were obtained by multiplying the corresponding beam-tip loads by the moment arm to the critical section at the column face. The theoretical moment values were obtained assuming linear strain distribution in the concrete, a parabolic concrete stress distribution and based on the actual concrete and steel strengths. The experimental to theoretical yield moments for the joints T-S1, T-S5 and T-S4R varied from 1.1 to 1.15 and the experimental to theoretical ultimate moments varied from 0.98 to 1.09. For joint T-S1RR, the ratios between the experimental and

theoretical yield and ultimate moments were 1.41 and 1.21, respectively. This is because the contribution of the composite sheets was ignored when calculating the theoretical moments.

3.6.4 Shear deformation of beam-column joints

Beam-column joint deformation was measured using a pair of diagonal transducers (LVDT's) mounted on the joint. The measurements were then converted into a shear deformation using Equations (2-3), (2-4) and (2-5). The joint shear deformation was plotted versus the storey shear for each joint as shown in Figure 3-16a to Figure 3-16d. The storey shear was estimated as described before in Section 2.10.5, taking into consideration the P-Δ effect.

Joint T-S1 showed rapid increase in the joint deformation occurred after initiating the joint cracking. At a DDF of 2.0, the joint reached rotation of 0.0125 radians, accompanied with deterioration of storey shear. At the end of the test, the joint reached ultimate shear deformation of 0.022 radians. Joint T-S1RR exhibited recoverable joint shear deformation of about 0.002 radians when loading the joint up to a DDF of 2.0. The composite jacket was strained to about 0.2% and 0.6% in the vertical and the horizontal directions, respectively. When loading the specimen to a DDF of 3.0, debonding of the jacket and increase of the joint deformation to 0.015 radians occurred. This caused disintegration of the concrete joint and led to joint shear failure. At DDF of 4.0, the transducers detached from the concrete surface, so the joint deformations could no longer be measured. Joint T-S5 exhibited joint shear deformations of approximately 1/5 of the deformation of control joint T-S1 at a DDF of 2.0. The maximum joint deformation was

recorded at DDF of 3 to be 0.0025 radians with strain in the composite sheets of 0.38% in the horizontal direction. When reaching a DDF of 4.0, the composite sheets debonded from the joint surface, the LVDT's installed at the joint also detached from the joint, so the joint deformation could no longer be determined. Joint T-S4R showed the best joint behaviour. To the end of test, at a DDF of 4.0, the joint deformation was as low as 0.0018 radians. The jacket remained intact with the concrete with a maximum strain in the hoops direction of 0.125%.

The envelopes of the joint shear force-deformation relationships are shown in Figure 3-17. The elastic desirable behaviour of joint T-S4R against the nonlinear response of joint T-S1 is obvious.

3.6.5 Moment-rotation relationships

The rotation of the beam section at 175 mm from the column face was recorded for each joint. This rotation was plotted versus the beam moment at the column face, as shown in Figure 3-18a to Figure 3-18d. The recorded rotation involved the rotation due to yielding of the reinforcement bars and the rotation due to slippage of the bars. The high rotation values of joint T-S4R at the end of the test occurred as a result of the torsional moment in the beam section caused by the fracture of beam steel bar. Average curvature of beam critical section was evaluated, knowing the beam-section rotation θ, as:

$$\phi = \frac{\theta}{l} \tag{3-1}$$

where l, is the gauge length in the region at which the curvature was measured, i.e. 175 mm.

The bending stiffness EI of the beam was then estimated at maximum moment as:

$$EI = \frac{M}{\phi} \tag{3-2}$$

The bending stiffness was compared to the empirical equations given by CSA A23.3 (1994) Clause 8.6.2 and is presented in Table 3-1, where E_c is the concrete modulus of elasticity and I_g is the gross sectional moment of inertia. Joint T-S1RR showed the highest stiffness due to the contribution of the GFRP sheet extended onto the beam. The bending stiffness was as low as 3% of the initial uncracked stiffness, indicating the severe effect of cyclic loading on the beam stiffness and consequently on the beam deformation.

3.6.6 Shear in beam

The shear in beam was resisted by the concrete shear strength and the beam steel stirrups. Two strain gauges were mounted on the second and third stirrups from the column face. The strain readings were then converted into stresses in the stirrups and the stirrups contribution in carrying beam shear force was evaluated as described in Section 2.10.8. The variation of tensile strain along stirrup legs was ignored. The concrete contribution was evaluated by subtracting the beam shear force from the stirrups contribution. The steel and concrete contributions to the shear resistance are plotted versus the displacement ductility factor for the four joints in Figure 3-19a to Figure 3-19d.

According to the CSA A23.3 (1994) provisions, the concrete shear strength for nominal ductility members (DDF of 2) is less than $0.2\sqrt{f_c'}$. For ductile members (DDF >

2), the maximum concrete shear strength is less than $0.1\sqrt{f_c^{'}}$ in case of application compression stress of $0.1\,f_c^{'}$ on the member and equals zero if no compression stress is applied to the section. For all the joints, the concrete resistance to the negative beam shear force was less than its resistance to the positive shear. This was because of the pre-cracking of the concrete compression diagonal struts during the positive part of the loop. The concrete resistance was estimated at different ductility levels for each joint and presented in Table 3-2. At DDF of 2, joint T-S1 had concrete shear strength of $0.205\sqrt{f_c^{'}}$, whereas the concrete shear strength of joint T-S4R was very low. This occurred due to the unexpected torsional moment induced to the beam section of joint T-S4R.

3.6.7 Shear in beam-column joints

The joint shear stress was evaluated as:

$$v_j = \frac{V_j}{b_j\, d_j} \tag{3-3}$$

where, v_j is the joint shear stress, V_j is the joint shear force, b_j is the effective joint width (250 mm) and d_j is the joint effective depth.

The maximum shear stress was estimated for each joint and presented in Table 3-1. The joints exhibited maximum shear stress ranging from 0.92 to $1.06\sqrt{f_c^{'}}$, which is approximately 2/3 of the joint shear resistance specified by CSA A23.3 (1994) Clause 21.6.4. However, joint T-S1 exhibited a rapid degradation in shear strength, joint T4R showed the most stable shear strength to failure. The induced shear stresses in the beam-

column joints was resisted by the concrete alone for joint T1, and partially resisted by the concrete and the FRP sheets for the strengthened joints. The contribution of concrete shear strength and FRP sheets in carrying the joint shear was estimated as described before in Section 2.10.9. Figure 3-20a to Figure 3-20d show the contributions of concrete shear strength and FRP sheets in carrying the shear forces. Table 3-3 shows the deterioration of concrete shear strength with increasing the displacement ductility factor. Whereas, the concrete shear strength reached almost zero at DDF of 4.0 for joint T-S1RR, joint T-S4R preserved its concrete shear strength to the end of the test. This was a result of the confining pressure produced on the concrete core by the FRP jacket, which maintained the concrete integrity and strength. However, the reduction in the concrete shear strength of joint T-S4R was due to the deterioration of the specimen lateral strength when the beam flexural hinge formed.

3.6.8 Joint contribution to storey drift

Figure 3-21a and Figure 3-21b show the contribution of beam-column joint shear deformation to the storey drift. Increasing the joint deformation will increase the joint contribution to the storey drift. Satisfactory joint response is characterized by lower joint contribution in storey drift as increasing the drift angle. Joint T-S1 showed an increased joint contribution to storey drift. The joint contribution increased from 6% at a negative storey drift of 1.5% (yield cycle) to 22% at a storey drift of 3.5%. The strengthened joint T1RR showed less contribution of the beam-column joint deformation in storey drift. The joint contributed 8% of the storey drift at drift angle of 1.5%, and 18% of the storey drift at drift angle of 3.5%. After the GFRP jacket debonding from the concrete surface, the

joint contribution increased significantly to 22% at negative storey drift of 4.8%. Joint T-S5 showed lower joint contribution to the storey drift up to failure. Joint T-S4R contributed less than 4% of the storey drift to the end of the test.

3.6.9 Stiffness

The stiffness degradation of the tested joints is shown in Figure 3-22. Joints T-S1 and T-S5 showed high initial stiffness as compared to joints T-S1RR and T-S4R because of the pre-cracking of the latter joints before strengthening. After cracking, joints T-S1 and T-S5 lost more than half of their initial stiffness. Joint T-S1RR showed the same stiffness level of joint T-S4R until debonding of the composite sheets took place. After debonding, the joint stiffness degraded more rapidly. In general, it was found that the rehabilitation schemes improved the joint stiffness as compared to the control joint.

3.6.10 Energy dissipation

The area enclosed by a hysteretic loop in a given cycle represents the energy dissipated by the joint during this cycle. The ability of the structure to dissipate energy has a strong influence on the response of the structure to an earthquake loading. Figure 3-23 shows the cumulative energy dissipated by the tested joints. Joint T-S4R showed the lowest energy dissipation ability until steel yielding because of the pre-cracking of the beam from the previous test before rehabilitation. The ductile behaviour of the joint after yielding increased its energy dissipation ability to about three times the energy dissipated by the control joint T-S1. Joints T-S1RR and T-S5 dissipated almost twice the energy dissipated by the control joint.

3.6.11 Strain in FRP jacket

The horizontal and vertical strains in FRP jackets were monitored during the test. A well-designed strengthening jacket should maintain the concrete integrity in the joint zone and reduce the concrete dilation. Due to the strain compatibility between the FRP jacket and the confined concrete, reducing the concrete dilation is equivalent to reducing the strains in FRP jacket. For the three joints, the horizontal strain reached multiples of the vertical strain, as shown in Figure 3-24. The ratio between the horizontal and vertical strain in the FRP jacket was 2.1, and 11.9 for joints T-S1RR, and T-S5, respectively, indicating that mounting the FRP sheets parallel to the beam direction is more effective than mounting the sheets parallel to the column direction. Joint T-S4R showed the lower strain in the horizontal and vertical directions, which indicates the effectiveness of the CFRP jacket to reduce the concrete dilation.

3.7 SUMMARY

In this chapter, the behaviour of four beam-column subassemblies, with joint shear strength deficiency, was discussed and the processed data was presented. The control joint showed a joint shear failure mode with severe strength deterioration, stiffness degradation, and low energy dissipation ability. The other three joints were strengthened using composite sheet jacket. In general, the strengthened joints showed more favourable failure mode. Gradual strength deterioration and stiffness degradation were recoded. The joints showed more energy dissipation capability. The shear behaviour

of the joint zone remained elastic. The composite sheets showed to be less effective if they are oriented in the column direction. FRP anchors were successfully used to prevent the sheet debonding from the concrete surface.

Table 3-1 Comparison of Shear-deficient joints behaviour

Parameter	Joint T-S1	Joint T-S1RR	Joint T-S5	Joint T-S4R
Yield displacement (mm)	28.0	30.0	30.0	26.0
Experimental yield load (kN)	+110.0 -99.1	+135.0 -129.3	+108.0 -99.3	+107.0 -107.0
Experimental ultimate load (kN)	+116.0 -101.9	+143.0 -131.2	+112.5 -107.4	+128.4 -128.0
Theoretical yield load (kN)	95.87	96.00*	96.49	97.09
Theoretical ultimate load (kN)	118.56	118.32*	117.78	117.61
Maximum displacement ductility factor	2.5	4	3	4
Concrete tensile stress (MPa)	$0.34\sqrt{f_c^{'}}$	$0.62\sqrt{f_c^{'}}$	$0.56\sqrt{f_c^{'}}$	N/A
Bending stiffness at maximum moment	$0.043E_cI_g$	$0.088E_cI_g$	$0.031E_cI_g$	$0.032E_cI_g$
Maximum joint rotation (rad)	0.0220	0.0150	0.0025	0.0018
Maximum joint shear stress (MPa)	$\sqrt{f_c^{'}}$	$1.06\sqrt{f_c^{'}}$	$0.92\sqrt{f_c^{'}}$	$0.93\sqrt{f_c^{'}}$

* Contribution of GFRP sheets to beam strength was ignored.

Table 3-2 Beam concrete shear resistance as a fraction of $\sqrt{f_c^{'}}$

DDF*	Joint T-S1	Joint T-S1RR	Joint T-S5	Joint T-S4R
-4	----	0.017	----	0
-3	----	0.041	0	0.005
-2	0	0.136	0	0.021
-1	0.046	0.071	0.127	0.115
1	0.080	0.175	0.151	0.093
2	0.205	0.136	0.106	0
3	----	0.066	0.109	0
4	----	0.024	0.051	0

* The negative sign represent the part of the cycle where the beam-tip is pulled down.

Table 3-3 Joint concrete shear resistance as a fraction of $\sqrt{f_c^{'}}$

DDF*	Joint T-S1	Joint T-S1RR	Joint T-S5	Joint T-S4R
-4	----	0.017	----	0.334
-3	----	0.203	0.331	0.704
-2	0.704	0.900	0.647	0.817
-1	1.000	0.840	0.615	0.696
1	0.946	0.992	0.772	0.685
2	0.814	0.909	0.781	0.803
3	---	0.507	0.527	0.763
4	----	0.211	----	0.204

* The negative sign represent the part of the cycle where the beam-tip is pulled down.

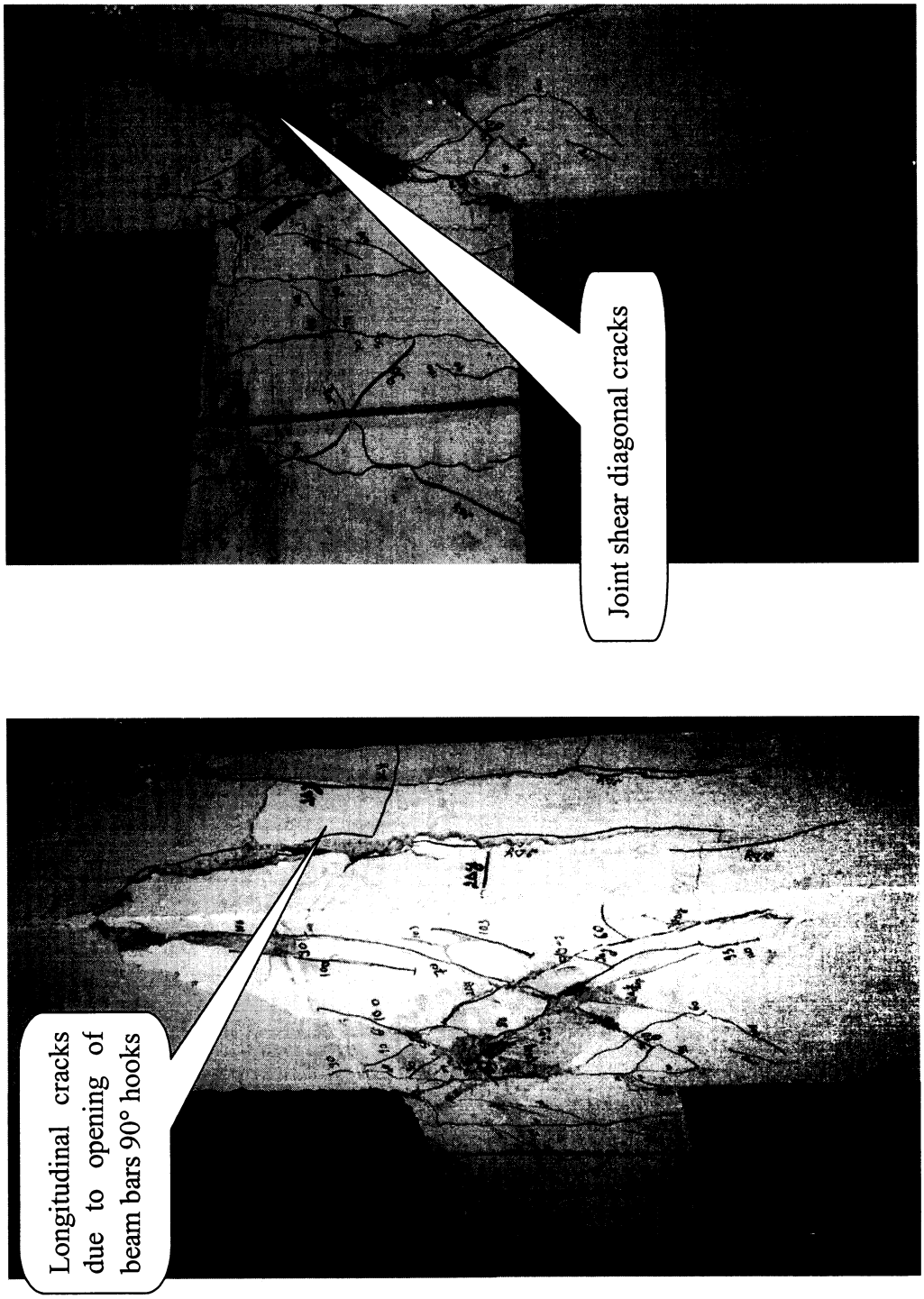

Figure 3-1 Failure pattern of joint T-S1

Figure 3-2 Strengthening scheme of joint T-S1RR

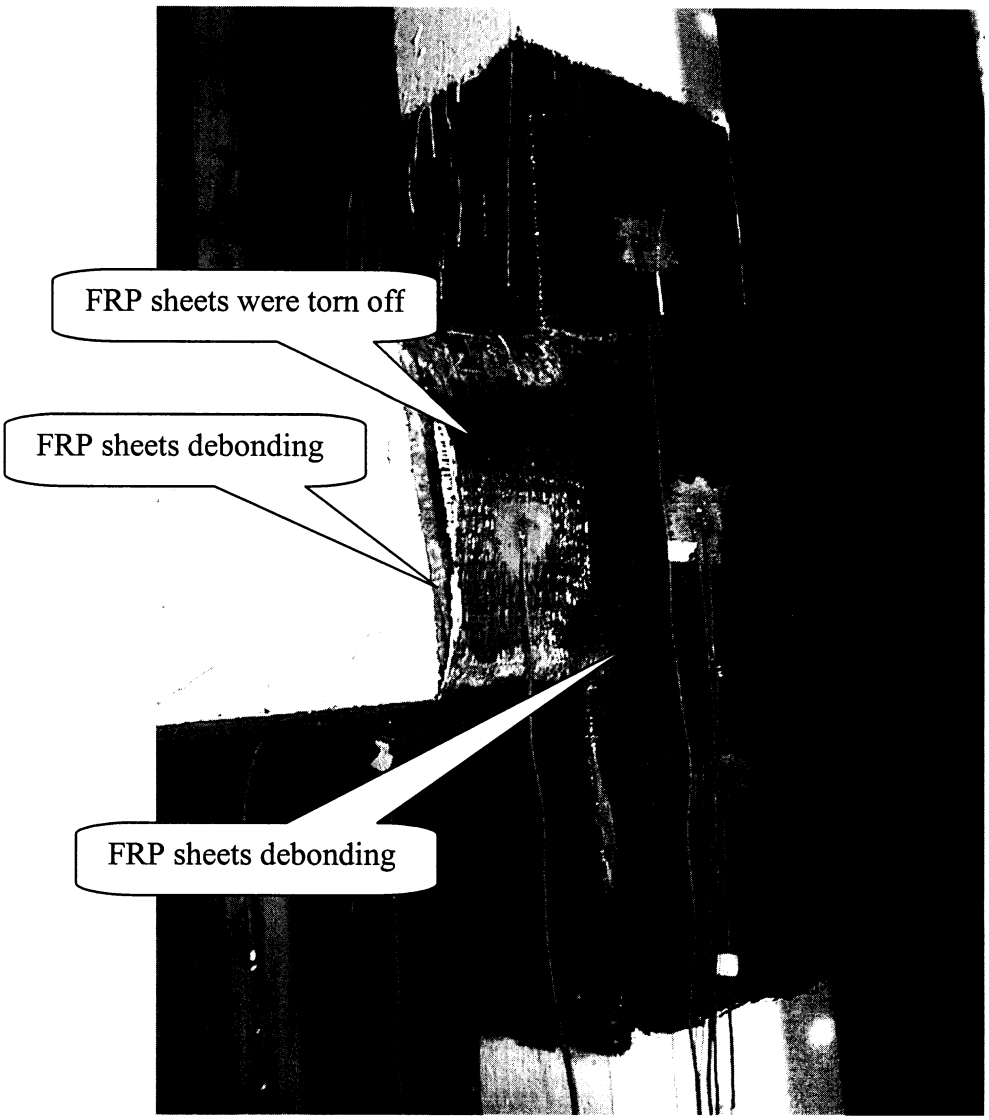

Figure 3-3 Debonding of FRP sheets wrapped around joint T-S1RR

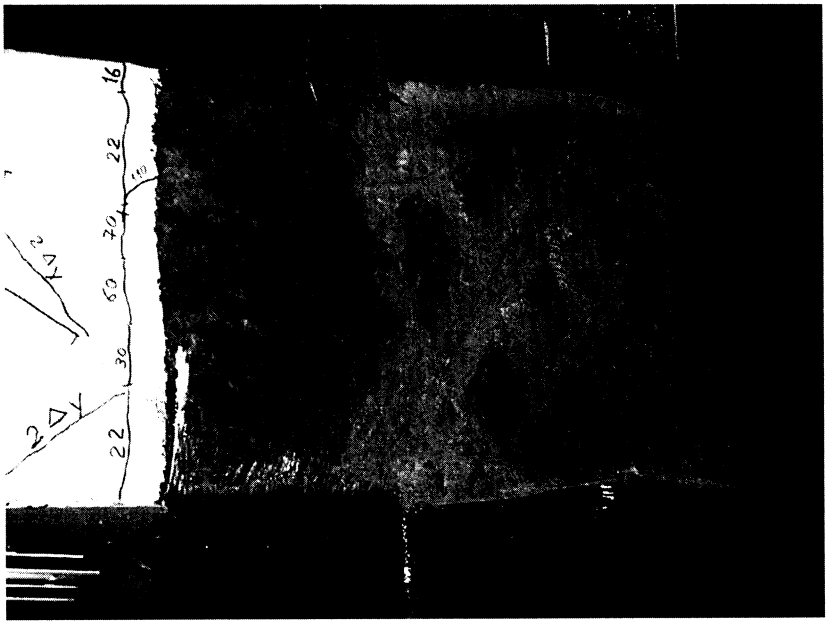

Figure 3-4 Cracking of joint T-S1RR after removing the GFRP jacket

Figure 3-5 Buckling of column reinforcement bars of joint T-S1RR

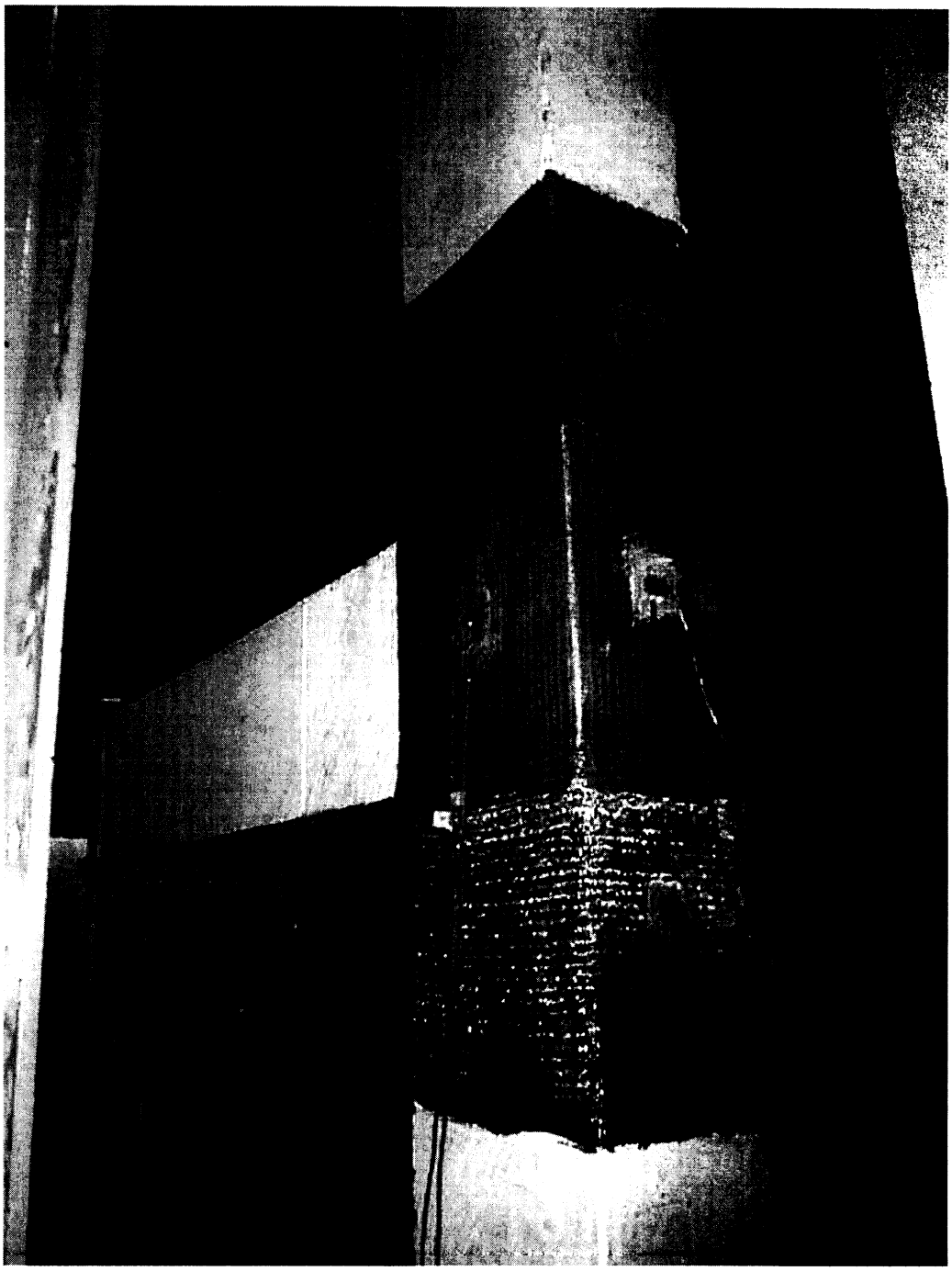

Figure 3-6 Strengthening scheme of joint T-S5

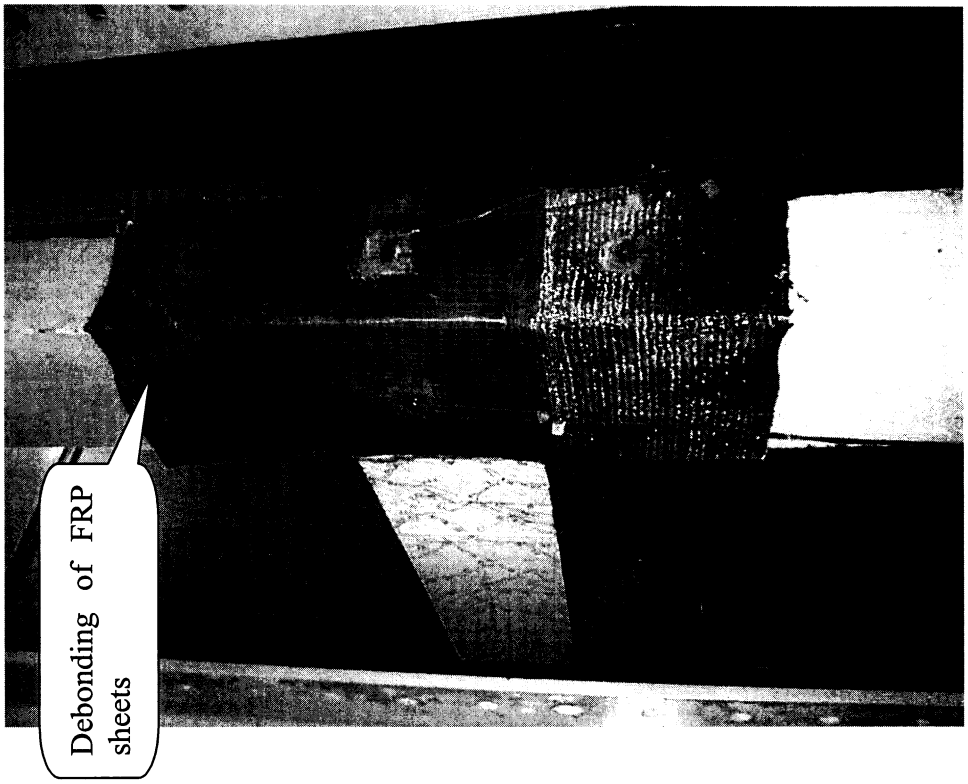

Figure 3-7 Debonding of GFRP sheets from column sides of joint T-S5

Figure 3-8 cracking and spalling of concrete after removing the from joint T-S5

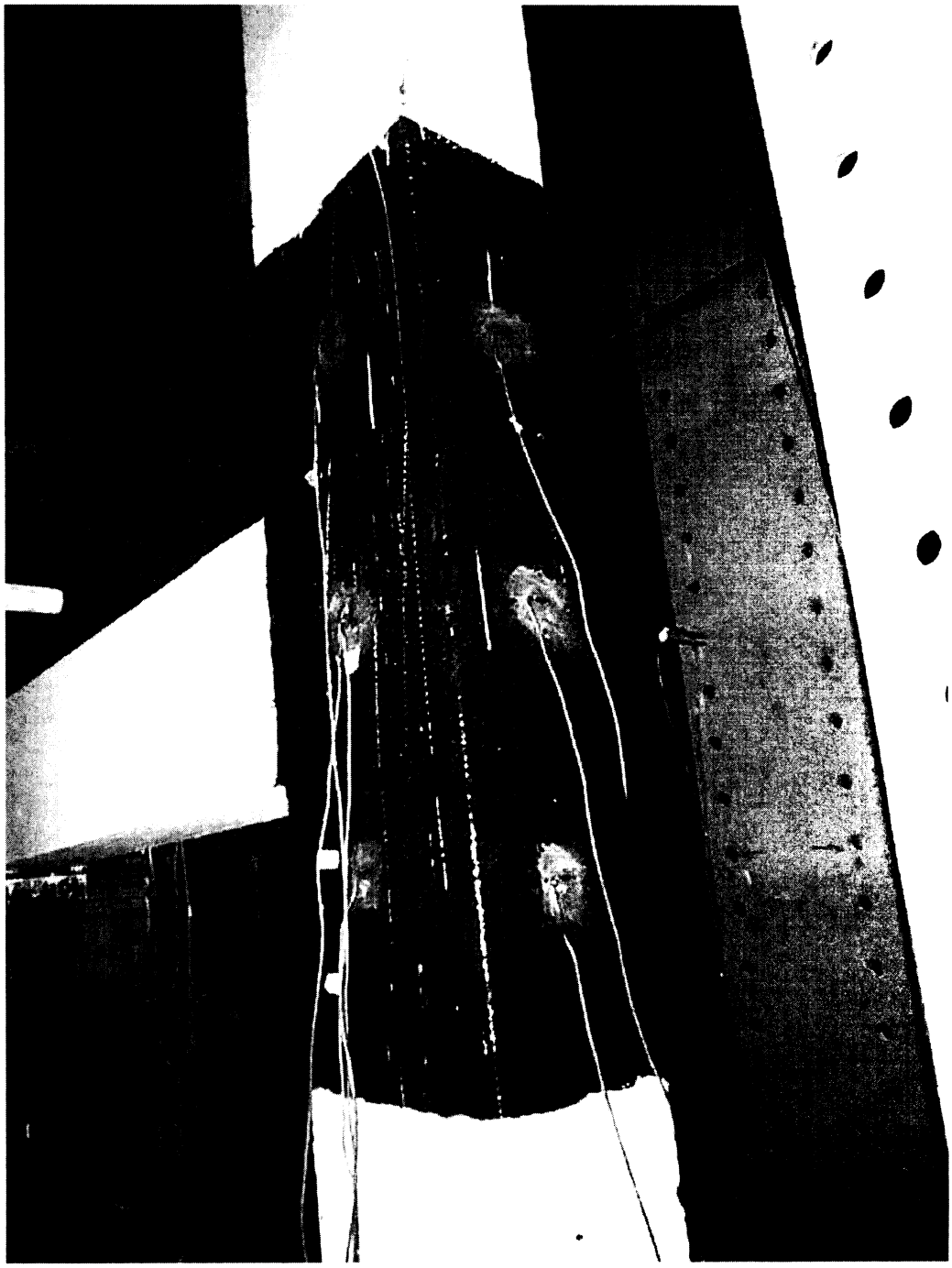

Figure 3-9 Strengthening scheme of joint T-S4R

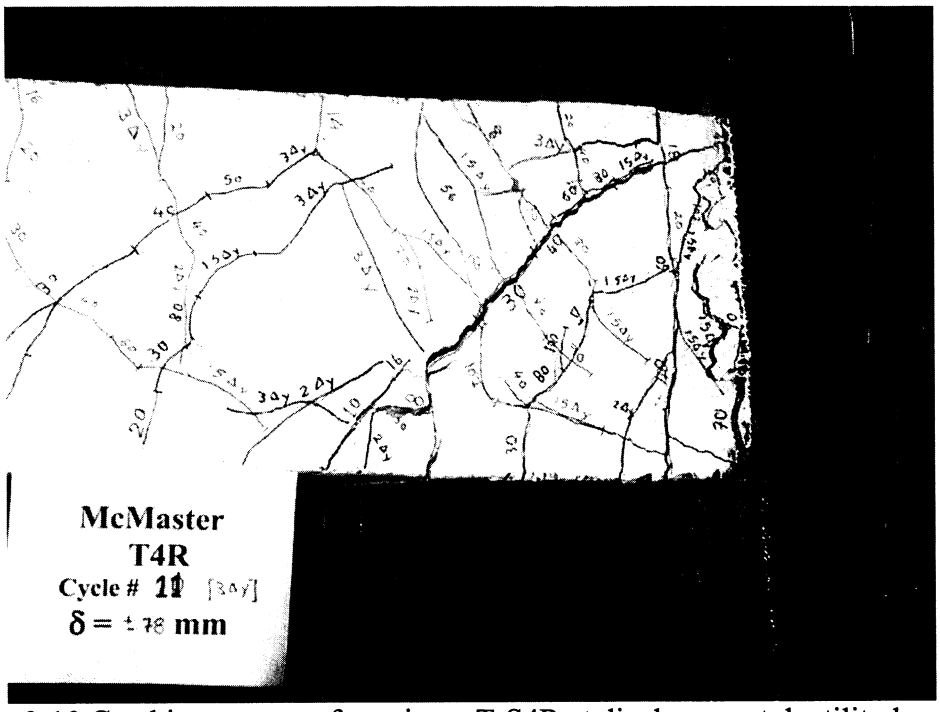

Figure 3-10 Cracking pattern of specimen T-S4R at displacement ductility level of 3

Figure 3-11 Flexural hinging of joint T-S4R

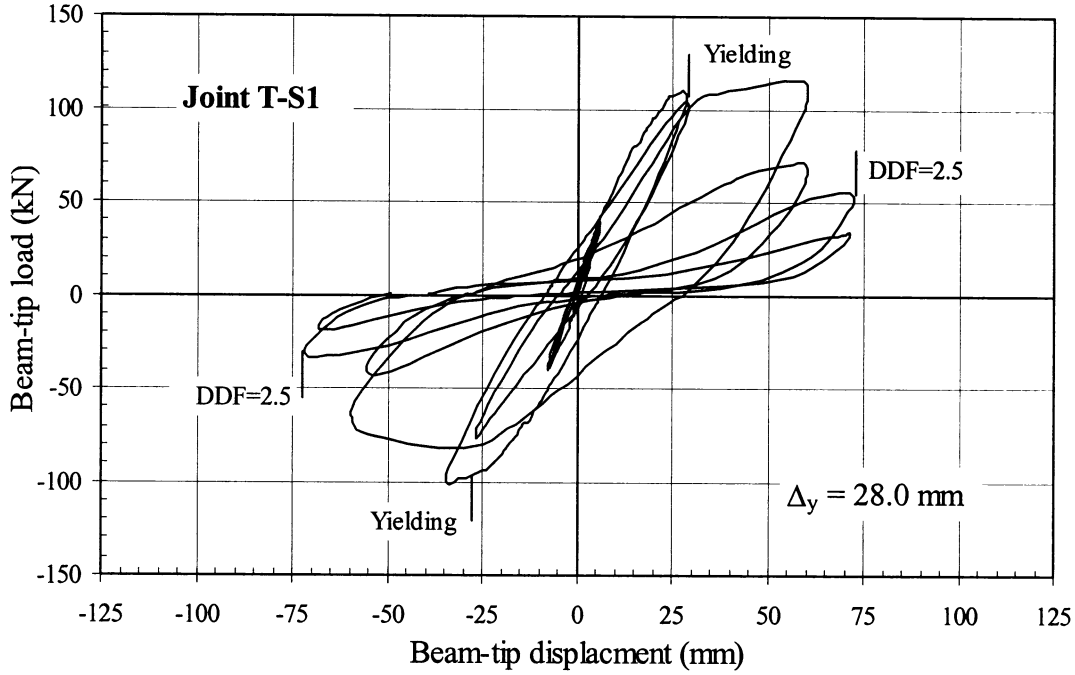

Figure 3-12a Beam-tip load–displacement relationship of joint T-S1

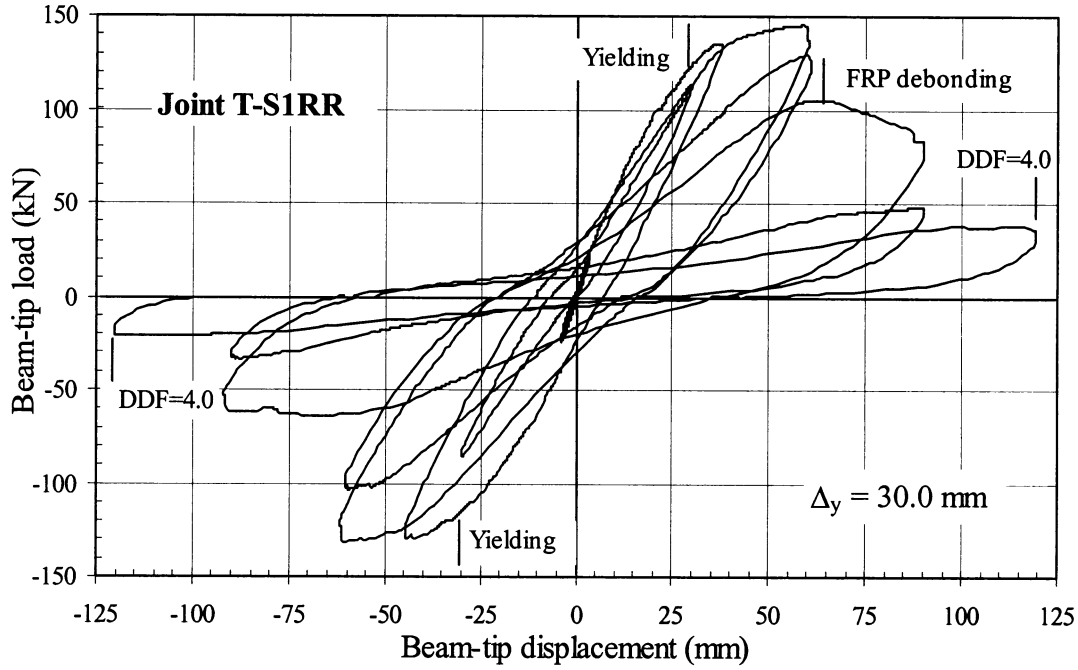

Figure 3-12b Beam-tip load–displacement relationship of joint T-S1RR

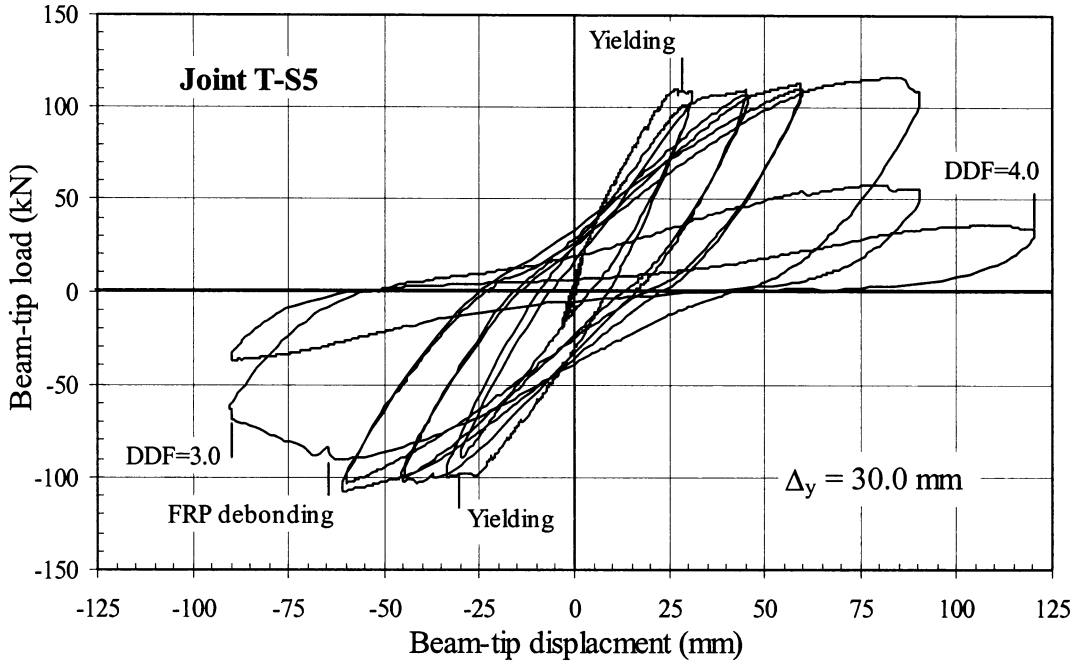

Figure 3-12c Beam-tip load–displacement relationship of joint T-S5

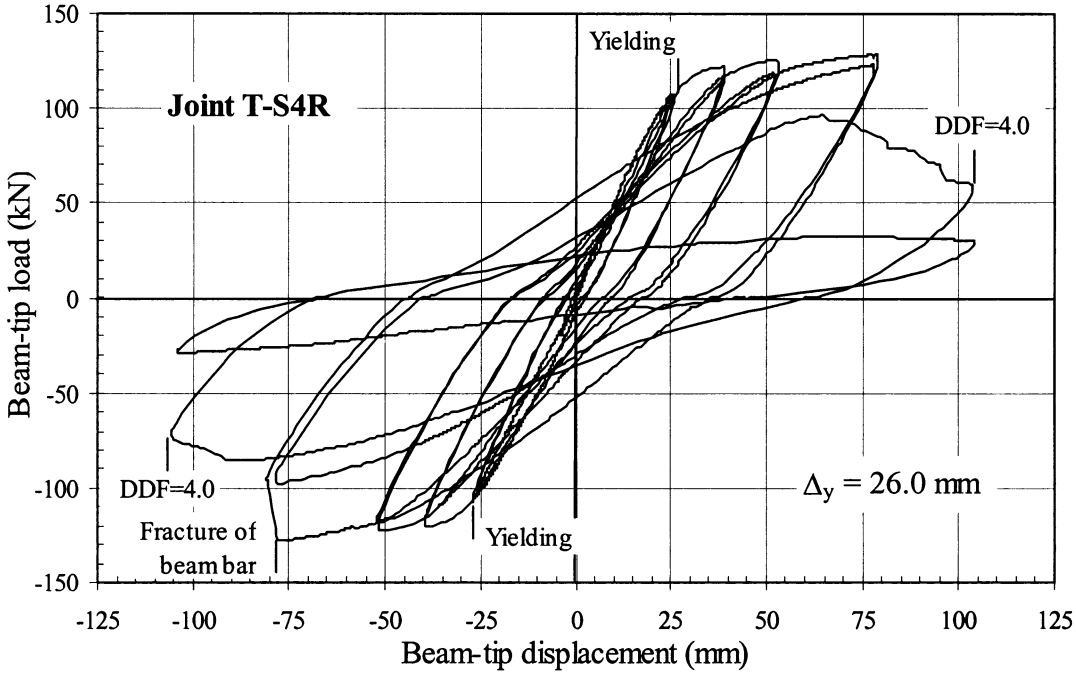

Figure 3-12d Beam-tip load–displacement relationship of joint T-S4R

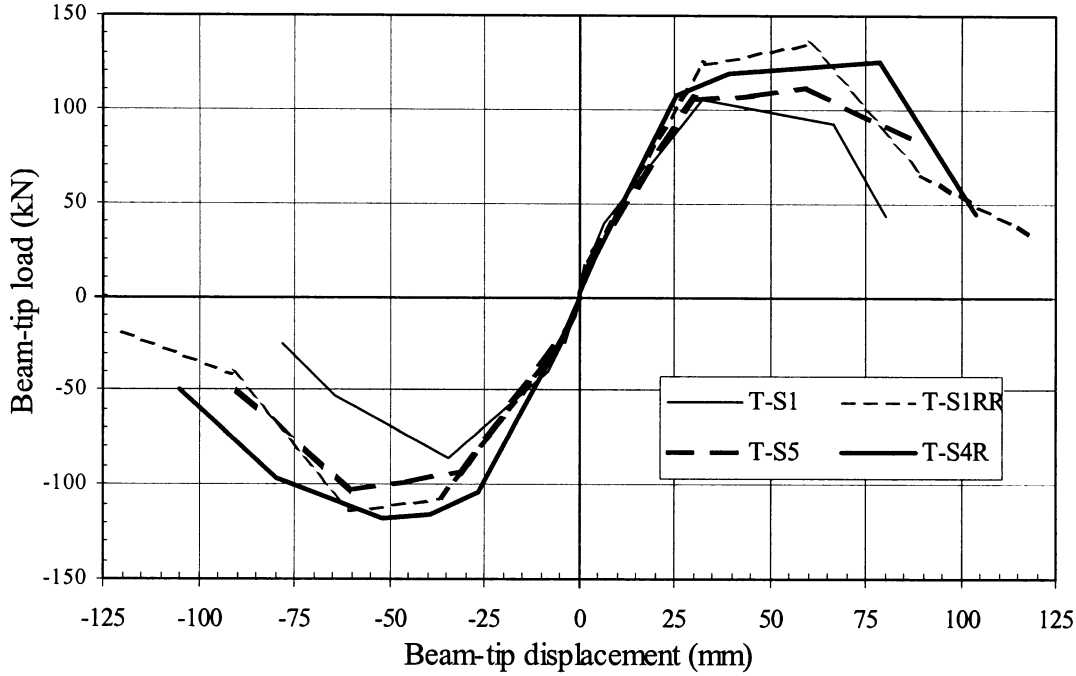

Figure 3-13 Envelopes of the loading loops for the tested joints

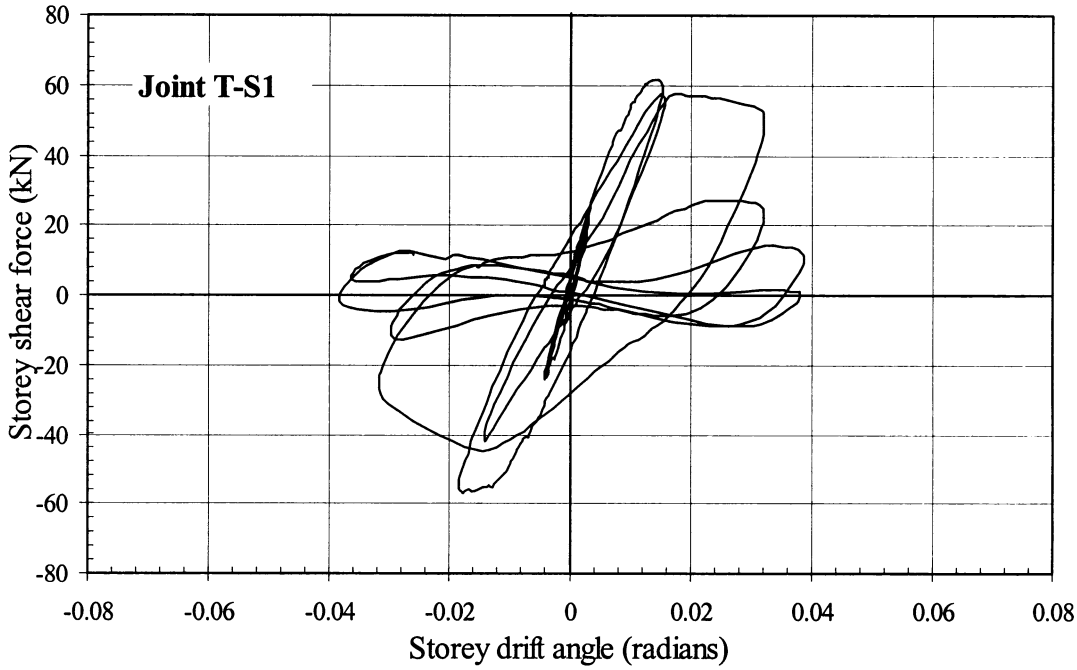

Figure 3-14a Storey shear force–drift angle relationship of joint T-S1

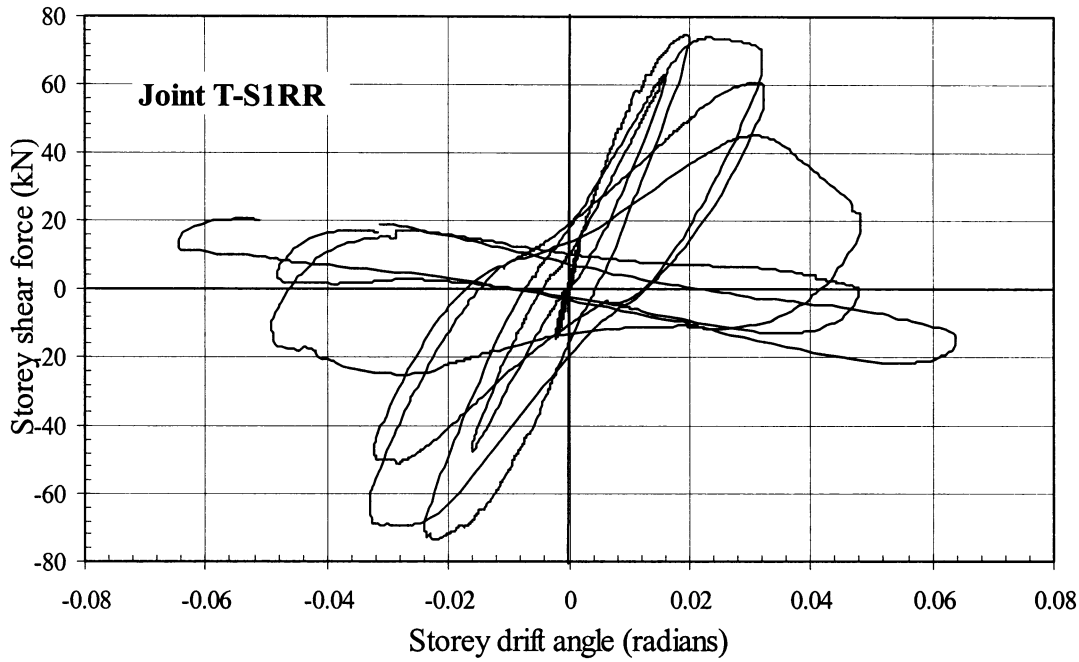

Figure 3-14b Storey shear force–drift angle relationship of joint T-S1RR

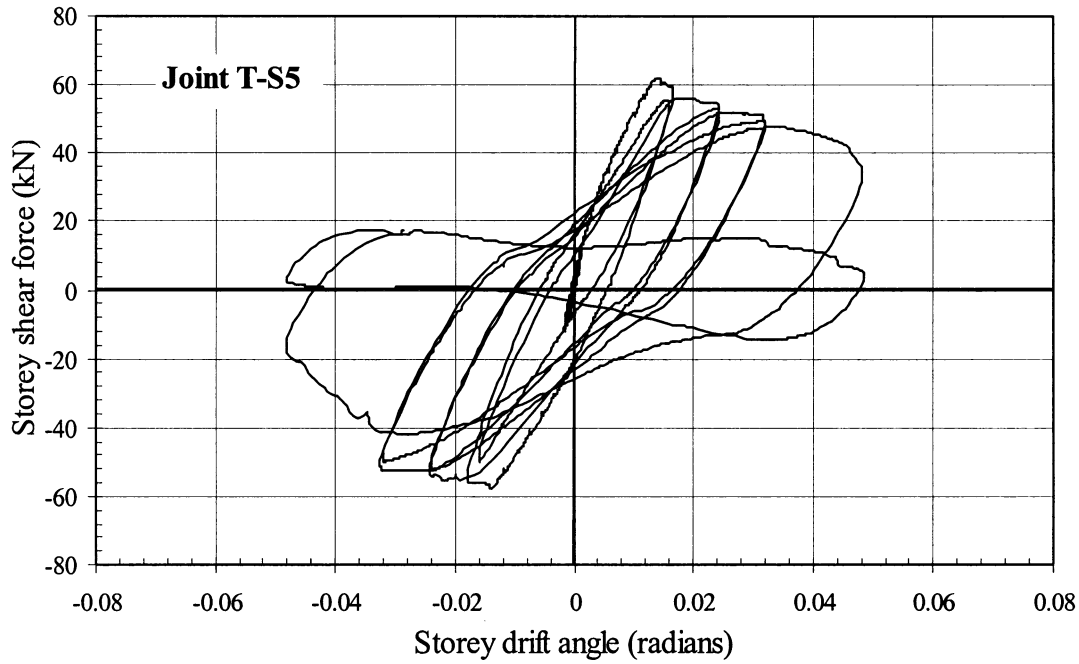

Figure 3-14c Storey shear force–drift angle relationship of joint T-S5

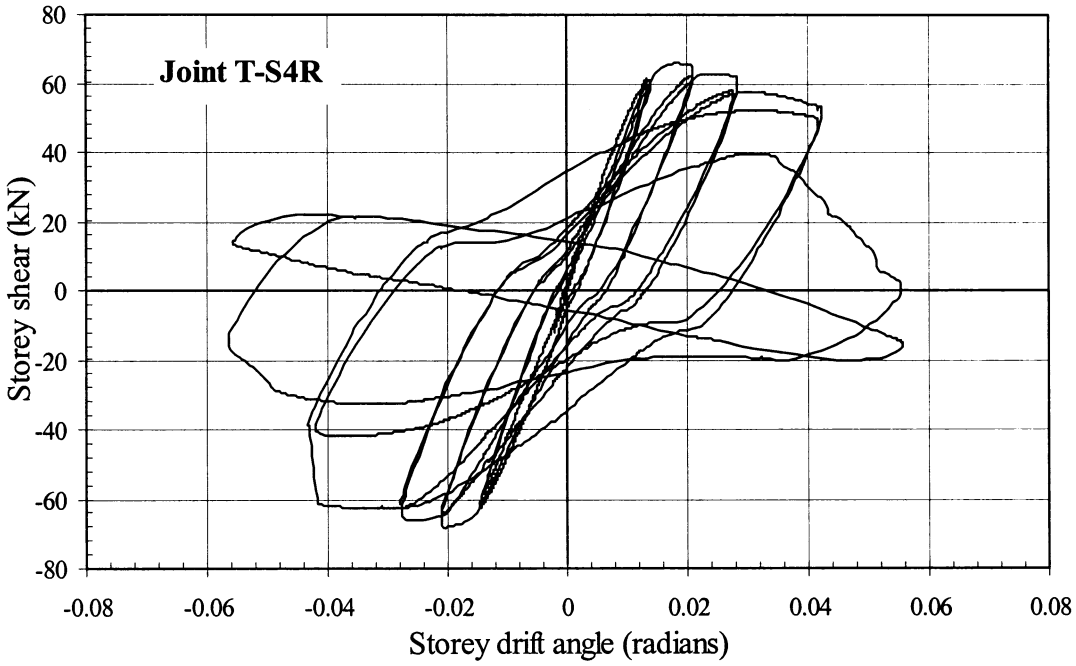

Figure 3-14d Storey shear force–drift angle relationship of joint T-S4R

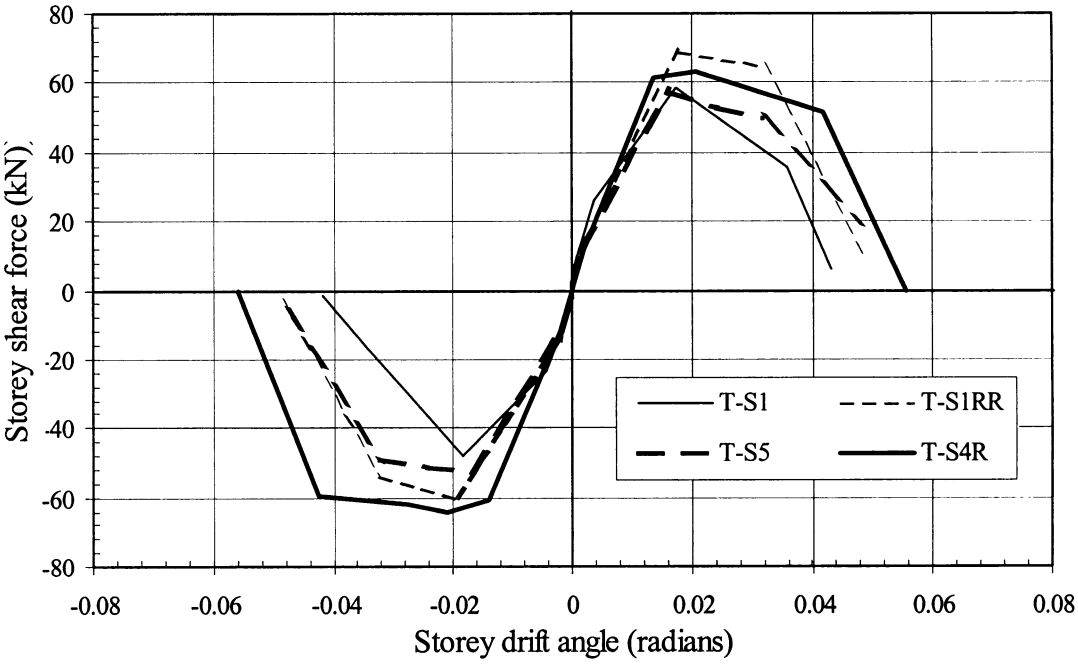

Figure 3-15 Envelopes of storey shear-drift angle relationships of the tested joints

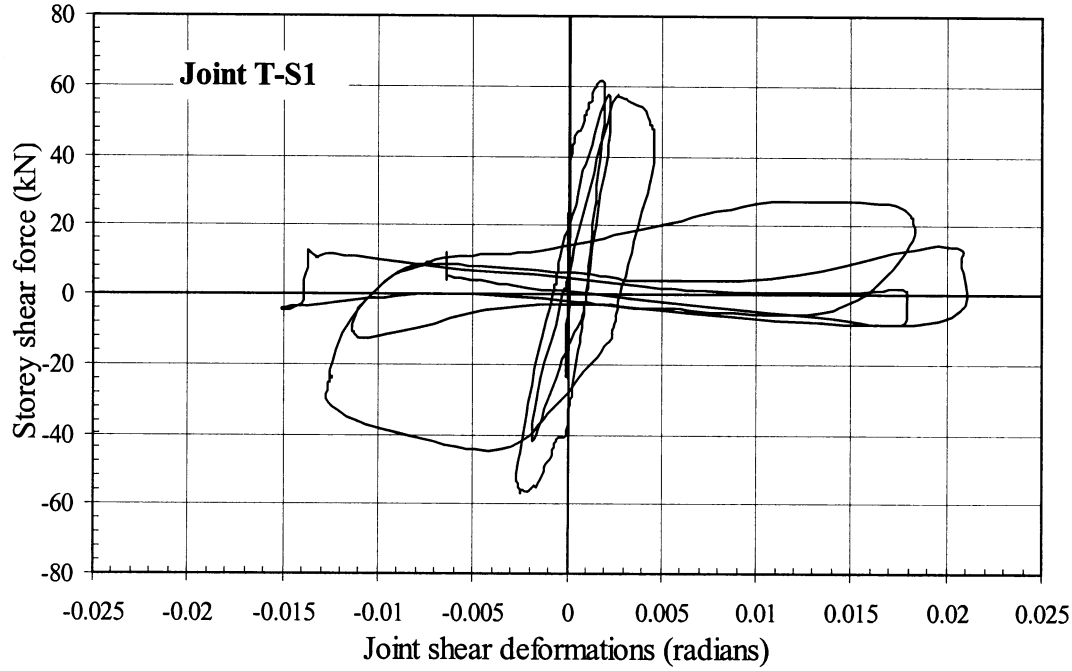

Figure 3-16a Joint shear deformation-storey shear force relationship of joint T-S1

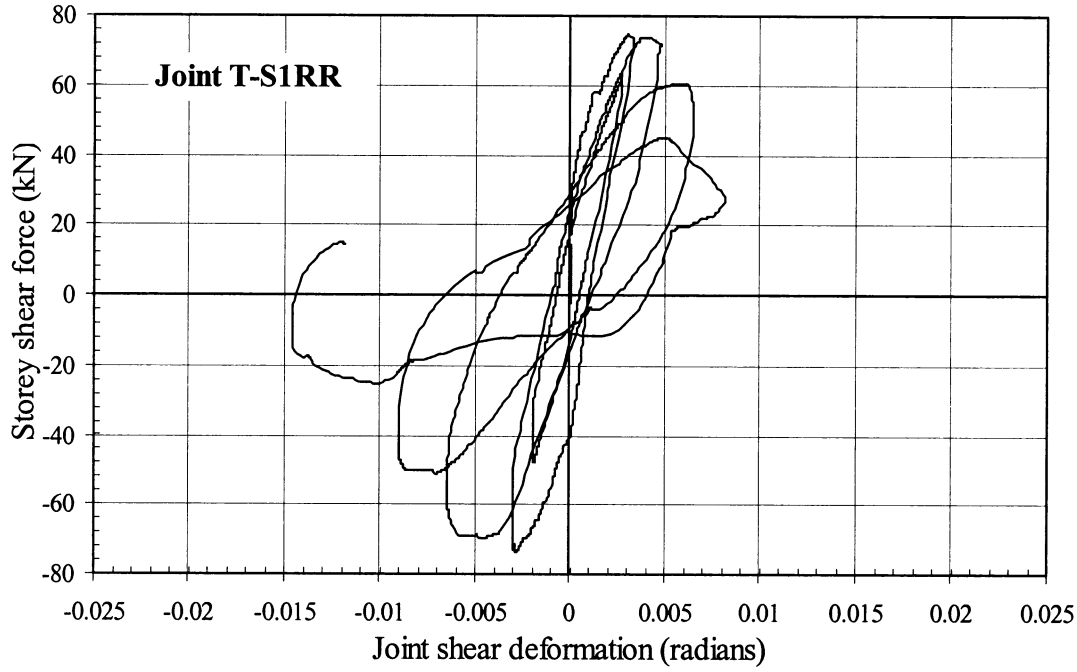

Figure 3-16b Joint shear deformation-storey shear force relationship of joint T-S1RR

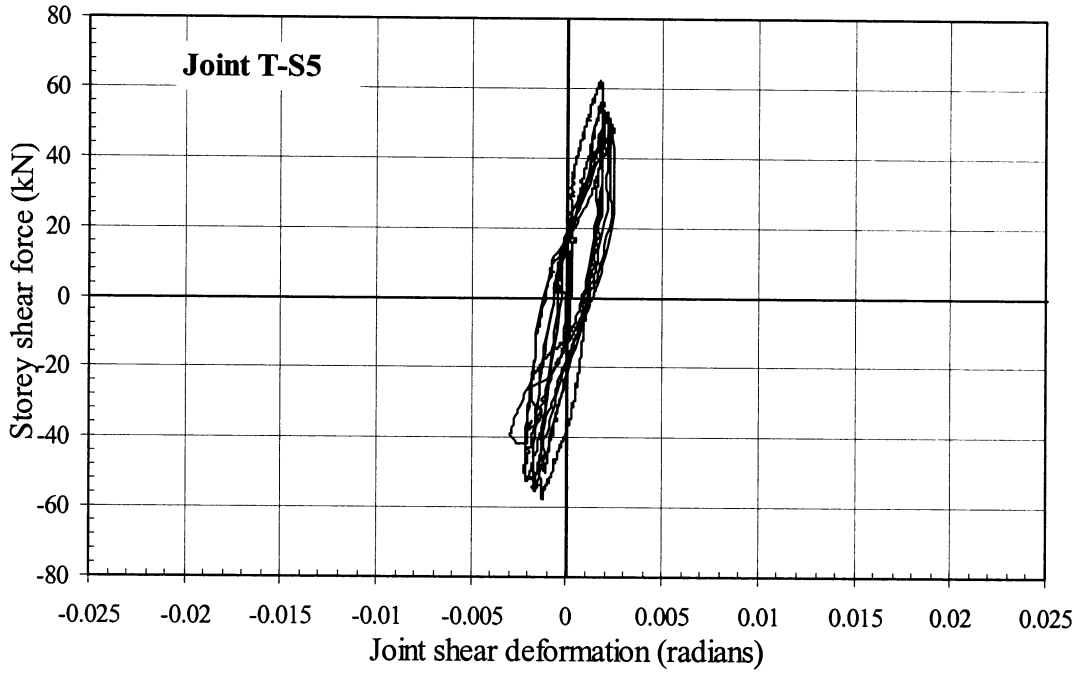

Figure 3-16c Joint shear deformation-storey shear force relationship of joint T-S5

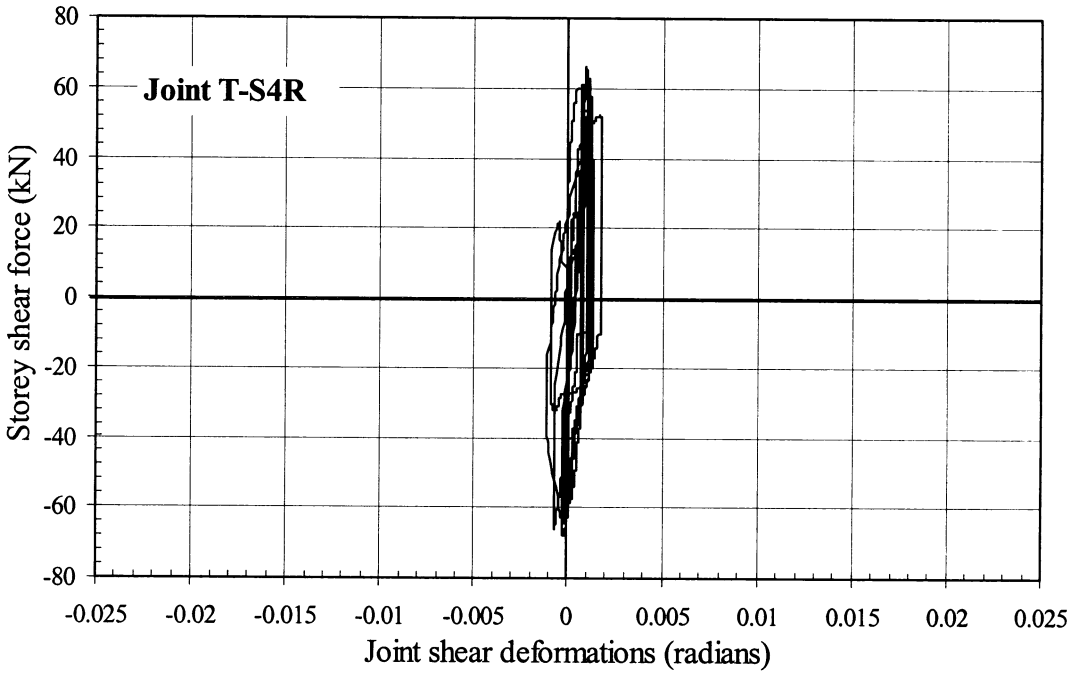

Figure 3-16d Joint shear deformation-storey shear force relationship of joint T-S4R

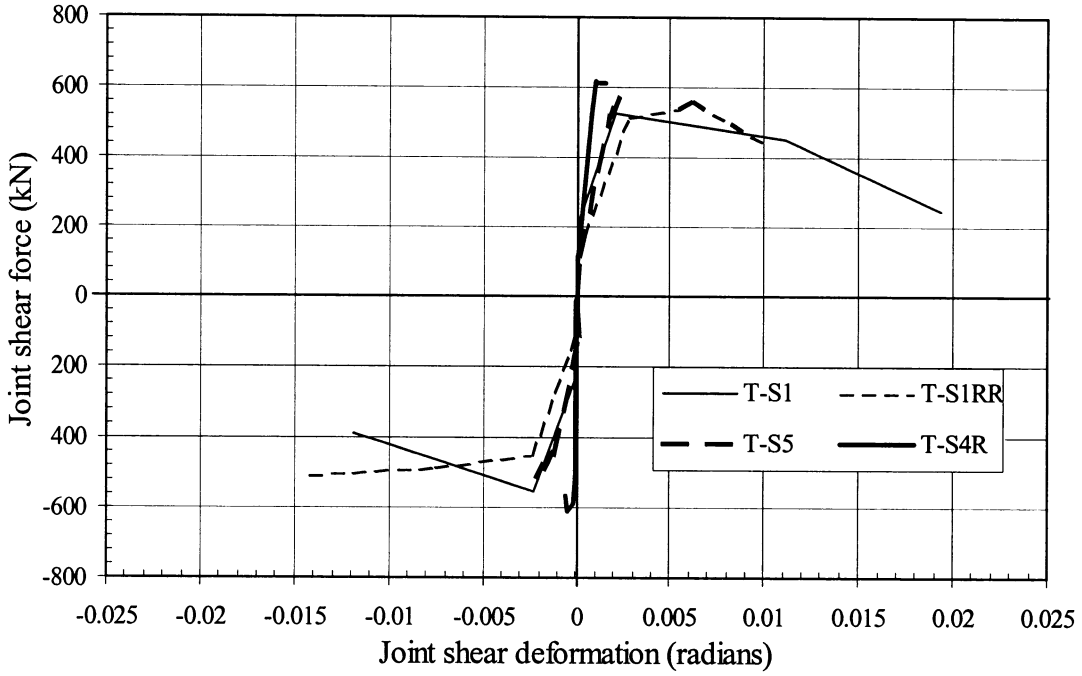

Figure 3-17 Envelopes of joint shear force-deformation of the tested joints

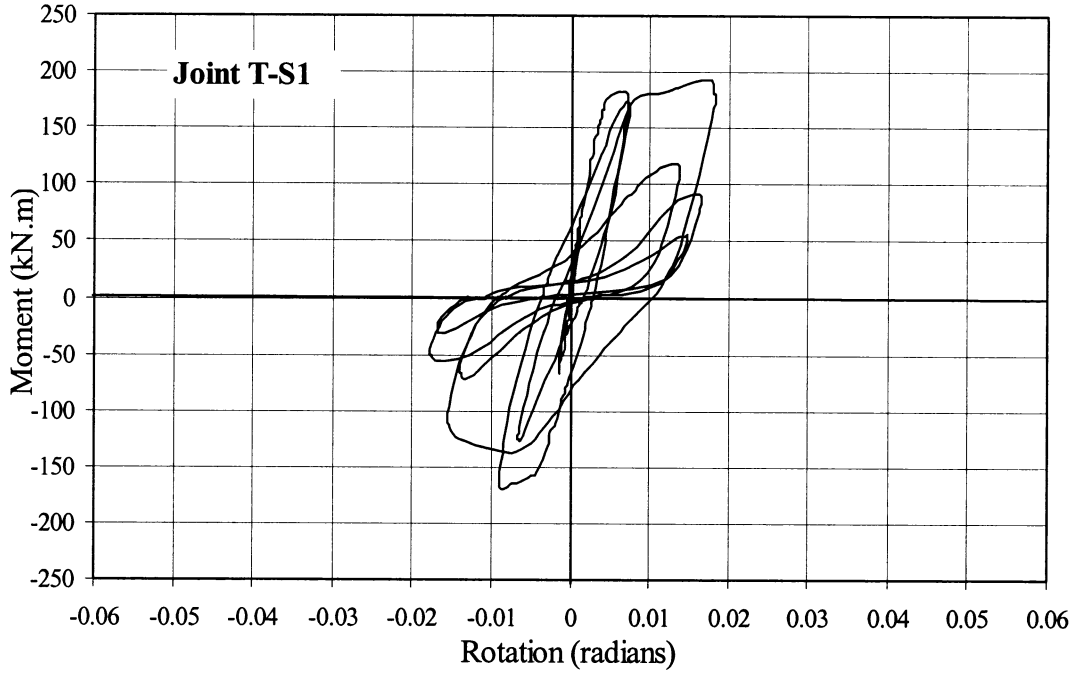

Figure 3-18a Beam moment-rotation at 175 mm from column face of joint T-S1

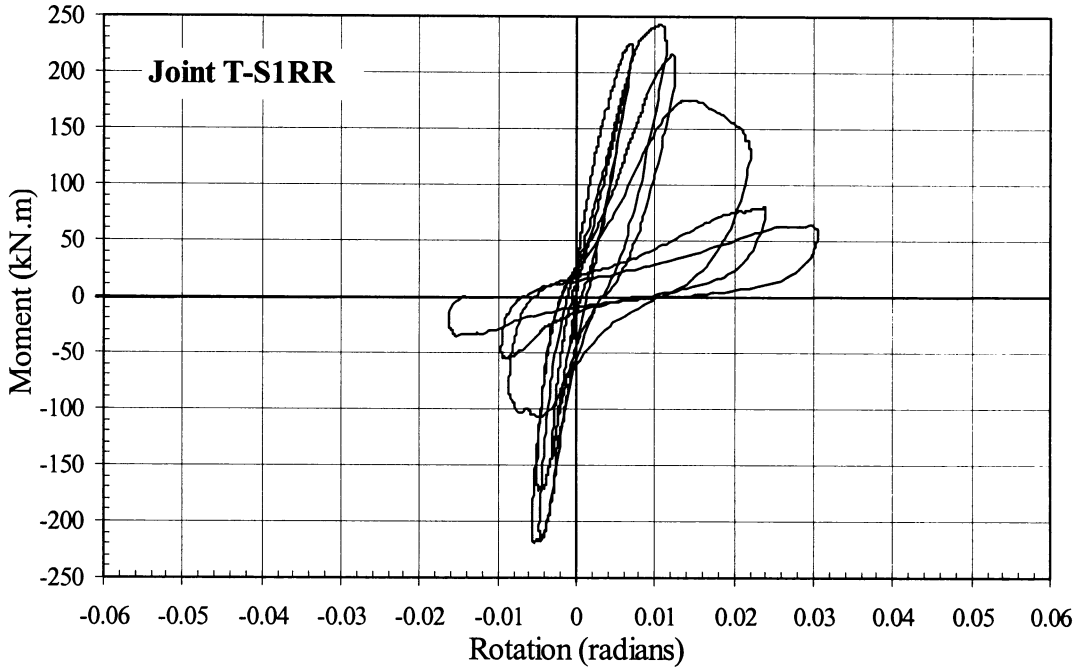

Figure 3-18b Beam moment-rotation at 175 mm from column face of joint T-S1RR

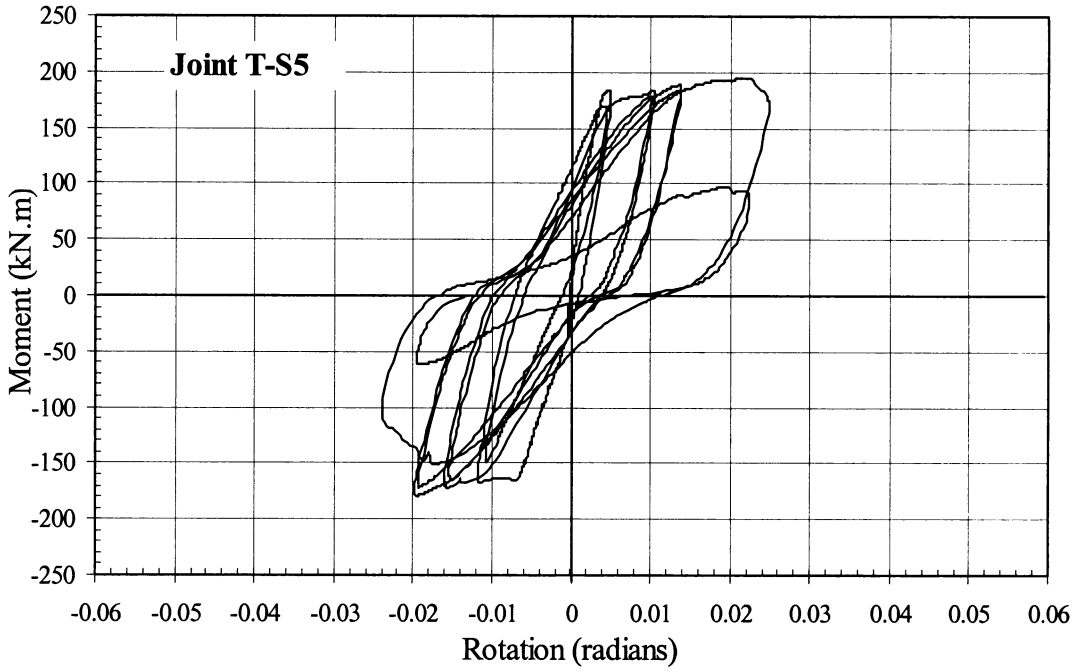

Figure 3-18c Beam moment-rotation at 175 mm from column face of joint T-S5

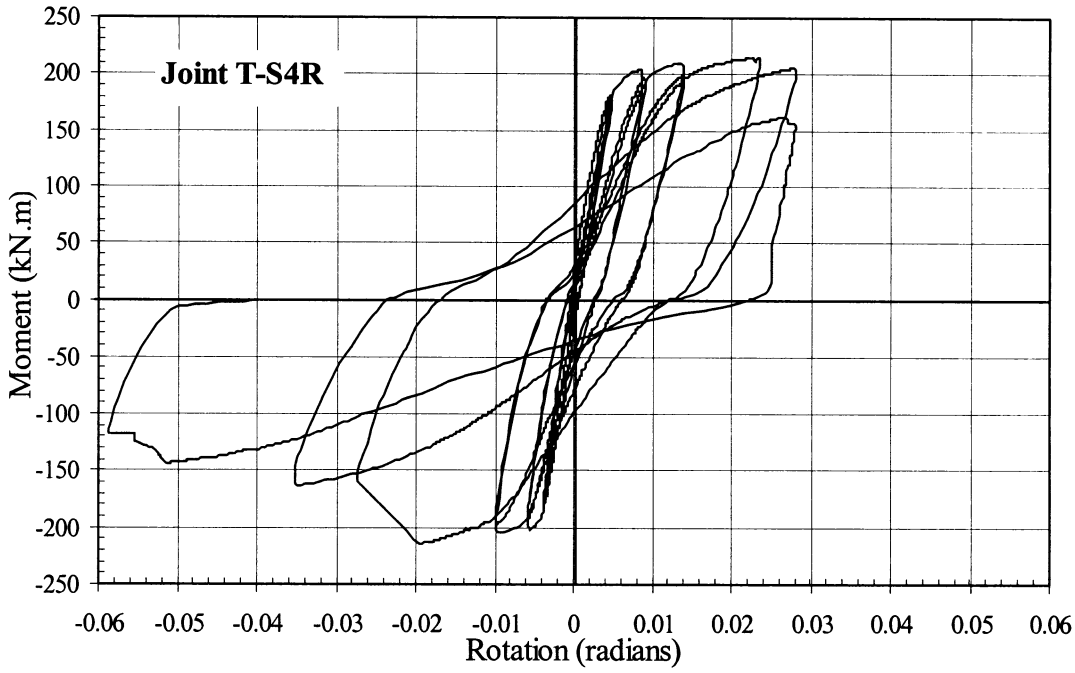

Figure 3-18d Beam moment-rotation at 175 mm from column face of joint T-S4R

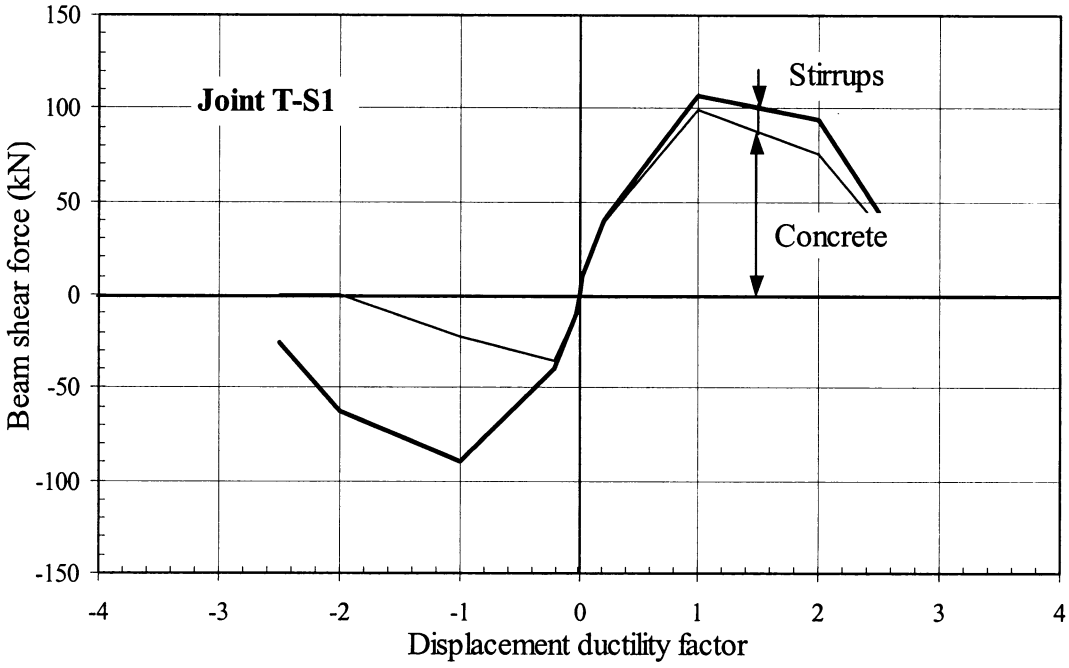

Figure 3-19a Beam shear force resisted by concrete and stirrups of joint T-S1

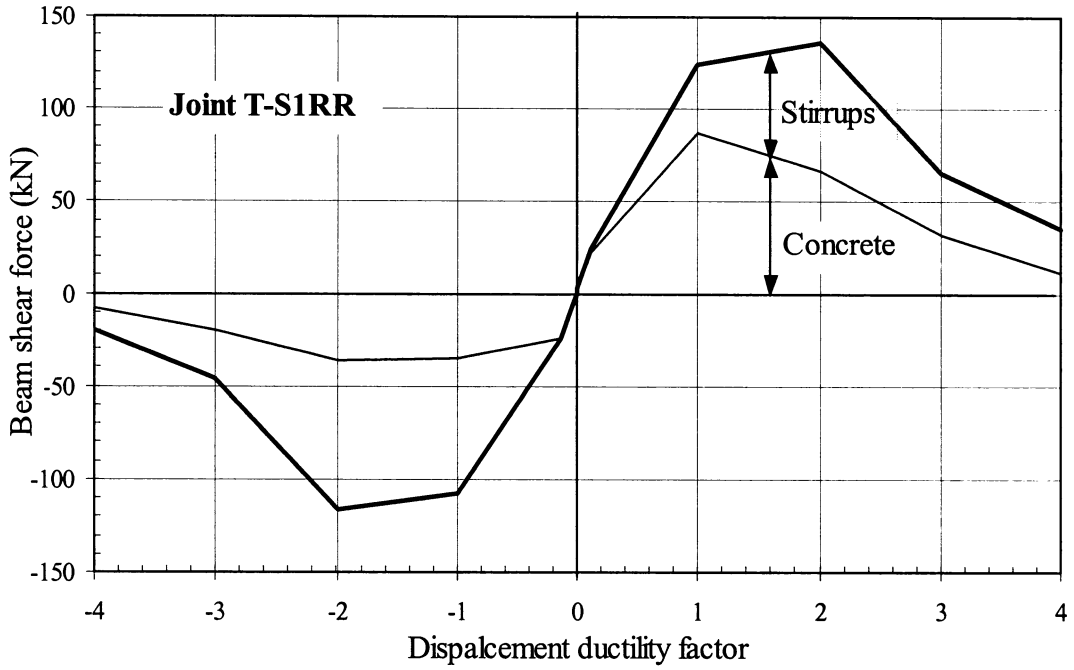

Figure 3-19b Beam shear force resisted by concrete and stirrups of joint T-S1RR

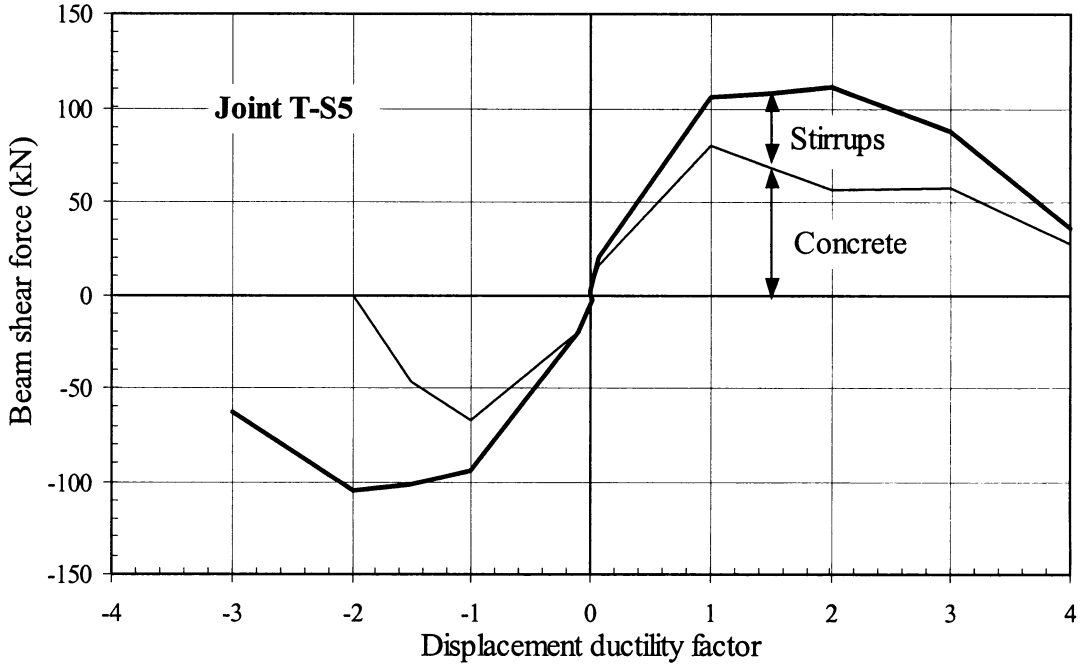

Figure 3-19c Beam shear force resisted by concrete and stirrups of joint T-S5

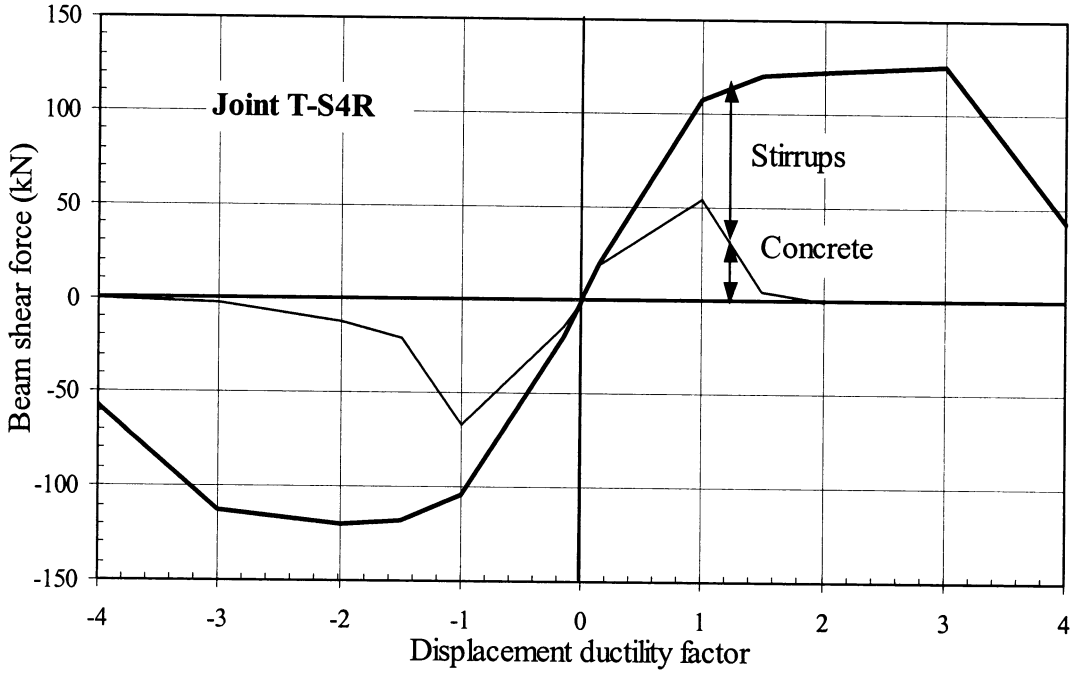

Figure 3-19d Beam shear force resisted by concrete and stirrups of joint T-S4R

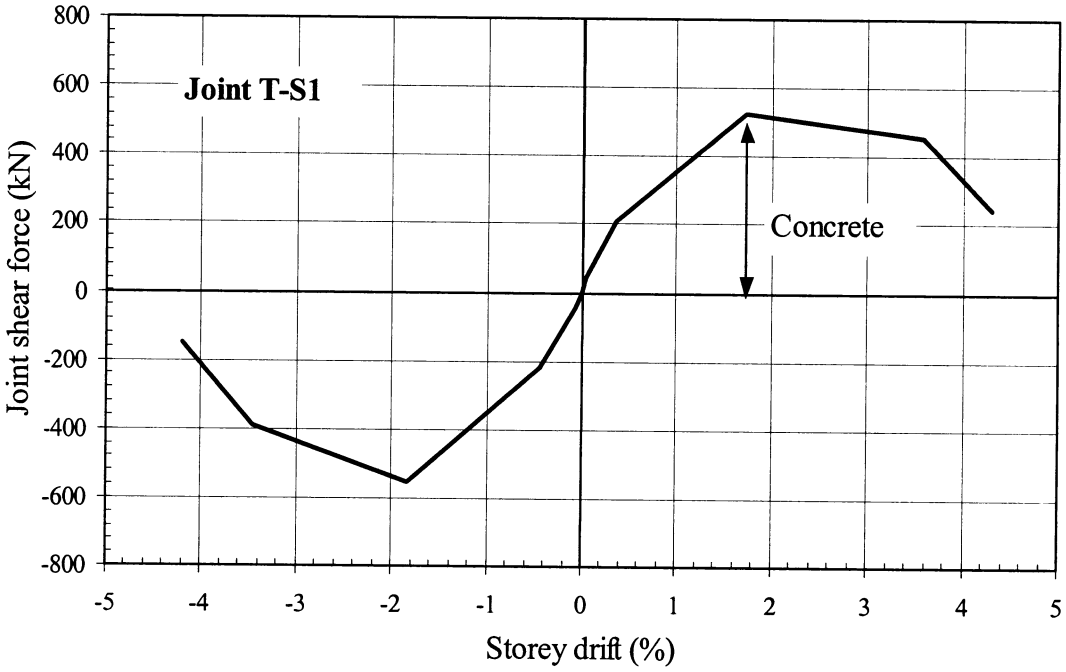

Figure 3-20a Joint shear force resisted by concrete of joint T-S1

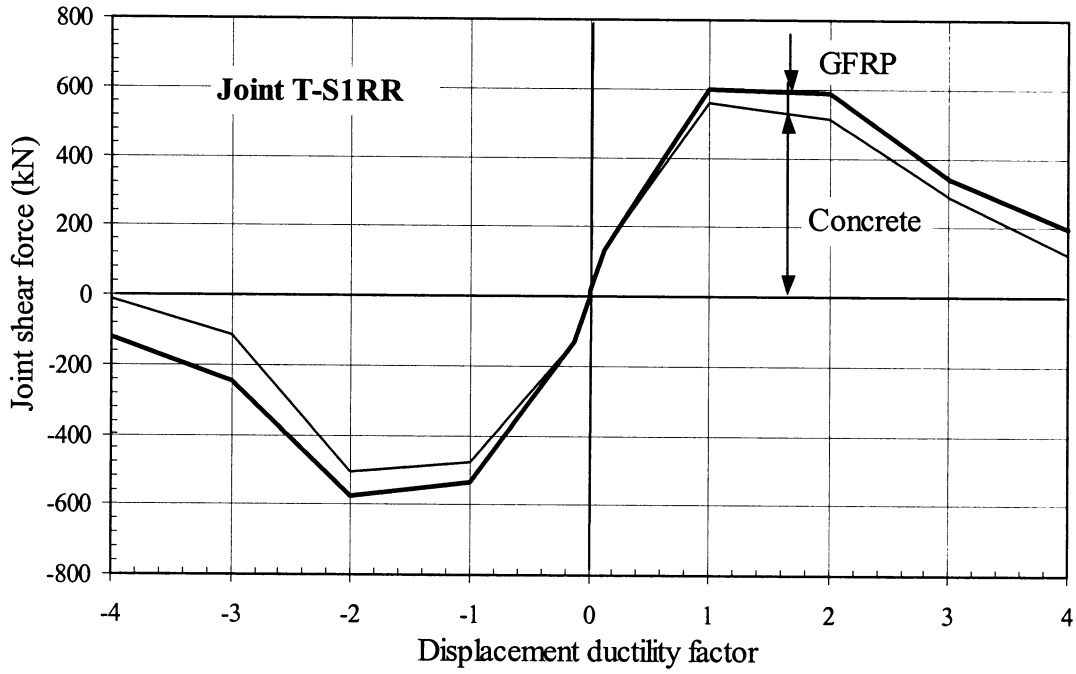

Figure 3-20b Joint shear force resisted by concrete and composite sheets of joint T-S1RR

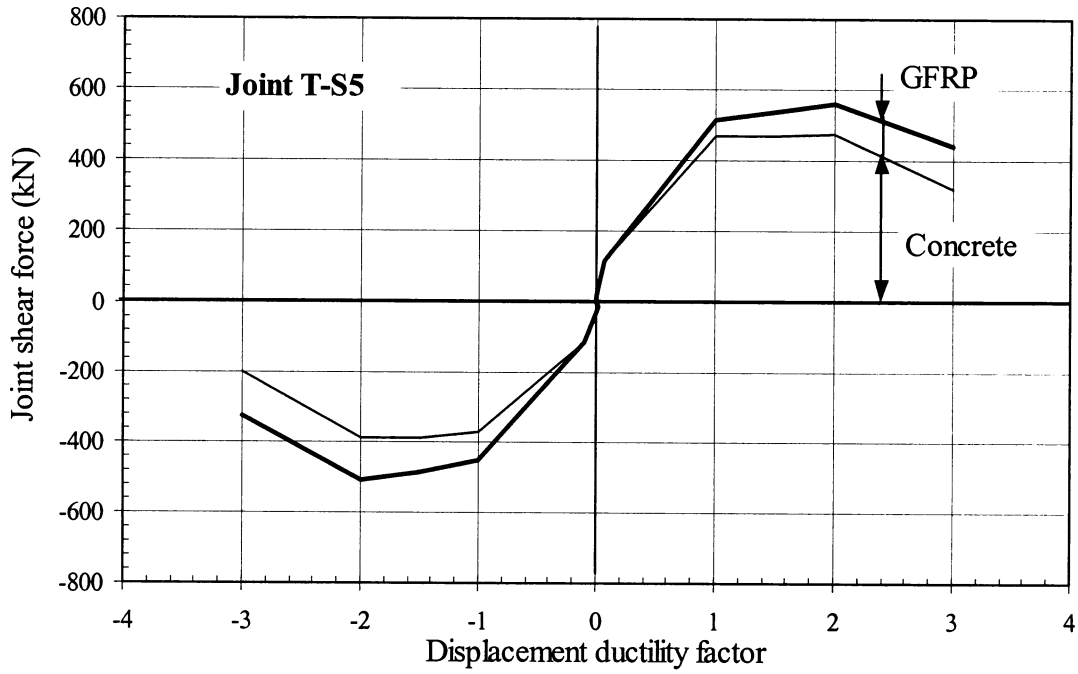

Figure 3-20c Joint shear force resisted by concrete and composite sheets of joint T-S5

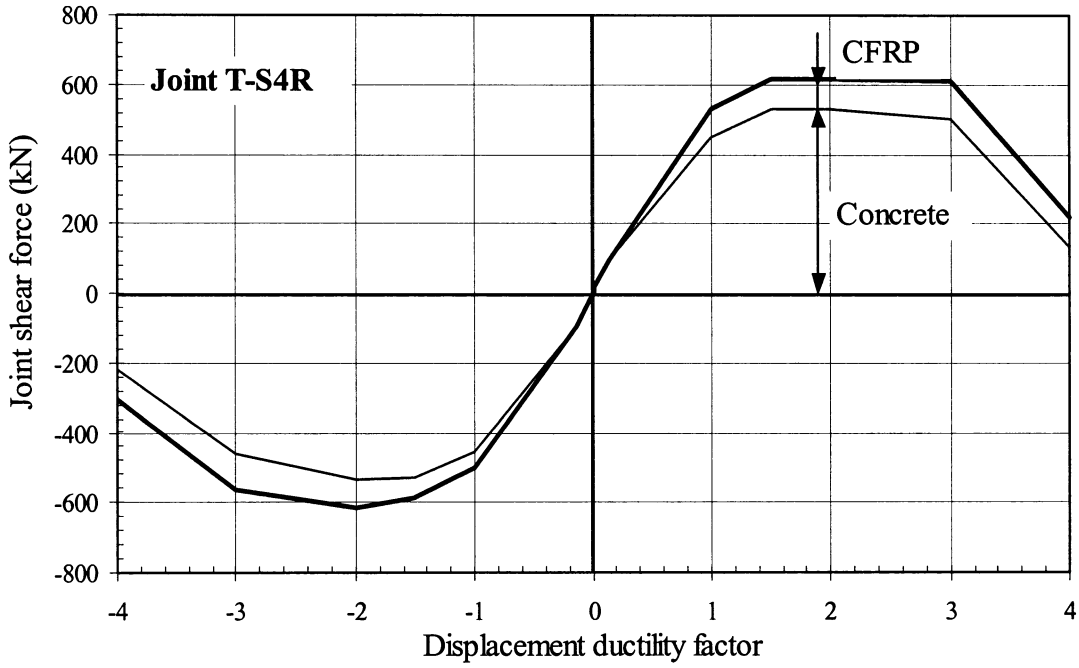

Figure 3-20d Joint shear force resisted by concrete and composite sheets of joint T-S4R

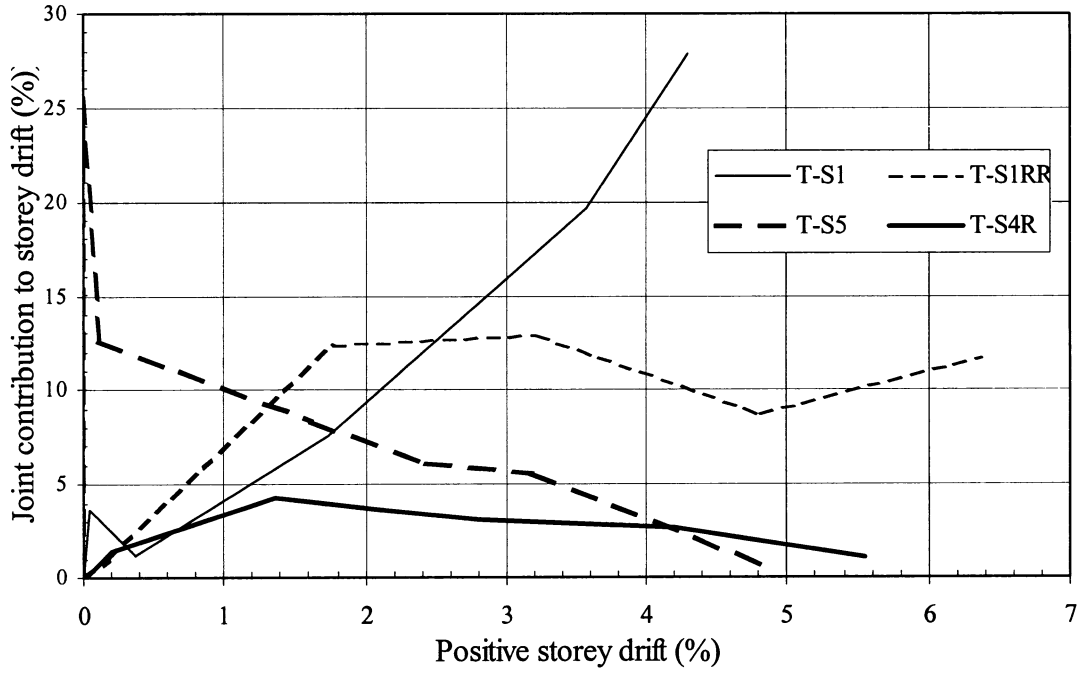

Figure 3-21a Contribution of joint shear deformation to positive storey drift

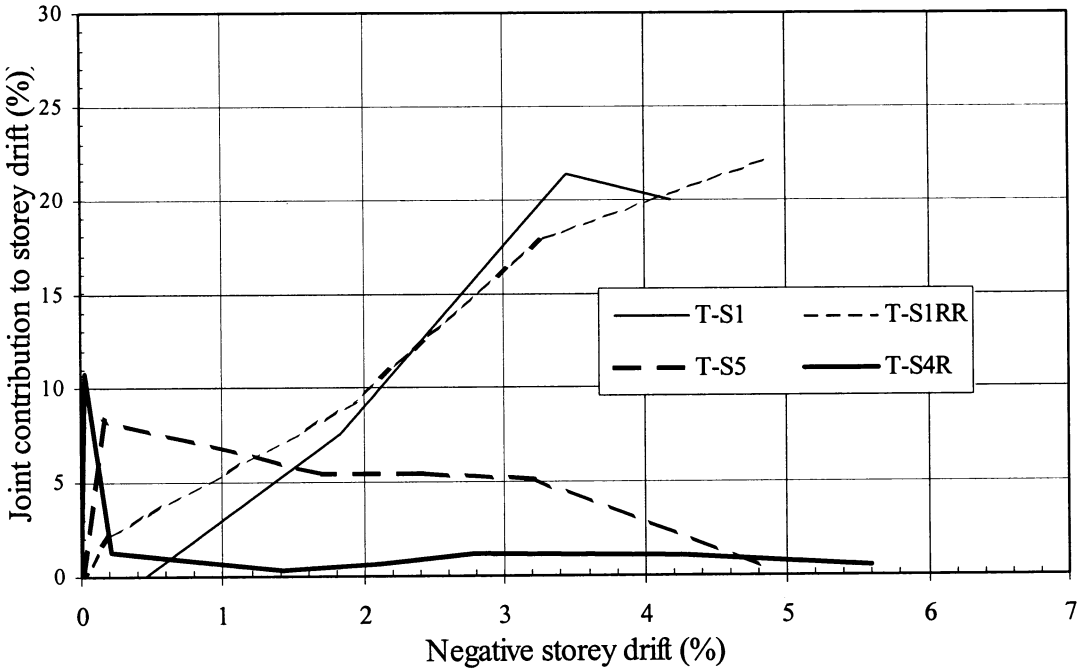

Figure 3-21b Contribution of joint shear deformation to negative storey drift

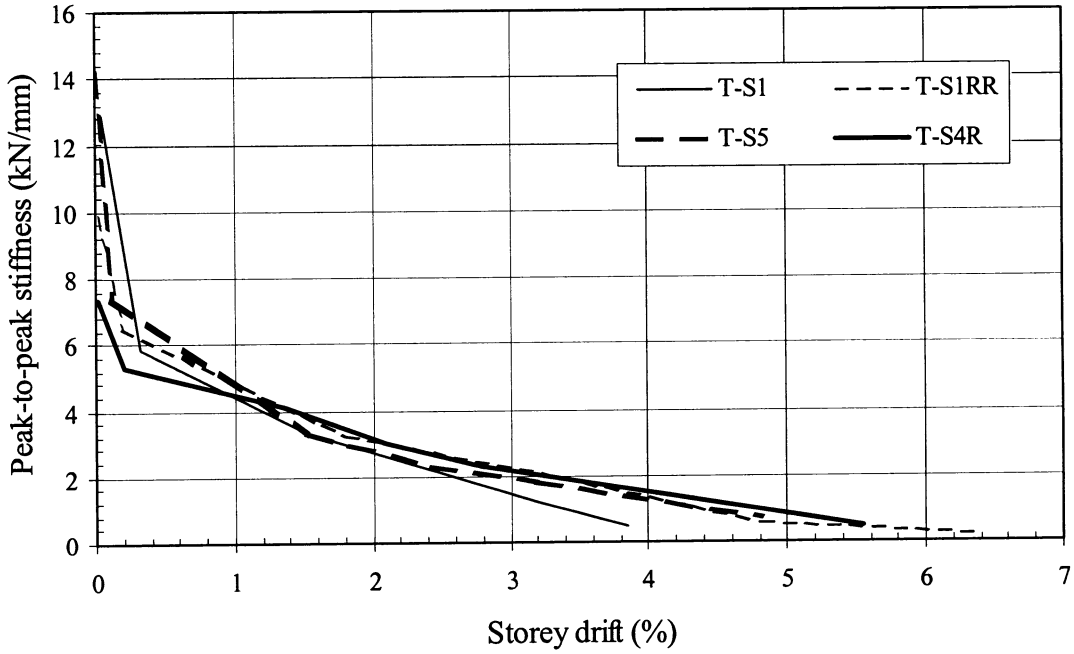

Figure 3-22 Stiffness degradation with storey drift

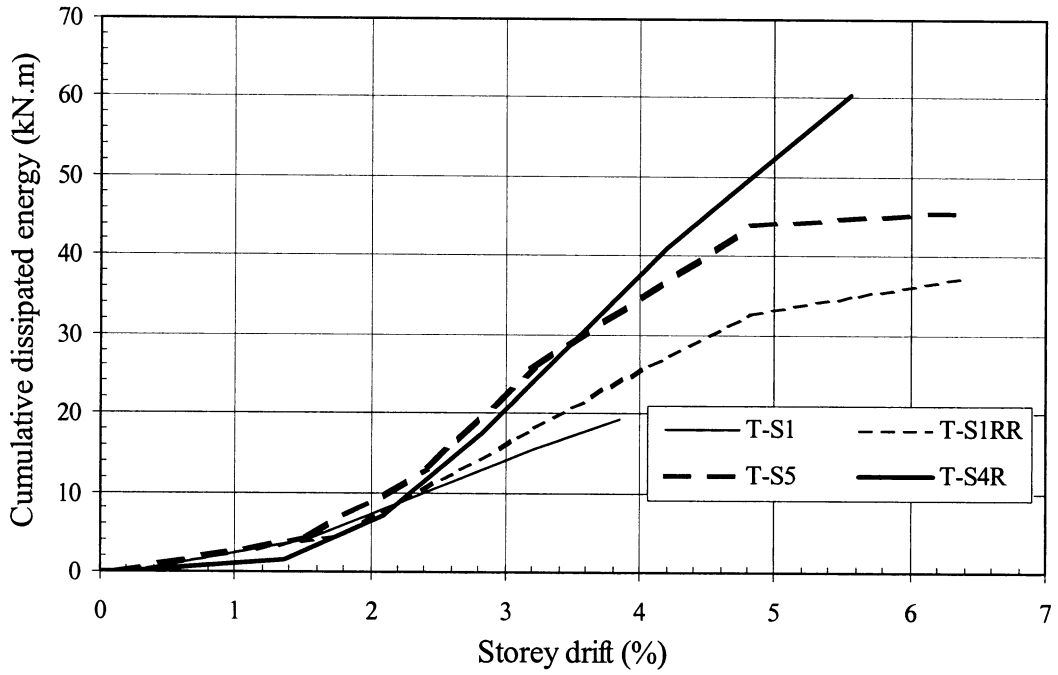

Figure 3-23 Cumulative energy dissipated by tested joints

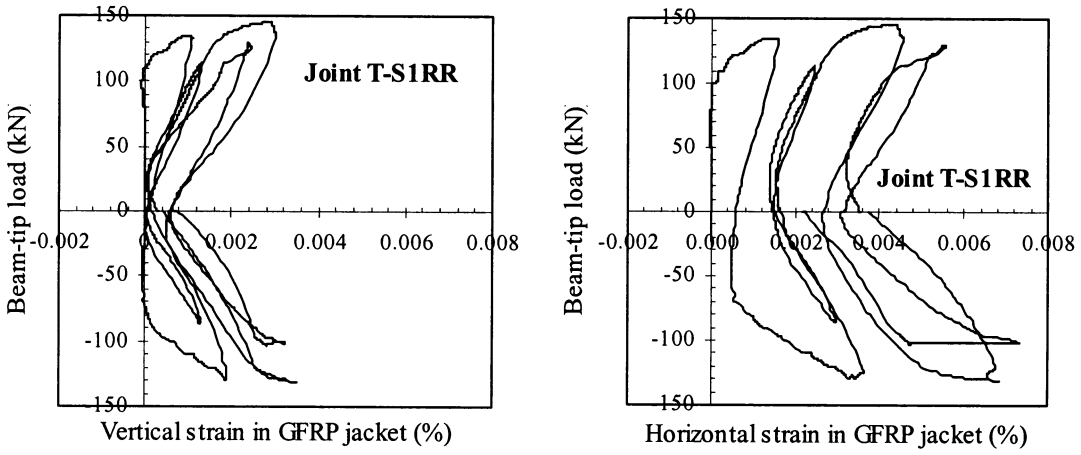

(a) Joint T-S1RR

Figure 3-24 Strain in FRP jacket

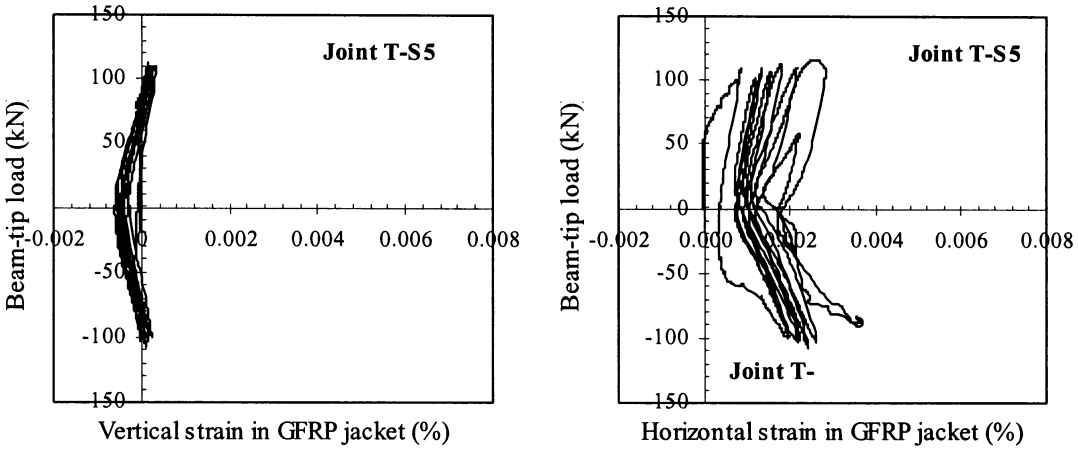

(b) Joint T-S5

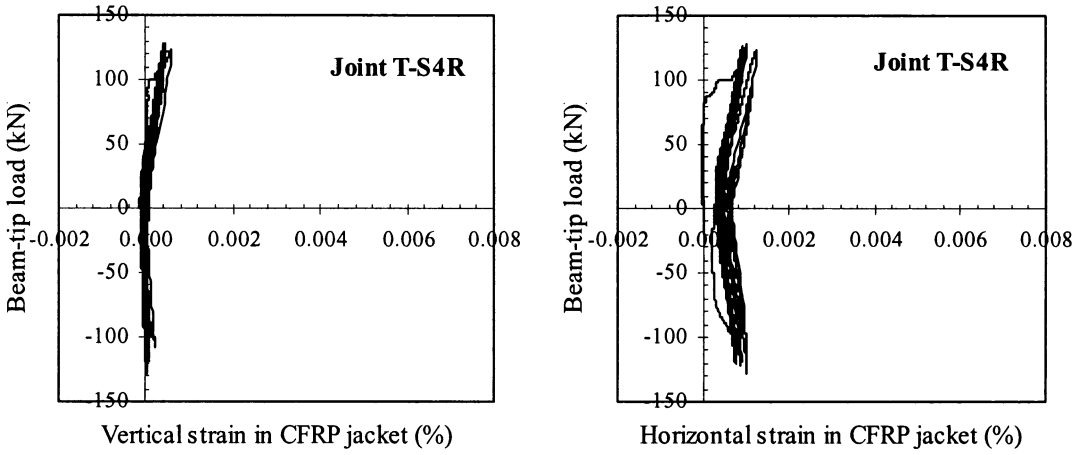

(c) Joint T-S4R

Figure 3-24 Strain in FRP jacket (cont.)

This page is intentionally left blank

Chapter 4

BEHAVIOUR OF BOND-DEFICIENT JOINTS

4.1 INTRODUCTION

In reinforced concrete structures, one of the main causes of brittle failure is the sudden loss of bond between reinforcement bars and concrete in anchorage zones. Brittle bond failure may cause severe local damage of the structural elements or even collapse of structures during strong earthquakes.

The behaviour of the Bond-deficient joints, T-B10, T-B11, and T-B12 is discussed in this chapter. The joint T-B10 represented the control joint with inadequate anchorage length of beam bottom bars, as the bars were anchored 150 mm into the beam-column joint. The other two joints were strengthened using steel elements and carbon fibre reinforced polymer (CFRP) sheets. After strengthening of the joint zone, the beam-column subassemblies were set up with the column vertical inside the loading frame and tested. The effectiveness of the strengthening schemes in improving the joint behaviour was assessed.

4.2 JOINT T-B10

This joint was designated as the control joint. The beam bottom bars were anchored 150 mm into the column which represents 26% of the bond length required by the CSA-A23.3 (1994) provisions to develop the yield strength of the bars. To avoid joint

shear failure, four #10 ties were installed inside the beam-column joint zone. Due to the inadequate bond length of the bars, bond-slip failure mode was expected to occur.

The first beam crack occurred at the column face at a load of 13.0 kN. In the fourth cycle, when a positive beam-tip load of +15.0 kN was applied, a major crack occurred at the beam-column interface. A corresponding abrupt reduction in the slope of beam-tip load-displacement relationship was observed. In the sixth cycle, a vertical crack and a horizontal crack were formed in the joint region along the bottom bars embedment length at a beam-tip load of +39.0 kN, as a result of slippage of the beam bottom bars. An increase in beam-tip displacement without corresponding increase in the load was recorded. During the eighth cycle, in spite of the inadequate development length of the beam bottom bars, the bars yielded at a load of 52.9 kN. This was due to the confinement conditions of the anchorage zone as will be discussed later. The beam top bars yielded at a load of 46.0 kN. The corresponding displacement of 18.25 mm was used as a yield displacement Δ_y for the displacement control phase.

During the tenth cycle, the specimen reached a displacement ductility factor (DDF) of 1.5 (±27.4 mm). When pushing up, the beam-tip load degraded to +38.1 kN, whereas the load increased to 51.5 kN when pulling down. At a DDF of 2.0 (±36.5 mm), the beam-tip load dropped to 20.7 kN when pushing up, whereas it increased to 54.0 kN when pulling down. As the beam was pushed up the splitting crack at the column face widened and extended through the beam depth due to the beam bottom bars slippage. The load carrying capacity degraded with severe pinching. As the beam was pulled down the load carrying capacity was maintained and slightly increased. The test was terminated at

a DDF of 5.0 (±91.25 mm) as the load carrying capacity was greatly reduced.

The final failure pattern is shown in Figure 4-1. Severe cracks at the beam-column interface, due to the beam bars slippage, were noted. The overall behaviour of the joint was brittle, with low ductility and severe strength deterioration.

4.3 JOINT T-B12

Joint T-B12 was rehabilitated using two MBrace CF 130 carbon fibre reinforced polymer (CFRP) sheets. The sheets were attached to 1000 mm of the beam bottom face and extended 500 mm along the column face. Using the described configuration, the resultant of the tensile forces developed in the composite sheets may cause debonding of the sheets from the concrete surface at the lower beam-column corner. To overcome this potential problem, a 150 x 150 x 12 mm steel angle was installed at that corner as shown in Figure 4-2. The angle was attached to the beam face using four HSL M16/25 Hilti expansion anchors and to the column using four HSL M20/30 Hilti anchors. Two 6 mm thick triangular steel plates were welded to the angle sides to stiffen the angle in an attempt to move the critical section away from the column face. The specimen was then set up inside the loading frame and tested.

The first beam crack occurred during the second cycle at load of 12.0 kN. During the seventh cycle, a major splitting crack formed at the column face at a load of 26.0 kN. Vertical and horizontal cracks appeared in the lower part of the joint at a beam-tip load of 36.0 kN as a result of the bars slippage. The top steel bars yielded at a load of 40.1 kN and a displacement of 18.0 mm which was designated as the yield displacement.

At a DDF of 2.0 (±36.0 mm), the joint reached its positive ultimate strength of 46.8 kN. Both the CFRP sheets and the bottom steel bars reached the same strain level of approximately 0.25%. When repeating this cycle, a sudden drop of the beam-tip load from 33.0 kN to 28.7 kN occurred with increase in the beam-tip displacement from 34.5 mm to 41.3 mm. At a DDF of 3.0 (±54.0 mm), the joint positive load resistance degraded to 20.6 kN with severe pinching of the hysteretic loop. The crack at the beam-column interface widened and spalling of concrete above the steel angle was noted, as shown in Figure 4-3. Debonding of the composite sheets underneath the steel angle occurred as the specimen was pushed up. The steel angle did not have the strength to force the crack to occur at the toe of the angle instead of at the beam-column interface. The weak component was the strength of the four expansion anchors. When pushing the beam up, a gap was created between the angle and the composite sheets, which allowed the sheets to debond from the concrete surface. The sheets reached a maximum strain of 0.27%. The composite sheets were able to carry some load to a DDF of 3.0 until they fractured at the beam-column corner under the steel angle, as shown in Figure 4-4.

The test was terminated at a DDF of 5 (±90.0 mm), as the positive joint strength was degraded to 5.4 kN. The negative strength was maintained and reached 55.0 kN at the last cycle. The composite sheets were completely debonded from the beam and column faces. Examining the hysteretic loops of the specimen showed severe deterioration of the specimen strength in the push-up loading direction with considerable pinching and stiffness degradation.

4.4 JOINT T-B11

Four MBrace CF 130 CFRP sheets were attached to the beam bottom face and extended along the column face with the same configurations as joint T-B12. To avoid the 90° change in the sheets direction, a circular concrete haunch, of 200 mm diameter, was poured at the bottom beam-column corner. A 6 mm thick steel plate composed of two straight parts and a quarter circle was used as a form to pour this haunch. The same plate was used later to prevent debonding of the CFRP sheets from the concrete surface. After applying the CFRP sheets, the steel plate was attached to the beam using two pairs of A375-16 mm diameter steel bolts, welded to the beam bottom bars, and to the circular hunch using two inclined pairs of A375-16 mm diameter bolts welded to beam and column bars. Four 25 mm diameter external threaded rods with 400 x 200 x 25 mm steel plate were used to clamp the curved plate to the back of the column, as shown in Figure 4-5. To prevent the debonding of the sheets from the beam bottom face, 3 mm thick U-shaped steel plate was installed at the tip of the composite sheet, as shown in Figure 4-5. The specimen was set up in the loading rig and tested.

The first beam crack occurred during the second cycle at a load of 20.0 kN. During the fourth cycle, the top steel yielded at a load of 67.0 kN and a displacement of 20.67 mm (Δ_y). The CFRP sheets reached tensile strain of three times the strain in the beam bottom bars, which indicates the effectiveness of the strengthening system in carrying the developed tensile forces. Shear cracks appeared at the joint region when pushing up the beam at a load of 55.0 kN. The bottom beam reinforcement yielded at a load of 80.0 kN and at a displacement of 22.0 mm.

At a DDF of 1.5 (±31.0 mm), the CFRP sheets reached their maximum strain of 0.37%. As the joint was pulled down, a wide crack appeared at the column, indicating the commencement of beam flexural hinging. During the eighth cycle, the specimen was loaded to a DDF of 2.0 (±41.3 mm). The cracks distributed over a length of 1.5 of the beam depth as the specimen was pulled down, whereas the crack at the column face widened and the specimen strength slightly degraded as it was pushed up. The composite sheets transferred its load to the column via bearing on the steel plate; as a result, the inclined bolts carried high tensile forces. At a DDF of 4.0 (±82.6 mm), the welds of the bolts in the curved part of the steel plate fractured at the end of the push-up part of the loading cycle, and sudden drop of the specimen strength to 28.0 kN occurred. After the weld fracture, as shown in Figure 4-6, the external tie rods transferred the tensile forces from the composite sheets to the column and the positive joint strength started recovering. The test was halted after reaching a DDF of 10.0 (±206.7 mm) as the loading actuator was out of stroke.

At the end of the test, the positive joint strength recovered to 43.0 kN with severe pinching and large amount of energy dissipating in deforming the steel plate, as shown in Figure 4-7. During the test, the CFRP sheets showed the ability to carry tensile and compressive forces without peeling off or debonding from the concrete which indicated the effectiveness of the U-shaped steel plate and the curved steel plate to anchor the composite sheets. The joint maintained its strength when pulling down on the beam to the end of the test.

4.5 ANALYSIS OF EXPERIMENTAL RESULTS

In this section, the behaviour of the joints and the effectiveness of the strengthening schemes are evaluated. The hysteretic behaviour of the joints, joint displacement ductility factor, beam rotation, behaviour of beam-column joint, cracking and yielding moments, contribution of concrete shear strength and steel elements in carrying the joint and beam shear forces, energy dissipation ability and joint stiffness are discussed. In the following analysis, a positive sign is given for the push up beam-tip load and the corresponding beam-tip displacement, displacement ductility factor, drift angle, storey shear, beam moment, beam rotation and beam-column joint deformation.

4.5.1 Bond behaviour in joints

The bond behaviour between the concrete and the reinforcing bars under cyclic loads is an important parameter in the analysis of joint performance. Under severe earthquake loading, the bond stresses along the bars embedded in the beam-column joint may be high and exceed the maximum concrete bond strength. In such cases, premature bond deterioration and slip of bars within the joint would be initiated. This results in loss of stiffness of the frame due to the fixed-end rotation of members adjacent to the joint (Popov, 1984). Moreover, the bond response of longitudinal bars plays an important role in the shear behaviour of the beam-column joints.

Three factors contribute to the bond between the reinforcing bars and concrete. These are:

(1) Chemical adhesion.

(2) Friction.

(3) Mechanical interlock between concrete and the ribs in steel bars.

Bond of deformed bars depends primarily on mechanical interlock (Lutz and Gergely, 1967). The chemical adhesion between the bars and the concrete is lost when small bar slip occurs, whereas the friction between the bars and the surrounding concrete depends primarily on the bar surface conditions.

Flexural cracks along the beam-column face affect the distribution of bond stresses along the bars. Under such conditions, some separation of the bar and the concrete occurs in the vicinity of the cracks. Internal inclined cracks, which are referred to as *"bond cracks"*, initiate after formation of the flexural cracks due to the tensile stresses in the concrete around the bars caused by high bearing pressure on the concrete ahead of the bar ribs. After initiation of bond cracks, the steel forces transfer by mechanical interlock between the concrete and steel bars. This mechanism induces compressive forces spreading from the bar ribs to the concrete accompanied by circumferential tensile stresses which cause splitting cracks. These splitting cracks may be generated under low bond stress of $0.36\sqrt{f_c^{'}}$ (Eligehausen et al., 1983), which may occur under elastic cyclic loads. Widening of these cracks can be controlled by providing confining pressure to the anchorage zone. This pressure can be applied by the compressive flexural forces from the adjacent elements or from the transverse reinforcement provided inside the joint. For longitudinal beam bars passing through the joint, the least bond resistance is where the column bars are in tension because of the flexural cracks at the column face.

4.5.2 Beam-tip load-displacement relationships

The beam-tip load-displacement relationships of the tested joints are shown in Figure 4-8a to c. The displacement corresponding to yielding of the beam bars was used to determine the displacement ductility level of the joint. The corresponding yield load was recorded and compared to the theoretical load obtained from the beam theory. The theoretical yield and ultimate loads are presented in Table 4-1.

The hysteretic behaviour of joint T-B10 is not symmetric with respect to the loading direction, as shown in Figure 4-8a, as a result of the pull out of the beam bottom bars. Bond-slip of the beam bottom bars was initiated at a load of 40.0 kN during the sixth cycle. Surprisingly, beam bottom bars reached the yield stress during the eighth cycle. The splitting bond cracks did not widen due to the confinement provided by the joint ties. Therefore, the steel bars could reach a high stress level in spite of their short embedded length. Dramatic deterioration of joint strength occurred at beam-tip displacement of 27.4 mm (DDF of 1.5). Pinching was recorded in the following cycles to the end of the test.

Joint T-B12 exhibited almost elastic behaviour up to yielding of the top steel bars. Strength deterioration occurred when reaching a beam-tip displacement of 36.0 mm (DDF of 2.0). The expansion anchors, used to install the steel angle in place, loosened and detached from the holes as the beam tip was pushed up. This caused debonding of the composite sheets underneath the steel angle. A reduction in the negative joint strength, as compared to the control joint, was recorded due to the reduction of the section effective width and the mechanical drilling of the holes required for the anchors. Pinching of the

hysteretic loops was noted in the next cycles with severe strength deterioration.

For joint T-B11, the concrete haunch stiffened the beam and moved the critical section away from the column face. This increased the development length of the beam bars and hence reduced the bond-slip of the bars. The composite sheets attached to the beam also contributed to the strength of beam section. The joint ultimate positive and negative strength increased to +86.0 kN and –78.0 kN. Pinching of the hysteretic loops was observed after the welded bolts fractured, as large deformation was required to force the steel tie rods to start carrying tensile forces.

Figure 4-9 shows the envelopes of the hysteretic loops of the three tested joints. Joint T-B10 suffered a sudden drop in strength at a beam-tip displacement of 27.4 mm (storey drift of 1.5%). Joint T-B12 showed a similar drop but at a higher beam-tip displacement (36.00 mm, or storey drift of 2%). Joint T-B11 reached the highest strength. Strength deterioration occurred at a beam-tip displacement of 82.6 mm (storey drift of 4.4%) followed with a gradual strength recovery to the end of the test.

4.5.3 Storey shear-storey drift angle relationships

The lateral earthquake forces are transferred from one floor to another by horizontal shear forces through the columns. The storey shear was estimated as described before in Section 2.10.5, taking into consideration the P-Δ effect. To reduce the P-Δ effects on structural elements, the National Building Code of Canada (1990) limited the interstorey drift to 1% for post-disaster buildings and to 2% for other buildings. So, the structural strength must be maintained until reaching these drift angles. Storey shear-drift angle relationships are shown in Figure 4-10a to c. Strength deterioration of joint T-B10

occurred at a storey drift angle less than 0.015 radians whereas joint T-B12 was able to sustain the lateral loads to drift angle of 0.02 radians. However, the negative beam-tip load of joint T-B11 was maintained, the joint exhibited a severe deterioration of storey shear beyond a storey drift angle of 0.05 radians.

To demonstrate the *P-Δ* effect on the storey shear, consider a concrete column of length *L*, fixed at both ends and laterally displaced at one end by a displacement Δ. The shear force at the support is estimated as:

$$V = \frac{2M}{L} - \frac{P\Delta}{L} \tag{4-1}$$

Where *M* and *P* are the moment and the axial load at the column end, respectively.

Pre-ultimate response would be governed by the first term of Equation (4-1). Thus, a positive slope of the storey shear-drift angle relationship is recorded. However, the second term of Equation (4-1) would govern the post-ultimate response. Thus, a negative slope or degradation of storey shear would be recorded. Thus, increasing the storey drift would significantly reduce the storey shear capacity.

4.5.4 Moment-rotation relationships

In moment resisting frames, deterioration of the bond conditions of the beam bars leads to significant fixed-end rotation at beam-column interface. This is because the high beam bending moments, acting at the column face, cause yielding of the main bars anchored in the joint and high shear forces that induce cracks into the joint panel and damage the bond of the embedded bars. Moreover, in case of short straight development length, where the bars are not hooked inside the joint, deterioration of the bond along the

bars is severe. The bars are eventually pulled out from the joint, causing fixed-end rotation that may contribute significantly to the overall deflection of the beam-column joint.

The rotation of the beam section at 175 mm from the column face was recorded for each joint. This rotation was plotted versus the beam moment at the column face in Figure 4-11a to c. The recorded rotation involved the rotation due to yielding of the reinforcement bars and the rotation due to slippage of the bars.

Before yielding, joint T-B10 exhibited elastic rotation of 0.002 radians in both loading directions. Yielding of the beam reinforcement caused permanent rotation. After yielding, large angle of rotation was measured in the positive direction due to the slippage of the beam bottom bars that caused fixed end rotation. For joint T-B12, a jump in the beam-section rotation occurred at a DDF of 2.0, due to the slippage of the steel bars and failure of the mechanical expansion anchors. The rotation could not be recorded beyond this displacement due to the loss of the bottom LVDT when its attachment detached from the concrete surface. Yielding of the beam top bars of joint T-B11 before the bottom bars caused an increasing permanent negative rotation. Therefore, the joint showed a negative rotation much larger than the positive rotation. As compared to control joint T-B10, joint T-B11 showed much smaller rotation at different moment values.

The bending stiffness of the beam at the maximum moment is presented as a ratio of E_cI_g and is given in Table 4-1, where E_c is the concrete modulus of elasticity and I_g is the gross sectional moment of inertia. The beam bending stiffness is estimated as explained before in Section 3.6.5. The control joint T-B10 showed the lowest flexural

stiffness. Joint T-B12 showed the highest stiffness due to the installed steel angle. Joint T-B11 showed an intermediate value due to the flexibility of the steel plate used to hold the composite sheets in place. The bending stiffness was as low as 1.3% of the initial stiffness, indicating the severe effect of cyclic loading on the beam stiffness and consequently on the beam deformation.

The measured rotation of the beam section at the column interface is composed of a rotation due to the elongation of the bars and a rotation due to the bar slip as a rigid body. The beam deflection due to the beam rotation can be estimated using Equation (2-2). For joint T-B10, the beam rotation contributed 38.7, 81.3 and 87.3% of the total beam deflection at a DDF of 1.0, 2.0 and 5.0, respectively. These values reflect the significant contribution of the bar slip to the overall beam deflection. For joint T-B11, the rehabilitation scheme was capable of reducing the contribution of beam rotation to 15.7 and 18.2% of the total beam deflection at a DDF of 1.0 and 2.0, respectively.

4.5.5 Cracking, yield and ultimate moments

The cracking moment was obtained by multiplying the cracking beam-tip load by the distance from the centre of the applied load to the column face. The concrete tensile stress was compared with the modulus of rupture given by CSA A23.3 (1994) Clause 8.6.4, which equals $0.6\sqrt{f_c^{'}}$. The results are shown in Table 4-1. The measured concrete tensile strength ranged from 0.56 to $0.64\sqrt{f_c^{'}}$ with an average value of $0.59\sqrt{f_c^{'}}$.

The yield and ultimate moments (M_y, M_u) were obtained by multiplying the corresponding beam-tip loads by the moment arm to the critical section at the column

face. The theoretical moment values were obtained assuming linear strain distribution in the concrete, a parabolic concrete stress distribution and based on the actual concrete and steel strengths. The moment values were verified using the computer program "RESPONSE2000" developed by Bentz (2000). The experimental to theoretical yield moments for the joints T-B10 and T-B12 were 0.96 to 1.20, respectively, and the experimental to theoretical ultimate moments were 0.80 to 0.93, respectively. For joint T-B11, the ratios between the experimental and theoretical yield and ultimate moments were 1.89 and 1.48, respectively. This was because the contribution of the composite sheets was ignored when calculating the theoretical moments.

4.5.6 Response of beam-column joints

Although the shear strength of beam-column joint was not of great concern in this group of test specimens, the joint shear behaviour was monitored to evaluate the current code provisions for designing the beam-column joints. The joint shear deformation of all the tested joints was minimal. A maximum deformation of 25×10^{-6} and 35×10^{-5} radians was measured for joints T-B10 and T-B12, respectively. Joint T-B11 reached a joint deformation of 22×10^{-4} radians at the end of the test, as shown in Figure 4-12. The shear deformation of the joint T-B10 was much larger than that of joints T-B10 and T-B12 due to the high beam-tip load and the consequent joint shear force. In general, the behaviour of the three tested joints was satisfactory, with minimal shear deformation and no strength deterioration.

According to the CSA A23.3 (1994) Clause 21.4.4, the area of the ties inside the joint should equal to the larger of:

$$A_{sh} = 0.3sh_c \frac{f_c^{'}}{f_{yh}}(\frac{A_g}{A_{ch}} - 1) \tag{4-2}$$

$$A_{sh} = 0.09sh_c \frac{f_c^{'}}{f_{yh}} \tag{4-3}$$

where: A_{sh} is the cross sectional area of the tie legs

s is the ties spacing

h_c is the column core dimension normal to the shear force

A_g is the joint gross cross sectional area

A_{ch} is the joint core cross sectional area

$f_c^{'}$ *and* f_{yh} are the concrete compressive strength and ties yield strength

Equation (4-2) gives A_{sh} as 320.63 mm^2, whereas Equation (4-3) gives A_{sh} as 114.8 mm^2. Only four ties of 10 mm diameter were installed in the joint zone to avoid congestion. Although the area of the existing ties is 200 mm^2, the joint behaved elastically with no excessive cracking. This may indicate the need of estimating the area of the ties in the joint zone based on the actual shear force developed into the joint zone.

The joint shear force is carried by diagonal concrete struts and steel ties. Figure 4-13 shows the contribution of steel ties and concrete shear resistance in carrying the developed joint shear force of joint T-B10. The joint shear force is mainly carried by the concrete shear strength whereas the steel ties confine the joint core and preserve its integrity, which comply with the current code philosophy.

4.5.7 Shear in beam

The shear in beam was resisted by the concrete shear strength and the beam steel

stirrups. The contribution of each mechanism was calculated following similar approach to that of joints T-S. The steel and concrete contributions to the shear resistance were plotted versus the storey drift as shown in Figure 4-14a to c.

In general, the concrete resistance to beam shear force during the first half of the each loop was larger than that during the second half of the loop. This was because of pre-cracking of the concrete compression diagonal struts during the first part of the loop. The concrete resistance was estimated at different ductility levels for each joint and presented in Table 4-2. Joint T-B10 had maximum concrete shear strength of $0.1\sqrt{f_c^{'}}$, which was similar to joint T-B11. For all joints, the concrete shear resistance deteriorated with increasing the DDF.

4.5.8 Stiffness

Various experimental studies and site investigations of reinforced concrete structures subjected to ground excitation demonstrated that the major concern in the structural seismic response is the degradation of stiffness. The principal effects of stiffness degradation are:

(1) Increase in the flexibility of the structure and the period of vibration.

(2) Decrease in energy dissipation capacity.

(3) Redistribution of internal forces leading to excessive deformation in some regions.

These three effects will change the overall structural response under ground excitations. The stiffness degradation is caused by concrete cracking, opening and closing of residual cracks, concrete spalling, bond degradation, shear sliding in regions with

cracks running through the entire beam depth and the Bauschinger effect in the reinforcing bars. Except for the Bauschinger effect of the reinforcing bars and concrete spalling, all other factors are related to cyclic bond deterioration between the steel bars and the surrounding concrete.

Joints T-B12 and T-B11 showed initial stiffness as much as double the initial stiffness of the control joint T-B10. After cracking, a reduction of 30, 70 and 65% of the initial stiffness was recorded for joints T-B10, T-B12 and T-B11, respectively. Whereas joint T-B12 showed almost the same stiffness of joint T-B10 at different storey drift, joint T-B11 showed almost twice the stiffness of the control joint, as shown in Figure 4-15.

4.5.9 Energy dissipation

Figure 4-16 shows the cumulative energy dissipated by the three beam-column joints. Although the rehabilitated joint T-B12 could dissipate almost the same amount of energy dissipated by the control joint T-B10, joint T-B11 was capable of dissipating twice the energy dissipated by the control joint at the same storey drift. The total energy dissipated by joint T-B11 at the end of the test was as much as five times the energy dissipated by the control joint.

4.5.10 Strains in beam reinforcement bars and CFRP sheets

Stress-strain relationship for reinforcing steel bars under cyclic loading is affected by plastic strains of the previous cycles. The pronounced feature of the cyclic stress-strain behaviour is the absence of yield plateau after the first yielding of the bar. To demonstrate the behaviour of steel bars under cyclic loads with adequate and inadequate anchorage conditions, Figure 4-17 shows the strain of the top and beam bottom bars of

joint T-B10. The beam top bars showed repeated yielding occurrence due to the good anchorage condition of the bars. However, the bottom bars showed the onset of first yielding with limited post-yield plastic strains due to the anchorage failure of the bars.

The distribution of the strain in the CFRP sheets in the positive and negative loading directions of joint T-B11 is shown in Figure 4-18. The strains are measured at 400, 650 and 900 mm from the column face along the beam bottom side and at 400 mm below the joint along the column side. At the specimen ultimate strength (DDF of 1.5), The sheets reached a maximum strain of 0.0037. Due to the load recovery at the end of the loading historey, the strain at a DDF of 10.0 was larger than that at a DDF of 7.0. The sheets reached a compression strain more than 0.003 in the negative loading direction which indicated the effectiveness of the U-shaped steel plate to prevent the buckling of the sheets. The maximum strain was measured at a DDF of 4.0 which corresponds to the ultimate pull-down beam-tip load.

4.6 SUMMARY

In this chapter, the behaviour of three beam-column subassemblies was discussed and analyzed. The specimens had inadequate anchorage length of the beam bottom bars. The control joint T-B10 showed a bond-slip failure mode with severe strength deterioration, stiffness degradation, and low energy dissipation ability. Joint T-B12 was strengthened using two CFRP sheets anchored using mechanical expansion steel anchors with steel angle. Limited improvement in specimen ductility was achieved without a significant improvement in joint strength or stiffness. Bond-slip failure mode was

recorded after the fracture of the CFRP sheets. Joint T-B11 was strengthened with four CFRP sheets anchored using steel bolts, welded to the existing steel reinforcement, and steel plate. Significant improvement in the joint strength, ductility, stiffness, and energy dissipation were achieved. A ductile failure mode of beam flexural hinging was recorded.

Table 4-1 Behaviour of Bond-deficient joints

Parameter	Joint T-B10	Joint T-B12	Joint T-B11
Yield displacement (mm)	18.25	18.00	20.67
Experimental yield load (kN)	+52.0, -46.0	-40.1	+80.0, -67.0
Experimental ultimate load (kN)	+52.0, -54.4	+46.8, -55.0	+86.6, -79.2
Theoretical yield load (kN)	43.17	41.90	42.20
Theoretical ultimate load (kN)	58.80	58.70	58.68
Maximum displacement ductility	3.0	3.0	10.0
Concrete tensile stress (MPa)	$0.56\sqrt{f_c^{'}}$	$0.58\sqrt{f_c^{'}}$	$0.64\sqrt{f_c^{'}}$
Bending stiffness at maximum moment	$0.0135E_cI_g$	$0.0530E_cI_g$	$0.0213E_cI_g$

Table 4-2 Concrete shear resistance as a fraction of $\sqrt{f_c^{'}}$ for beams

DDF*	Joint T-B10	Joint T-B12	Joint T-B11
-5	0.001	0.002	0.010
-4	0.007	0.018	0.064
-3	0.024	0.049	0.106
-2	0.102	0.059	0.101
-1	0.091	0.056	0.107
1	0.094	0.064	0.104
2	0.034	0.064	0.078
3	0.026	0.014	0.040
4	0.025	0.012	0.048
5	0.024	0.011	0.000

* The negative sign represent the part of the cycle where the beam tip is pulled down.

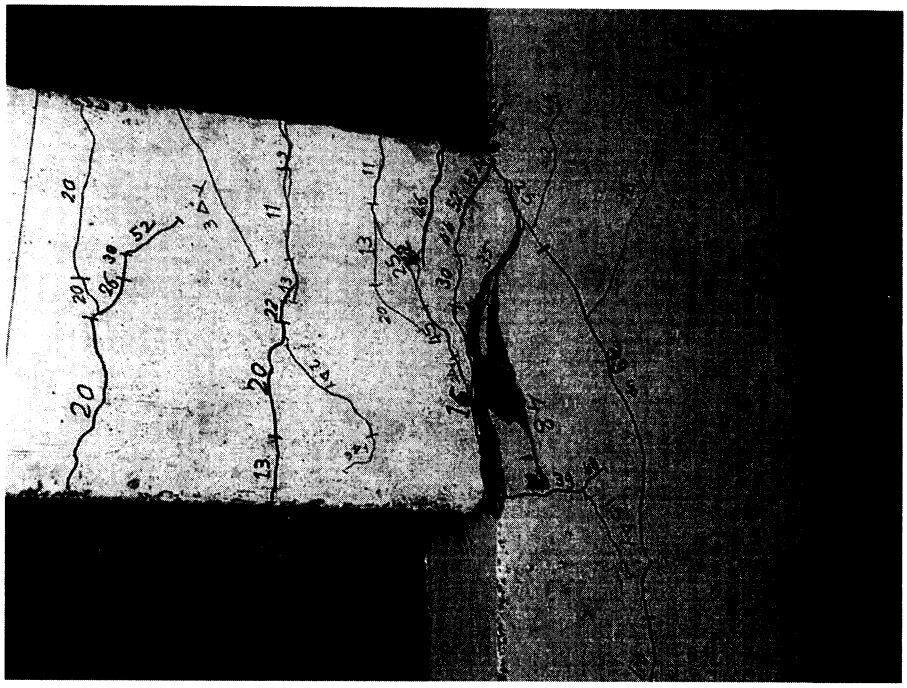

Figure 4-1 Bond-slip cracks of joint T-B10

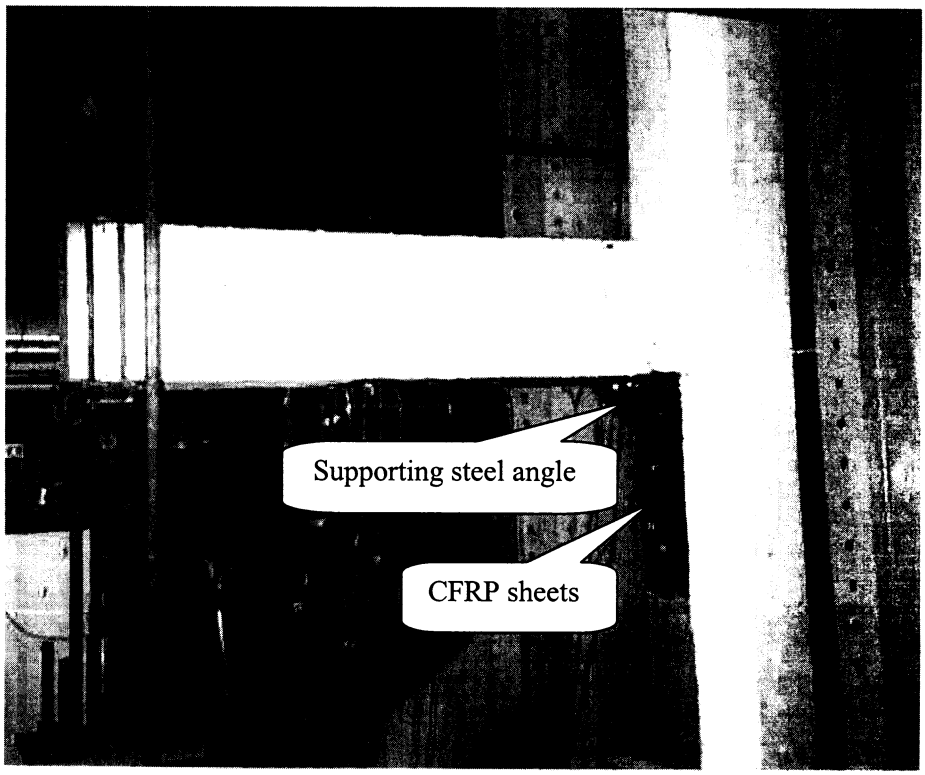

Figure 4-2 Strengthening of joint T-B12

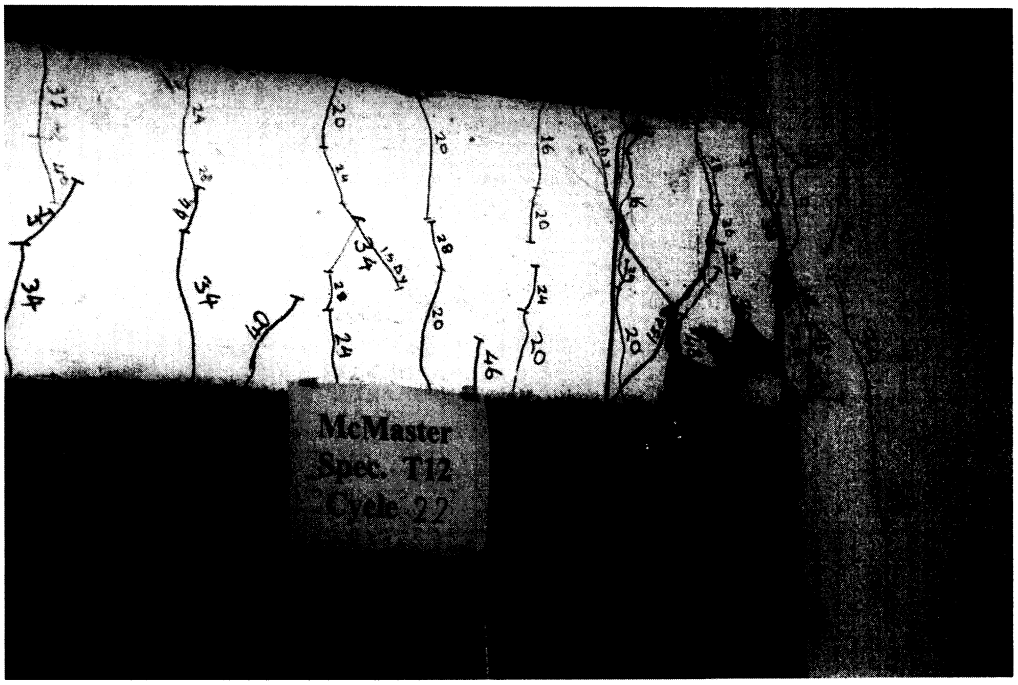

Figure 4-3 Cracking of joint T-B12 at a DDF of 3.0

Figure 4-4 Fracture of the CFRP sheets of joint T-B12

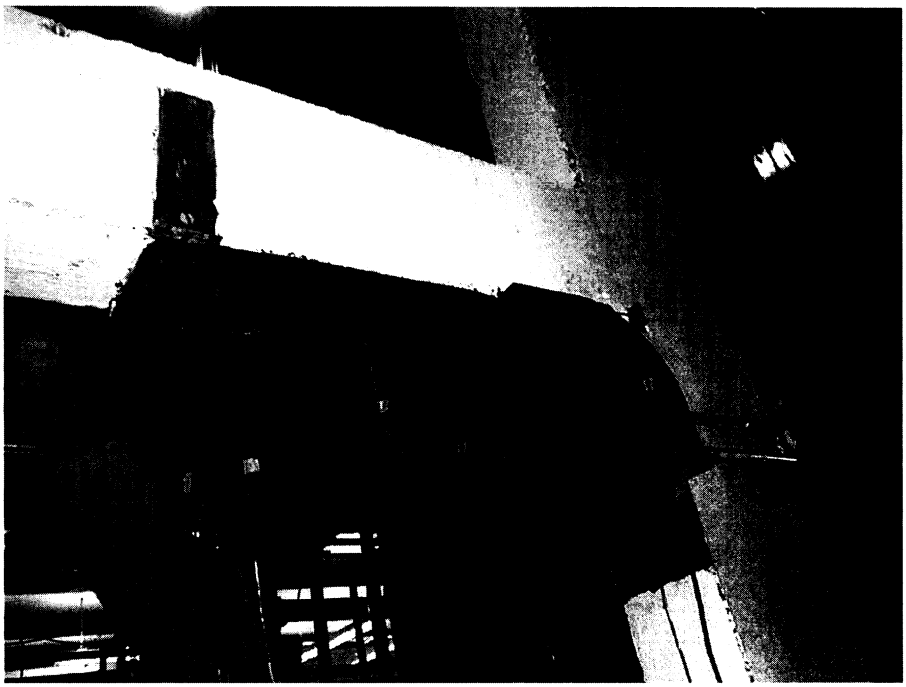

Figure 4-5 Strengthening of joint T-B11

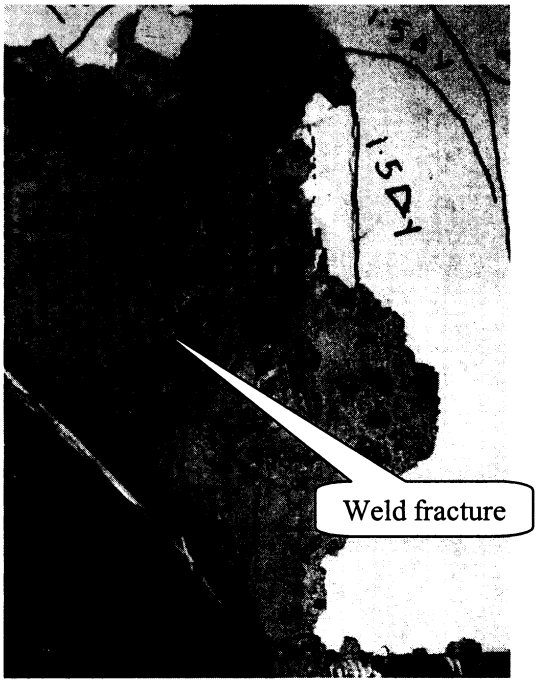

Figure 4-6 Weld failure of angle-supporting bolts of joint T-B11

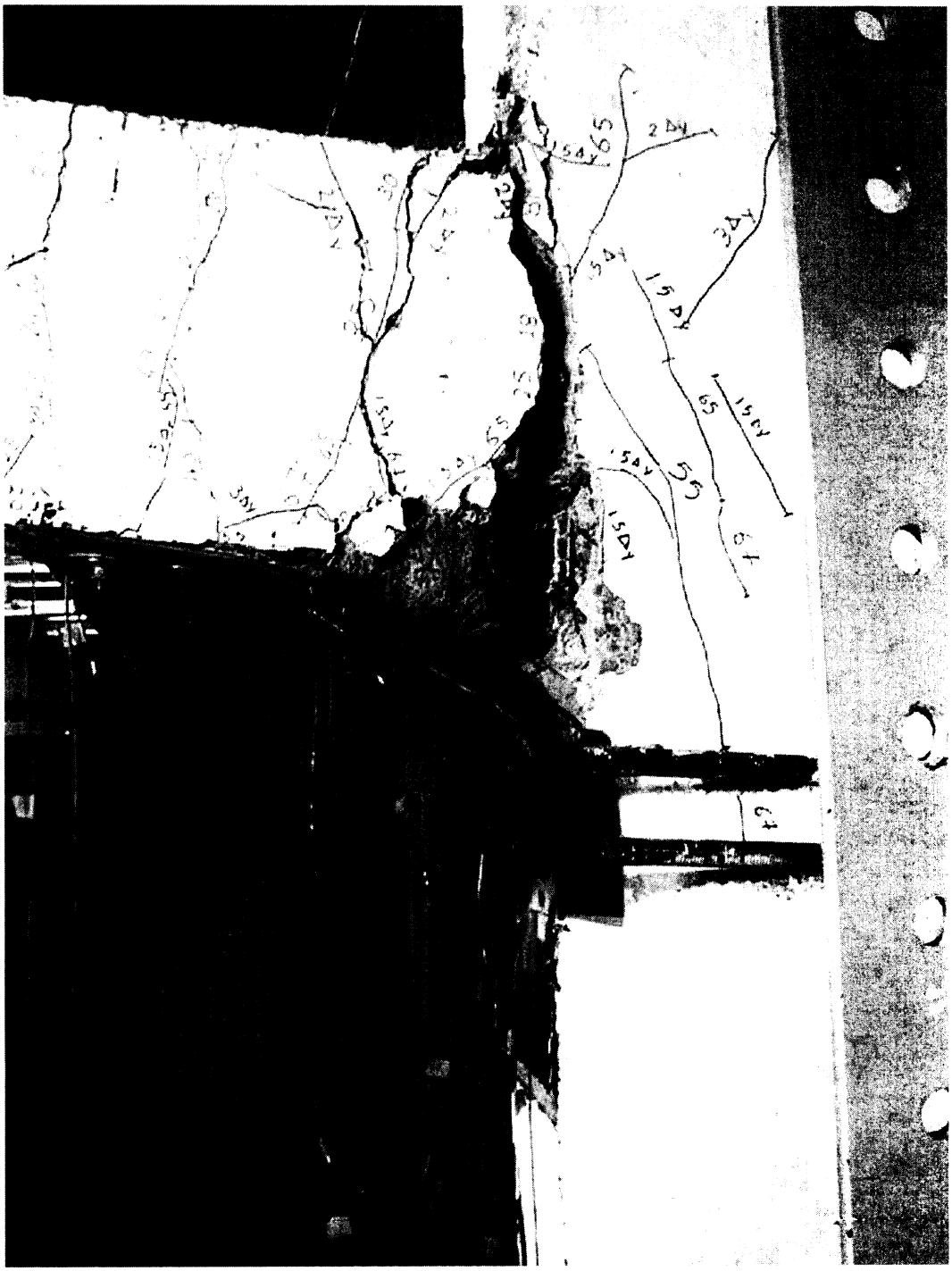

Figure 4-7 Cracking and spalling of concrete of joint T-B11

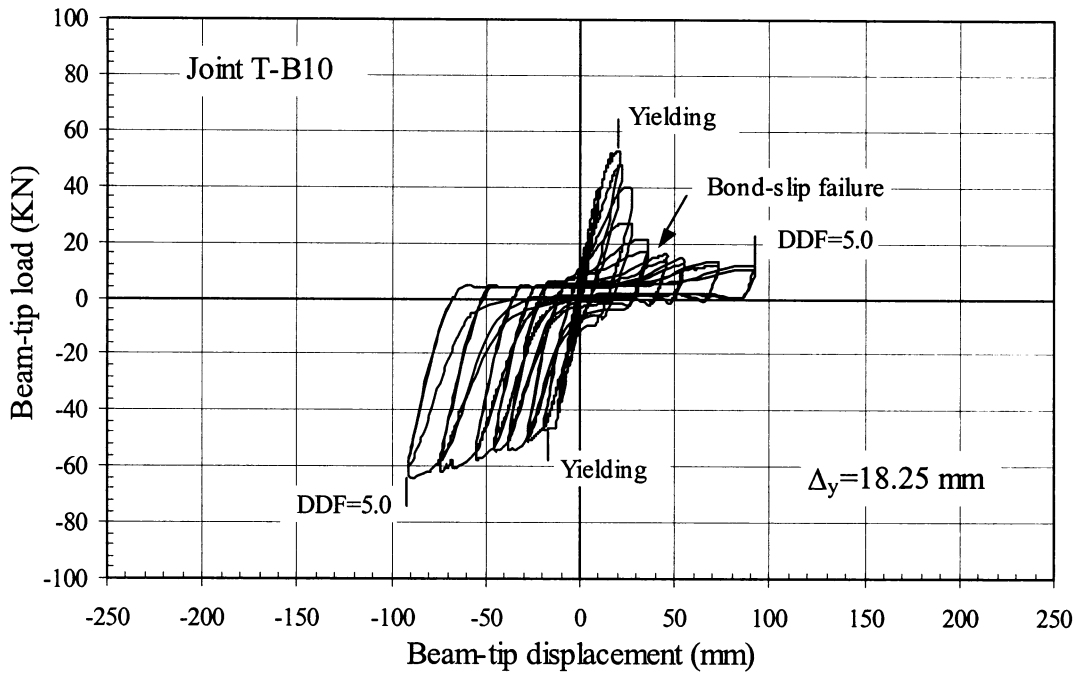

Figure 4-8a Beam-tip load-displacement relationship of joint T-B10

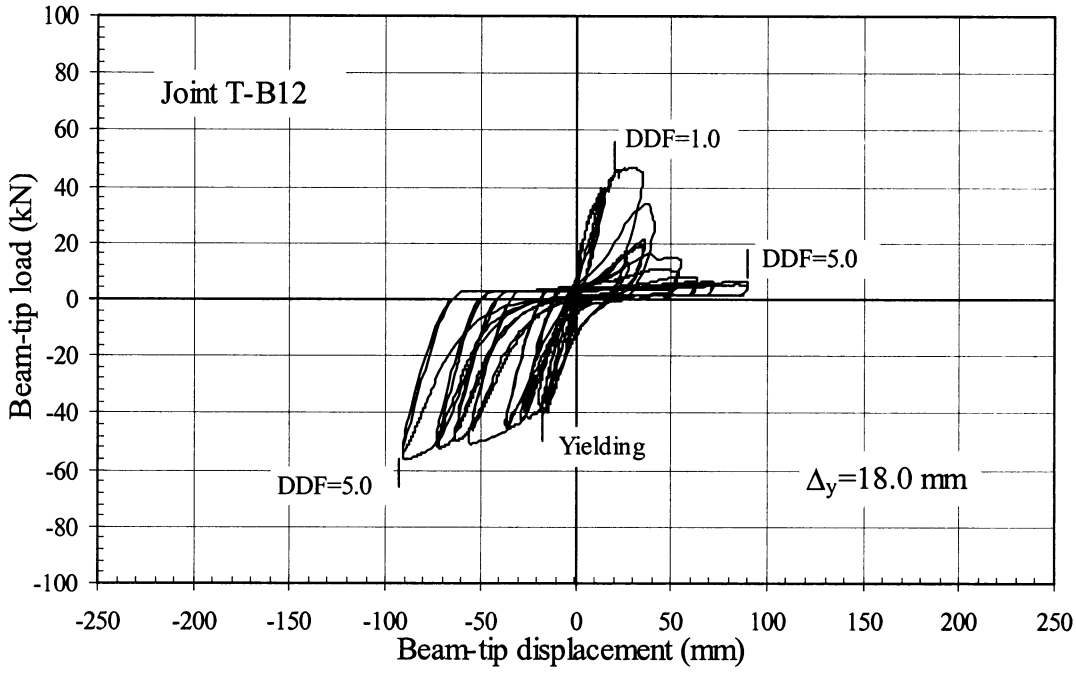

Figure 4-8b Beam-tip load-displacement relationship of joint T-B12

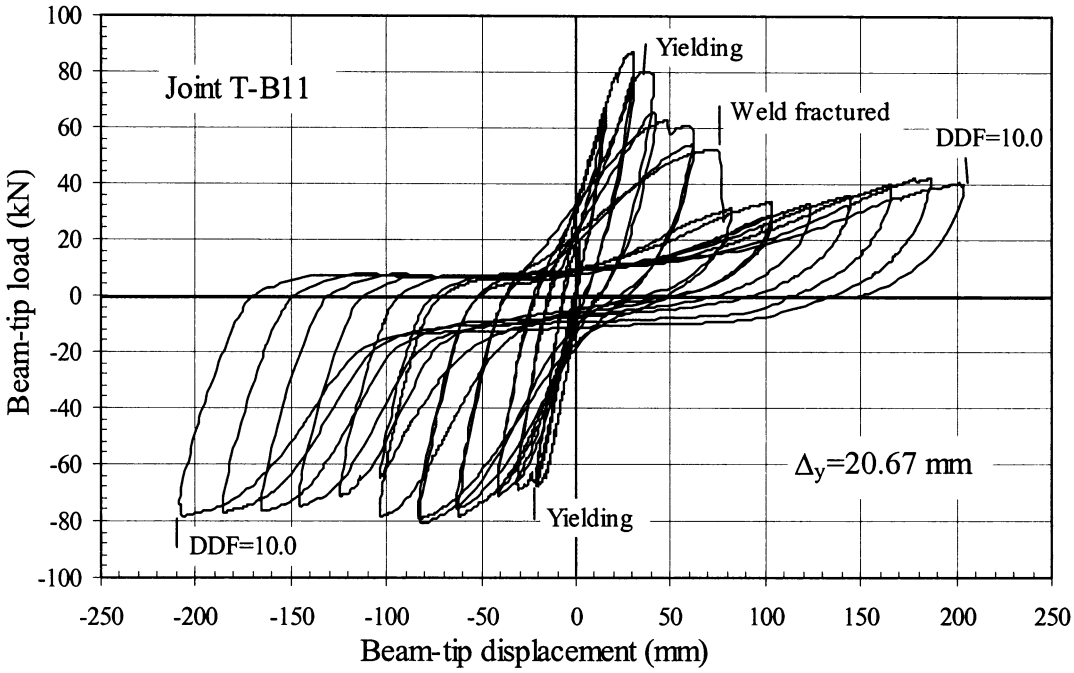

Figure 4-8c Beam-tip load-displacement relationship of joint T-B11

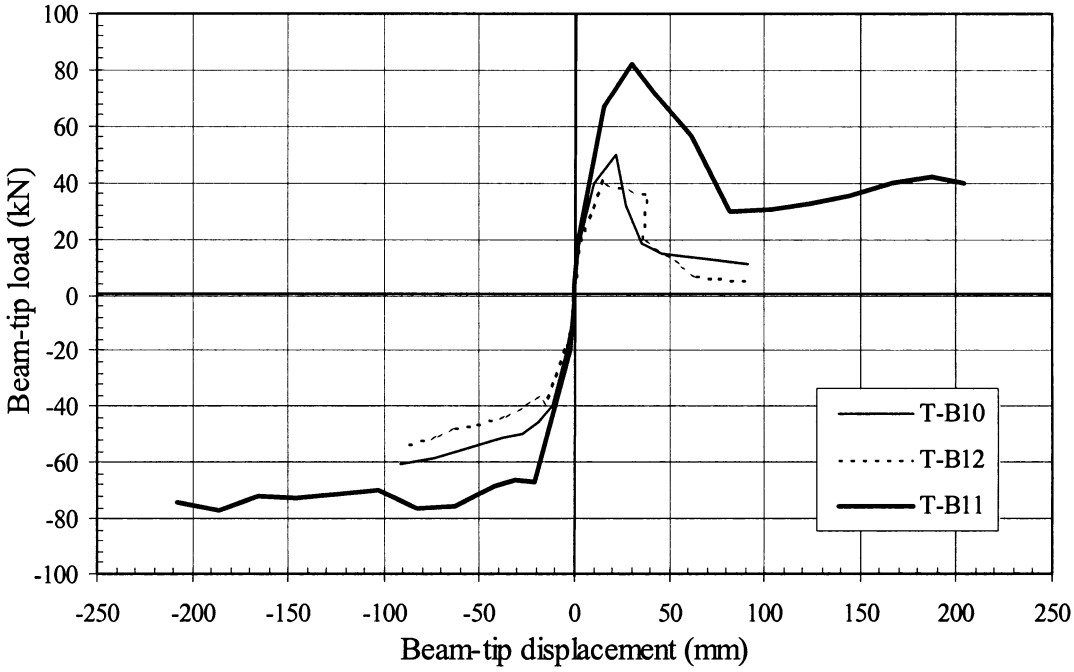

Figure 4-9 Hysteretic loops envelopes of the tested joints

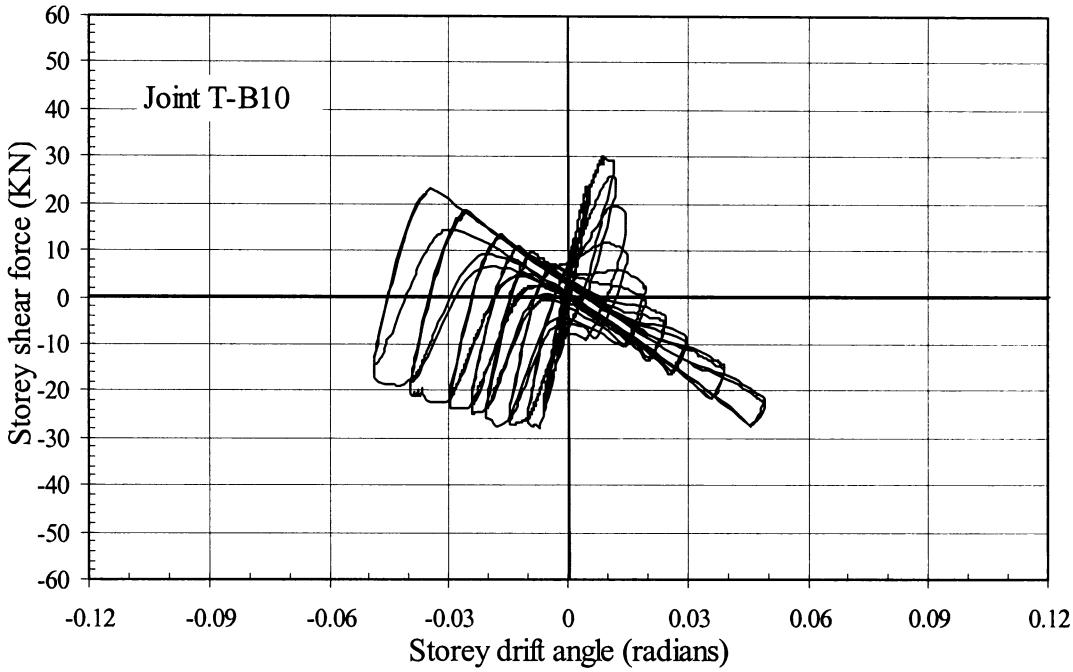

Figure 4-10a Storey shear – drift angle relationship of joint T-B10

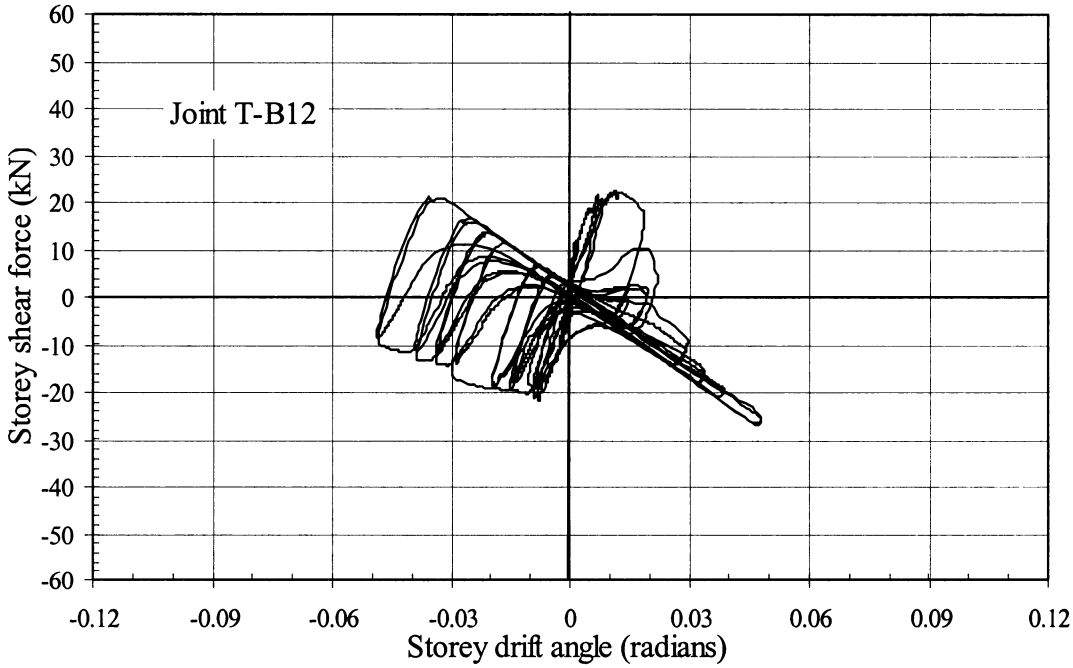

Figure 4-10b Storey shear – drift angle relationship of joint T-B12

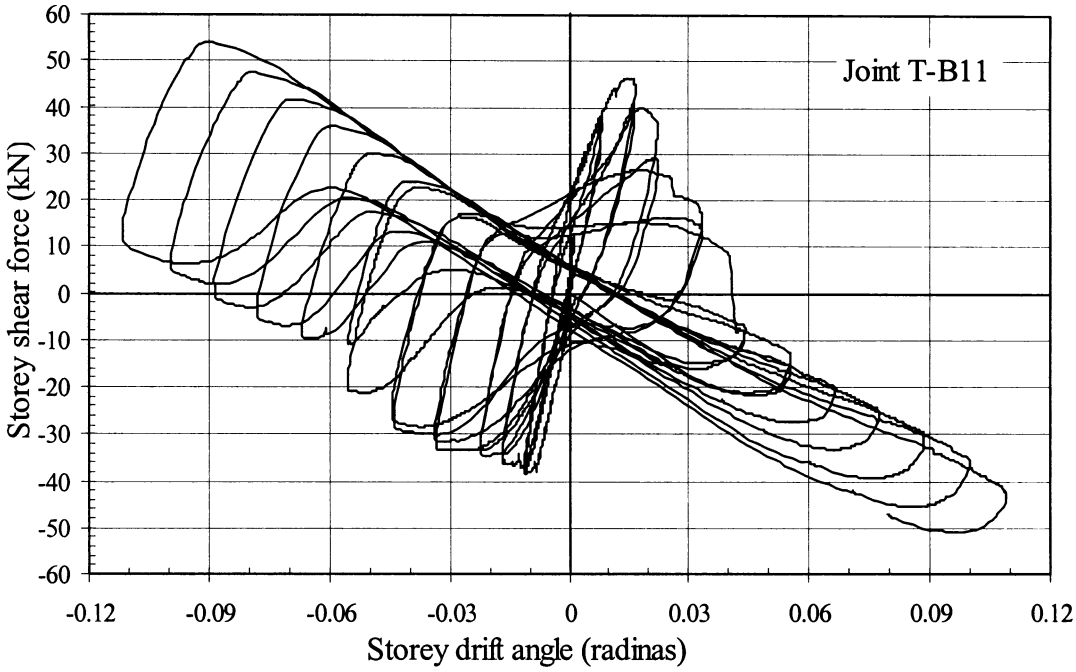

Figure 4-10c Storey shear – drift angle relationship of joint T-B11

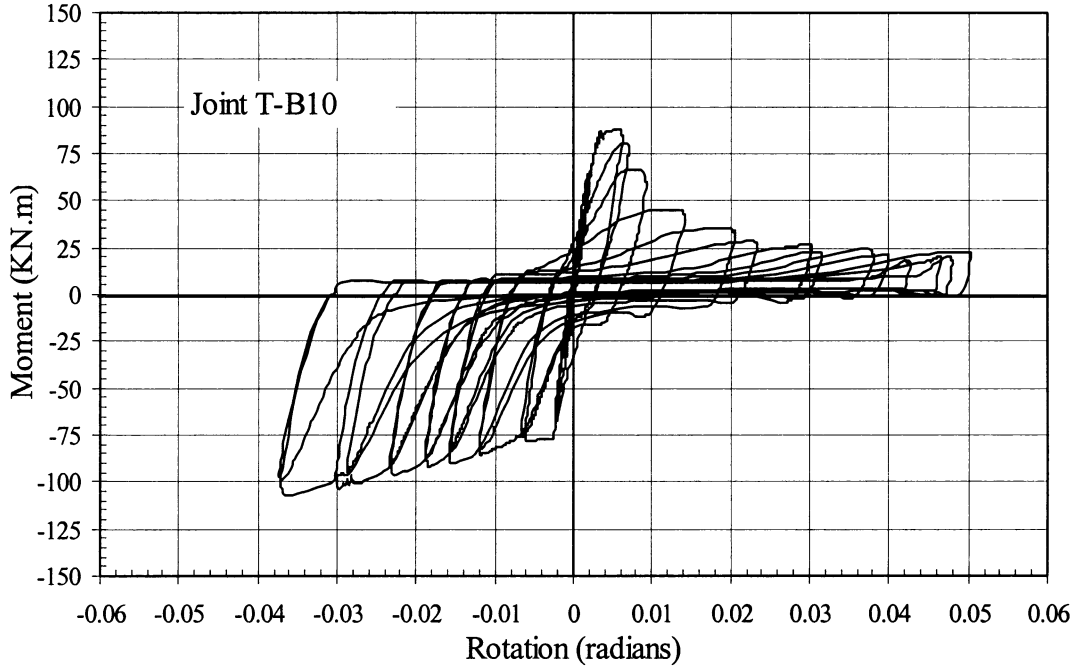

Figure 4-11a Beam moment-rotation at 175 mm from column face of joint T-B10

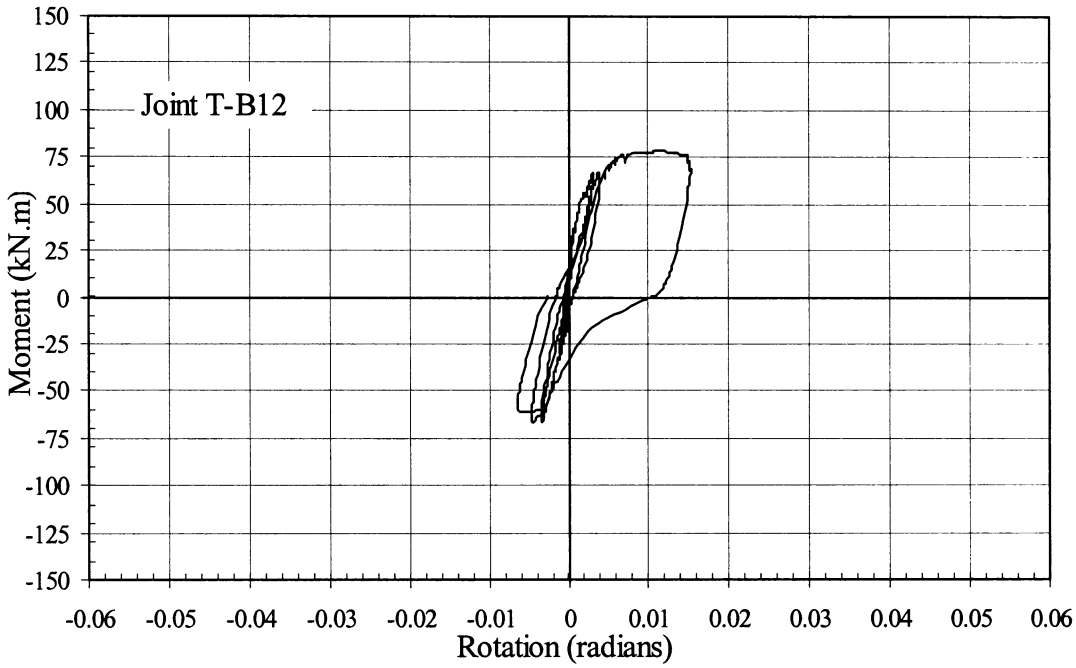

Figure 4-11b Beam moment-rotation at 175 mm from column face of joint T-B12

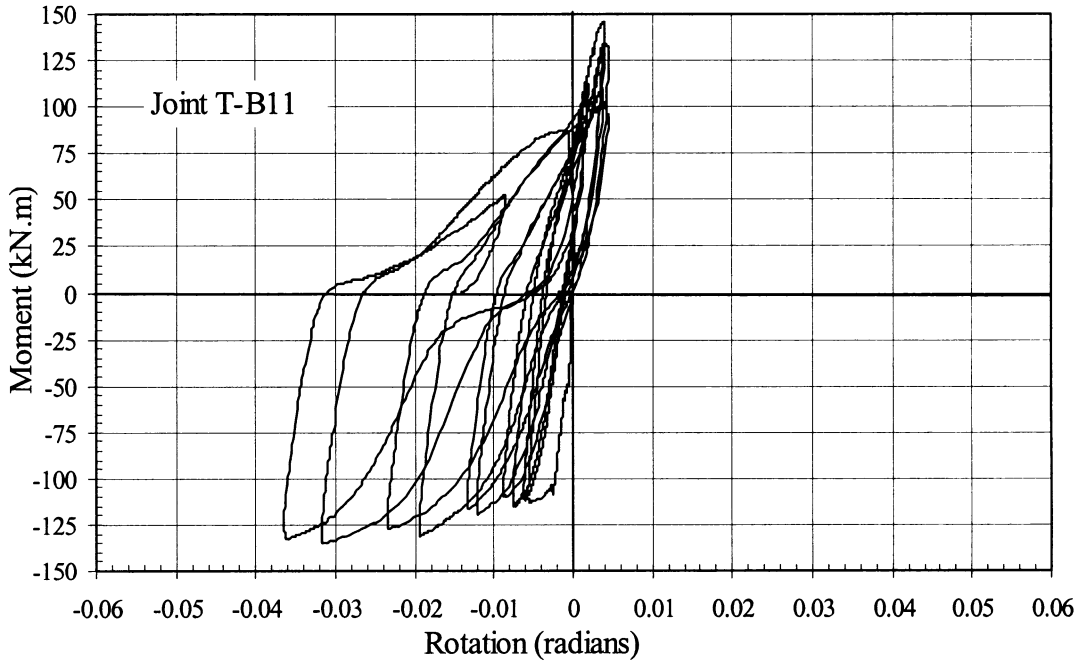

Figure 4-11c Beam moment-rotation at 175 mm from column face of joint T-B11

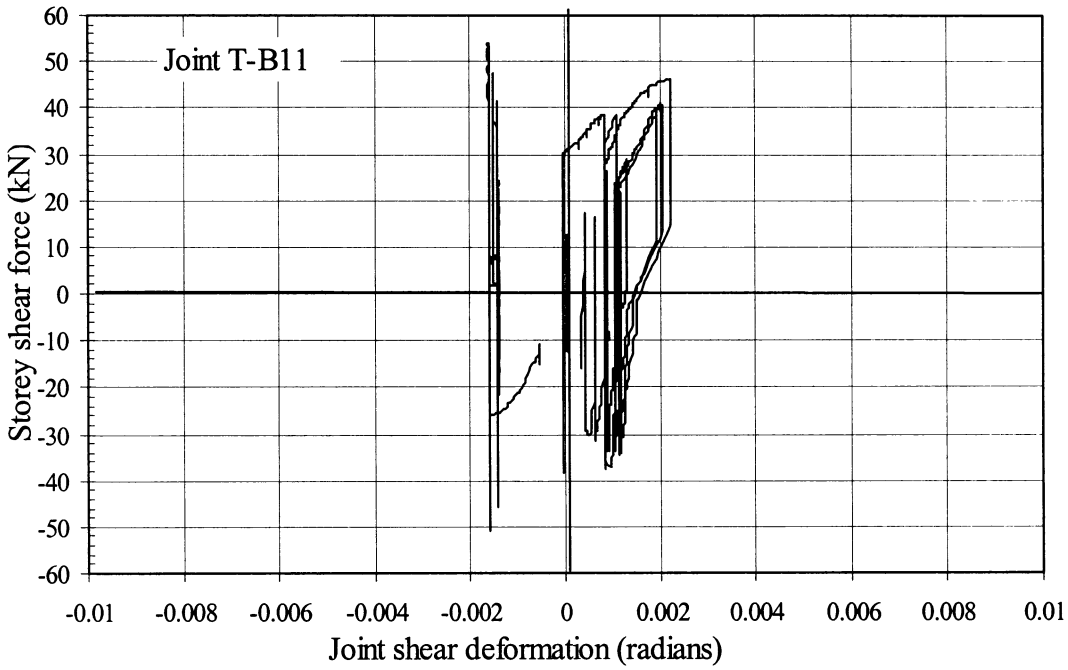

Figure 4-12 Joint shear deformation – storey shear force of joint T-B11

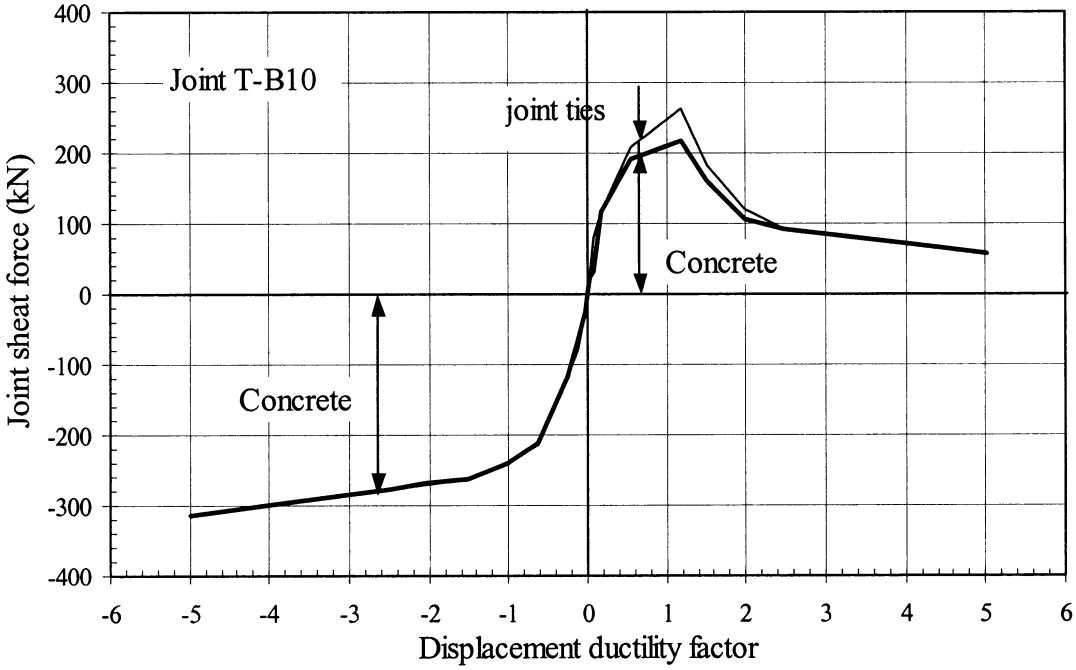

Figure 4-13 Contribution of concrete shear strength and steel ties in carrying the joint shear force of joint T-B10

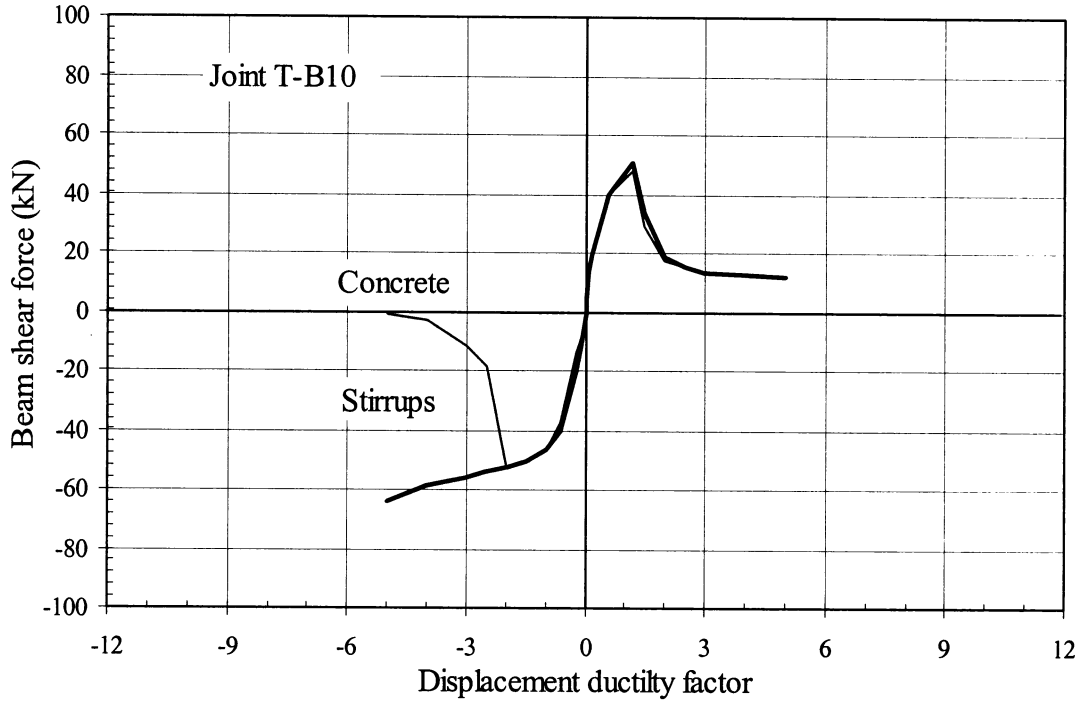

Figure 4-14a Beam shear force resisted by concrete and stirrups of joint T-B10

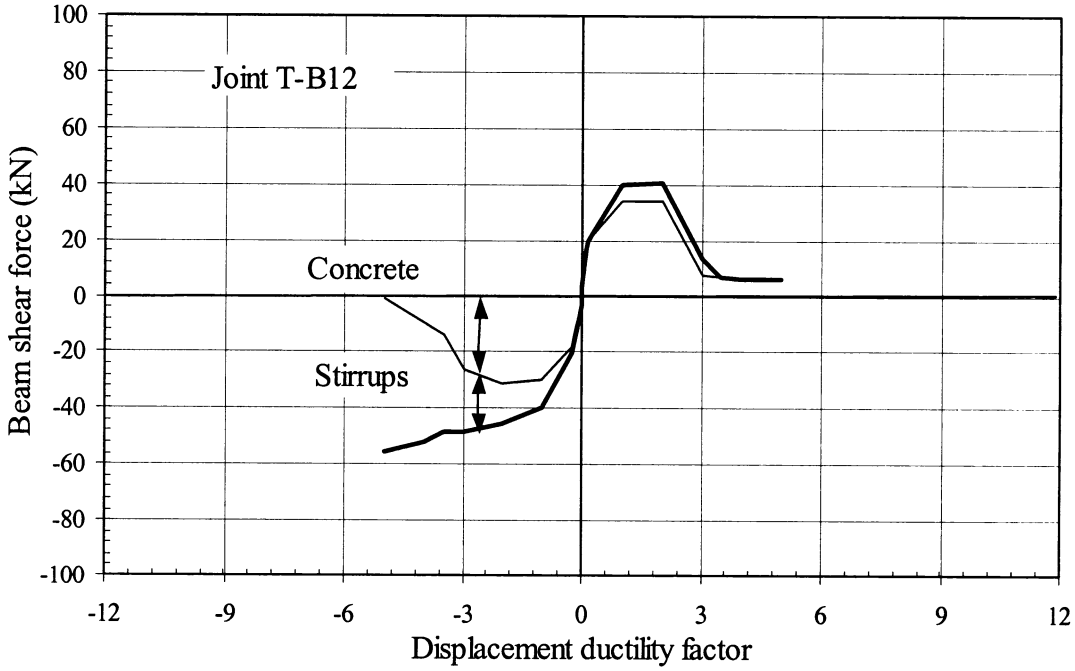

Figure 4-14b Beam shear force resisted by concrete and stirrups of joint T-B12

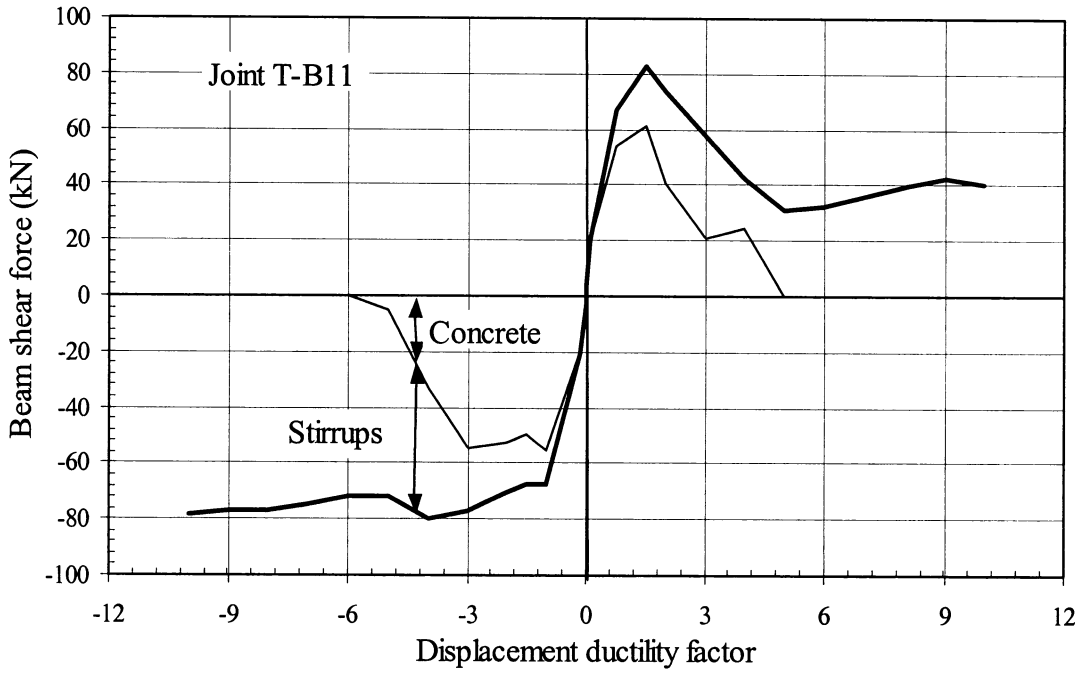

Figure 4-14c Beam shear force resisted by concrete and stirrups of joint T-B11

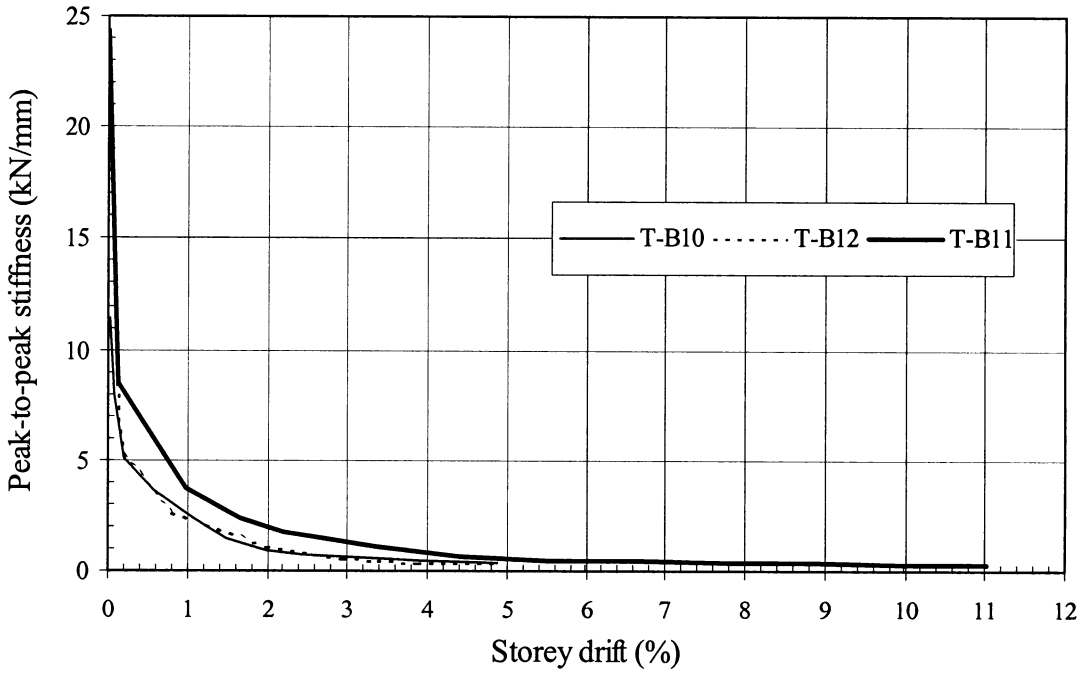

Figure 4-15 Stiffness degradation with storey drift

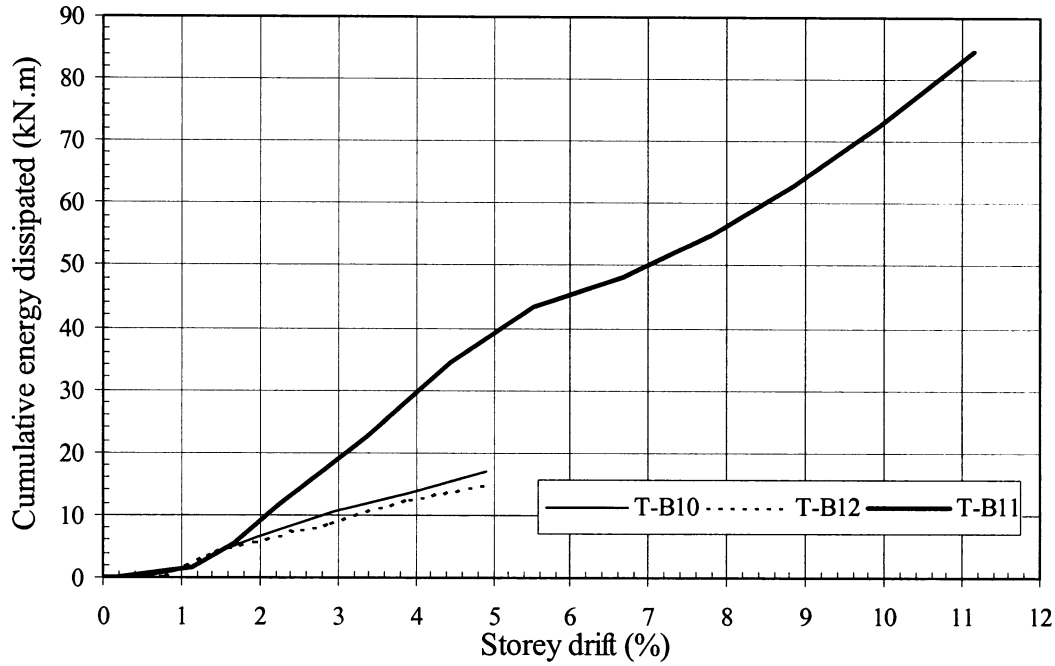

Figure 4-16 Cumulative energy disspated by joint group T-B

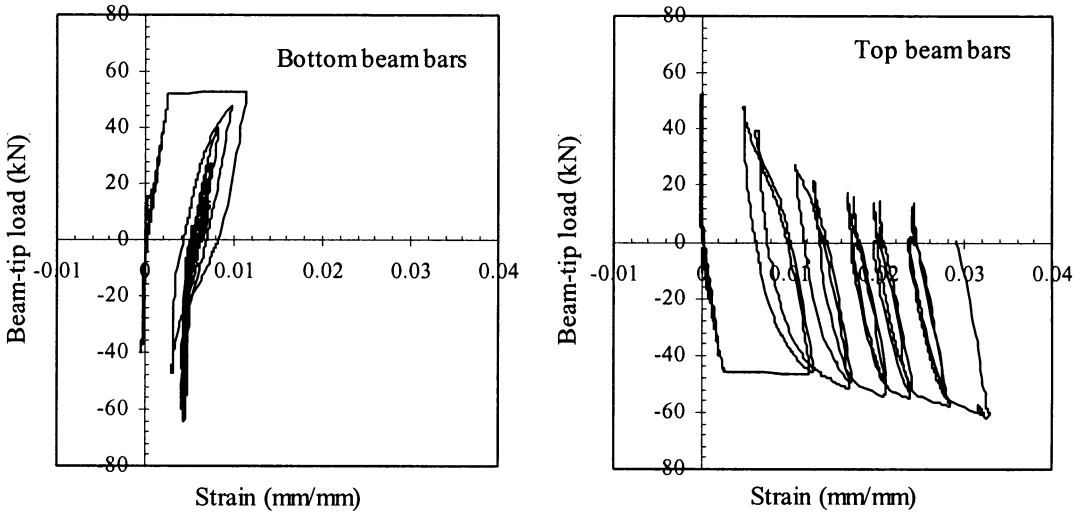

Figure 4-17 Steel bars strain-beam-tip load relationships of joint T-B10

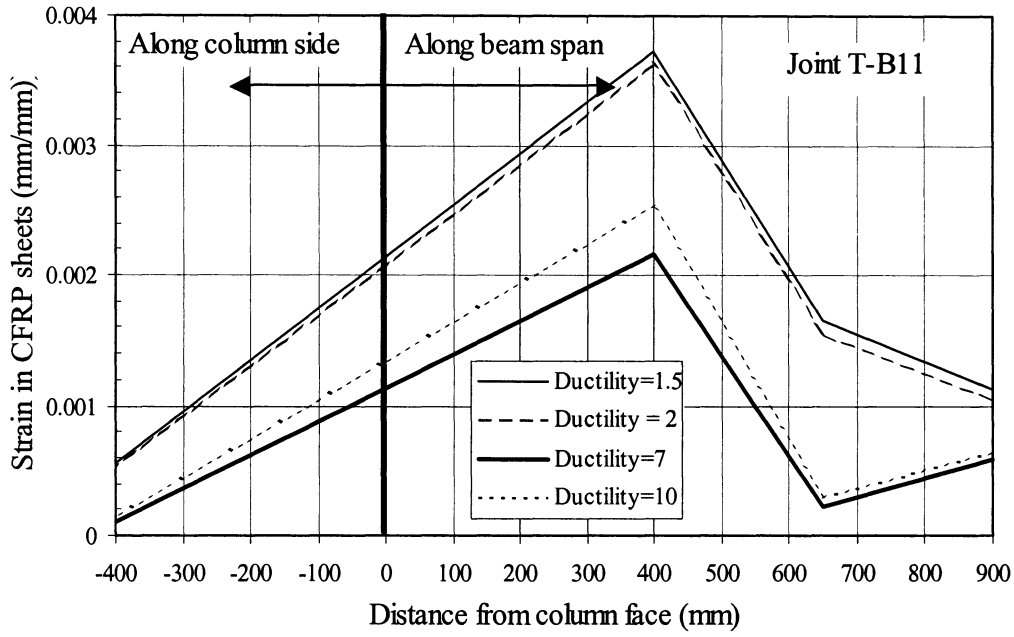

(a) Push-up loading direction

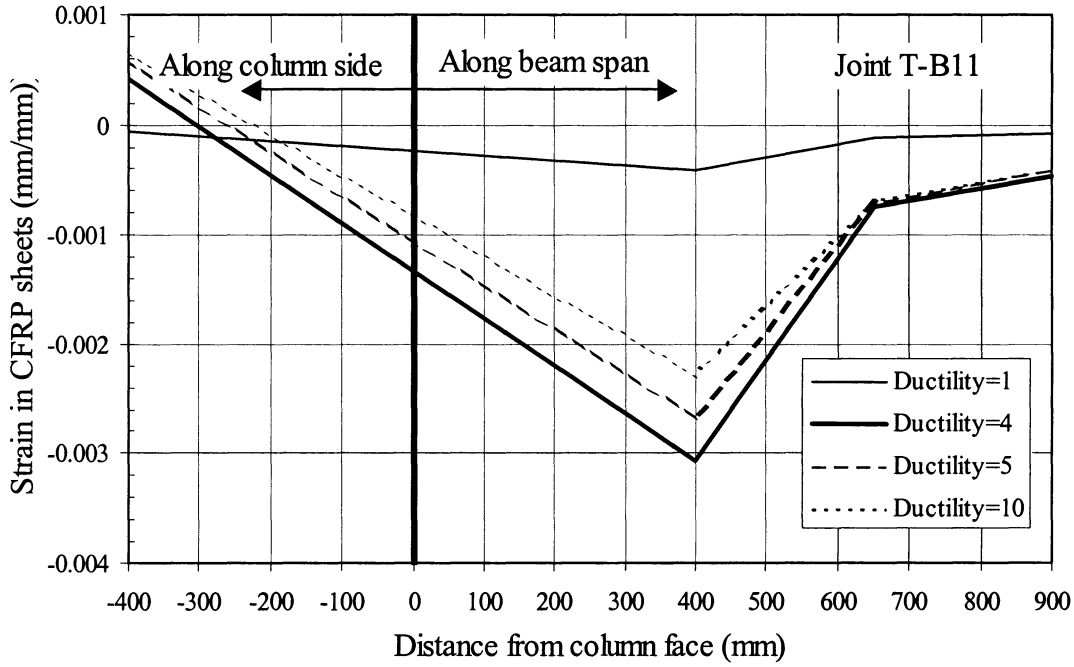

(b) Pull-down loading direction

Figure 4-18 Distribution of strain along the length of the CFRP sheets

Chapter 5

BEHAVIOUR OF SHEAR/BOND-DEFICIENT JOINTS

5.1 INTRODUCTION

The overall behaviour of five joints, T-SB3, T-SB3R, T-SB6, T-SB8, and T-SB7 is discussed in this chapter. The joints had the same concrete dimensions and reinforcement details. No ties were installed in the joint zone and the beam bottom bars were anchored 150 mm into the joint zone. These are typical reinforcement details of concrete moment resisting frames built before the development of seismic codes. Joint T-SB3 was tested to represent the as-built condition. The other joints were shear-strengthened using glass fibre reinforced polymer (GFRP) jacket. The strength deterioration due to the anchorage failure of beam bars was accounted for using GFRP sheets or steel elements.

5.2 JOINT T-SB3

The control specimen represented a typical joint built according to the pre-1970 seismic code. The joint was deficient in joint shear resistance and beam bars bond strength. The joint was tested under quasi-static load to failure.

The first beam crack was observed during the second cycle at the column face at a positive load of 7.7 kN. In the fourth cycle, the joint was loaded to ±30.0 kN. New

flexural and flexural-shear cracks formed along the length of the beam. In the sixth cycle, vertical cracks formed in the joint region at a beam-tip load of +35.5 kN due to the bond-slip of beam bottom bars. Under low cyclic loading, the bond forces are mainly transferred by bearing of the bar lugs on the concrete. Slip of the bars occurred due to crushing and cracking of the concrete ahead of the lugs. Unless the bond strength reached its maximum value, load recovery is expected to occur when exceeding the previous slip. During the eighth cycle, diagonal shear cracks developed in the joint region when pulling down. The joint reached a load of ±60.0 kN at a beam-tip displacement of 20 mm. Repeating the same cycle, the beam-tip load degraded and the beam bars started to slip out of the joint with associated reduction in the developed strain in the bars. The beam-tip displacement of 20 mm was used as a reference value for displacement control loading phase. The reason for selecting this arbitrary displacement was that yielding of the reinforcement bars was not expected to occur.

The specimen reached an ultimate positive and negative strength of 61.4 kN and 92.1 kN, respectively, at a displacement ductility factor (DDF) of 1.5. When the joint was pushed up, bond-slip of beam bars occurred and joint strength significantly deteriorated. When it was pulled down the diagonal shear cracks propagated in the joint zone, which caused disintegration of the concrete, deterioration of the bond condition of the beam top bars and degradation of the joint strength. The test was halted at a DDF of 2.5 (±50 mm) as the joint strength was greatly reduced.

The final failure pattern is shown in Figure 5-1. A reduction in the column axial load up to 10% of the original load was recorded in the last cycle due to joint shear

failure. Bond-slip was found to be a more brittle type of failure when compared with shear failure as it occurred earlier and is associated with higher of strength deterioration.

5.3 JOINT T-SB3R

After testing joint T-SB3, the spalled and cracked concrete was removed from the beam-column joint and the surrounding areas. New concrete was poured and then the joint was strengthened using glass fibre reinforced polymer (GFRP) sheets. The proposed rehabilitation scheme consisted of two systems. The first system was for upgrading the joint shear strength. The joint was wrapped with two U-shaped composite sheets. The first sheet was a bi-directional Tyfo BC sheet with the fibre direction at ±45°, and the second was uni-directional MBrace EG 900 sheet with the fibre direction parallel to the beam longitudinal axis. The ends of the sheets were anchored using steel plates and 12 mm diameter tie rods installed in holes drilled through the joint. This system was similar to previously tested system (Said, 2000) but differs in material design and details. The second system was for upgrading the beam bars bond-slip and was similar to the system used to strengthen joint T-B12. Four MBrace EG 900 uni-directional GFRP sheets were applied to the beam bottom face for a horizontal distance of 1000 mm and extended vertically along the inner column face for a distance of 500 mm, as shown in Figure 5-2. To prevent debonding of the composite sheets from the concrete surface at the beam-column interface, a 150 x 150 x 16 mm steel angle was installed at the lower beam-column corner. To install the angle in place, the beam bottom bars were exposed for a

distance of 150 mm from the column face and the heads of A375 20 mm diameter steel bolts were welded to the beam bars in two rows. Four 28 mm diameter and 170 mm deep holes were drilled in the column in two rows. The steel angle was fixed in place using washers and nuts to the bolts welded to the beam reinforcement and using Hilti HVA 5/8x6-5/8 adhesive anchors to the column.

The first beam crack occurred in the new concrete during the second cycle at a load of 14.0 kN. Before yielding, the joint behaviour was almost elastic with no residual deformation was observed. Examining the strain values showed that the GFRP sheets attached to the beam face were carrying most of the developed tensile forces, indicating that the sheets were working effectively. During the sixth cycle, vertical cracks appeared in the lower column below the joint region. A corresponding drop in the beam-tip load from +58.0 kN to +53.0 kN was recorded. During the test, the debonding of FRP sheets was regularly checked by tapping on the sheets. In the tenth cycle, the beam top steel bars reached the yield strain at a beam-tip displacement of 25 mm and a beam-tip load of -110.0 kN. This displacement was designated as the yield displacement Δ_y, and the displacement control loading phase was initiated.

During the twelfth cycle, a DDF of 1.5 (±37.5 mm) was reached. The GFRP sheets attached to the beam bottom face reached a strain of 0.45% when the joint was pushed up. As the joint was pulled down, the fibre-sheets buckled and debonded from the beam face, as shown in Figure 5-3. In the following cycles, as the tension in the composite sheets was lost due to debonding, the existing beam reinforcement resisted the developed tension force. The tension force in the bars was transferred to the column by

bond, welded bolts and the steel angle. The joint maintained its strength as it was pulled down. During the sixteenth cycle, at a DDF of 3.0 (±75.0 mm), successive failure of the welded bolts occurred, causing the beam bars to slip out of the joint. Therefore, a sudden drop in the beam load was observed. During the next cycle, the joint strength dropped when pushing up, whereas the joint strength was maintained when pulling down indicating no shear failure in the joint region occurred.

The final failure mode is shown in Figure 5-4. The composite sheets were completely debonded from the beam and column faces. Examining the hysteretic loops of the specimen showed that the behaviour remained almost elastic up to the first steel yield, and severe pinching and stiffness degradation occurred in the last two cycles following the weld fracture.

5.4 JOINT T-SB6

The joint shear strength was upgraded using the same system described for joint T-SB3R, except only two vertical steel plates were used to tie the composite sheets ends. Eight MBrace EG 900 sheets were attached to the beam bottom face and extended on the inner column face with the same configuration of joint T-SB3R and provided with two 3 mm thick U-shaped steel plates to enhance the bond between the GFRP sheets and the concrete surface. A 500 mm long 225 x 225 x 9 mm steel angle was used to alleviate the possible debonding of the composite sheets. The angle was tied to the beam bottom surface using eight A375 20 mm diameter steel bolts welded to the beam bottom bars in

two rows, and to the column face using four 25 mm diameter external threaded rods tied against a 500 x 200 x 25 mm steel plate at the back of the column, as shown in Figure 5-5 and Figure 5-6.

The first beam crack occurred during the second cycle at a load of 20.0 kN while the joint was pulled down. During the fourth cycle, vertical cracks appeared in the lower column under the joint region at a beam-tip load of 75 kN. The first yield of the beam top bars occurred at a beam-tip displacement of 26.5 mm and beam-tip load of 114.5 kN. This displacement was designated as the yield displacement, Δ_y, and the displacement control loading phase was initiated. Debonding of the wrapped sheets around the beam-column joint region was initiated during the sixth cycle.

At a DDF of 2.0, a drop in the beam-tip load accompanied with large inelastic deformation was observed when the joint was pushed up. At a DDF of 3.0 (±79.5 mm), the specimen ultimate strength of -131.0 kN was recorded. This high load caused new cracks in the column above the joint zone and initiated joint shear failure. Deterioration of specimen strength was observed in the following cycles. At a DDF of 5.0 (±132.5 mm), the joint strength degraded to +74.0 kN and -89.0 kN. The strain in the GFRP reached approximately 0.5% in both tension and compression. Shear cracks in the upper column part and inelastic deformation of the steel angle were recorded at this ductility level, as shown in Figure 5-7. At a DDF of 6 (±159 mm), the joint resistance dropped to 52.0 kN. During the next cycle, the joint was loaded to a DDF of 7.0 (±185.0 mm) and the joint strength dropped to 32.0 kN. The test was terminated as a result of this severe

strength deterioration.

Shear failure of beam-column joint zone was obvious after removing the tie rods and lifting the GFRP sheets, as shown in Figure 5-8. Although the joint failed in shear, the overall joint performance was much more ductile as compared to the control joint T-SB3. The forces developed in the composite sheets were transferred to the column by the steel angle and the tie rods. Fracture of the composite sheets at the beam-column interface, as occurred for joint T-B12, was avoided due to the high deformability of the steel angle. During the test, it was confirmed that the plastic deformation capacity of the steel angle provided significant ductility to the joint behaviour. The two U-shaped steel plates were effective in preventing fibre debonding from the concrete face to the end of the test.

5.5 JOINT T-SB8

A new technique for strengthening the bond-slip of beam bars was used to upgrade joint T-SB8. The idea was to replace the action of the existing inadequately anchored bars with new well-anchored steel reinforcement. The beam bottom bars were exposed for a length of 1000 mm from the column face. Two 35 mm diameter holes were drilled right through the column below the beam steel bars. Seven pairs of 12 mm diameter and 100 mm deep holes were drilled close to beam stirrups. Two 32 mm diameter threaded rods were inserted into the two column holes with their ends extending out from the column backside. Hydrostone mortar was poured to fill in the holes. Seven

U-shaped steel ties of 200 mm width and leg length of 150 mm were inserted into the pre-drilled holes in the beam. Epoxy mortar Sikadur 31-Hi-Mod-GEL type was used to bond the steel ties to the concrete, as shown in Figure 5-9. New grout was poured to maintain a minimum concrete cover of 30 mm. Therefore, in the repair zone the beam depth was increased to 480 mm. The rods were anchored to the column backside using washers, nuts and a 250 x 250 x 25 mm steel square plate. The joint shear strength was upgraded using the same system used in joint T-SB6 with few modifications. One bi-directional Tyfo BC sheet with the fibre direction at ± 45° and two uni-directional MBrace EG 900 sheets were wrapped around the joint. In addition, 400 mm above and below the joint were wrapped with one uni-directional MBrace EG 900 sheet. The joint was set up vertically inside the loading frame, as shown in Figure 5-10, and tested.

The first beam crack occurred at a load of 22.0 kN, which was higher than the cracking load of the other joints. This was expected due to the increase in the beam depth (from 400 mm to 480 mm). During the fourth cycle, while pushing up, an inclined splitting crack occurred at the corner where the beam depth was increased, at a load of 35.0 kN. Examining the strains of the original beam bottom bars and the threaded rods, showed that the threaded rods were stressed more than twice of the reinforcement bars. The top reinforcement bars yielded at a load of 131.5 kN and a displacement of 34.0 mm. The threaded rods yielded at the same load level and at a displacement of 26.0 mm. The average of the two displacements (30.0 mm) was designated as the yield displacement.

At a DDF of 1.5 (±45.0 mm), the joint reached its ultimate strength of –127.6 kN and +152.0 kN in the negative and positive loading direction, respectively. The inclined

splitting crack expanded parallel to the threaded rods and extended close to the column. At a DDF of 2.0 (±60.0 mm), the joint strength dropped from 115.0 kN to 61.0 kN at the end of the positive part of the cycle. The crack between the old and new concrete extended and the joint failure was initiated. The negative joint strength also was degraded to 110.0 kN. When repeating this cycle, the joint strength degraded to +40.0 and –101.0 kN and severe pinching was recorded. At a DDF of 3.0, the positive strength deteriorated whereas the negative strength was kept at the same level. The test was terminated as the joint strength dropped to about 14.6 kN. The failure mode is shown in Figure 5-11. Delamination of the new concrete caused the disfunction of the installed threaded rods. Following this, consequent bond-slip of the existing beam reinforcement occurred.

5.6 JOINT T-SB7

A steel bridle was used to anchor the existing beam bottom bars to the column backside. The concrete cover and 100 mm above the beam bottom bars were removed for a distance of 250 mm from the column face. The beam bars were then slightly ground to remove any remaining concrete chunks. Two steel plates 500 x 130 x 20 and 500 x 70 x 20 mm were inserted above the bars, separated by a beam stirrup, and then welded to the beam bars. New concrete was poured to cover the rebars and the plates, leaving a length of 125 mm of the plates projecting out from each side of the beam. Four steel plates were welded to the overhanging parts. Four 25 mm diameter threaded rods were welded to the four plates and tied to the column backside using a 500 x 250 x 25 mm steel plate, as

shown in Figure 5-12. The idea was to transfer the beam bars tensile forces to the steel plates through the weld lines, then to the threaded rods through the second weld lines and then to the column by bearing. To strengthen the joint shear resistance, GFRP sheets were used with the same configuration as used for joint T-SB8.

The first beam positive crack occurred during the second cycle at a load of 22.0 kN, whereas the negative crack occurred during the same cycle at a load of 12.0 kN. Yielding of the top steel bars was reached during the fourth cycle at a load of 106.9 kN and a displacement of 26.0 mm. Pushing the beam up to the same displacement level, a positive joint strength of 105.0 kN was recorded. A major crack at the beam column interface was also recorded.

During the sixth cycle, a DDF of 1.5 (± 39.0 mm) was reached. The bottom steel bars yielded at a load of 110.0 kN and at a displacement of 28.7 mm. At a DDF of 2.0 (± 52.0 mm), the joint strength reached 116.0 kN in both positive and negative directions. Positive ultimate joint strength of 124.6 kN was attained at a DDF of 3.0 (± 78.0 mm). As the beam was pushed up and down, the tie rods were bent in the positive and negative loading directions, as shown in Figure 5-13. The symmetric behaviour of the hysteretic loops indicated the effectiveness of the technique in upgrading the joint strength. Negative ultimate joint strength of 127.9 kN was attained at a DDF of 4.0 (± 104.0 mm). Pinching of the hysteretic loops was recorded, however, it was much less than pinching of control joint T-SB3. At a DDF of 5.0 (± 130.0 mm), slight deterioration of the positive joint strength to 98.5 kN was recorded. During the sixteenth cycle, a DDF of 6.0 (± 156.0

mm) was reached. The negative joint strength dropped to 96.9 kN, whereas at a positive displacement of 112.7 mm the top tie rod fractured at the tip of the weld lines and the nut of the bottom rod dropped off, as shown in Figure 5-14. A consequent reduction of the joint positive strength from 68.4 kN to 5.3 kN was recorded, and the test was terminated.

To the end of the test, excellent behaviour of the joint jacket with no debonding of the GFRP sheets was recorded. The tying mechanism of the bottom bars was effective in preventing the bottom bars pull-out and upgrading the joint positive strength.

5.7 ANALYSIS OF EXPERIMENTAL RESULTS

In this section, the behaviour of the joints and the effectiveness of strengthening schemes are evaluated. The joint hysteretic behaviour, displacement ductility factor, beam-column joint shear deformations, cracking and yielding moments, contribution of concrete shear strength and beam stirrups in carrying the beam shear force, energy dissipation ability and joint stiffness are discussed.

5.7.1 Beam-tip load-displacement relationships

The beam-tip load-displacement relationships of the tested joints are shown in Figure 5-15a to Figure 5-15e. The theoretical yield and ultimate loads are presented in Table 5-1.

For joint T-SB3, bond slip cracks occurred in beam-column joint region during the sixth cycle at a load of 35.5 kN. This is corresponding to a bond stress of $1.48\sqrt{f_c^{'}}$ where the average bond stress U, is evaluated as:

$$U = \frac{f_s\, d_b}{4 l_b} \tag{5-1}$$

where f_s is the steel bar stress

d_b is the steel bar diameter

l_b is the bond length

The allowable average bond stress f_b as given by ACI (1992) is estimated as:

$$f_b = 9.5\sqrt{f_c^{'}} / d_b \quad \leq 800\ psi \tag{5-2}$$

For 20 mm diameter steel bar, the allowable bond stress is $1.0\sqrt{f_c^{'}}$. Comparing the cracking bond stress to the allowable stress gives insight into the conservative approach of the code. Bond cracks would result in degradation of the beam bar tensile force and increase of the bar slippage. Significant pinching of the hysteretic loops occurred at a DDF of 2.0. At a DDF of 2.5, severe strength deterioration and stiffness degradation occurred and hence the test was terminated. Yielding of the top and bottom steel bars was not reached as a result of disintegration of the concrete in the anchorage zone.

For joint T-SB3R, the GFRP sheets debonded from the beam bottom face at a DDF of 1.5. No significant pinching or strength degradation was recorded till this ductility level. At a DDF of 3.0, a progressive failure of the bolts welded to the beam bars occurred. A consequent degradation of the positive specimen strength was recorded.

For joint T-SB6, strength dropped from 109.1 kN to 85.7 kN due to the debonding of the FRP sheets, at a DDF of 1.5. Following this, joint positive strength was maintained until reaching a DDF of 5.0. Joint negative strength gradually degraded due to reduction

of joint shear strength. At a DDF of 7.0, the FRP jacket completely debonded and the joint strength was dramatically degraded, therefore the test was terminated. Pinching of the hysteretic loops was noted at a DDF of 3.0 and gradually increased to the end of the test.

Joint T-SB8 showed the highest positive strength among the joints. A positive strength of 152.0 kN was recorded. Delamination of the new poured concrete occurred at a DDF of 2.0, causing dramatic strength deterioration. Severe pinching and stiffness degradation occurred when the test proceeded beyond this ductility level.

Joint T-SB7 showed symmetric hysteretic behaviour in both positive and negative directions. Plastic hinge formed at the beam column interface at a DDF of 5.0. The joint maintained its strength until reaching a DDF of 6.0 when fracture of the external tie rods occurred.

Figure 5-16 shows the envelopes of the hysteretic loops of the joints. The control joint T-SB3 showed very poor behaviour, as compared to the other joints. Joint T-SB8 showed the highest strength but with insufficient ductility capacity. Joints T-SB6 and T-SB7 showed the best behaviour. The behaviour of joint T-SB7 was very stable until the external tying mechanism failed. Joint T-SB6 showed stable behaviour until the joint shear strength dropped.

5.7.2 Storey shear-storey drift angle relationships

The storey shear was estimated as described before in Section 2.10.5, taking into consideration the P-Δ effect. The beam-tip displacement was converted to drift angle using Equation (2-8). Storey shear-drift angle relationships are shown in Figure 5-17a to

Figure 5-17e. Figure 5-18 shows the envelopes of storey shear-drift angle relationships of the tested joints. Degradation of the storey shear of joint T-SB3 occurred at drift angle less than 0.015 radians in both loading directions. Storey shear force in the negative loading direction was maintained for joint T-SB3R, however in the positive loading direction, severe degradation of storey shear occurred after fracture of welds. Joint T-SB6 maintained the storey shear force up to drift angle of 0.04 radians in the negative loading direction. Beyond this drift level, degradation of storey shear was recorded due to the *P-Δ* effect, as discussed in Section 4.5.3. Joint T-SB7 showed the best behaviour. The joint maintained the storey shear in both loading directions up to storey drift of 0.04 radians, whereas beyond this drift level, degradation of storey shear was recorded.

5.7.3 Cracking, yield and ultimate moments

The cracking moment was obtained by multiplying the cracking beam load by the distance from the centre of the applied load to the column face. The concrete tensile stress was compared with the modulus of rupture given by CSA A23.3 (1994) Clause 8.6.4, which equals $0.6\sqrt{f_c^{'}}$. The results are shown in Table 5-1. The measured tensile strength of concrete ranged from 0.35 to $0.94\sqrt{f_c^{'}}$.

The theoretical yield and ultimate moments were obtained assuming linear strain distribution in the concrete, a parabolic concrete stress distribution and based on the actual concrete and steel strengths. The deterioration of bond strength of beam bars and joint shear strength were not considered when estimating these moments. Thus, joint T-SB3 showed measured ultimate strength of 47% and 72% of the theoretical strength in

the positive and negative loading directions, respectively. Joints T-SB3R and T-SB6 showed reasonable agreement between the experimental measured strength and the analytical estimated strength. For joint T-SB8, the installed steel rods were not included in the analysis and therefore the experimental strength was much higher than the theoretical strength. On the other hand, very good agreement between the theoretical and experimental strengths was obtained for joint T-SB7.

5.7.4 Shear deformation of beam-column joints

Beam-column joint deformation was measured using a pair of diagonal transducers (LVDT's) mounted on the joint. The measurements were then converted into a shear deformation using Equations (2-3), (2-4) and (2-5). The joint shear deformation was plotted against the storey shear for each joint as shown in Figure 5-19a to Figure 5-19e.

For joint T-SB3, the first joint diagonal shear crack occurred at a load of 60.0 kN in the negative loading direction. Whereas vertical joint cracks occurred at +35.0 kN due to bars slippage. Slippage of the beam bottom bars reduced the shear stresses and deformation in the panel zone. Therefore, the joint experienced positive shear deformation of about 1/3 of the negative shear deformation. The positive shear deformation of joint T-SB3R was minimal, as compared to the negative deformation. After debonding of the composite sheets and the subsequent strength degradation, the recorded shear deformation also decreased. The maximum shear deformation was approximately 1/3 the shear deformation of the control joint. Joints T-SB6 exhibited positive shear deformation was about 1/2 of the negative deformation. This is because of

the change in the load transfer mechanism in the positive direction. The joint underwent less deformation than the control joint. Joint T-SB8 showed relatively higher deformation in the positive loading direction than that in the negative loading direction. This was due to the high positive strength, as compared to the negative strength. Joint T-SB7 showed symmetric loops in both loading directions up to drift angle of 0.055 radians. Following this, gradual increase in joint shear deformation in the negative loading direction and decrease in joint shear deformation in the positive loading direction were recorded. This was due to the degradation of the positive specimen strength. The joint showed about 2/3 the shear deformation of the control joint.

5.7.5 Moment-rotation relationships

The rotation of the beam section at 175 mm from the column face was recorded for each joint. This rotation was plotted versus the beam moment at the column face as shown in Figure 5-20a to Figure 5-20e. The recorded rotation involved the rotation due to yielding of the reinforcement bars and the rotation due to slippage of the bars.

An elastic section rotation was recorded for joint T-SB3 before developing the joint shear cracks. When these cracks were developed, inelastic negative rotation of 0.003 radians was recorded. As the beam bottom bars slipped, the column concrete cover disintegrated. This caused large negative readings by the bottom LVDT. Therefore, a negative rotation of roughly 10 times the positive rotation was recorded as shown in Figure 5-20a. Joint T-SB3R showed symmetric behaviour in positive and negative loading directions. A maximum rotation of 0.004 radians corresponding to top bars yielding was recorded. No further rotation could be recorded because the tie of the

bottom LVDT in the concrete failed. Joint T-SB6 showed always positive rotation that was higher than the negative one. This was attributed to the deformability of the steel angle. At a DDF of 1.5, inelastic positive rotation of 0.01 radians was recorded. As the ductility level increased, the rotation at the end of the cycle increased. Rotation beyond a DDF of 5.0 could not be recorded because the bottom LVDT lost its attachments to the concrete due to excessive cracking. Joint T-SB8, showed an inelastic rotation corresponding to yielding of the beam top bars. At a DDF of 1.5, a maximum rotation of -0.012 radians was recorded. The maximum recorded rotation of –0.02 radians occurred at a DDF of 2.0. Delamination of the new concrete occurred beyond this ductility level, making the LVDT readings unreliable. Almost symmetric loops in both loading direction were measured for joint T-SB7. A maximum rotation of -0.023 radian was recorded at DDF of 3.0. The LVDT attachment was lost beyond this ductility level and consequently no further rotation could be measured.

The beam bending stiffness at the ultimate moment was estimated as explained before in Section 3.6.5. The values were presented as a ratio of E_cI_g, where E_c is the concrete modulus of elasticity and I_g is the gross sectional moment of inertia, and listed in Table 5-1. It is clear from the given values that the ductility level has significant effect on the beam bending stiffness. Joint T-SB8 showed stiffness of 0.31 E_cI_g, which is close to the effective stiffness given by CSA A23.3 (1994) Clause 9.8.2.3. Joint T-SB6 showed stiffness that is twice the stiffness of joint T-SB7. This is attributed to the participation of the FRP sheets in increasing the joint stiffness.

5.7.6 Shear in beam

The shear force in the beam was resisted by the concrete shear resistance and the beam steel stirrups. The contribution of each was calculated as was discussed before for joints T-S. The steel and concrete contributions to the shear resistance are plotted against the storey drift as shown in Figure 5-21a to Figure 5-21d. The concrete and steel contribution to the beam shear resistance of joint T-SB3R could not be evaluated as the strain gauges on the beam stirrups were not working properly. The concrete shear resistance of the other joints was recorded in Table 5-2 as a ratio of $\sqrt{f_c^{'}}$ at different ductility levels.

In general, the concrete resistance to beam shear force during the first half of the each loop was higher than that during the second half of the loop. This was attributed to the pre-cracking of the concrete compression diagonal struts during the positive part of the loop. The strengthened joints showed a higher concrete shear resistance as compared to the control joint T-SB3.

5.7.7 Stiffness

Figure 5-22 shows the peak-to-peak stiffness of the joint against storey drift. Joint T-SB3R had half the initial stiffness of joint T-SB3. This was due to the pre-cracking of the joint. Whereas the initially un-cracked joints T-SB6 and T-SB7 had equal initial stiffness to the control joint stiffness while joint T-SB8 showed approximately 30% higher initial stiffness. The control joint T-SB3 experienced severe stiffness degradation with increasing storey drift. The strengthened joints showed more gradual stiffness

degradation. At a storey drift of 2%, the stiffness of the strengthened joints were 100, 84, 125 and 83% more than the stiffness of the control joint, for joints T-SB3R, T-SB6, T-SB8 and T-SB7, respectively.

5.7.8 Energy dissipation

The energy dissipated by the joints in each cycle was estimated as the area enclosed inside the beam-tip load-displacement relationship. Figure 5-23 shows the cumulative energy dissipated by the tested beam-column joints to the end of the test. At storey drift of 2%, the strengthened joints, T-SB3R, T-SB6, T-SB8 and T-SB7, were capable of dissipating energy that was 29, 29, 45, and 18% more than the energy dissipated by the control joint T-SB3. Joint T-SB7 showed the highest capability of energy dissipation.

5.7.9 Behaviour of rehabilitation schemes

The strains of different elements of the proposed rehabilitation schemes were measured during the test. These strains provided better understanding of the behaviour of the proposed schemes.

5.7.9.1 Joint T-SB6

The interaction between the various elements of this strengthening scheme needs to be described in detail. Before yielding, the GFRP sheets and the beam bottom bars shared the tensile and compressive forces developed in the section. The experimental data showed that the GFRP sheets carried most of the forces, as shown in Figure 5-24a and b. The forces in the composite sheets were transmitted to the column through the resin

layer. As yielding of beam top bars was approached, the interaction between the steel angle and the beam reinforcement bars became apparent. Bending of the angle, due to the downward movement of the beam, produced a tensile force in the reinforcement bars instead of the expected compression force. The tensile strain of the bars gradually increased while pulling the joint down until the bars yielded at a DDF of 4.0. Figure 5-24a shows the strain in the bars up to a DDF of 3.0 due to the failure of strain gauges after yielding onset.

When the joint was pushed up, the bottom steel bars were strained in tension as expected. The tensile strain in the reinforcement bars gradually decreased until it turned to compression at a DDF of 2.0, then it kept increasing until the bars yielded in compression at a DDF of 5.0. The angle vertical leg was bent in the direction of the tensile force in the composite sheets. A consequent tensile force in the top tie rod and compressive force in the bottom tie rod were developed. The deformation of the steel angle leg was resisted by the bolts welded to the beam bottom bars. Therefore, a compression force was created in the bars instead of the expected tensile force. The forces in the tie rods were transmitted to the beam-column joint by bearing.

Debonding of the composite sheets from the column face occurred at a DDF of 2.0. Therefore, the forces in composite sheets force were transmitted to the column through the tie rods. When pushing the beam up, the tensile forces developed in the composite sheets were resisted by a tensile force in the top tie rod and a compressive force in the bottom rod. When pulling the beam down, the steel angle was bent and caused compressive forces in the top and bottom tie rods as shown in Figure 5-24c and d.

A gradual increase in the strain of the top external tie rod was recorded until it yielded at a DDF of 4.0.

5.7.9.2 Joint T-SB7

Although the design of the tying mechanism of the beam bottom bars was based on transferring the forces in beam bottom bars; as tension in the tie rods; the recorded behaviour was found to be more complex. While pulling the beam down, the bottom reinforcement was anchoring into the joint, transferring its load by bearing at the bar tip and by bond along the anchorage length. So, there was no need for the anchoring ties in the negative loading direction. However, due to the bending of the reinforcement bars and consequently bending of the tie rods, a tension force in the top rod and compression force in the bottom rod developed, as shown in Figure 5-25a and b. These forces caused a resisting moment which contributed to the beam moment capacity. Whereas the tension force was resisted by bearing against the column backside, the compression force was resisted by friction between the rod threads and the bearing plate hole circumference. This was confirmed by the experimental observations where the nuts of the bottom tie rods became loose when pulling down.

When pushing the beam up, the tensile forces of the beam bottom reinforcement were transferred as tension force in the top tie rods. It should be noted that at the end of the pulling-down part of the cycle, the bottom tie rods became loose and therefore could not resist tensile forces until the gap created under the nut was eliminated.

5.8 SUMMARY

In this chapter, the behaviour of five external beam-column subassemblies was discussed and analyzed. The specimens had joint shear strength deficiency and inadequate anchorage length of beam bottom bars. The control joint showed a combined bond-slip and joint shear failure modes with severe strength deterioration, stiffness degradation, and low energy dissipation ability. The other four joints were strengthened using composite sheet jacket, FRP sheets and steel elements. In general, the strengthened joints showed more favourable failure modes. Gradual strength deterioration and stiffness degradation were recoded. The joints showed more energy dissipation capability. The FRP jacket at the joint behaved very well with no debonding and low joint shear deformation. The composite sheets were effective in strengthening the anchorage failure of beam bottom bars provided that the sheets are adequately anchored to prevent the debonding or buckling. The steel bridle used for anchoring the existing steel bars was effective in restoring the joint strength. However, proper attention should be given to the design of the external tie rods to avoid their brittle fatigue fracture under cyclic load.

Table 5-1 Comparison of Shear/Bond joints behaviour

Parameter	T-SB3	T-SB3R	T-SB6	T-SB8	T-SB7
Yield displacement (mm)	20.0*	25.0	26.5	30.0	26.0
Experimental yield load (kN)	-- --	-- -110.0	-- -114.5	+125.3 -131.5	+110.0 -112.1
Experimental ultimate load (kN)	+61.4 -92.1	+108.9 -127.4	+109.1 -131.3	+152.0 -131.5	+120.3 -127.9
Theoretical yield load (kN)	100.90	97.60	96.41	95.81**	95.81
Theoretical ultimate load (kN)	125.93	124.61	124.67	128.74**	128.74
Displacement ductility level	2.5	3.0	7.0	3.0	6.0
Concrete tensile stress (MPa)	$0.35\sqrt{f_c'}$	$0.53\sqrt{f_c'}$	$0.72\sqrt{f_c'}$	$0.67\sqrt{f_c'}$	$0.94\sqrt{f_c'}$
Bending stiffness at maximum moment	$0.113E_cI_g$ (DDF=1.5)	$0.235E_cI_g$ (DDF=1.0)	$0.110E_cI_g$ (DDF=3.0)	$0.314E_cI_g$ (DDF=1.0)	$0.064E_cI_g$ (DDF=3.0)

* Assumed during the test, as bars did not yield.

** Estimated values without considering the rehabilitation scheme.

Table 5-2 Shear resistance of concrete as a fraction of $\sqrt{f_c^{'}}$ for beams

DDF*	T-SB3	T-SB6	T-SB8	T-SB7
-7	---	0.049	---	----
-6	---	0.066	--	0.114
-5	---	0.1035	---	0.078
-4	---	0.134	---	0.057
-3	---	0.129	0.134	0.078
-2	0.092	0.21	0.159	0.129
-1	0.105	0.185	0.196	0.155
1	0.109	0.143	0.208	0.211
2	0.055	0.046	0.028	0.118
3	---	0.024	0.019	0.098
4	---	0.002	---	0.099
5	---	0	---	0.024
6	---	0	---	---
7	---	0	---	---

* The negative sign represent the part of the cycle where the beam tip is pulled down.

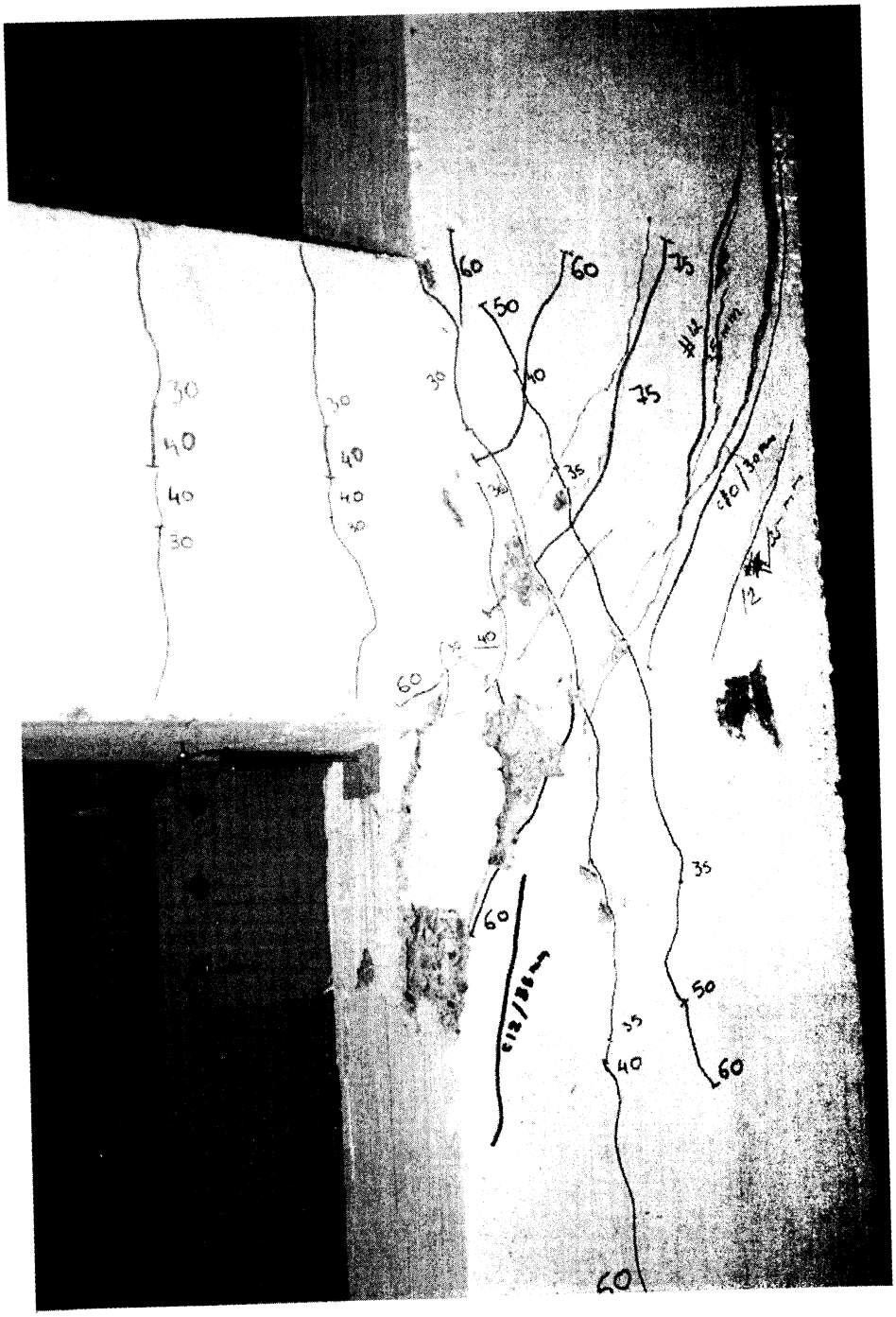

Figure 5-1 Failure pattern of joint T-SB3

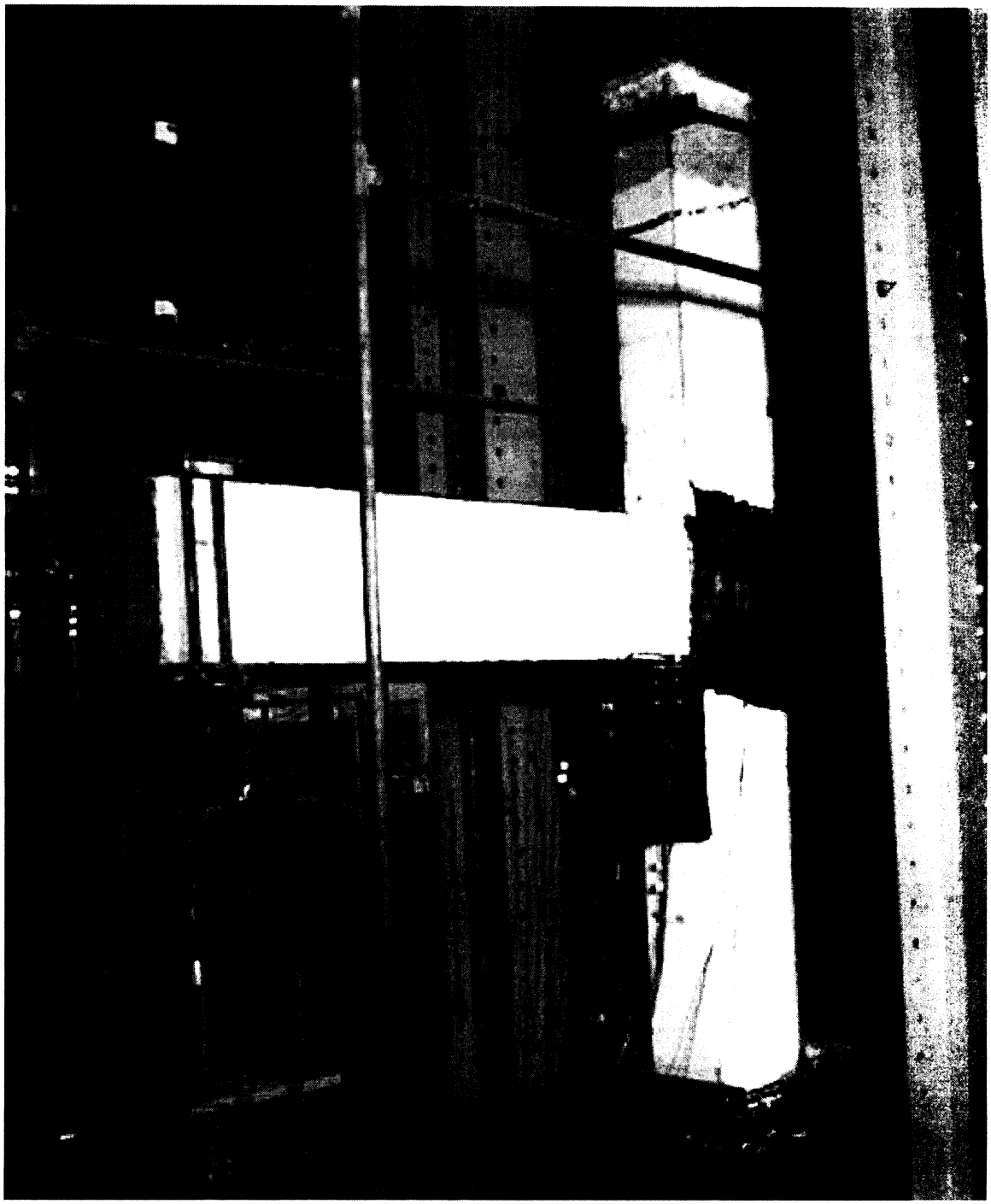

Figure 5-2 Strengthening of joint T-SB3R

Figure 5-3 Buckling of the composite sheets of joint T-SB3R

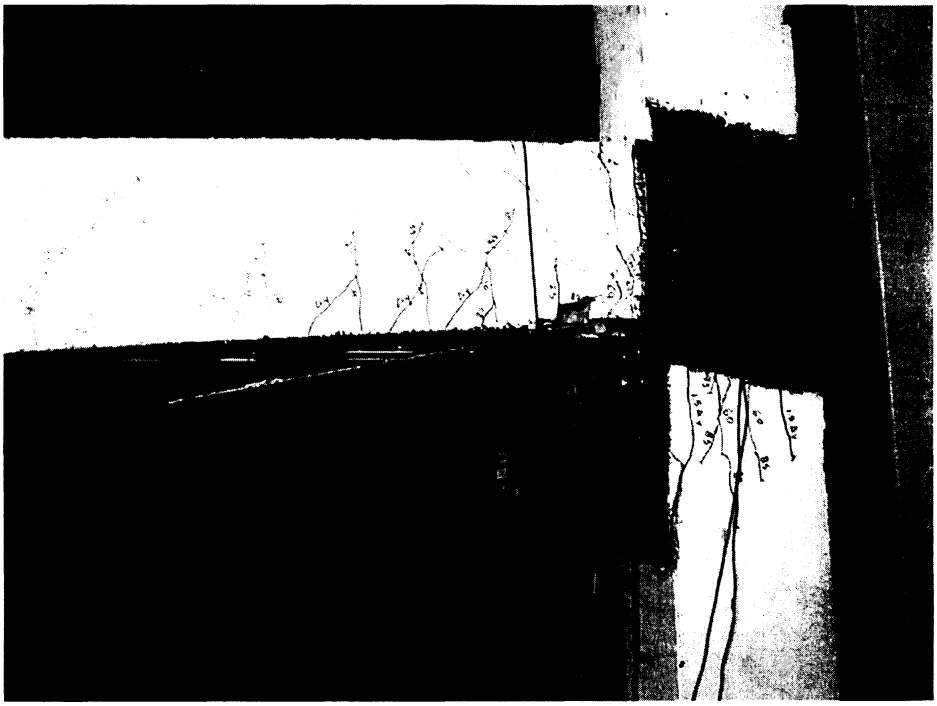

Figure 5-4 Debonding of the GFRP sheets of joint T-SB3R

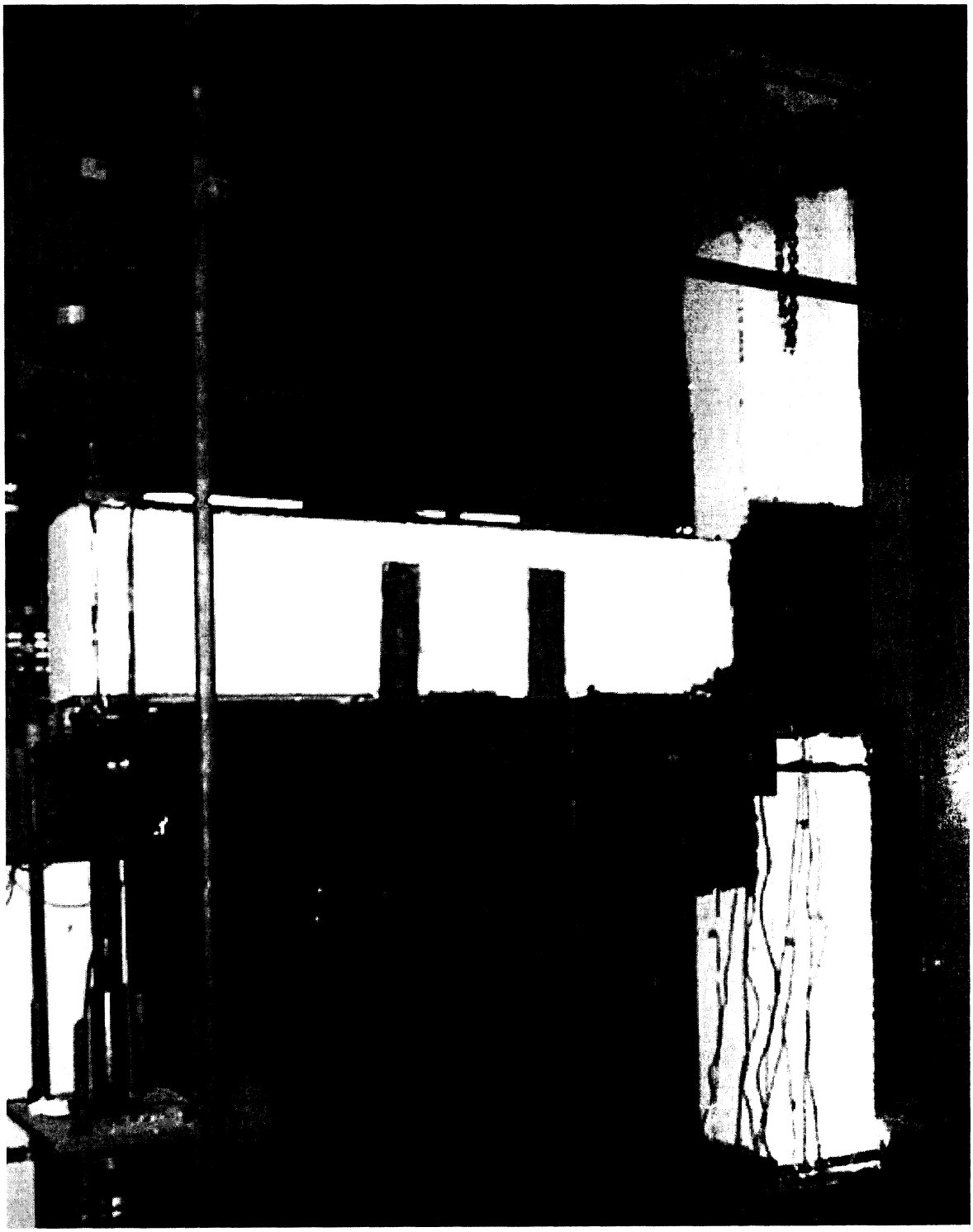

Figure 5-5 Strengthening of joint T-SB6

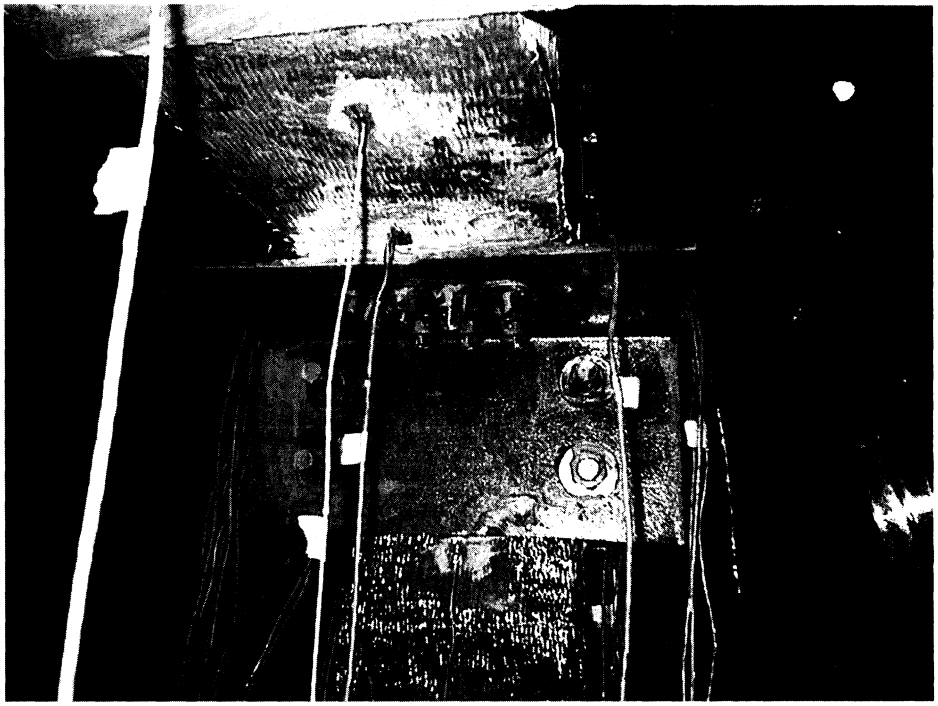

Figure 5-6 Steel angle attached to joint T-SB6

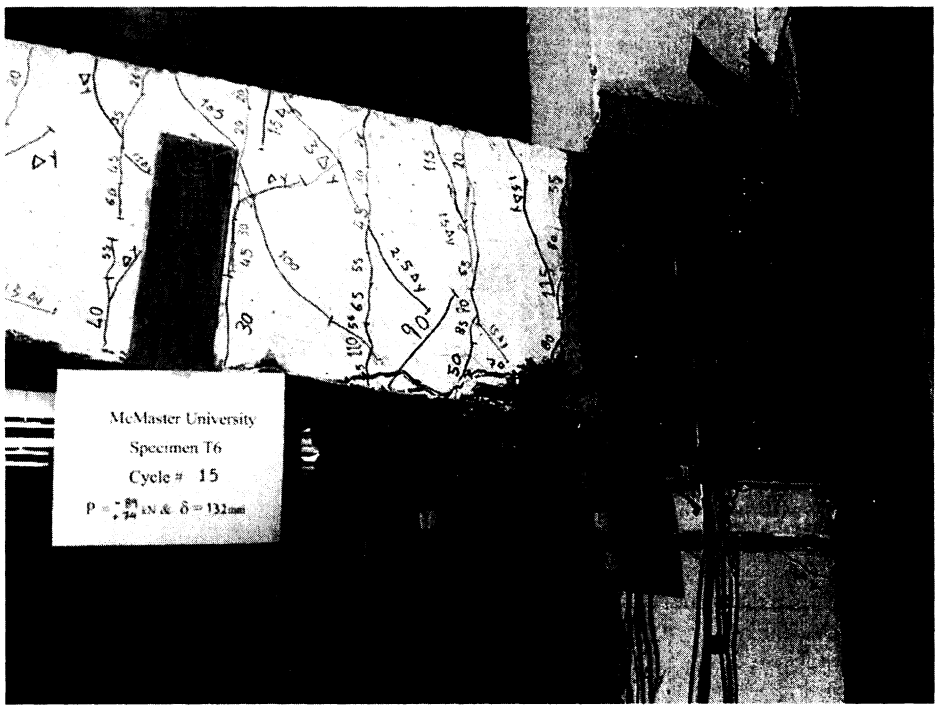

Figure 5-7 Deforming of the steel angle joint T-SB6

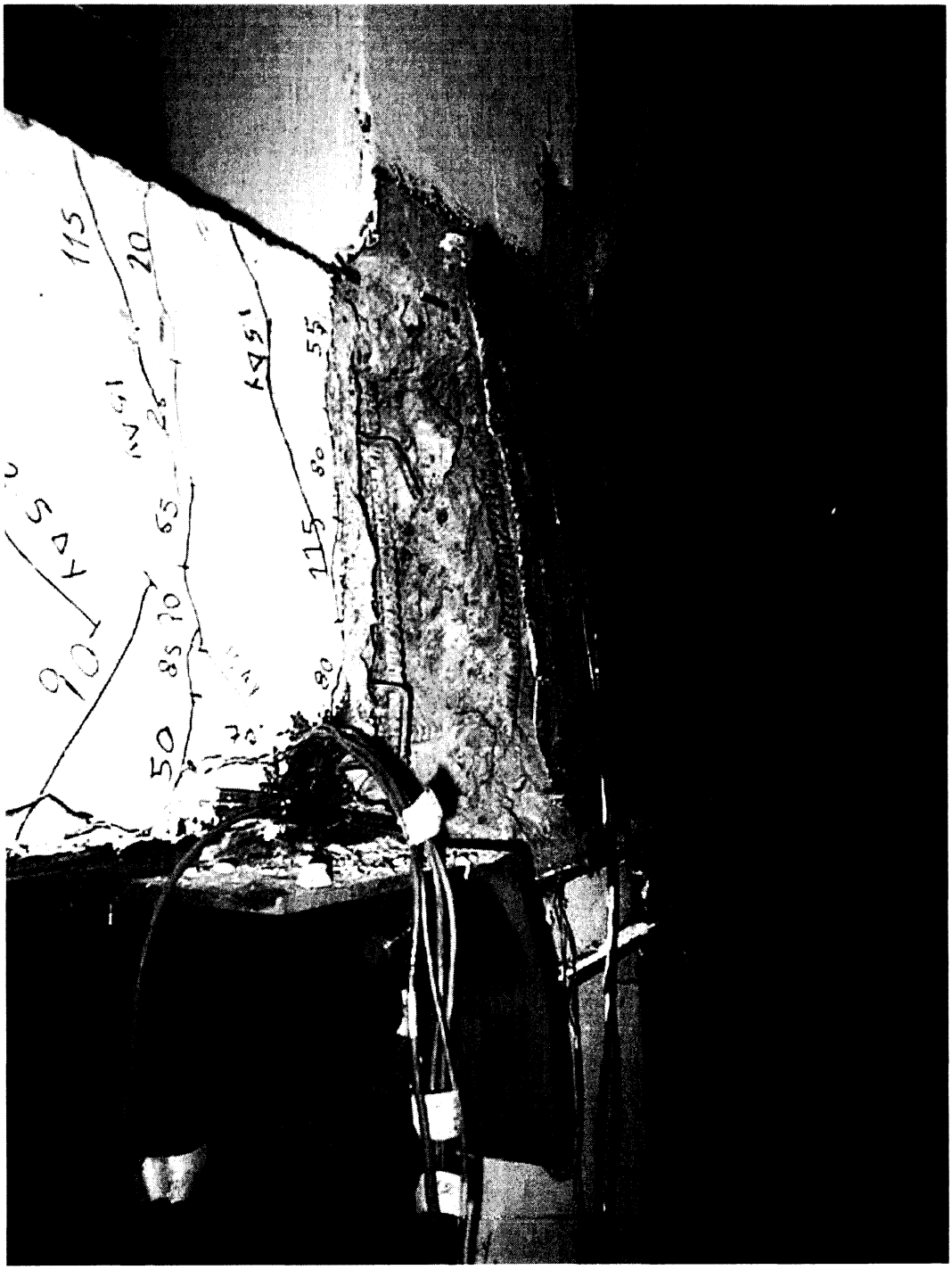

Figure 5-8 Failure pattern of joint T-SB6

Figure 5-9 Steel rods installed to joint T-SB8

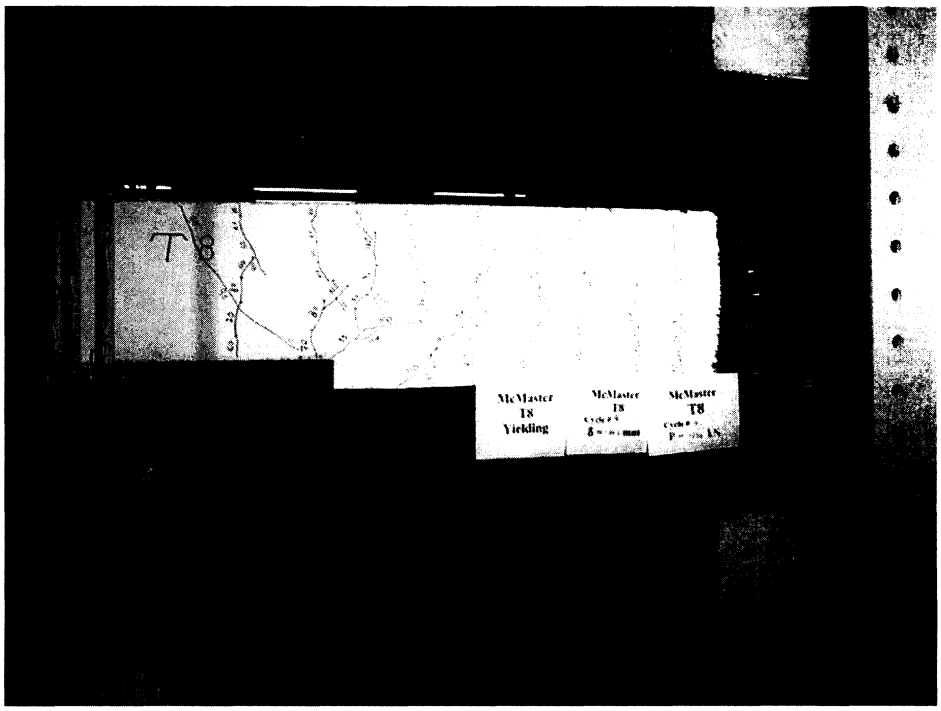

Figure 5-10 Strengthening of joint T-SB8

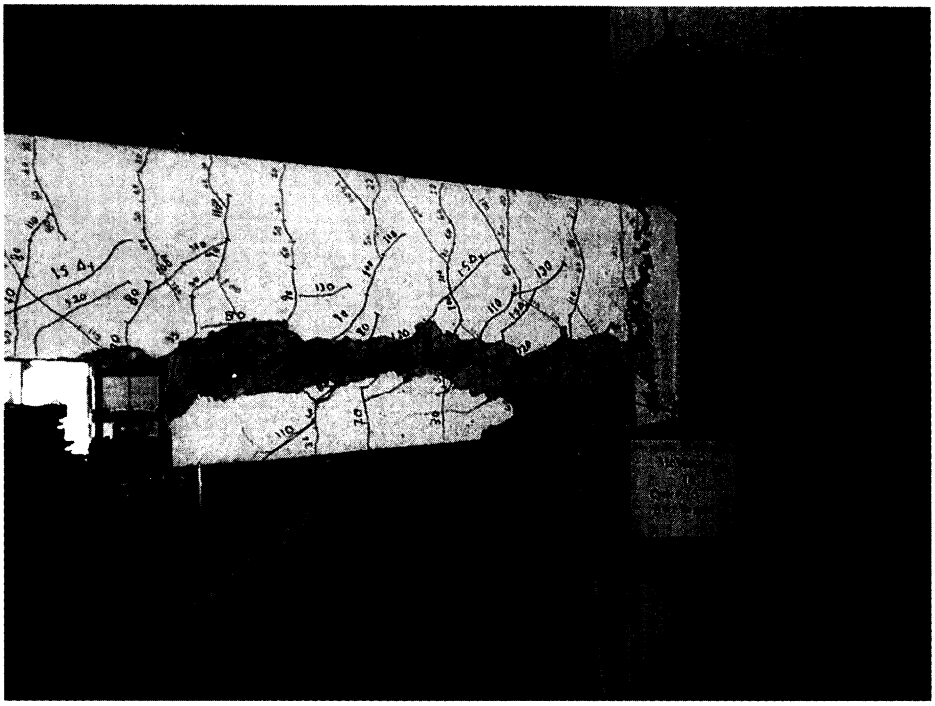

Figure 5-11 Failure pattern of joint T-SB8

Figure 5-12 Anchoring of the beam bottom reinforcement of joint T-SB7

Figure 5-13 Bending of the tie rods in positive loading direction of joint T-SB7

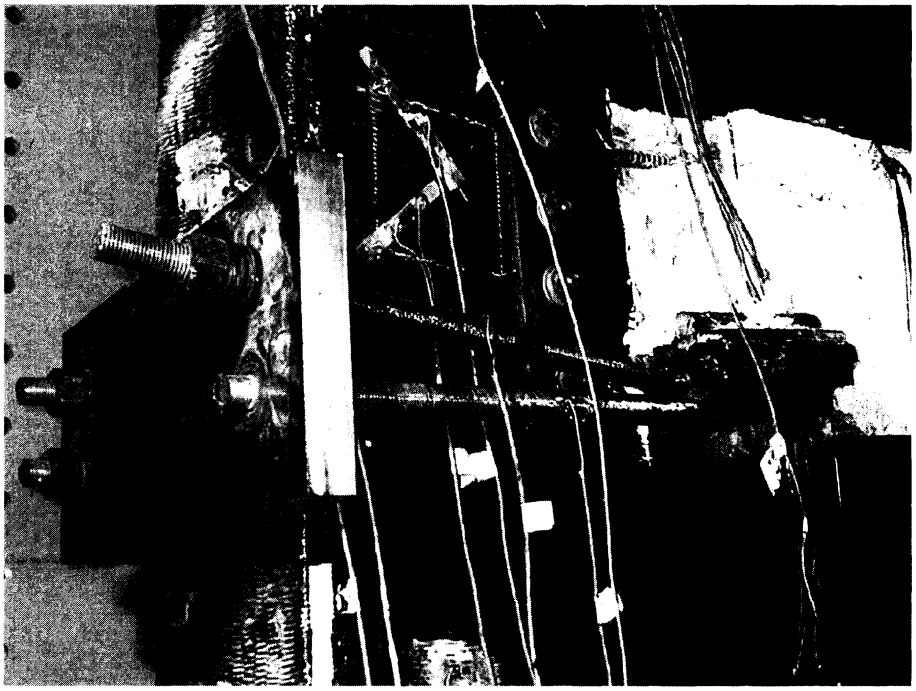

Figure 5-14 Failure of the external tie rods of joint T-SB7

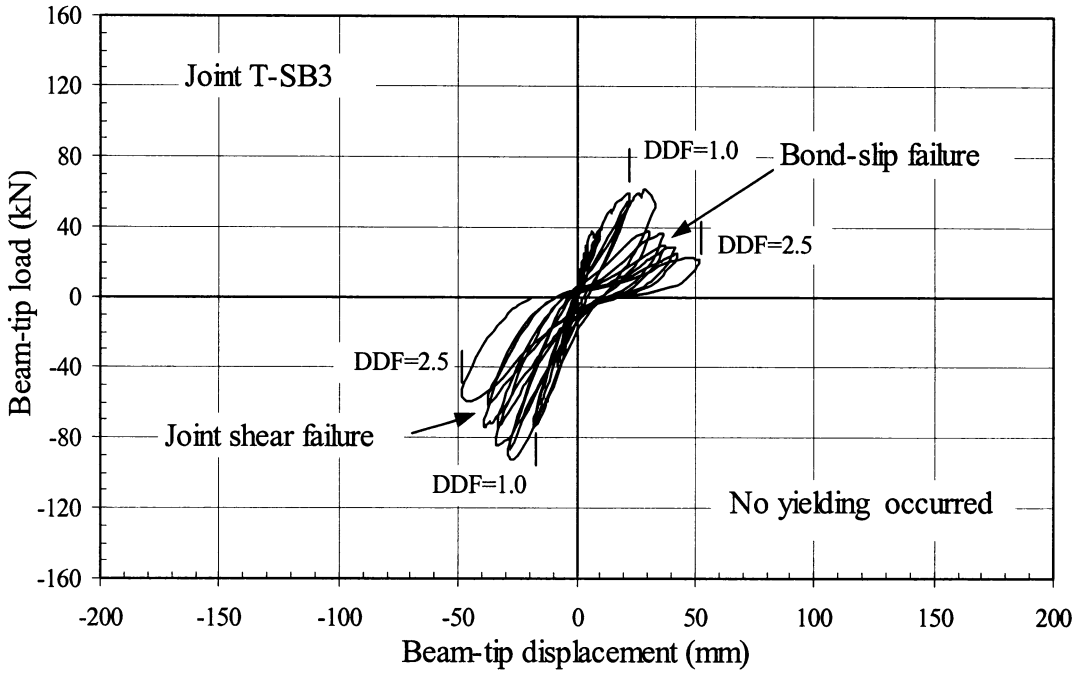

Figure 5-15a Beam-tip load-displacement relationship of joint T-SB3

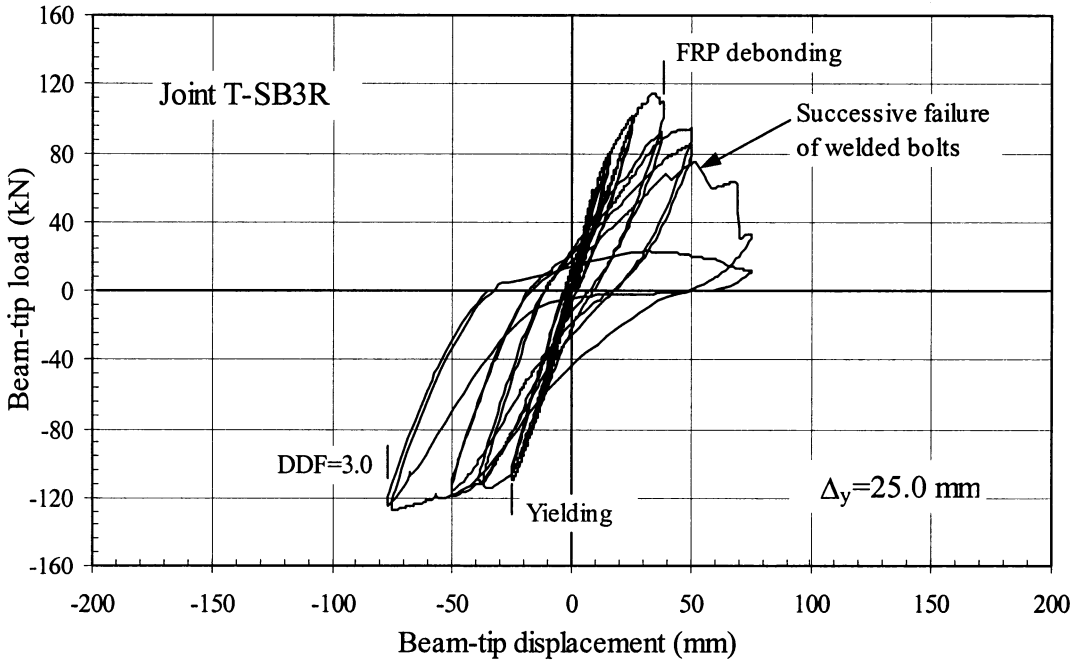

Figure 5-15b Beam-tip load–displacement relationship of joint T-SB3R

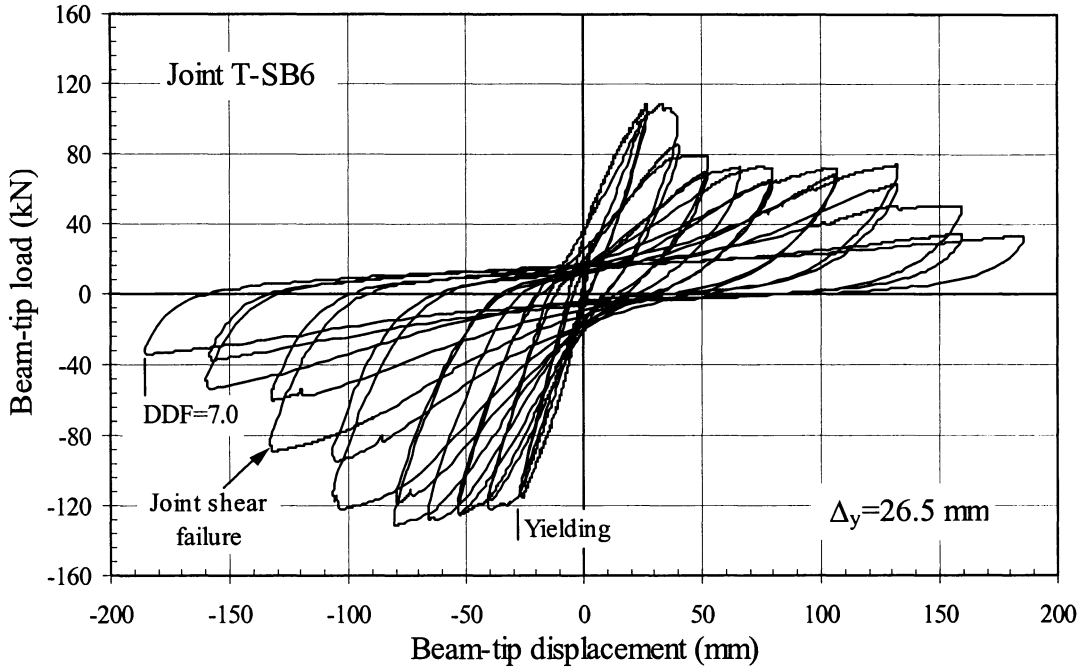

Figure 5-15c Beam-tip load–displacement relationship of joint T-SB6

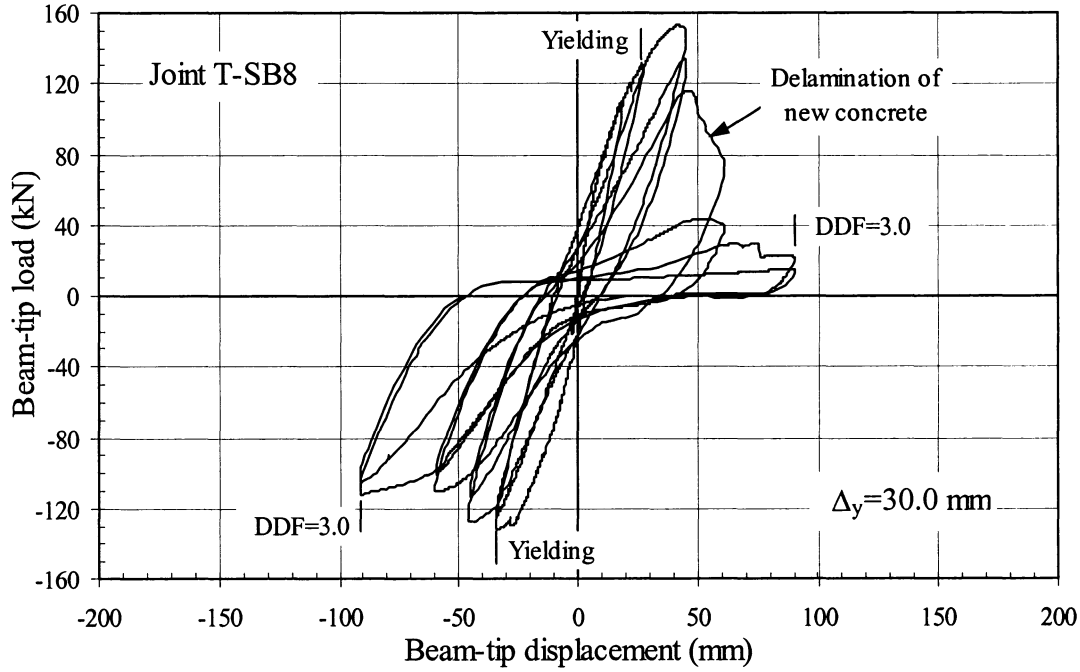

Figure 5-15d Beam-tip load–displacement relationship of joint T-SB8

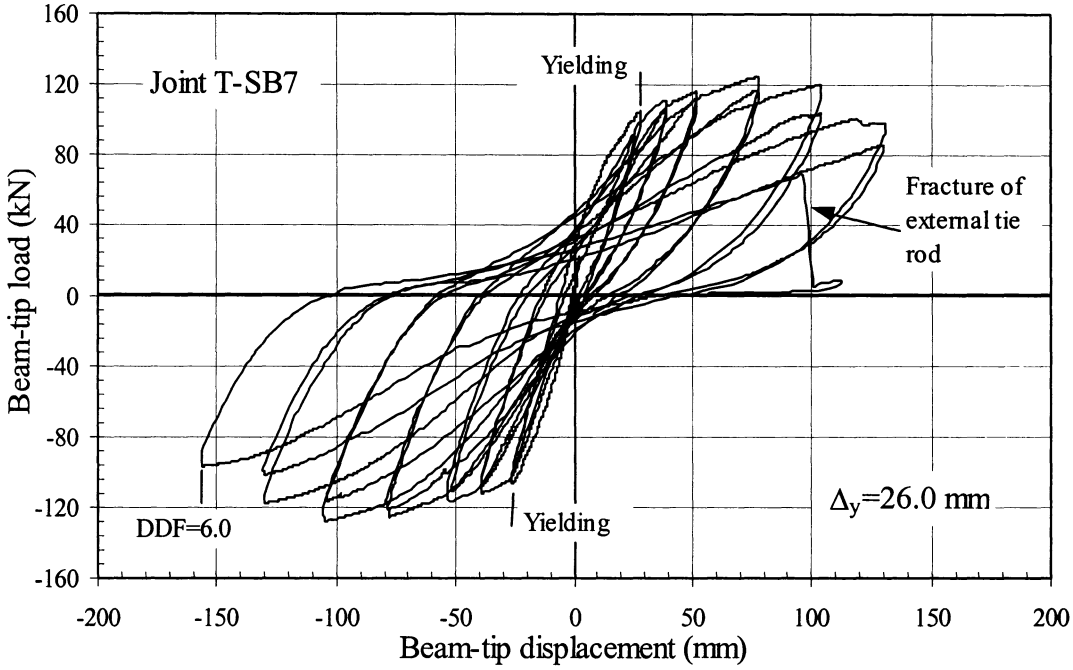

Figure 5-15e Beam-tip load–displacement relationship of joint T-SB7

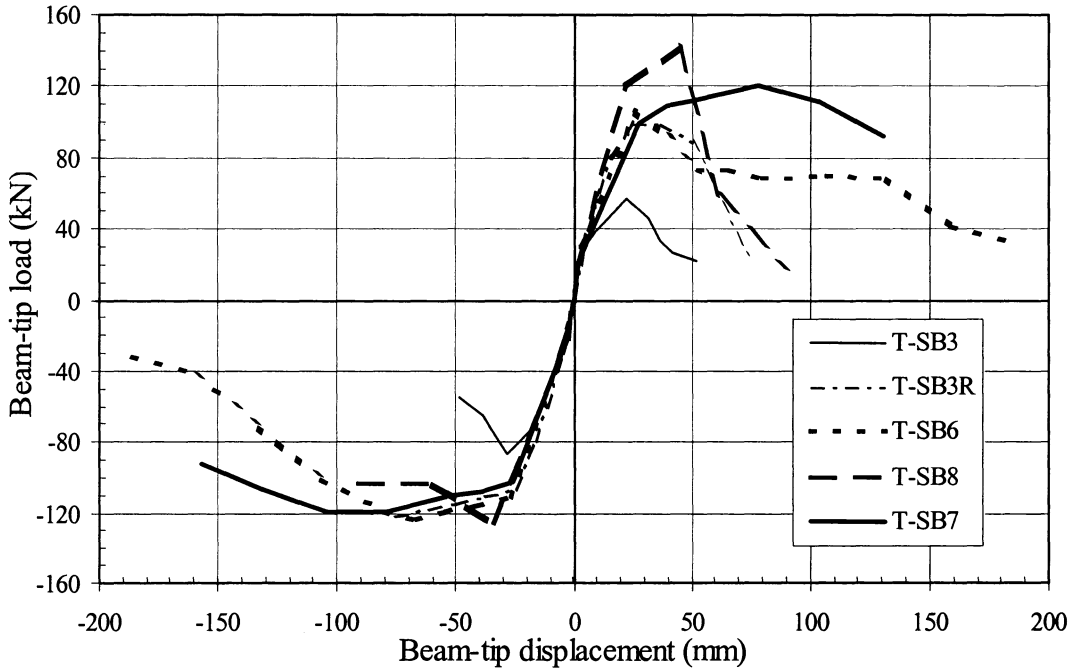

Figure 5-16 Envelopes of the hysteretic loops of the joint group T-SB

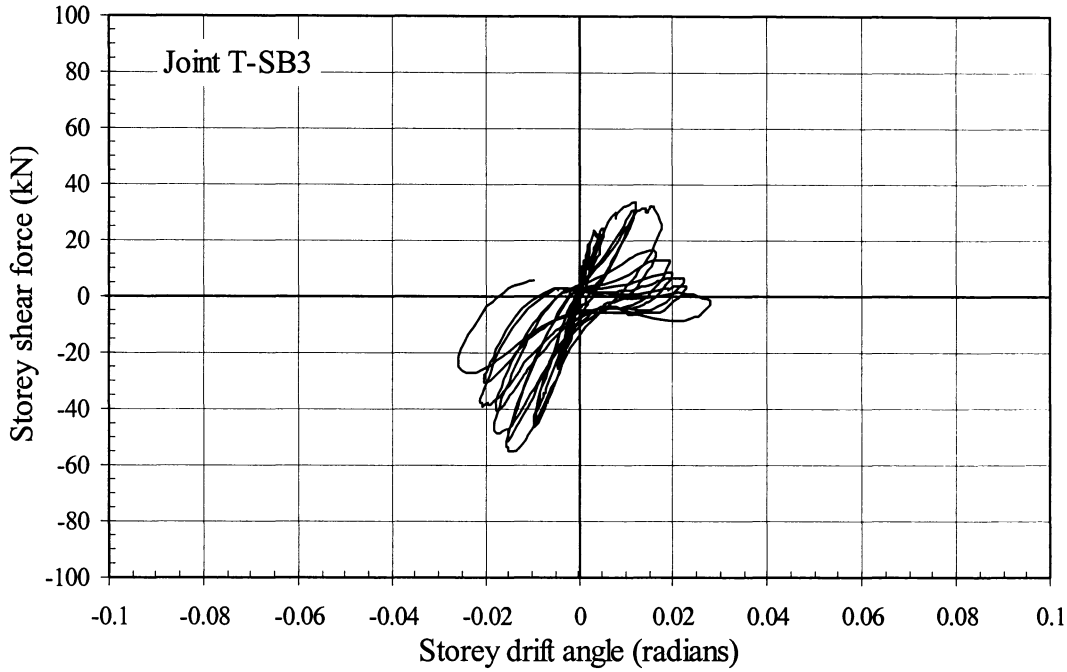

Figure 5-17a Storey shear-drift angle relationship of joint T-SB3

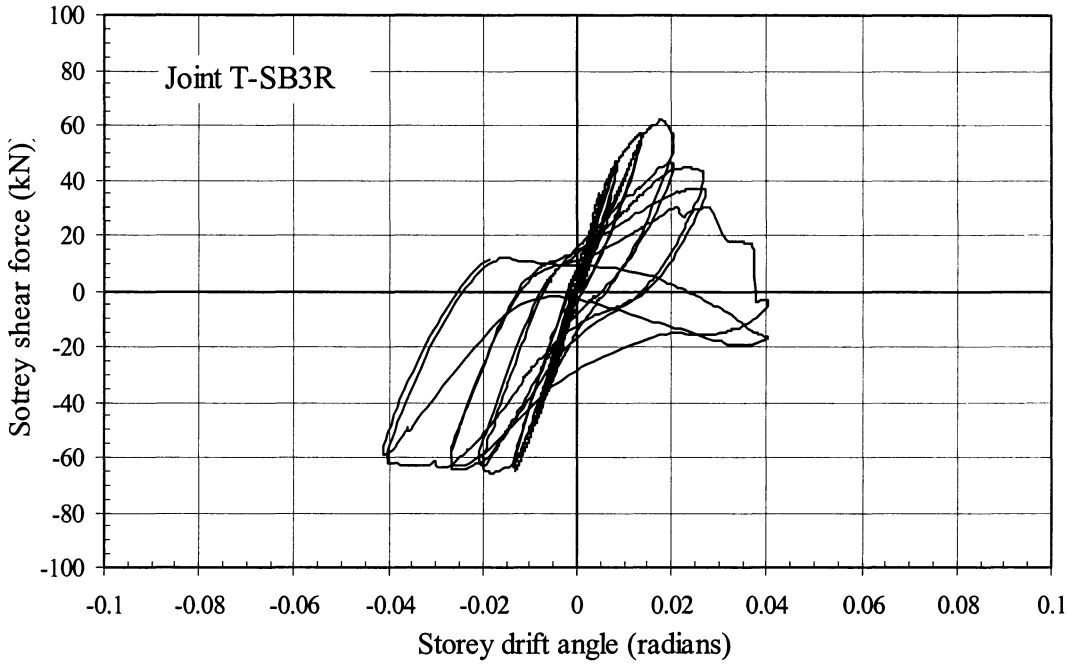

Figure 5-17b Storey shear-drift angle relationship of joint T-SB3R

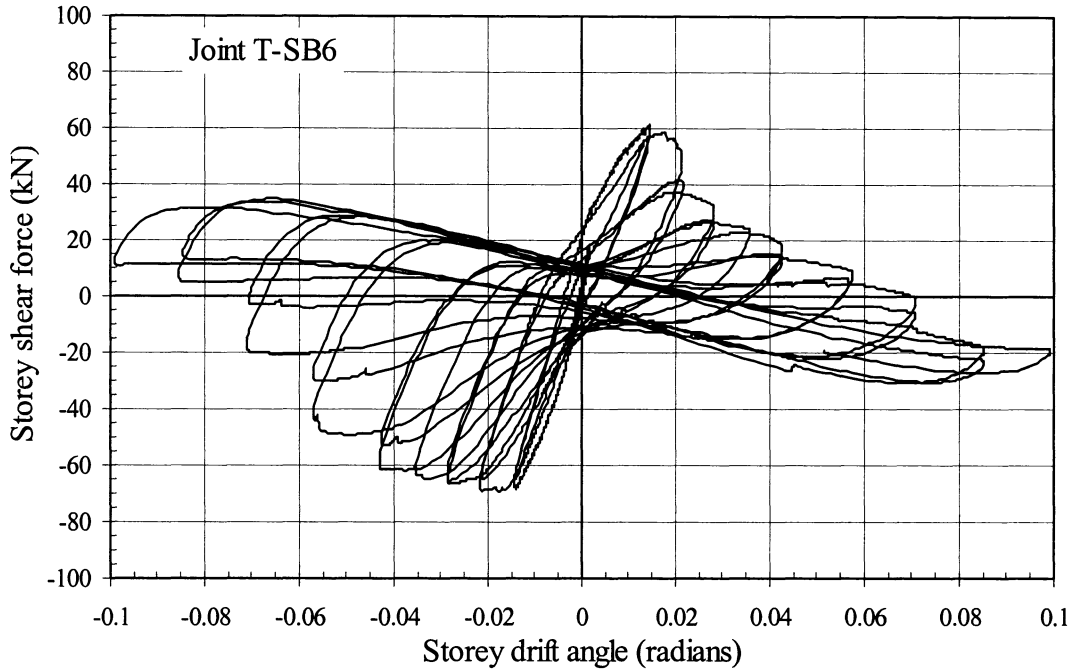

Figure 5-17c Storey shear-drift angle relationship of joint T-SB6

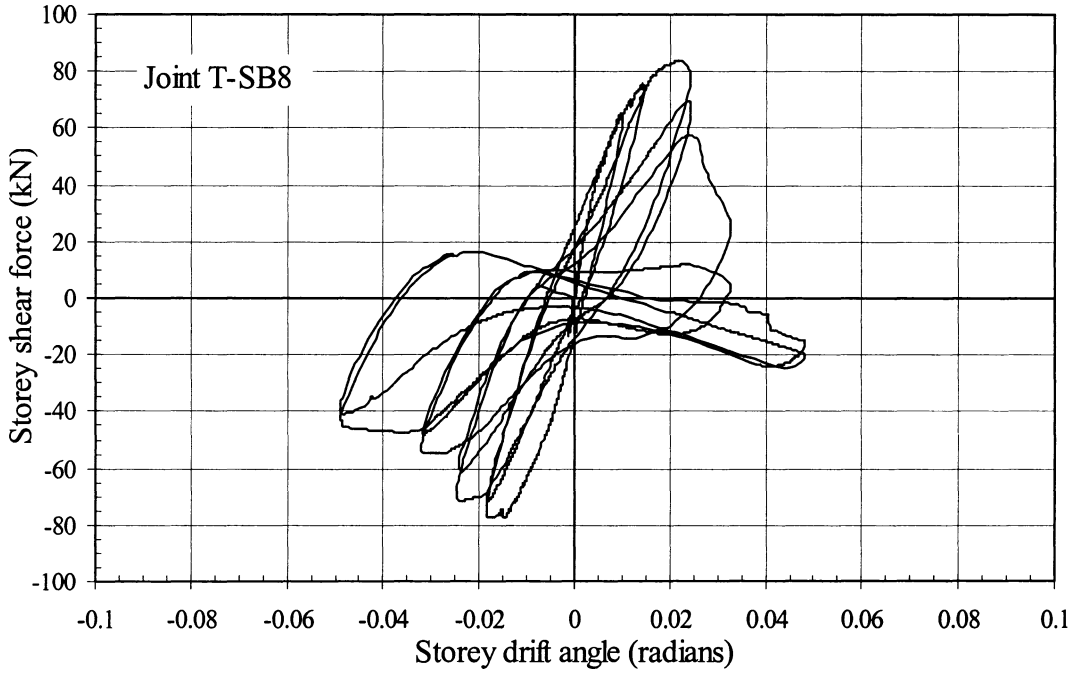

Figure 5-17d Storey shear-drift angle relationship of joint T-SB8

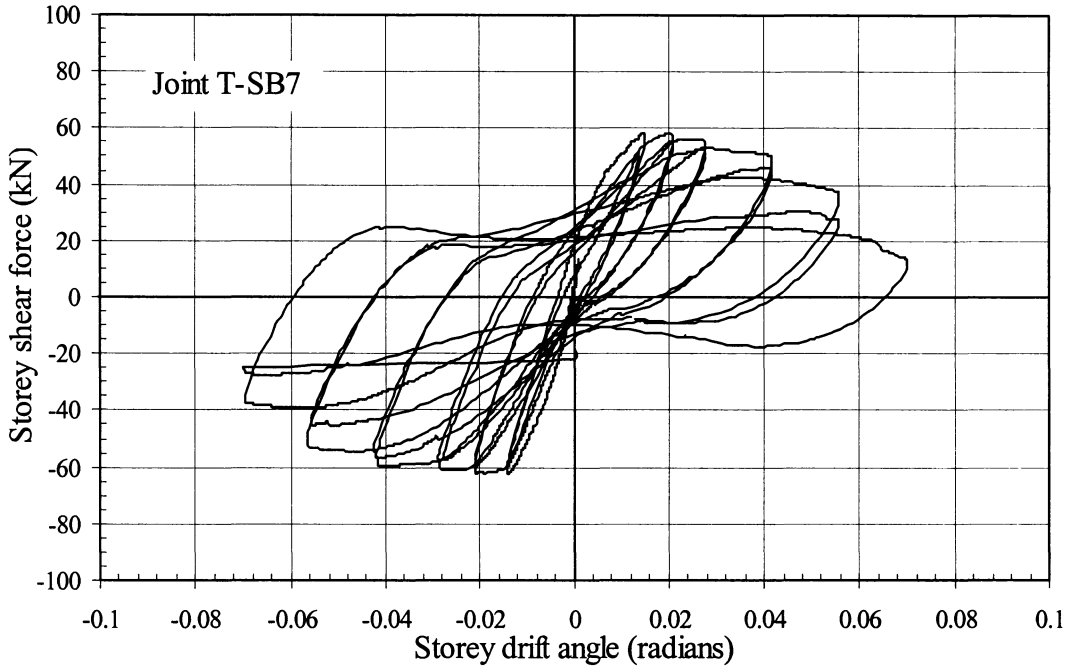

Figure 5-17e Storey shear-drift angle relationship of joint T-SB7

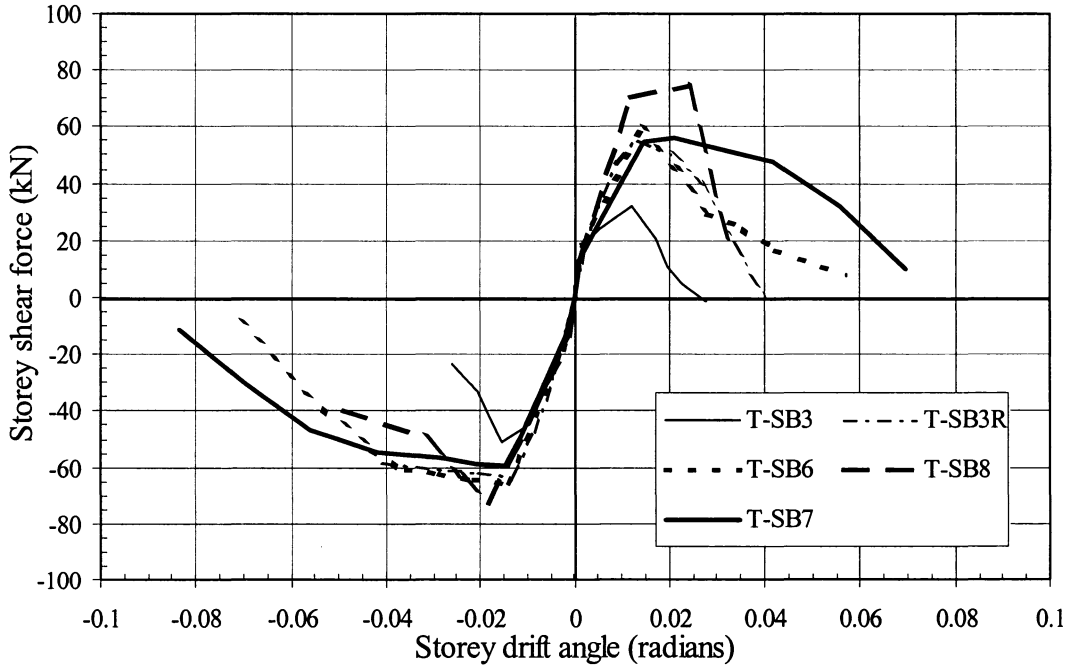

Figure 5-18 Envelopes of storey shear-drift angle relationships of joint group T-SB

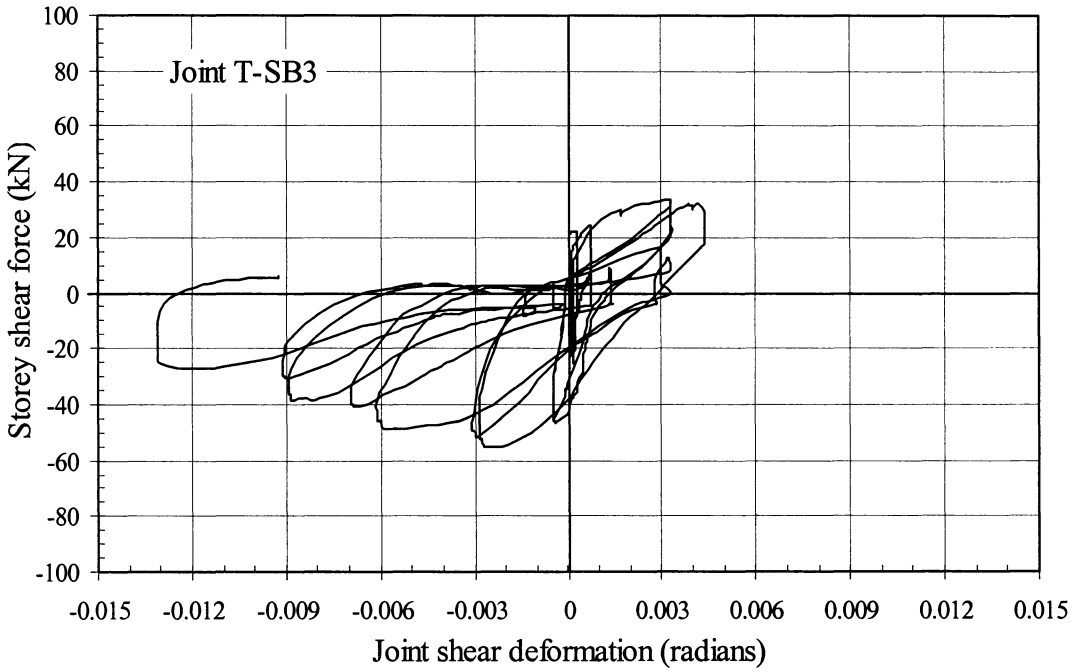

Figure 5-19a Joint shear deformation-storey shear of joint T-SB3

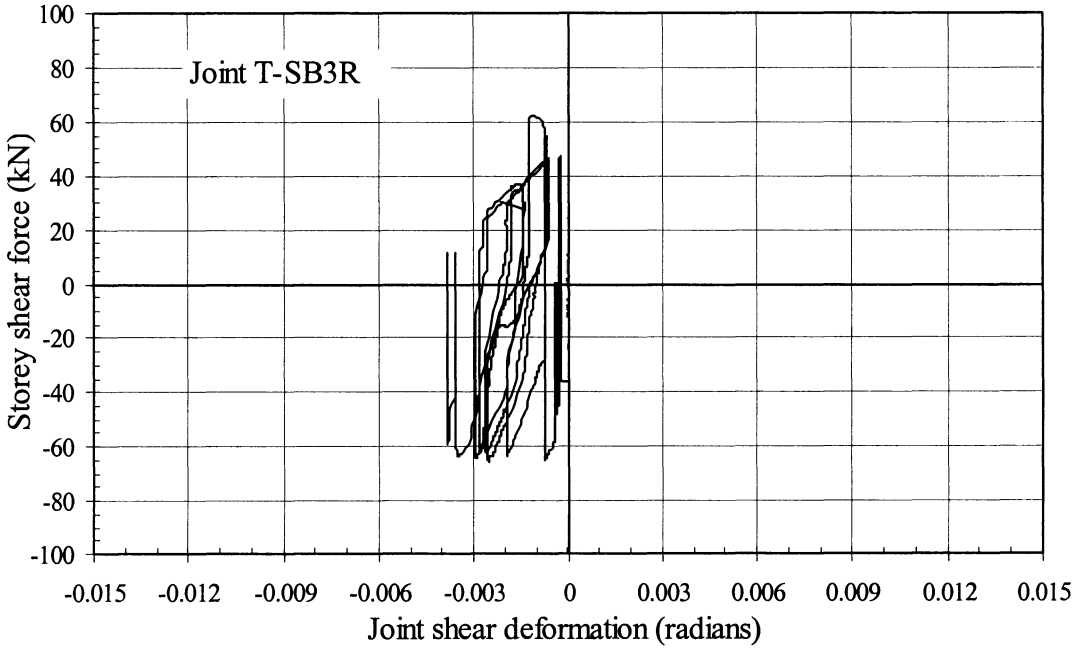

Figure 5-19b Joint shear deformation-storey shear of joint T-SB3R

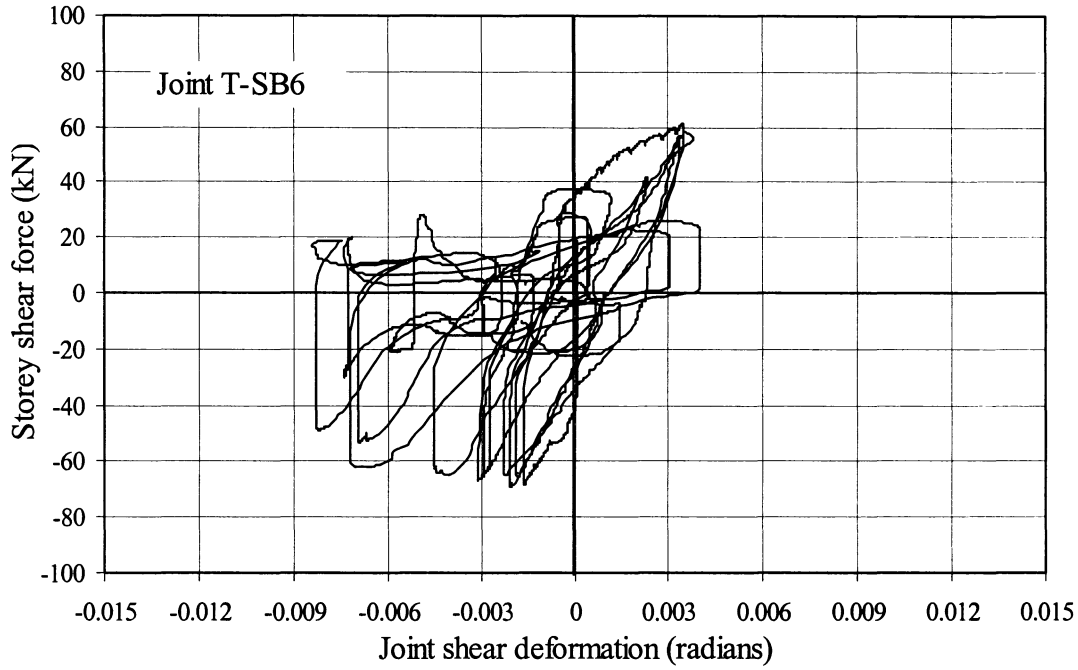

Figure 5-19c Joint shear deformation-storey shear of joint T-SB6

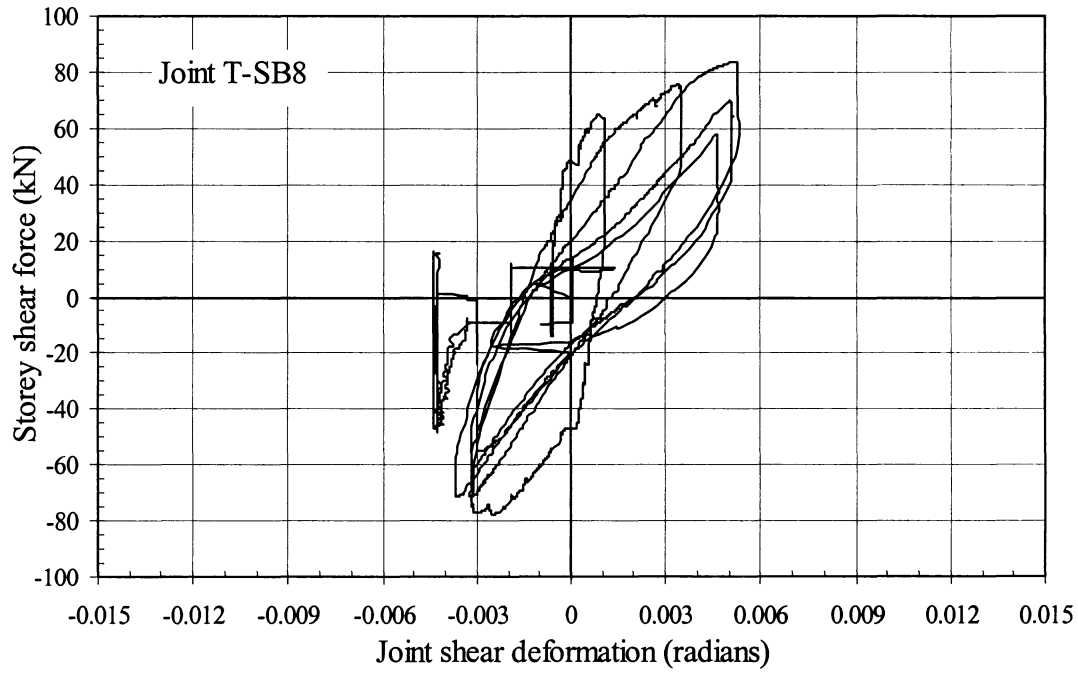

Figure 5-19d Joint shear deformation-storey shear of joint T-SB8

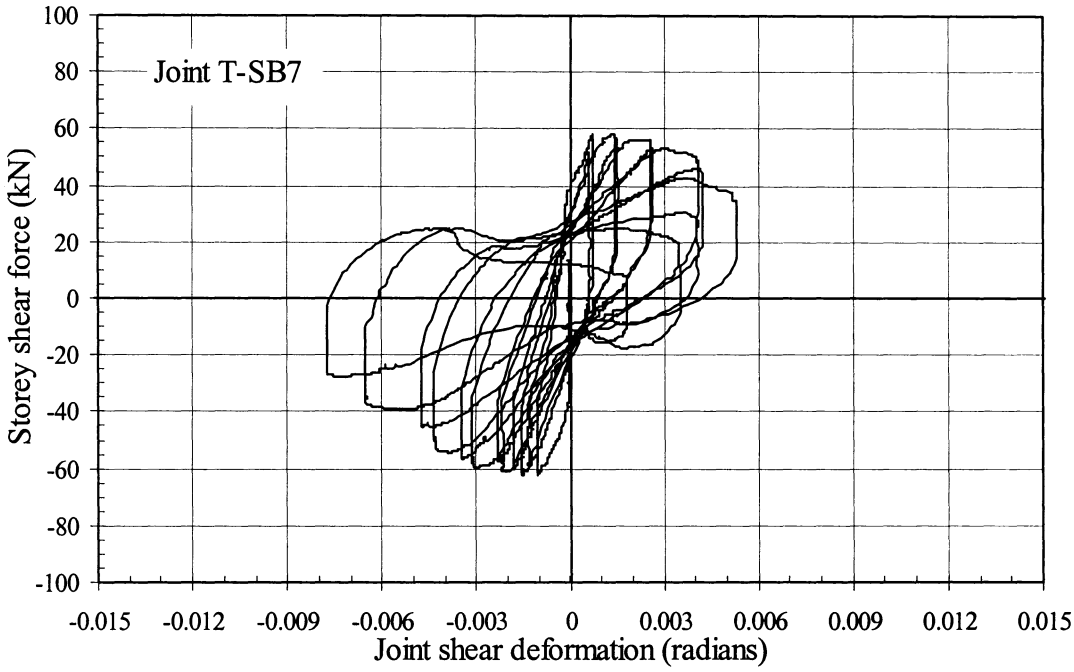

Figure 5-19e Joint shear deformation-storey shear of joint T-SB7

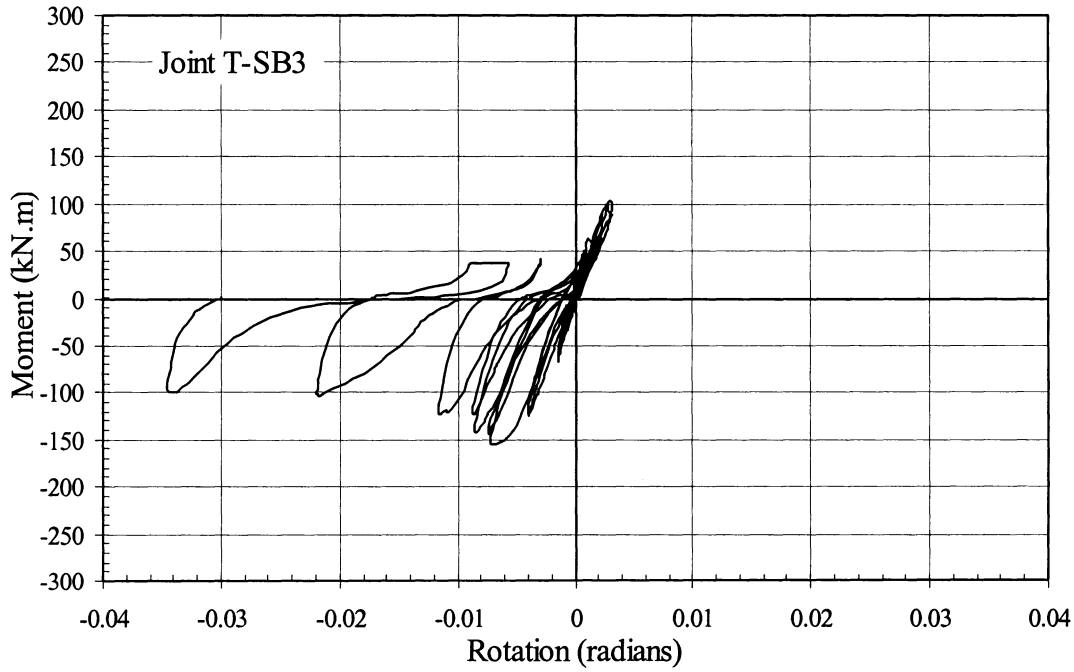

Figure 5-20a Beam moment-rotation at 175 mm from column face of joint T-SB3

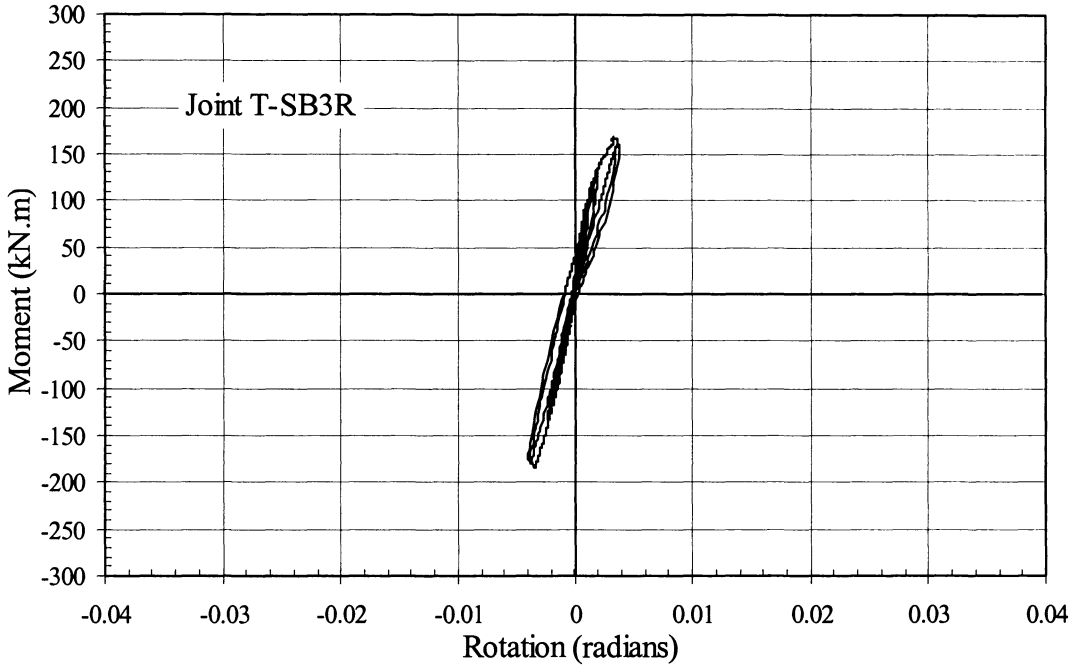

Figure 5-20b Beam moment-rotation at 175 mm from column face of joint T-SB3R

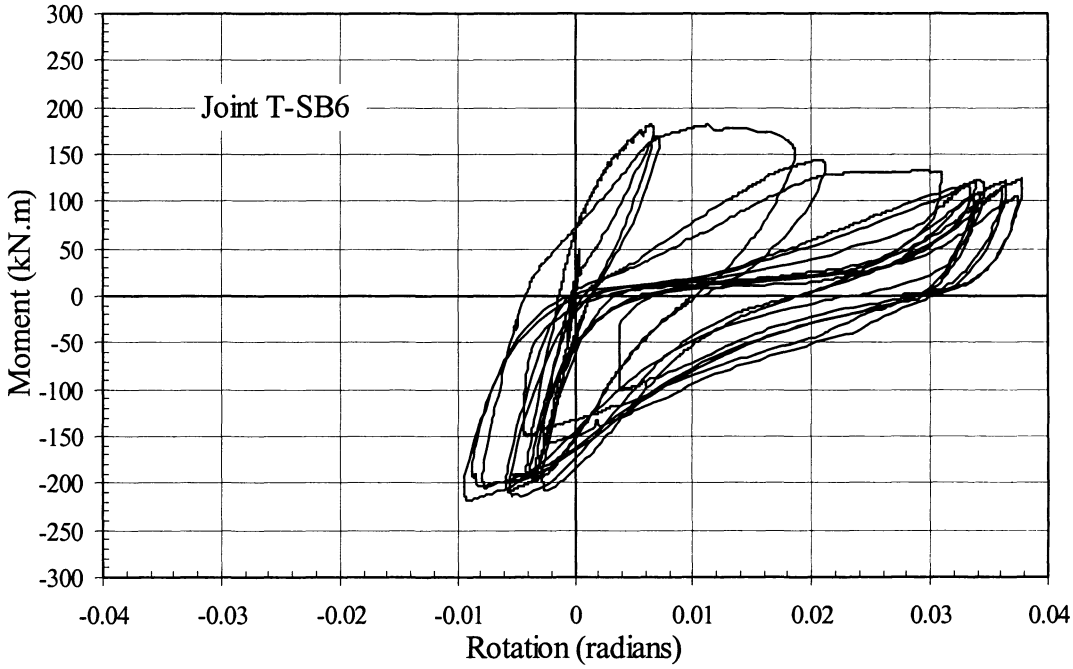

Figure 5-20c Beam moment-rotation at 175 mm from column face of joint T-SB6

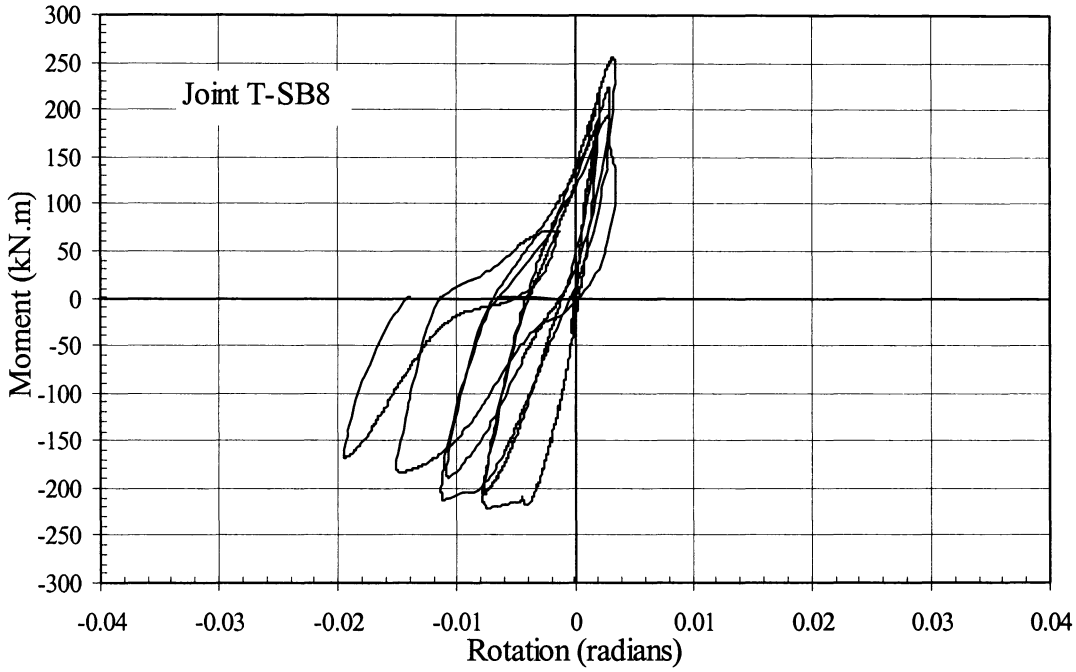

Figure 5-20d Beam moment-rotation at 175 mm from column face of joint T-SB8

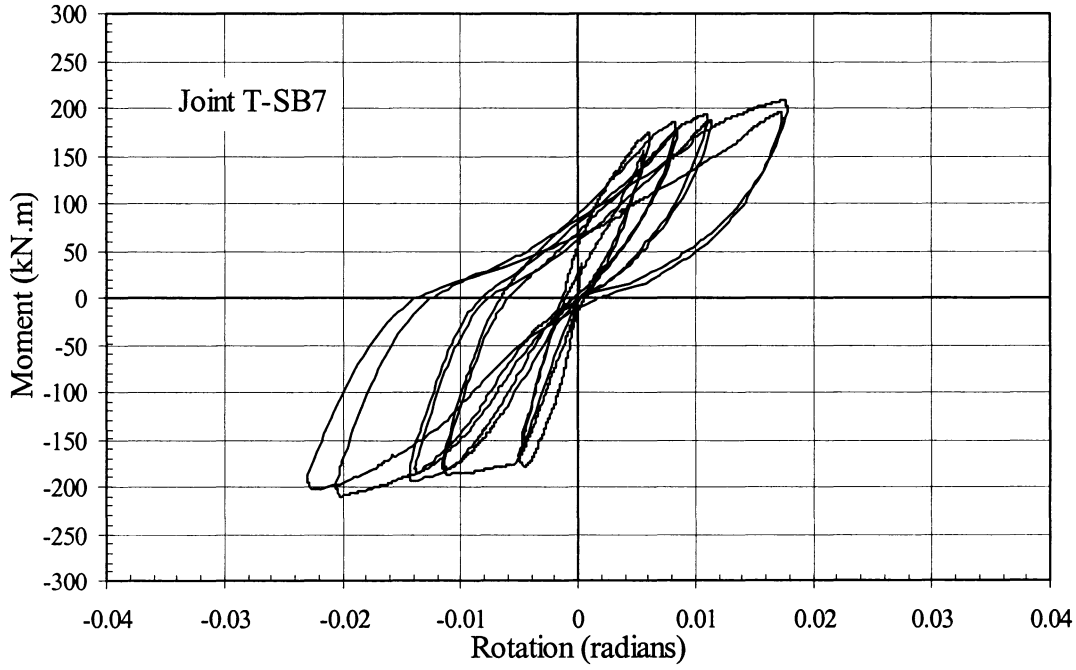

Figure 5-20e Beam moment-rotation at 175 mm from column face of joint T-SB7

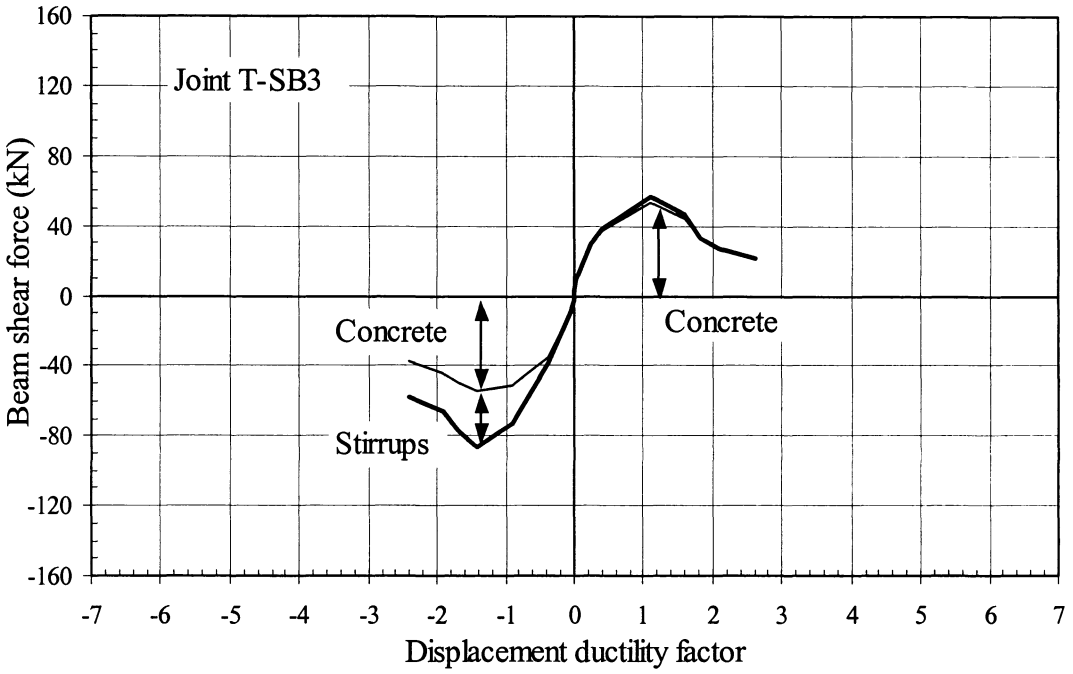

Figure 5-21a Beam shear force resisted by concrete and stirrups of joint T-SB3

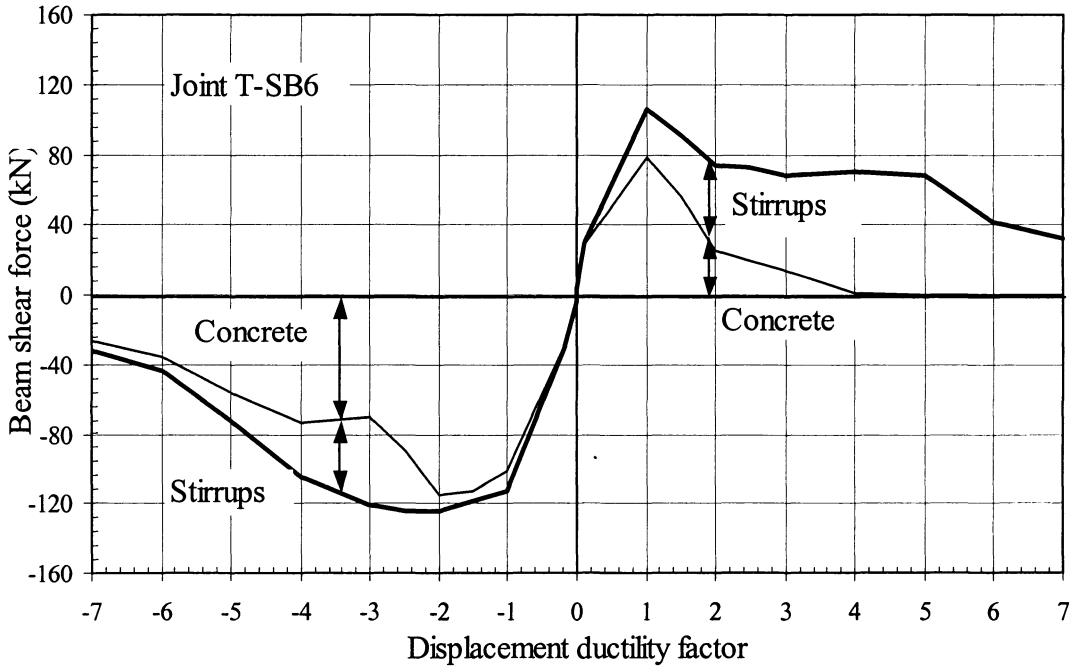

Figure 5-21b Beam shear force resisted by concrete and stirrups of joint T-SB6

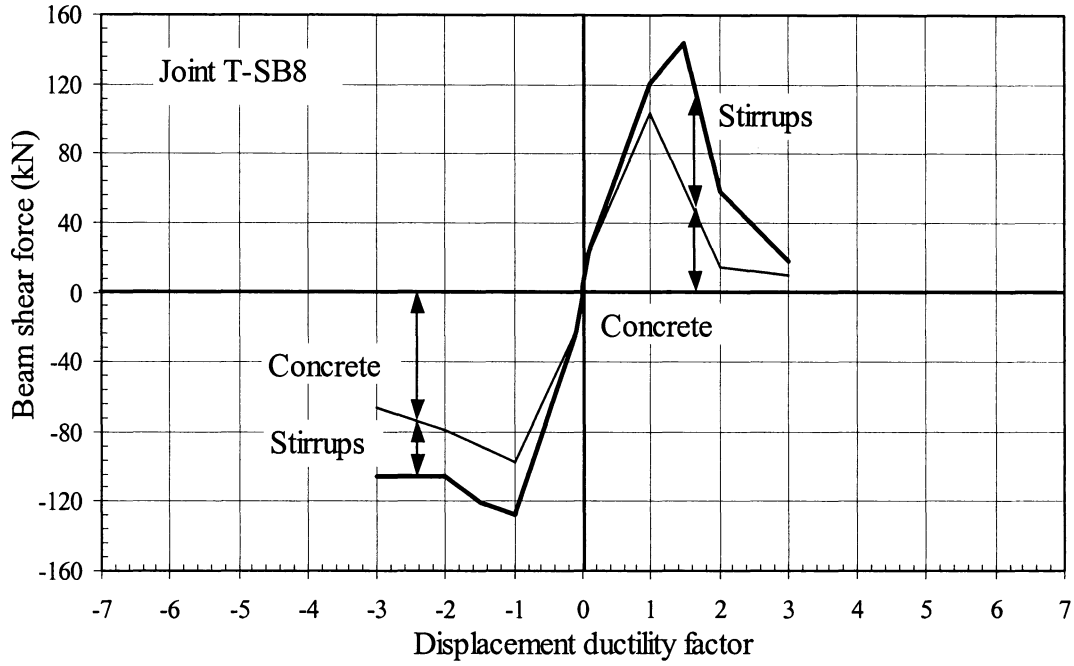

Figure 5-21c Beam shear force resisted by concrete and stirrups of joint T-SB8

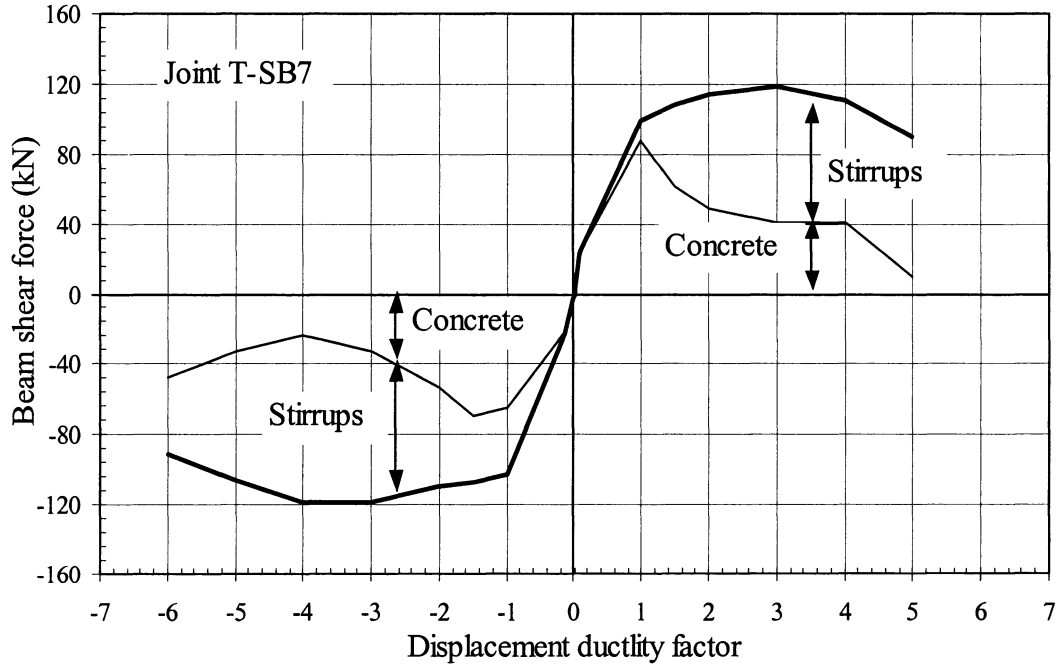

Figure 5-21d Beam shear force resisted by concrete and stirrups of joint T-SB7

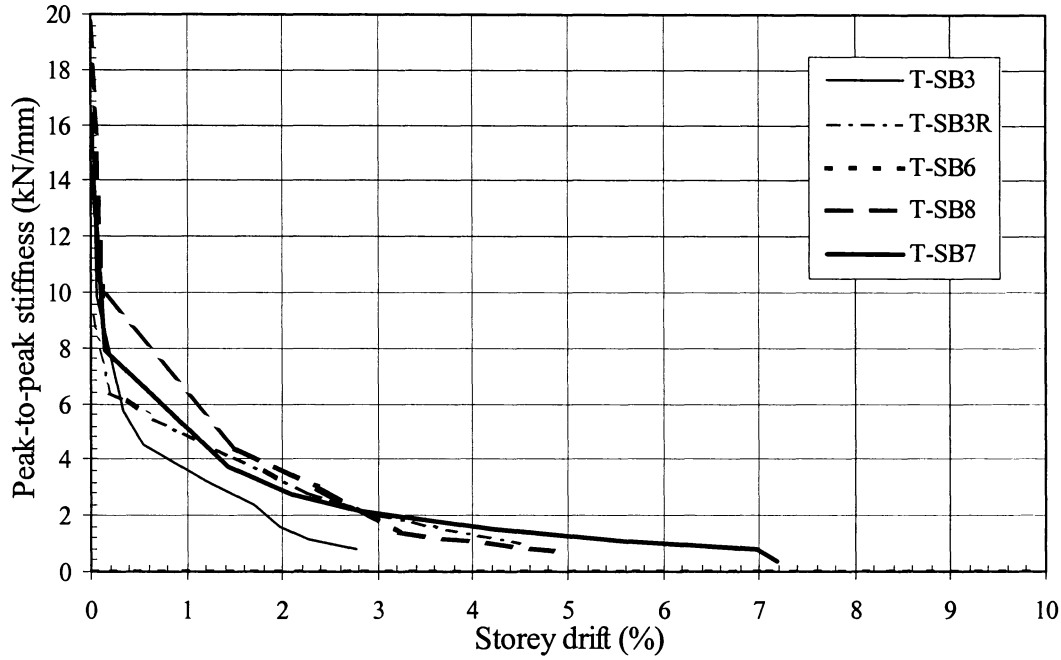

Figure 5-22 Stiffness degradation with storey drift

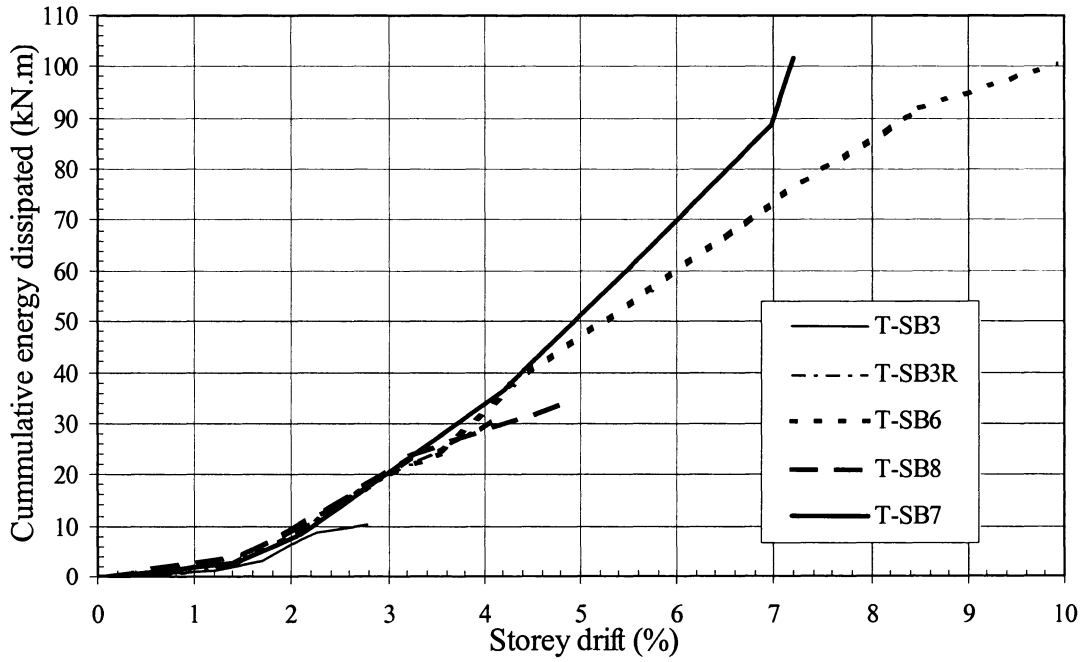

Figure 5-23 Cumulative energy dissipated with storey drift

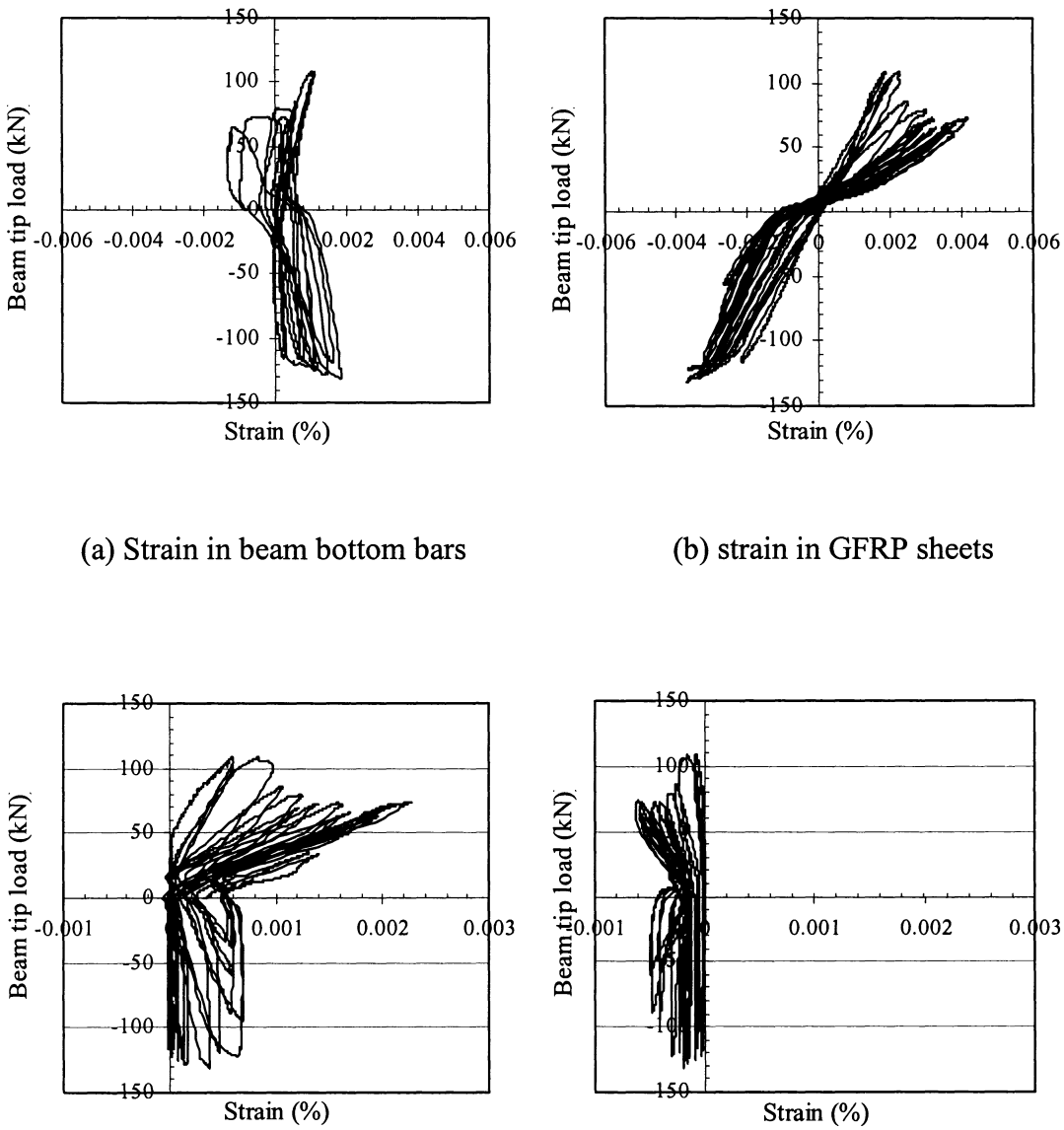

(a) Strain in beam bottom bars

(b) strain in GFRP sheets

(c) Strain in top tie rod

(d) Strain in bottom tie rod

Figure 5-24 Strain in rehabilitation scheme elements of joint T-SB6

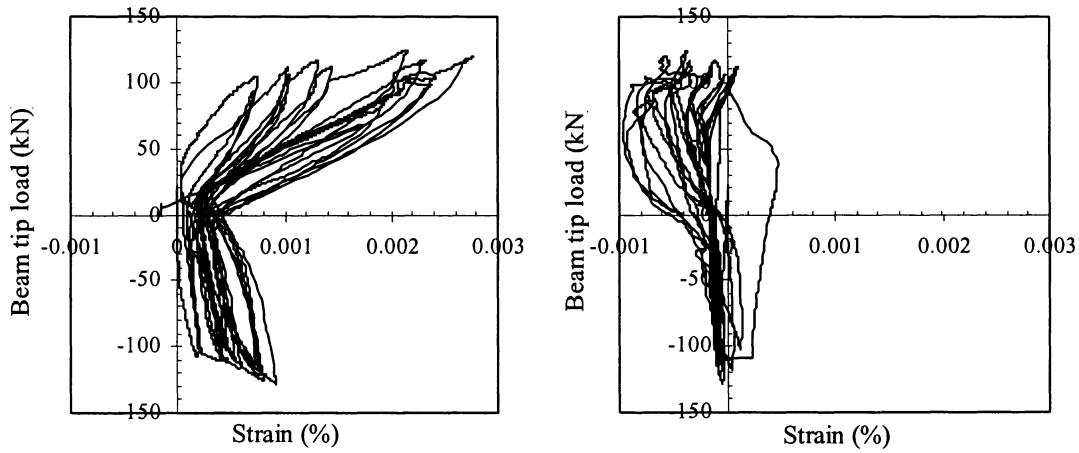

(a) Strain in top tie rod (b) Strain in bottom tie rod

Figure 5-25 Strain in external tie rods of joint T-SB7

This page is intentionally left blank

Chapter 6

MATERIAL MODELS

6.1 INTRODUCTION

The response of concrete structures is determined in part by the response of the concrete and steel materials under different load histories. The nonlinear response is caused by the cracking of concrete in tension, concrete crushing in compression, yielding of the reinforcement and the interaction between the steel and the surrounding concrete or bond-slip behaviour.

In this chapter, constitutive models for concrete under compression or tension loads are proposed. The effect of steel or FRP confinement on concrete behaviour is included. Constitutive relationship of the FRP sheets under compressive or tensile stresses is proposed. A steel model that accounts for the interaction between the reinforcing bars and the surrounding concrete is also proposed.

In the current study, the concept of "*macromodeling*" is adopted. In this type of model, the non-linear behaviour of concrete members will be lumped at the members' ends represented by non-linear springs. The proposed constitutive relationships will be used to predict the monotonic response of these inelastic springs.

6.2 CONCRETE MODEL

The concrete model refers to the relationship between the force and the deformation (displacement) of the spring representing the concrete. This concept was used by several researchers (Lai et al., 1984; Ghusn and Saiidi, 1986; Li et al., 1988; and Jiang and Saiidi, 1990). The developed models included some simplifications, such as using a bilinear model for concrete in compression, ignoring concrete tensile strength, ignoring the confinement effect of the steel ties, and oversimplifying the deformation of concrete spring. In this study, the concrete compression envelope proposed by Popovics (1973) for unconfined concrete elements and modified by Mander et al. (1988) for steel-confined concrete elements are adopted. A new model for FRP-confined concrete elements is proposed.

6.2.1 Compression envelope of unconfined concrete

The monotonic concrete compression response follows the model of Popovics (1973). The model defines the complete behaviour of unconfined concrete under compression including the softening part of the response using one simple formula. The concrete stress f_c that corresponds to concrete strain ε_c is given as:

$$f_c = \frac{f_c^{'} x r}{r - 1 + x^r} \tag{6-1}$$

where

$$x = \frac{\varepsilon_c}{\varepsilon_o} \tag{6-2}$$

and

$$r = \frac{E_c}{E_c - E_{\sec}} \tag{6-3}$$

where $f_c^{'}$ is the ultimate concrete strength, ε_o is the concrete strain that corresponds to $f_c^{'}$, E_c is the initial concrete stiffness and E_{sec} is the secant stiffness at the ultimate concrete strength. Typical values of ε_o and E_c are -0.002 mm/mm and $5000\sqrt{f_c^{'}}$, respectively. For 30 MPa concrete, the model prediction of the stress-strain relationship is shown in Figure 6-1.

6.2.2 Compression envelope for concrete confined with steel ties

The concrete confinement by transverse steel reinforcement is represented by Mander's model (Mander et al., 1988). The ultimate concrete stress and the corresponding strain were modified to include the effect of confining ties. The confined concrete strength $f_{cc}^{'}$ was related to the confining stress $f_l^{'}$ due to the transverse reinforcement, as:

$$f_{cc}^{'} = f_c^{'}(2.254\sqrt{1+\frac{7.94 f_l^{'}}{f_c^{'}}} - 2\frac{f_l^{'}}{f_c^{'}} - 1.254) \tag{6-4}$$

The corresponding concrete strain ε_{cc} is given as:

$$\varepsilon_{cc} = \varepsilon_o[1 + 5(\frac{f_{cc}^{'}}{f_c^{'}} - 1)] \tag{6-5}$$

The confining stress $f_l^{'}$ was related to the yield stress of the steel ties f_{yh}, the

confinement effectiveness coefficient k_e and the transverse reinforcement ratio ρ_s, by the equation:

$$f_l^{'} = k_e f_{yh} \rho_s \tag{6-6}$$

Therefore, the concrete stress-strain relationship can be written in a similar form to Equation (6-1) as:

$$f_c = \frac{f_{cc}^{'} x r}{r - 1 + x^r} \tag{6-7}$$

where

$$x = \frac{\varepsilon_c}{\varepsilon_{cc}} \tag{6-8}$$

The confinement effectiveness coefficient, k_e is used to represent the effect of shape of the concrete cross section on confinement efficiency (Mander et al., 1988). It is noted that the linear behaviour of steel ties before yielding was ignored and the ties were assumed to apply a constant confining pressure after yielding. The axial response of a circular concrete column of 300 mm diameter, $f_c^{'}$ of 30.0 MPa and reinforced with circular hoops of 10 mm diameter at 150 mm spacing is shown in Figure 6-1 by the solid line labelled Mander.

6.2.3 Compression envelope of concrete confined with FRP sheets

6.2.3.1 Introduction

Several experimental studies (Saadatmanesh et al., 1994; Howie and Karbhari,

1995; Nanni and Bradford, 1995; and Ilki et al., 2002) examined concrete confinement using FRP materials. Analytical studies were conducted to predict the response of concrete elements confined with FRP composites (Samaan et al., 1998; Spoelstra and Monti, 1999; Fam and Rizkalla, 2001; Assa et al., 2001; and Wang and Restrepo, 2001). Most of these models focused on circular concrete sections, rather than square or rectangular sections. In this study, a model is proposed to predict the response of rectangular concrete sections confined with FRP sheets and subjected to a monotonic axial compressive stress. The lateral strain compatibility between the FRP jacket and the concrete section is considered and a constant concrete Poisson's ratio is assumed.

6.2.3.2 Model development

The response of concrete elements changes significantly under confining lateral pressure. For steel-confined concrete, the confining pressure increases until a constant confining pressure, that corresponds to the yield stress of the steel ties, is developed (Mander et al., 1988). FRP jacket applies an increasing confining pressure up to failure. This is due to the elastic behaviour of the FRP materials. The confining pressure is created as a result of the lateral dilation of concrete section. The concrete lateral dilation could be represented as a ratio of the axial strain using Poisson's ratio. Therefore, the interaction between the FRP jacket and the concrete section need to be considered until failure of the jacket.

Under axial stress, the unconfined concrete section deforms laterally as:

$$\varepsilon_x = \nu_c \varepsilon_c \tag{6-9}$$

where ε_x is the lateral concrete strain in x-direction, ε_c is the axial concrete strain and ν_c is the concrete Poisson's ratio.

Thus, the unrestrained lateral deformations in x and y directions, u_{xf} and u_{yf}, respectively, as shown in Figure 6-2a, are:

$$u_{xf} = \nu_c \, b_x \, \varepsilon_c \qquad \text{and} \qquad u_{yf} = \nu_c \, b_y \, \varepsilon_c \tag{6-10}$$

where b_x and b_y are the section dimensions in x and y directions, respectively.

FRP jacket produces uniform lateral confinement pressure on the circular section; however, the FRP confining effect is applied to the concrete rectangular and square sections by arching action at the corner. Thus, the corner must be chamfered to an appropriate diameter. The effective confined section depends on the arching angle. For steel-confined concrete sections, arching angle of 45° was assumed (Mander et al., 1988). An investigation was carried out to determine a suitable arching angle for FRP-confined sections (Wang and Restrepo, 2001). The arching angle was found to vary between 42° and 47°; depending on the number of plies. An average value of 45° was suggested.

For simplicity, the concentrated corner confining pressure is distributed as uniform lateral pressure along the section sides. Thus, the confining lateral pressure, as shown in Figure 6-2b, equals:

$$\sigma_x = 2\,\sigma_r \frac{r_c}{b_y} \qquad \text{and} \qquad \sigma_y = 2\,\sigma_r \frac{r_c}{b_x} \tag{6-11}$$

where σ_x, σ_y and σ_r are the confining lateral pressure in x, y and radial directions, respectively, and r_c is the chamfer radius.

Using simple elasticity rules, the sectional lateral displacement due to lateral confining pressure, u_{xr} and u_{yr}, can be estimated, as shown in Figure 6-2b, as:

$$u_{xr} = \frac{2\sigma_r r_c}{E_c}\left(\frac{1}{b_y} - \frac{\nu_c}{b_x}\right) b_x \quad \text{and} \quad u_{yr} = \frac{2\sigma_r r_c}{E_c}\left(\frac{1}{b_x} - \frac{\nu_c}{b_y}\right) b_y \tag{6-12}$$

where E_c is the concrete modulus of elasticity.

The tensile stress induced in the jacket, σ_j due to the lateral pressure at the corner, as shown in Figure 6-2d, is:

$$\sigma_j = \sigma_r \frac{r_c}{t_j} \tag{6-13}$$

where t_j is the FRP jacket thickness, and equals the thickness of one FRP sheet multiplied by the number of sheets.

The lateral deformation of the jacket due to this lateral pressure, u_{xj}, as shown in Figure 6-2c, is:

$$u_{xj} = \frac{\sigma_r r_c}{E_j t_j} b_x \tag{6-14}$$

To estimate the lateral confinement pressure, the lateral displacement compatibility is considered. The compatibility equation is written as:

$$u_{xf} - u_{xr} = u_{xj} \tag{6-15}$$

Thus, the confinement pressure equals:

$$\sigma_r = \frac{\nu_c}{\frac{r_c}{E_j t_j} + \frac{2r_c}{E_c}(\frac{1}{b_x} - \frac{\nu_c}{b_y})} \varepsilon_c \tag{6-16}$$

One of the main uncertainties in this approach is the evaluation of the Poisson's ratio, as it varies with the imposed axial strain and confinement pressure. So far, different techniques for predicting Poisson's ratio have been proposed. These techniques include using a constant average Poisson's ratio (Wang and Restrepo, 2001), using simple regression analysis to correlate Poisson's ratio with different constant confining hydrostatic pressure (Fam and Rizkalla, 2001), and evaluating the lateral concrete deformation using empirical formulas (Spoelstra and Monti, 1999). The lateral strain of several GFRP-confined concrete cylinders were measured when tested under static load and used to estimate the tangent Poisson's ratio which when integrated gives the concrete Poisson's ratio (Mirmiran and Shahawy, 1997). When comparing the results of these approaches, a wide range of values of Poisson's ratio, ranging from 0.15 at low strain level to more than 2.0 near failure, was obtained.

In this study, a constant value of Poisson's ratio of 0.50 is adopted. It was found that this value gives a conservative estimate for the most of axial strain values (Wang and Restrepo, 2001). This value was also selected considering the scatter of the results of the various procedures, and the complexity of the problem.

To account for the fact that a part of the concrete section is not affected by the confinement jacket, a confinement efficiency factor k_e is introduced:

$$k_e = 1 - \frac{\sum_i w_i^2}{6 b_x b_y} \tag{6-17}$$

where w_i is the length of unconfined region in the concrete section, as shown in Figure 6-2e.

Thus, the confined concrete strength, as proposed by Mander et al. (1988), is:

$$f_{cc}^{'} = f_c^{'}(2.254\sqrt{1 + \frac{7.94\, k_e (2\frac{r_c}{b_x}\sigma_r)}{f_c^{'}}} - 2\frac{k_e (2\frac{r_c}{b_x}\sigma_r)}{f_c^{'}} - 1.254) \tag{6-18}$$

and the corresponding concrete strain is:

$$\varepsilon_{cc} = \varepsilon_o [1 + 5(\frac{f_{cc}^{'}}{f_c^{'}} - 1)] \tag{6-19}$$

where $f_c^{'}$ is the unconfined concrete strength and ε_o is the corresponding strain.

Hence, the concrete strength f_c that corresponds to a certain strain ε_c is given as before in Equation (6-7).

6.2.3.3 Model Verification

The proposed model was used to predict the response of six confined concrete rectangular sections. Three specimens were wrapped with CFRP sheets (Hosotani et al., 1997), and the others were wrapped with GFRP (Cole and Belarbi, 2001).

Three square concrete stubs of cross section 200 x 200 mm and height of 600 mm were wrapped with layers of CFRP sheets. The corners of the section were chamfered with a radius of 30 mm. The CFRP sheet reinforcement ratios were 0.056, 0.111 and

0.167% for specimens S9, S10, and S11, respectively. The column stubs were reinforced with 6 mm diameter longitudinal reinforcement bars of ratio 1%; which was neglected in the model; and had no lateral reinforcement. The unconfined concrete strength was found to be 38.7 MPa with an assumed corresponding strain of 0.002. The elastic modulus of the CFRP sheets was 230 GPa. The confinement efficiency factor was estimated to be 0.673. The axial stress-axial strain relationships were analytically predicted and compared to the experimental measurements, as shown in Figure 6-3. Good agreement between the predicted and the measured response is noted.

Three square concrete stubs of cross section of 181 x 181 mm and 914 mm high were wrapped with one, two and three layers of MBrace™ EG 900 GFRP sheets (1 GFRP, 2 GFRP and 3 GFRP). The corners of the cross section were chamfered with a radius of 13 mm. The properties of the composite sheets can be found in Table 2-4. The unconfined concrete compressive strength was 21.0 MPa with an assumed corresponding strain of 0.002. The confinement efficiency factor is estimated to be 0.511. The deformation of the specimens under axial load was predicted using the proposed model and compared to the experimental response, as shown in Figure 6-4. The agreement between the predicted and the measured response is reasonably good.

6.2.4 Concrete tension envelope

A linear stress-strain relation is assumed for concrete in tension till cracking. The concrete tensile stress f_{ct} - strain ε_c relationship, is written as:

$$f_{ct} = E_c \varepsilon_c \tag{6-20}$$

where E_c is the concrete elastic modulus.

The response of the concrete members after cracking was studied by several researchers (Vecchio and Collins, 1982; Collins and Mitchell, 1987; and Tamai et al., 1988). The cracked concrete may still have tensile strength known as tension stiffening. The element response after cracking depends on the reinforcement ratio of the section. For an unreinforced member, the concrete tensile strength rapidly reduces to zero. At the other extreme, considerable average tensile strength could remain in the concrete after cracking of a member reinforced with large percentage of well-distributed steel. The amount of average tensile stress transferred to the concrete is a function of the bond characteristics between the concrete and steel.

In this study, the tension stiffening relationship developed by Stevens et al. (1987) was adopted. The relationship is shown in Figure 6-5. The concrete tensile stress f_{ct} is related to tensile strain ε_c by the expression:

$$f_{ct} = f_{cr}[(1-\alpha_t)e^{-\lambda_t(\varepsilon_c-\varepsilon_{cr})} + \alpha_t] \tag{6-21}$$

where f_{cr} is the concrete cracking strength, α_t is a factor that defines the residual concrete tensile strength and λ_t is a factor that controls the decay rate of the response. These factors were given as:

$$f_{cr} = 0.33\sqrt{f_c^{'}} \tag{6-22}$$

$$\alpha_t = 75\rho_x / d_b \tag{6-23}$$

$$\lambda_t = 270/\sqrt{\alpha_t} \quad \leq 1000 \tag{6-24}$$

where, d_b is the longitudinal bar diameter and ρ_x is the longitudinal steel ratio.

It should be noted that f_{cr} is the concrete cracking strength resulting from a direct tensile test which is different from the modulus of rupture which results from a bending test. Equation (6-23) gives the value of α_t for the case of axial tensile stresses, where the reinforcement bars are parallel to the tensile stresses. In case of bi-directional loading, where the principal tensile stress is inclined to the reinforcement bars in x-direction with an angle θ, then:

$$\alpha_t = \cos^2\theta \;\; \alpha_{tx} + \sin^2\theta \;\; \alpha_{ty} \tag{6-25}$$

Where α_{tx} and α_{ty} can be estimated using Equation (6-23) after replacing ρ_x with the reinforcement ratio in x and y directions, respectively.

6.3 MODELING OF EXTERNALLY BONDED FRP SHEETS

The FRP model refers to the relationship between the forces in the FRP sheets bonded to concrete and the corresponding deformation, in tension or compression. Most of the existing FRP models represent the FRP sheets as linear elastic material that has boundary conditions similar to those in a coupon test. In the proposed model, the tensile elongation of composite sheets associated with the flexure of the retrofit steel angle at the beam-column interface, and the buckling of the sheets under compression forces are

considered.

6.3.1 FRP tension envelope

The FRP sheets and the retrofit steel angle are represented by a bilinear inelastic zero-length spring. The inelastic behaviour of the spring is caused by the inelastic behaviour of the steel angle, as shown in Figure 6-6a and b. The tensile force acting on the FRP sheets is assumed to be zero at the free end and maximum at the face of the column. The vertical leg of the steel angle is represented by zero length steel spring attached at the end of the FRP elastic element, as shown in Figure 6-6b. The angle's leg is represented as a steel beam that is fixed at one end and laterally guided at the other end, as shown in Figure 6-6c. The lateral load on the angle's leg is a result of the tension in the FRP sheets. The steel spring is represented by a bi-linear force-deformation curve, as shown in Figure 6-6d. The parameters of this curve are:

$$P_{spy} = \frac{f_y\, b_a\, t_a^{\,2}}{2 l_1} \tag{6-26}$$

$$\delta_{sy} = \frac{f_y\, l_1^2}{4 E_s\, t_a} \tag{6-27}$$

$$k_{s1} = P_{sy} / \delta_{sy} = \frac{2 E_s\, b_a\, t_a^{\,3}}{l_1^3} \tag{6-28}$$

$$k_{s2} = \beta\, k_{s1} \tag{6-29}$$

where f_y is the yield stress of the steel retrofit angle.

E_s is the modulus of elasticity of steel (200,000 MPa).

β is the ratio of post yield to pre-yield slopes of the steel stress-strain relationship.

l_l is the unsupported length of the steel angle leg.

b_a and t_a are the width and the thickness of the steel angle leg, respectively.

The FRP sheet is represented as an elastic element as shown in Figure 6-6b, with a specified modulus of elasticity E_{frp}. The element stiffness, k_{frp}, is:

$$k_{frp} = \frac{E_{frp} A_{frp}}{L} \tag{6-30}$$

where A_{frp} and L are the cross sectional area and length of the FRP sheet, respectively.

The FRP element with the steel spring at its end is represented by an equivalent bilinear inelastic spring of the characteristics shown in Figure 6-7b. The equivalent stiffness of the elastic and inelastic segment of the bilinear behaviour are:

$$\frac{1}{k_1} = \frac{1}{k_{s1}} + \frac{1}{k_{frp}} \tag{6-31}$$

$$\frac{1}{k_2} = \frac{1}{k_{s2}} + \frac{1}{k_{frp}} \tag{6-32}$$

6.3.2 FRP compression envelope

Modeling the behaviour of FRP sheets when subjected to axial compression forces has not received much attention. This is because the application of FRP sheets in structural engineering was limited to strengthening concrete members in tension. However, in case of cyclic loading, the development of compression stresses in the FRP sheets is inevitable.

The FRP sheets are modeled as a simply supported beam subjected to axial

compression force. The beam is laterally supported by the epoxy layer which is modeled as discrete tensile springs of stiffness k_p, as shown in Figure 6-7a. Hence, the equilibrium equation of the composite sheets is given as:

$$E_{frp} I_{frp} w_f^{iv} + P_f w_f'' + k_p w_f = 0 \tag{6-33}$$

where I_{frp} is the moment of inertia of the FRP sheets

w_f is the lateral deflection of the FRP sheets

P_f is the applied compression force

The boundary conditions of this differential Equation (6-33) are that the displacement and the curvature of the beam at the supports vanish; and the solution is of the form:

$$w_f = C_1 \sin \frac{n\pi}{L} x \qquad n = 1,2,3,... \tag{6-34}$$

where C_1 is a constant and L is the FRP sheet length

Substituting of Equation (6-34) into Equation (6-33) gives the expression:

$$P_f = (\frac{n\pi}{L})^2 E_{frp} I_{frp} + (\frac{L}{n\pi})^2 k_p \tag{6-35}$$

The critical buckling load, P_{cr} is the smallest value of P_f

In the proposed model, the FRP sheets would be modeled as an elastic material to the onset of buckling which represents the failure, as shown in Figure 6-7b. The post-buckling behaviour of the sheets will not be considered because it is assumed that buckling is a result of debonding of the FRP sheets from the concrete surface.

6.4 STEEL MODEL

The steel model in this study refers to the relationship between the forces and deformations in the steel bars. The steel bars are modeled as inelastic springs. The inelastic steel constitutive relationship and the steel-to-concrete bond law are the main sources of the spring inelasticity. The deformation of an embedded steel bar in concrete element is a result of the bar extension and bar anchorage-slip. Tests showed that at displacement ductility level of four or more, fixed end rotation caused by slip of the main steel bars along their embedment length may contribute up to 50% of the total beam deflection (Takeda et al., 1970; and Ma et al., 1976).

6.4.1 Background

The interaction between steel bars and the surrounding concrete received considerable attention from researchers during the last three decades. The behaviour of steel bars embedded in concrete elements was investigated experimentally (Marques and Jirsa, 1975; Viwathanatepa el al, 1979; Ueda et al., 1986; Soroushian et al., 1988; Soroushian and Choi, 1989; and Soroushian et al., 1991a). Several analytical models were developed to predict the bond-slip behaviour of steel bars. A simple model was developed assuming a linear strain distribution along the development length of the bar (Otani and Sozen, 1972). A more accurate model was proposed by dividing the embedded bar length into finite elements (Ciampi et al., 1982). Incremental displacement was applied at the bar free end to failure. Bond stress was applied along each element. For each displacement increment, the equilibrium and compatibility equations were

applied to each element to estimate the deformation and the steel stress at the end of each element, starting with the bar free end and moving till reaching the bar lead end. Numerical difficulties, such as snap-back response and strain localization, are expected to arise due to the softening behaviour of the bond stress–slip law. Similar studies were later conducted (Filippou et al., 1983; Russo et al., 1990; and Youssef, 2000). Various finite element models were proposed to predict the response of steel bars anchored in concrete elements. The steel-concrete interaction was represented in the model by inelastic bond springs, which were included in the model tangent stiffness matrix (Soroushian and Choi, 1991; Soroushian et al., 1991b; and Ustuner, 1992). In another model, the embedded steel bar was divided into a series of two-node elements, where the bar forces, bond stress and the displacement were applied at the nodes (Monti et al., 1997).

In this study, a simple but sufficiently accurate model (Alsiwat and Saatcioglu, 1992) was adopted, refined and then used to plot the monotonic response of embedded steel bars. The model results were verified using some of the existing experimental results.

6.4.2 Material constitutive relationships

The bond characteristic of steel bars can be described by the relationship between local bond stress, τ, and pertinent local slip, s, of the bar, where bar slip is defined as the relative displacement of the bar with respect to the concrete. Defining the constitutive bond stress-slip relationship is a complex task because of the large number of factors involved. These factors include the steel bar diameter, the distribution of the lugs on the

bar circumferential surface, the spacing between the longitudinal bars, the concrete tensile and compression strengths, the aggregate size, the level of axial load, the distribution and the diameter of the confining stirrups. The interaction between these different factors adds to the difficulty in separating the effect of each factor.

Several attempts were performed to study the constitutive bond stress–slip relationship. Experimental program was proposed to predict a rational and an accurate bond stress–slip relationship (Viwathanatepa et al., 1979; and Eligehausen et al., 1983). Chemical adhesion between the concrete and the bar surface contributes to the bond resistance. This adhesion fails at very small slip values. Hence, the bond forces are transferred through mechanical interlock between the concrete and the steel bar. High tensile stresses are created in the concrete ahead of the bar lugs and eventually cause inclined cracks, called *bond cracks*. Some crushed concrete in front of the lugs occurs, which reduces the stiffness of the element. After the formation of these cracks, the bar force is transferred to the concrete through a compression stress zone in front of the bar lugs. These compression stresses cause an internal pressure on the concrete surrounding the bar and tensile hoop stresses, which result in splitting cracks. These splitting cracks would be counteracted by concrete tensile strength and confining stirrups. With inadequate amount of the confining stirrups, these cracks would propagate and widen and the bond resistance would drop to zero. If the concrete is well confined, the load can be increased further, until concrete shear cracks between the lugs are initiated. The bar tensile force drops until the concrete between the lugs is completely sheared off.

Following this, the only mechanism left is the frictional resistance between the rough concrete at the cylindrical surface where the shear failure occurred. The different stages of the bond stress–slip relationship as presented by Eligehausen et al. (1983) are shown in Figure 6-8.

The bond stress – slip relationship is idealized, as shown in Figure 6-9b, as:

$$\tau = \tau_1 (\frac{s}{s_1})^a \qquad s < s_1 \tag{6-36}$$

$$\tau = \tau_1 \qquad s_1 \leq s < s_2 \tag{6-37}$$

$$\tau = \tau_1 - \frac{(\tau_1 - \tau_3)}{(s_3 - s_2)}(s - s_2) \qquad s_2 \leq s < s_3 \tag{6-38}$$

$$\tau = \tau_3 \qquad s_3 \leq s \tag{6-39}$$

The definitions of the different parameters in these equations are shown in Figure 6-9b.

Based on extensive experimental program, values of these parameters were proposed (Eligehausen et al., 1983), as listed in Table 6-1. These values are for 25 mm diameter steel bar embedded in concrete block of 30 MPa strength and for clear bar spacing of 4 d_b. It is recommended that the bond stress parameters τ_1 and τ_3 be reduced by about 20% in case of close bar spacing of 1 d_b (Eligehausen et al., 1983).

A general equation was proposed by Soroushian et al. (1991b) to estimate the ultimate bond strength for different bar diameters and concrete strengths, as:

$$\tau_1 = (20 - d_b / 4)\sqrt{\frac{f_c'}{30}} \qquad in\ MPa \tag{6-40}$$

where d_b is the bar diameter in mm.

The frictional resistance of concrete, τ_3 is assumed related to the ultimate bond strength, τ_1 as:

$$\tau_3 = \tau_1 / 3 \tag{6-41}$$

The slip values s_1 and s_2 are assumed dependent on the concrete compressive strength (Alsiwat and Saatcioglu, 1992), such that:

$$s_1 = \sqrt{\frac{30}{f_c'}} \qquad in\ mm \tag{6-42}$$

$$s_2 = 3 s_1 \tag{6-43}$$

The slip value s_3 is assumed equal to the clear spacing between the lugs in the bar.

Several studies were conducted to experimentally evaluate the bond stress-slip relationship of hooked bars. A model that relates the bond stress along the hook length to the slip at the hook tip, that is similar to the bond-slip relationship of straight bars, was proposed (Filippou et al., 1983). A general model that relates the pullout force to the hook slip was also proposed (Soroushian et al., 1988). The model parameters, as shown in Figure 6-9c, are:

$$P_h = P_1 (\frac{s_h}{2.54})^{0.2} \tag{6-44}$$

$$P_1 = 271(0.05 d_b - 0.25) \qquad in\ kN \tag{6-45}$$

$$P_3 = 0.54 P_1 \tag{6-46}$$

$$s_{h1} = 2.54\ mm \tag{6-47}$$

$$s_{h2} = 3\ s_{h1} \tag{6-48}$$

$$s_{h3} = 15\ s_{h1} \tag{6-49}$$

Where P_h and s_h are the resistance force of the hook and the slip at the tip of the hook, respectively.

Different steel constitutive relationships were used when solving the boundary problem of a steel bar anchored in concrete element. These models ranged from elastic perfectly plastic model, bilinear model or piecewise models. In this study a bilinear model is adopted with two slopes. The first slope is up to the onset of yield strain and the second slope starts from yielding of the steel to the ultimate strength.

6.4.3 Proposed model

A simple approach with adequate accuracy was proposed by Alsiwat and Saatcioglu (1992) and recently refined by Galal (2002), to predict the behaviour of embedded steel bars in concrete elements under monotonic load. The model was used to predict the deformation of steel bars subjected to pull only, pull and push or hooked bars. The model can predict the two components of bar deformation; anchorage-slip and bar extension.

The extension of the steel bar is a result of the accumulation of elastic and plastic strains along the bar embedded length. The plastic region includes the yield plateau, strain hardening and pullout cone subregions as shown in Figure 6-10a. The bond stress

is assumed constant along the length of each subregion. An average bond stress u_e is assumed within the elastic region as:

$$u_e = \frac{f_y d_b}{4 l_d} \tag{6-50}$$

where f_y is the bar yield strength

d_b is the bar diameter

l_d is the bar development length

The length of the elastic region can be determined as:

$$L_e = \frac{f_y d_b}{4 u_e} \tag{6-51}$$

The yield plateau region is the portion of the bar over which the steel stress is approximately constant and equals the yield stress. The model does not account for this region, as it represents a small portion of the bar length and ignoring it will not significantly affect the results. In strain hardening region, it is assumed that the concrete in front of the bar lugs is crushed and uniform bond stress, u_f equals the frictional bond resistance, τ_3 exists. The length of this region depends on the status of bar stress. The last region is the pullout cone region, which is a constant stress and strain region. This region extends for the concrete cover where the concrete breaks in tension. Neglecting this region does not result in significant inaccuracies in computation of inelastic deformations caused by anchorage-slip (Alsiwat and Saatcioglu, 1992).

To plot the monotonic behaviour of an embedded bar in tension to failure, a

combined load and displacement controlled scheme is adopted. As a start, incremental steel stress is applied to bar yielding. At each increment, the elastic region length is estimated. The onset of bar slip occurs when the length of the elastic region exceeds the bar embedded length. The strain in each region was estimated and therefore the bar extension can be determined. End slip of the bar can be estimated from the bond-slip laws knowing the bond stress at the bar end. Once the bar end slip exceeds the slip value of s_1, the load application is changed to displacement control. Incremental bar end displacement was applied to failure. At each increment, the bond stress along the elastic region and its length are estimated. Thus, the length of the strain-hardening region would equal to the remaining embedded length, and the stress at the bar tip can be estimated. Figure 6-11 shows the steps of the solution scheme in the form of flow chart. For hooked bars, the hook contributes to the anchorage of reinforcement only if the straight lead length of the bar is not sufficient to develop the imposed force at the bar tip.

6.4.4 Model verification

Analytical results of two cases; bars with straight embedded length and with hooked end; are compared with the experimental data (Ueda et al., 1986; and Viwathanatepa et al., 1979), as shown in Figure 6-12. The behaviour of specimens B81 and B103 (Ueda et al., 1986), that had hooked end, is shown in Figure 6-12a and b, respectively. Figure 6-12c, d and e compare the analytical and the experimental behaviour of specimens S101, S61 and S64 (Ueda et al., 1986). Figure 6-12f compares the analytical and the experimental behaviour of specimen #3 (Viwathanatepa et al.,

1979). The specimens were tested under force-controlled loading. Thus, the post ultimate response could not be measured experimentally. Therefore, the analytical prediction of the post-ultimate response is omitted. The model predictions agree reasonably well with the experimental data.

6.5 SUMMARY

In this chapter, the proposed and adopted material models were discussed. The Popovics' model of unconfined concrete and the Mander's model for steel-confined concrete were adopted. A new model was proposed for FRP-confined concrete. The proposed model was verified using available experimental results. Good agreement was obtained. A new model for externally bonded FRP sheets under tensile or compressive stresses was developed. The steel model of Alsiwat and Saatcioglu (1992) was adopted with introduced refinement. The bond-slip effect on the steel bar stress and deformation was implicitly included in the model.

Table 6-1 Parameters of the bond stress–slip relationship (Filippou et al., 1983; and Eligehausen et al., 1983)

Parameter	Straight bars in confined concrete	Hooks in confined concrete	Unconfined concrete	
	Bar is pulled or pushed	Bar is pulled or pushed	Bar is pulled	Bar is pushed
s_1 (mm)	1.0	1.0	0.3	1
s_2 (mm)	3.0	3.0	0.3	3
s_3 (mm)	10.5	100.0	1	10.5
τ_1 (MPa)	13.5	22.0	5	20
τ_3 (MPa)	5.0	4.0	0	
a	0.40	0.20	0.40	

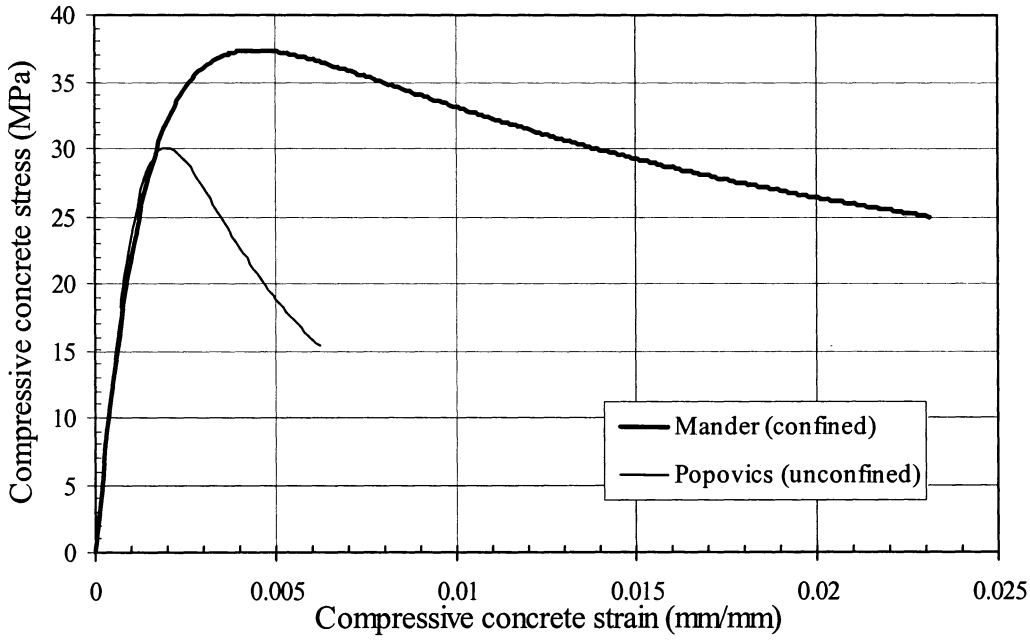

Figure 6-1 Stress-strain behaviour of unconfined and steel-confined concrete members

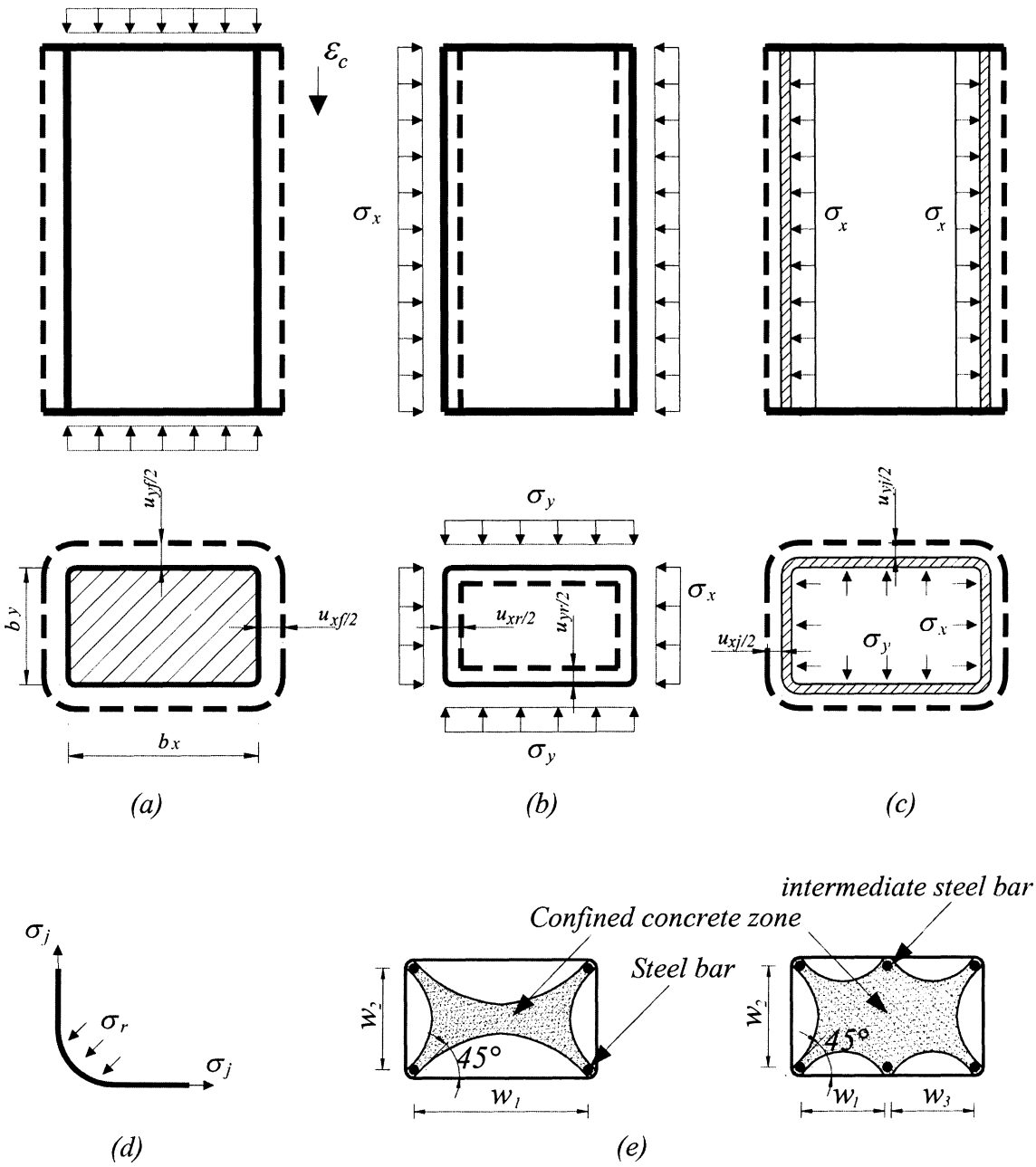

Figure 6-2 Confinement of rectangular concrete sections with FRP sheets

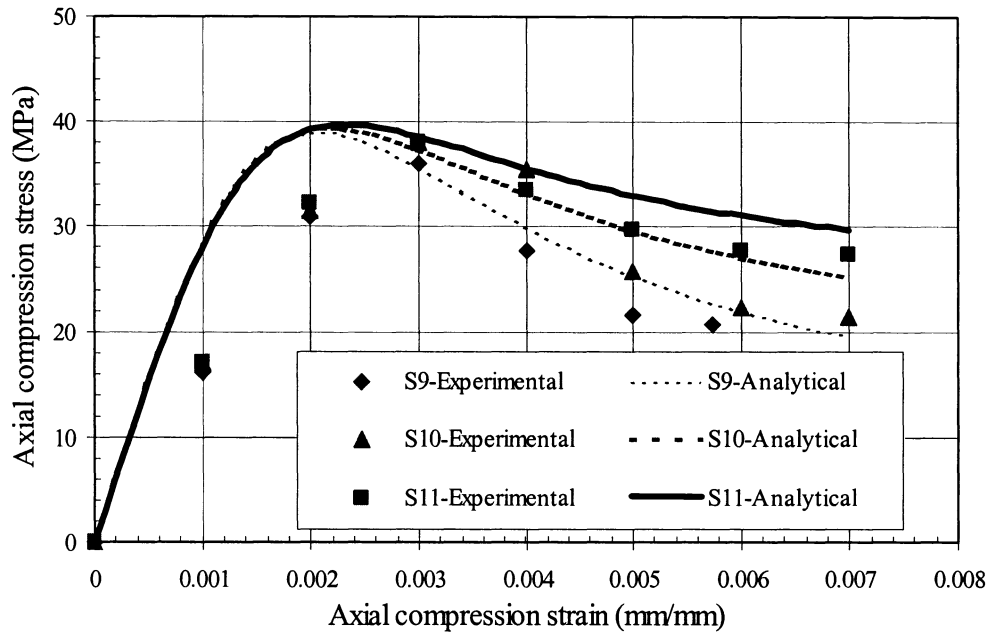

Figure 6-3 Experimental (Hosotani et al., 1997) and analytical stress-strain relationships

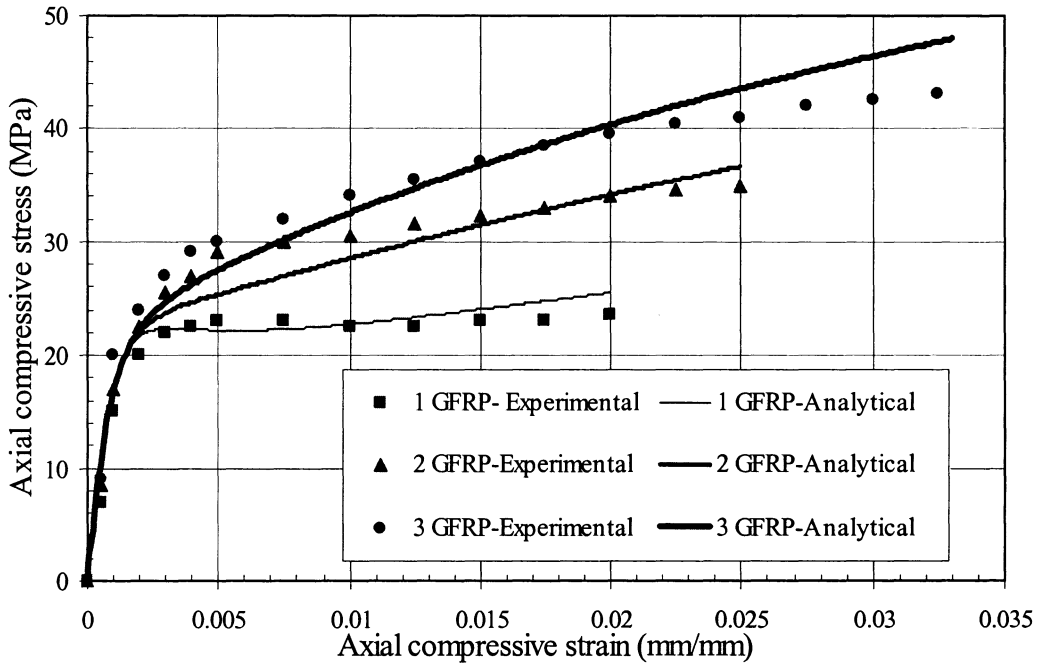

Figure 6-4 Experimental (Cole and Belarbi, 2001)and analytical stress-strain relationships

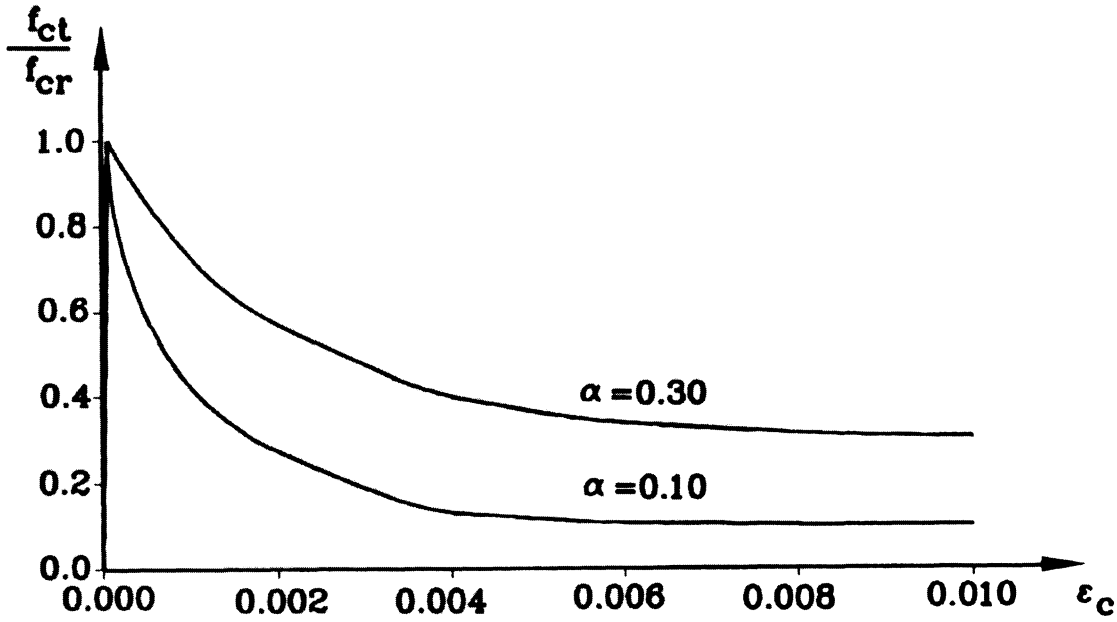

Figure 6-5 Concrete tension envelope (Stevens et al., 1987)

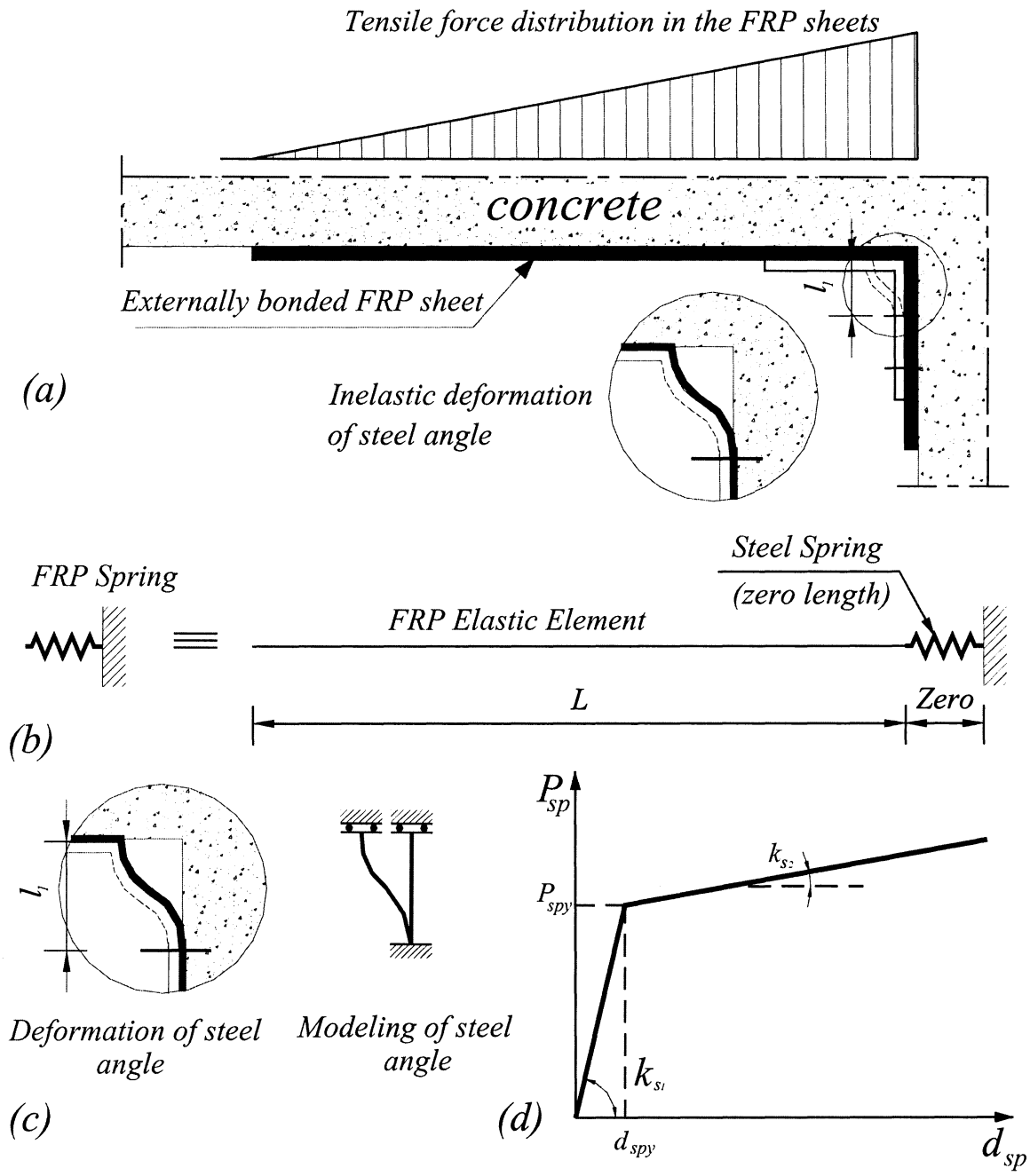

Figure 6-6 Behaviour of the FRP spring: (a) Deformation of FRP sheet in tension (b) FRP and steel angle model in tension (c) Modeling of the retrofit steel angle (d) Response of the retrofit angle

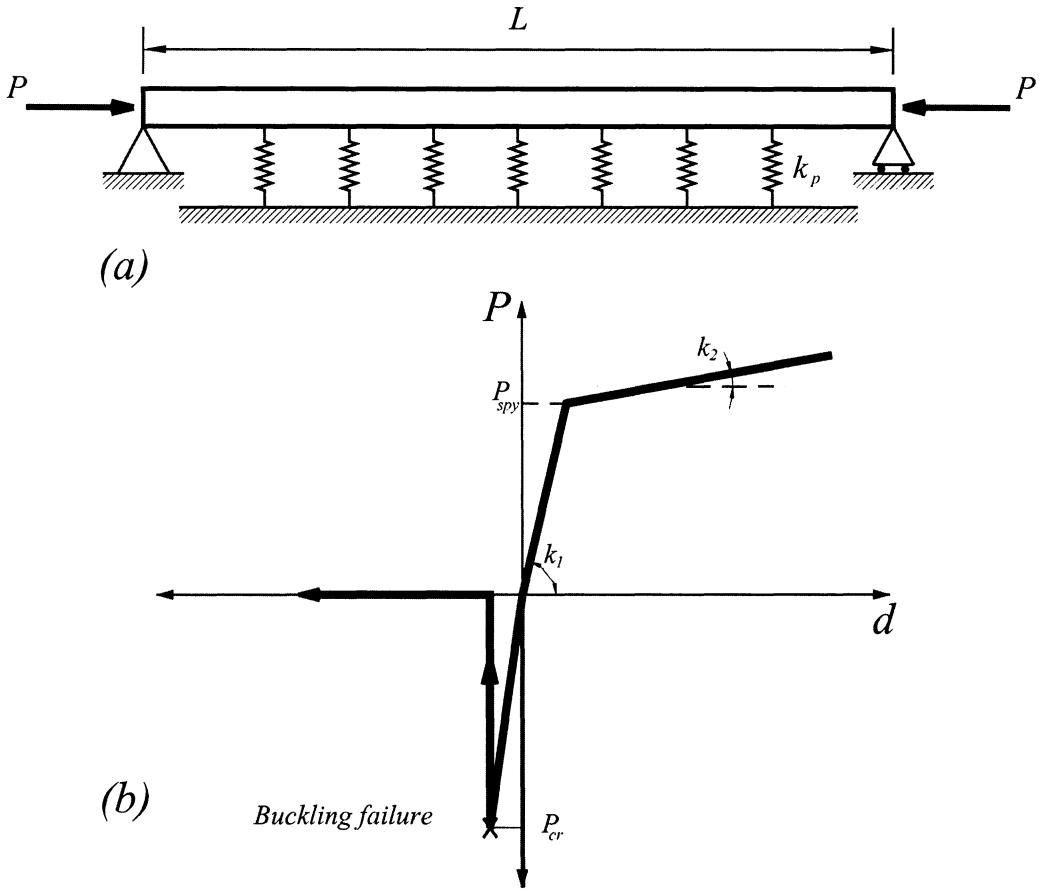

Figure 6-7 Response of FRP spring: (a) modeling of FRP in compression (b) Response of FRP spring in tension and compression

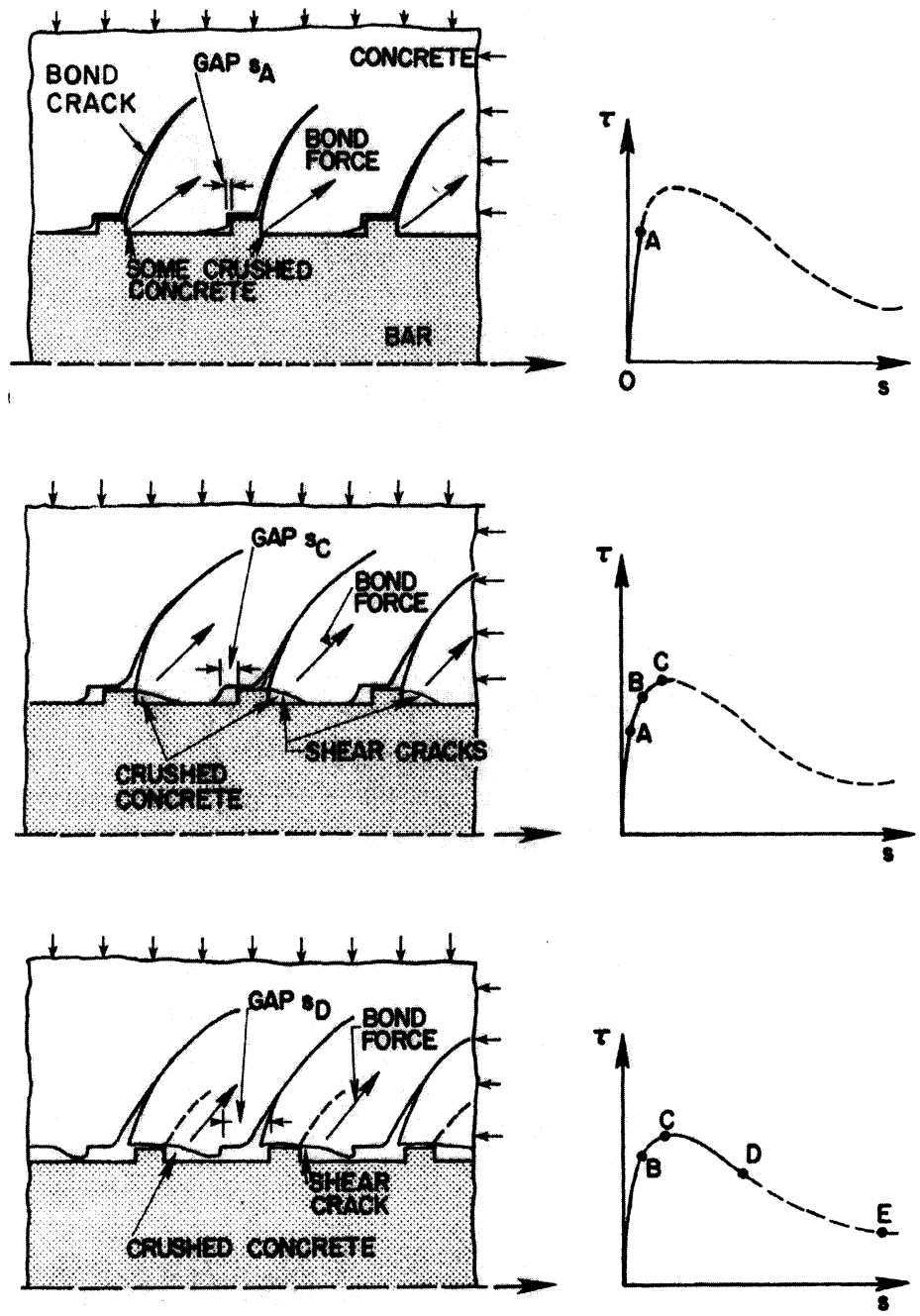

Figure 6-8 Different stages in developing the bond stress-slip relationship (Eligehausen et al., 1983)

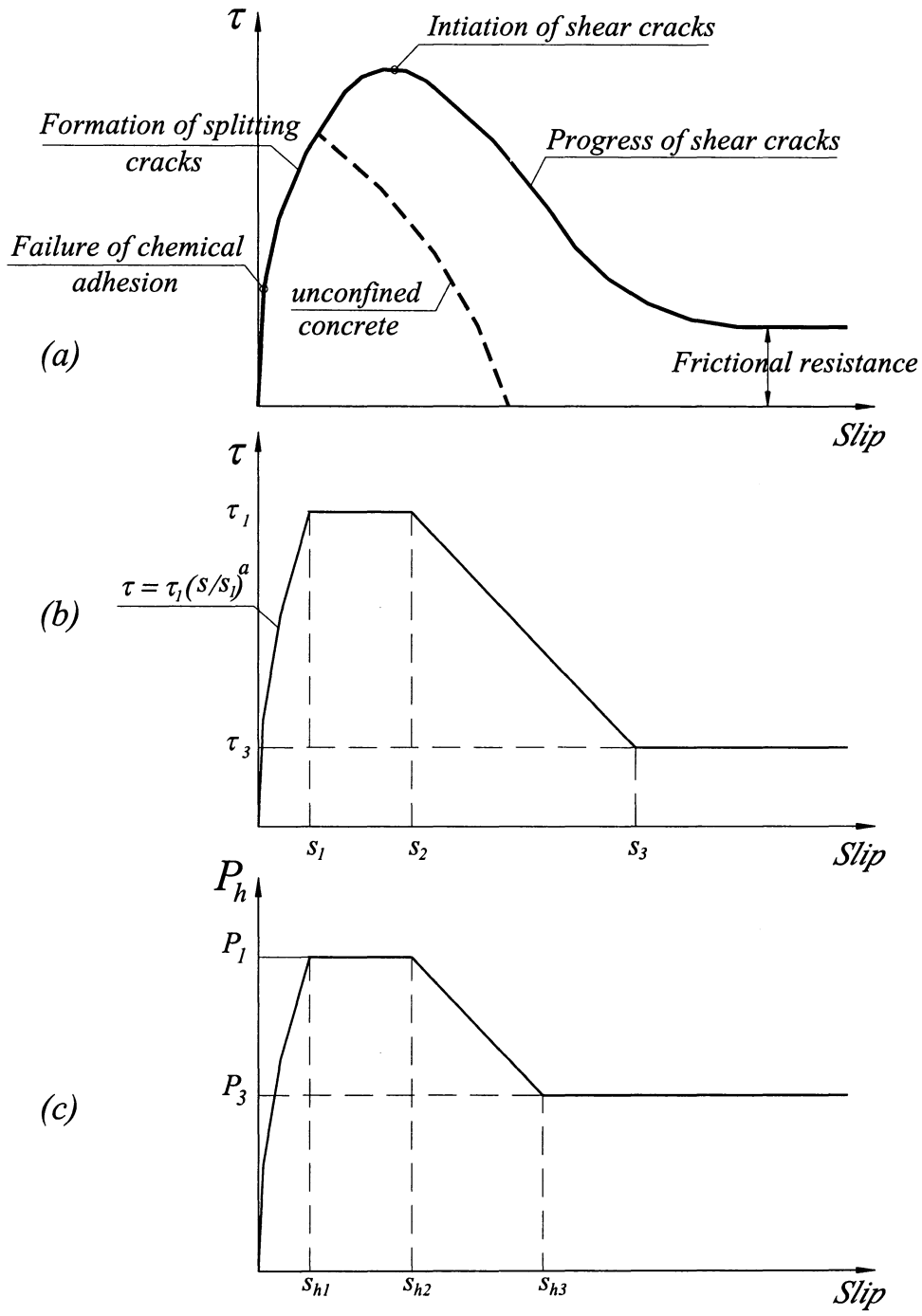

Figure 6-9 Bond stress-slip relationships: (a) Actual (b) Idealized for straight bars (Eligehausen et al., 1983) (c) Idealized for hooks (Soroushian et al., 1988)

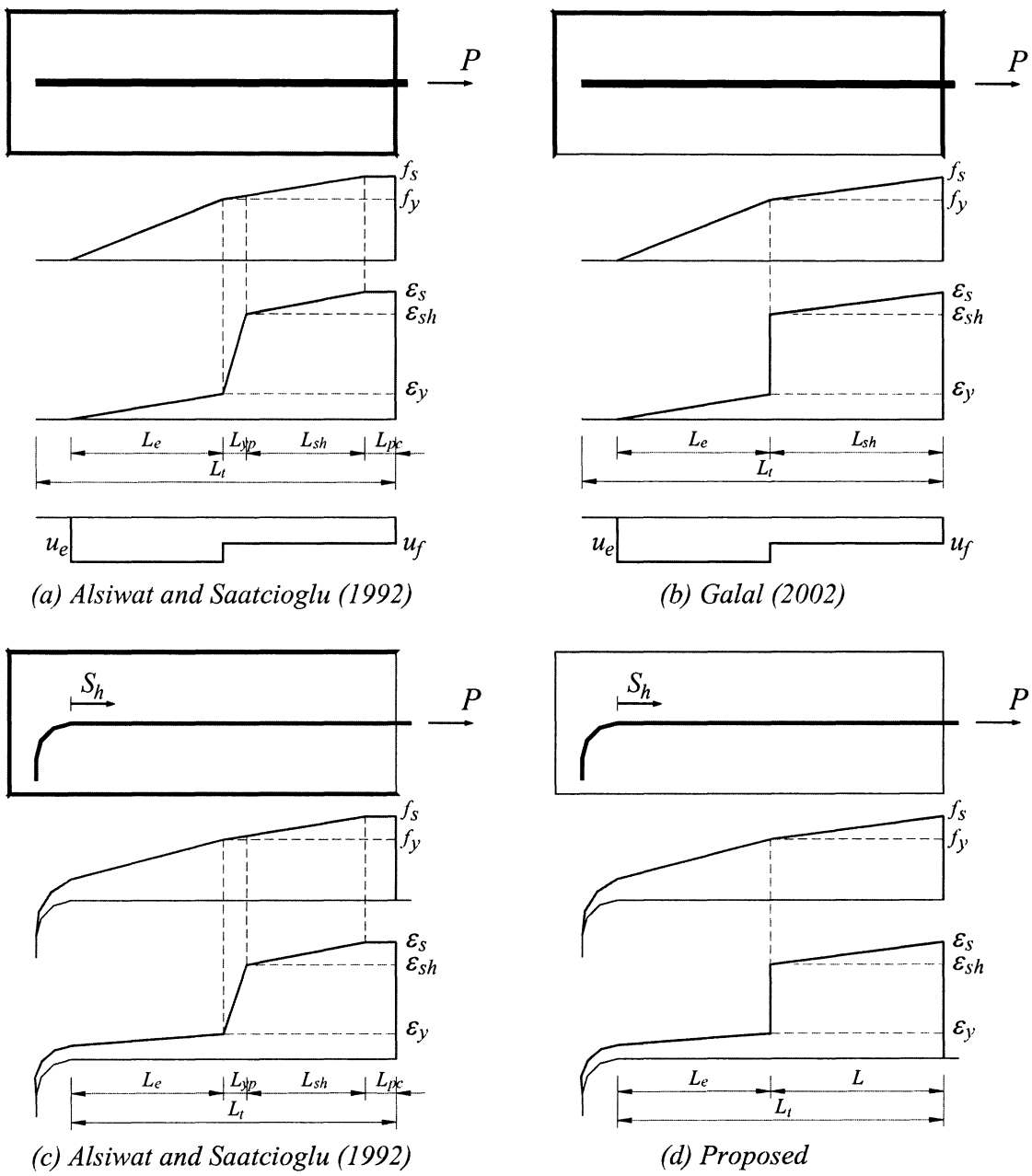

(a) Alsiwat and Saatcioglu (1992)

(b) Galal (2002)

(c) Alsiwat and Saatcioglu (1992)

(d) Proposed

Figure 6-10 Reinforcing bars with straight or hooked end embedded in concrete

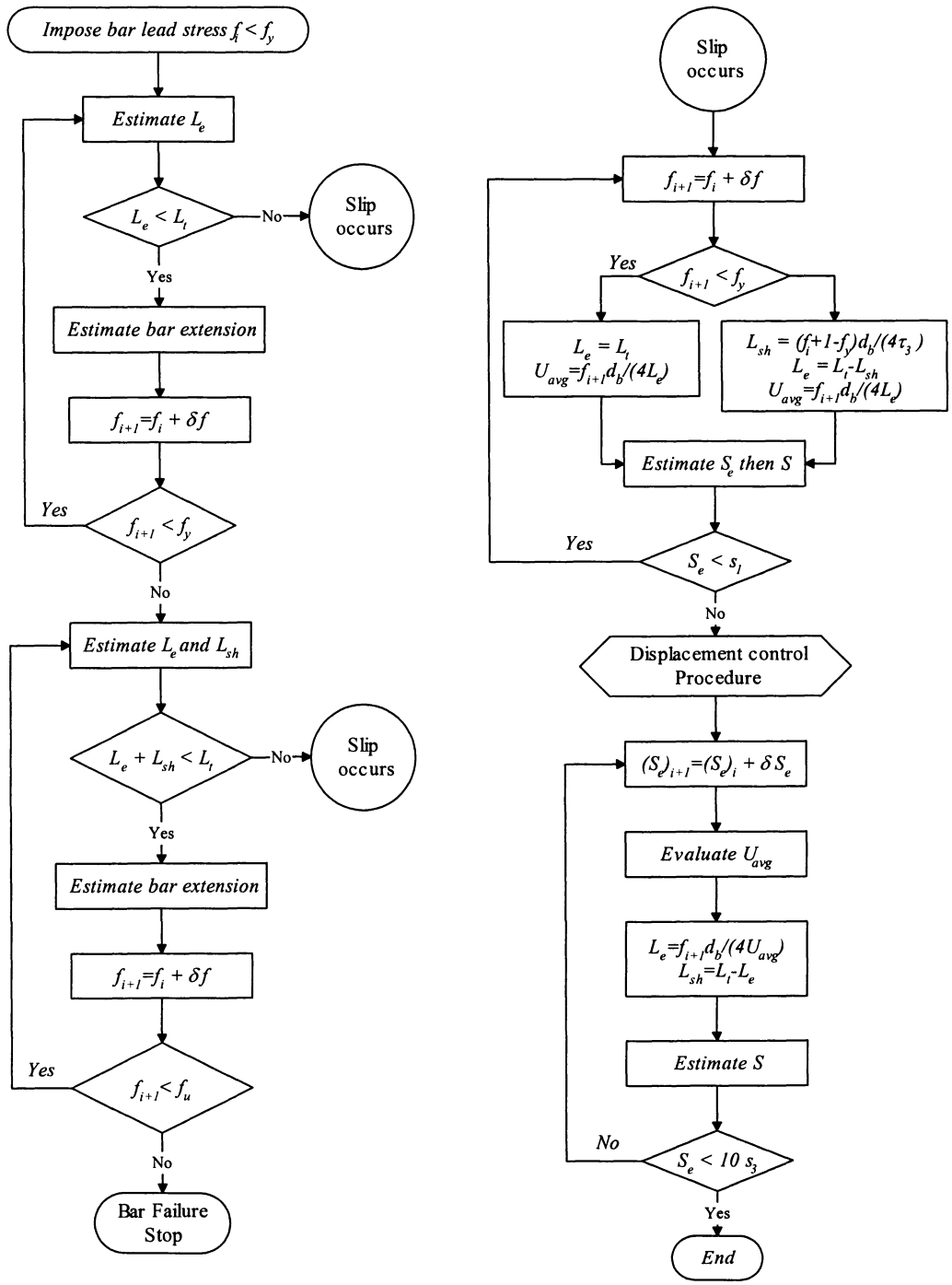

Figure 6-11 Solution algorithm of bond-slip model

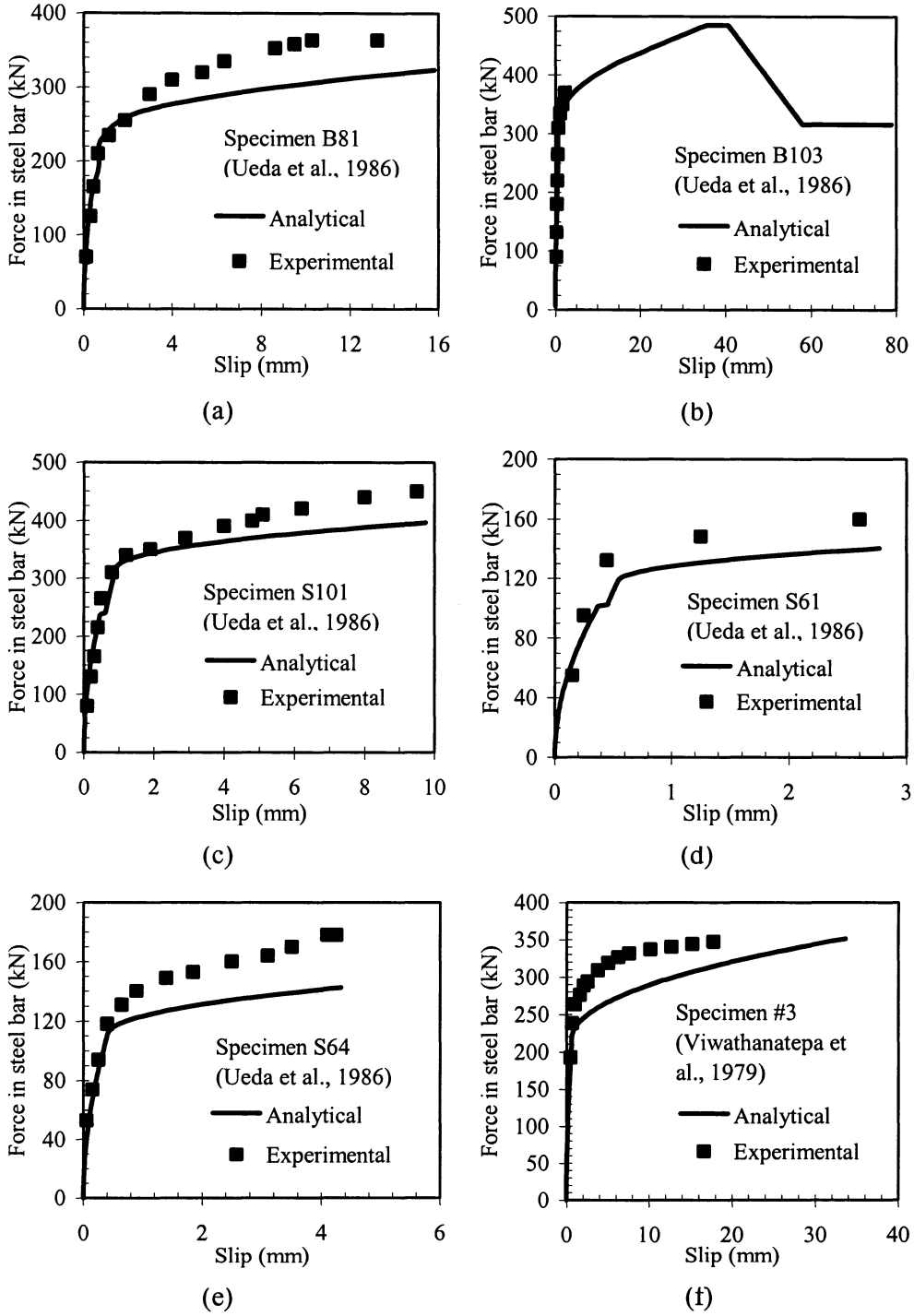

Figure 6-12 Force-displacement relationship for embedded steel bars tested under monotonic loads

Chapter 7

JOINT SHEAR MODELS

7.1 INTRODUCTION

The response of beam-column joints is mainly influenced by the shear behaviour of the joint and the bond-strength of anchored beam bars. Modeling of the joint shear response is a complex and difficult task, because the nonlinear nature of the problem and the interaction between the shear and axial strains. Most of the currently available models were developed for joints that were detailed and constructed according to the current codes. Very few models are available for predicting the response of existing joints and there are no models available for predicting the response of FRP-rehabilitated joints. This represents difficulties for engineers who are evaluating existing buildings for possible retrofit and assessing suitable rehabilitation techniques. Therefore, a robust model is needed to predict the response of concrete frame joints when subjected to dynamic loads. This model should be capable of evaluating the response of existing joints and predict the behaviour of rehabilitated ones. In this chapter three analytical shear models are proposed. These models can be used for evaluating the response of joints with steel ties, without steel ties or with externally bonded FRP sheets.

7.2 SHEAR MECHANISMS IN BEAM-COLUMN JOINTS

The success of an analytical model in evaluating the response of beam-column

joint is mainly based on the accurate prediction of a rational shear stress transfer mechanism. Traditionally, two mechanisms are assumed to transfer the beam and column forces across the joint core, namely, the truss mechanism and the concrete strut mechanism, as shown in Figure 7-1. In the truss model, the joint boundary forces are transmitted as tensile forces in the vertical and horizontal joint reinforcement and diagonal compression field in the concrete struts. The joint horizontal reinforcement is normally represented as equally spaced hoops in the joint panel whereas the interior column bars represent the joint vertical reinforcement. Deterioration of bond stresses along the embedment zone of the longitudinal beam and column bars would result in deterioration of the truss mechanism. Therefore, the reinforcement forces would transfer across the joint core through a diagonal compression strut, or strut mechanism.

7.3 MODELING OF BEAM-COLUMN JOINTS WITH SHEAR REINFORCEMENT

Recent design procedures of frame joints, that comply with the current code provisions, such as CSA A23.3 (1994) Clause 21.4.4 and ACI-ASCE Committee 352 (1997), provide adequate amount of ties in the joint zone. Thus, the joint boundary forces are transferred by truss mechanism. In this study, the Modified Compression Field Theory, MCFT, (Vecchio and Collins, 1986) is used to predict the monotonic response of concrete frame joints subjected to shear force and constant axial load. In the proposed model, the concrete model used in the MCFT is replaced by the confined concrete model (Mander et al., 1988) that accounts for the effect of steel ties on concrete strength and

ductility. The post-ultimate concrete strength behaviour is also included.

7.3.1 Model derivation

The MCFT is widely used as a general model for predicting load-deformation behaviour of two-dimensional cracked concrete element subjected to combined shear and normal stresses. The cracked concrete is treated as a new material at each strain increment. The smeared crack approach is implemented. Thus, the strains and stresses used in the constitutive relations are average values. Three sets of equations are solved (Vecchio and Collins, 1986; Collins and Mitchell, 1990), these are:

a) Constitutive Equations:

This set of equations describes the relationship between the average stresses and strains in the member. The concrete stress-strain relationship in this context will differ from the relationship obtained from the cylinder compression test, as the coexisting principal tensile stress will reduce the principal concrete compression strength.

The constitutive relation used in the original MCFT is replaced by the constitutive relationship proposed by Popovics (1973) and modified by Mander et al. (1988), as discussed in Section 6.2.3. The principal compressive concrete stress, f_2, is given as:

$$f_2 = \frac{f_{2\max} x\, r}{r - 1 + x^r} \tag{7-1}$$

where

$$x = \frac{\varepsilon_2}{\varepsilon'_{cc}} \tag{7-2}$$

where ε_2 and ε'_{cc} are the principal compression strain and the compression strain that

corresponds to the confined concrete strength $f_{cc}^{'}$ (Mander et al., 1988):

$$r = \frac{E_c}{E_c - E_{\sec}} \tag{7-3}$$

where

$$E_c = 5000\sqrt{f_c^{'}} \qquad in\ MPa \tag{7-4}$$

$$E_{\sec} = \frac{f_{cc}^{'}}{\varepsilon_{cc}^{'}} \tag{7-5}$$

f_{2max} is the maximum concrete strength that corresponds to the principal tensile strain, ε_1 and can be estimated as:

$$f_{2\max} = \frac{f_{cc}^{'}}{0.8 - 0.34\varepsilon_1 / \varepsilon_{cc}^{'}} \leq f_{cc}^{'} \tag{7-6}$$

A linear stress-strain relationship is assumed for concrete in tension until cracking. The concrete principal tensile stress f_1 that corresponds to concrete tensile strain ε_1 is given as:

$$f_1 = E_c \varepsilon_1 \tag{7-7}$$

The tension stiffening relationship developed by Stevens et al. (1987) for post cracking response of concrete elements is adopted. The concrete tensile stress f_1 that is related to tensile strain ε_1 is given as:

$$f_1 = f_{cr}[(1-\alpha_t)e^{-\lambda_t(\varepsilon_1 - \varepsilon_{cr})} + \alpha_t] \tag{7-8}$$

where the f_{cr} and ε_{cr} are the concrete cracking stress and strain and α_t and λ_t are factors as discussed in Section 6.2.4.

A penalty for using the average stress-strain relationship is that an explicit check must be made to ensure that the average stresses are compatible with the actual cracked condition of the concrete. In other words, the average principal tensile stress in concrete is limited to the ability of the crack surface to resist shear stresses.

The crack width w can be evaluated as:

$$w = \frac{\varepsilon_1}{\frac{\sin\theta}{S_{mx}} + \frac{\cos\theta}{S_{my}}} \tag{7-9}$$

where S_{mx} and S_{my} are the crack spacing in the x and y directions, respectively, and θ is the crack inclination to the horizontal.

Bhide and Collins (1989) used the CEB-FIP (1978) code provisions for calculating the crack spacing:

$$S_{mx} = 2(c + \frac{S_x}{10}) + 0.1\frac{d_b}{\rho_x} \tag{7-10}$$

where c is the section concrete cover, S_x is the spacing of the reinforcement in x-direction, d_b is the bar diameter and ρ_x is the reinforcement ratio.

Collins and Mitchell (1990) suggested a limiting value for the shear stress v_{ci} that could be transmitted across a crack as a function of the crack width and the aggregate size, a:

$$v_{ci} = \frac{0.18\sqrt{f_c'}}{0.3 + \frac{24w}{a+16}} \tag{7-11}$$

Hence, the maximum concrete tensile stress that can be transmitted across a crack is

(Collins et al., 1996):

$$f_{1\max} = v_{ci} \tan\theta \tag{7-12}$$

b) Compatibility Equations:

This set of equations relates the average axial and shear strains through Mohr's circle of strains. It is implicitly assumed that the angle of inclination of principal concrete stress equals to the angle of principal concrete strain and coincides with the crack inclination. From Mohr's circle, as illustrated in Figure 7-2, the angle of principal planes is:

$$\tan 2\theta = \frac{\gamma}{\varepsilon_v - \varepsilon_x} \tag{7-13}$$

where ε_x, ε_v are the axial strain in x and v directions, respectively, and γ is the shear strain and are expressed as:

$$\varepsilon_1 = \varepsilon_x + \frac{\gamma}{2} \cot\theta \tag{7-14}$$

$$\varepsilon_2 = \varepsilon_v - (\varepsilon_1 - \varepsilon_v)\cot^2\theta \tag{7-15}$$

$$\varepsilon_v = \varepsilon_1 + \varepsilon_2 - \varepsilon_x \tag{7-16}$$

The appropriate signs of the strain quantities in these equations must be adopted (i.e. negative sign for compression strain).

c) Equilibrium equations:

From the equilibrium of stresses in the concrete element, the following equation is obtained:

$$v = \frac{\frac{A_v f_v}{s\ b_v} + f_1}{\tan\theta} \tag{7-17}$$

or

$$V_j = \frac{\frac{A_v f_v d_v}{s} + f_1\ b_v\ d_v}{\tan\theta} \tag{7-18}$$

where v is the joint shear stress, V_j is the joint shear force, f_v is the steel stress, A_v is the area of the shear reinforcement, s is the spacing of the ties, b_v and d_v are width and depth of the effective shear section, respectively.

To satisfy the equilibrium of stresses of Mohr's circle, as shown in Figure 7-3, the following equation must be satisfied:

$$Error = (\cot\theta + \tan\theta)\frac{V_j}{b_v d_v} - f_1 - f_2 = 0 \tag{7-19}$$

The axial load capacity of the section is given as (Collins and Mitchell, 1990):

$$N = A_{sx} f_{sx} - V_j \cot\theta + f_1\, b_v\, d_v \tag{7-20}$$

where A_{sx} and f_{sx} are the longitudinal bars' cross sectional area and stress, respectively.

Solving these three sets of equations, the constitutive, compatibility and equilibrium equations, requires a robust iterative scheme. It should be noted that the MCFT is quite sensitive to the selection of the independent parameters. An algorithm was suggested (Collins and Mitchell, 1990), in which ε_l was assumed and then ε_v and θ were evaluated. The scheme fails in the post-ultimate concrete strength region. Another technique was suggested (Youssef, 2000), in which γ was imposed and then ε_l and θ

were evaluated. This algorithm had poor convergence characteristics. A successful technique (Bentz, 2000), based on solving a simple single finite element using the secant stiffness method, was suggested. The technique modeled the concrete element as a biaxial orthotropic model. However, the model was limited to a proportional loading case. In the current study, a better solution algorithm was found by assuming a value for γ and evaluating ε_x and ε_v. When the secant method is used, the convergence was fast. The solution strategy is shown in Figure 7-4.

7.3.2 Model verification

The proposed model was verified using the experimental results of two beam-column joints (Fuji and Morita, 1991). The two specimens, A4 and B4 represented 1/3 scale interior and exterior joint, respectively. The joint panel was 250 mm deep and 160 mm wide and was reinforced with 4 four-legged 6 mm diameter steel ties. The response of the two specimens was analytically evaluated and compared to the experimental results. Satisfactory results were obtained as shown in Figure 7-5. The proposed model was found to be effective in analyzing of the reinforced concrete joints under monotonic and cyclic loading, through envelope prediction. The experimental results of the selected joints represent the response of beam-column subassemblies, while the analytical results represent the behaviour of the joint panel only. Thus, many factors, such as the bond deterioration of the steel bars, degradation of the lap splice strength and variation of axial load, which normally occur during the experiments, are not included in the proposed model.

7.4 MODELING OF BEAM-COLUMN JOINTS WITH NO SHEAR REINFORCEMENT

The main characteristic of the existing beam-column joints (typically built before 1970) is the insufficient amount of lateral reinforcement in joint zone. The lack of shear reinforcement results in uncontrolled diagonal tension cracks in the joint panel, and eventual bond deterioration of the beam and column bars through the joint. Thus, the truss mechanism would not be fully developed and instead a strut mechanism is more applicable. A major diagonal compression strut would form to transmit the joint boundary forces. There is significant uncertainty in evaluating the shear transfer mechanism in the case of existing frame joints with very little or no shear reinforcement (Park, 2002).

In this model, the response of the joint panel before cracking will be different from the response after cracking. Before cracking, a concrete truss would form to transmit the joint boundary forces across the joint. After joint cracking, the boundary joint forces are transferred through the diagonal strut. The joint is treated as an isolated free body subjected to external boundary forces. The stresses are determined by equilibrium conditions.

7.4.1 Uncracked joint

The joint boundary forces are transmitted across the joint through concrete compression and tensile fields. The strain compatibility and stress equilibrium rules are applied. The equations described in Section 7.3 will be applied assuming no ties in the joint zone and the crack width equals zero. Thus, the joint shear stress will be resisted by

the tensile stress in concrete, or:

$$v = \frac{f_1}{\tan\theta} \tag{7-21}$$

The solution algorithm described in Section 7.3 is adopted herein.

7.4.2 Cracked joint

After joint cracking, and due to the absence of ties in the joint panel, severe deterioration of the concrete tensile strength would result in a similar deterioration of the truss mechanism. Thus, the shear forces are transferred through a major diagonal concrete compression strut, rather than a concrete truss mechanism.

Constructing a strut model is a challenging issue. The difficulties are in determining the strut dimensions and inclination. The strut dimensions are dependent on the compression block zones in the columns and the beams, which depend on the force in the reinforcement bars. Empirical strut dimensions were assumed by several researchers (Vollum and Newman, 1999; and Hwang and Lee, 1999 and 2000). Non-uniform stress trajectories develop inside the joint panel. Thus, the strut inclination varies along the joint depth.

In this study, a Fixed Angle Softened Strut Model is adopted. The strut is extended between the centre of the compression zones in the beam and the column (Vollum and Newman, 1999). The strut width is assumed based on a constant compression block depth in the beam and the column. The column compression block depth a_c, is assumed as (Paulay and Priestley, 1992):

$$a_c = (0.25 + 0.85\frac{P}{A_g f_c^{'}})\, h_c \tag{7-22}$$

where A_g is the column cross sectional area, h_c is the column depth and P is the axial load applied on the column.

The beam compression forces are transmitted within the depth of the compression zone. This depth is assumed to be:

$$a_b = 0.2\, d \tag{7-23}$$

where d is effective depth of the beam measured from the extreme compression concrete fibre to the tensile steel reinforcement. Thus, the depth of the strut a_{stu} is written as:

$$a_{stu} = \sqrt{a_c^2 + a_b^2} \tag{7-24}$$

The effective area of the diagonal strut A_{stu} is defined as:

$$A_{stu} = a_{stu}\ b_{stu} \tag{7-25}$$

where b_{stu} is the strut width which equals to the joint width.

The angle of inclination of the strut α is assumed to coincide with the inclination of the principal compression stresses, as shown in Figure 7-6. The softening concrete compression behaviour is also considered as given before by Equations (7-1) to (7-6). In order to comply with the CSA A23.3 (1994), the strut is assumed to fail at a principal compressive strain of -0.0035 mm/mm.

The joint shear force V_j is calculated as the horizontal component of the compression force in the diagonal strut:

$$V_j = f_2\ A_{stu}\ \cos\alpha \tag{7-26}$$

The vertical component of the force in the diagonal strut must be in equilibrium with the normal force applied on the section. Therefore, the normal force *N,* resisted by the section is:

$$N = A_s f_s - V_j \cot\alpha + f_1 b_j d_j \tag{7-27}$$

where, A_s is the column longitudinal reinforcement, f_s is the steel stress, b_j *and* d_j are the effective joint width and depth, respectively.

The shear strain γ can be determined from Mohr's circle as:

$$\gamma = 2(\varepsilon_x - \varepsilon_2)\cot\alpha \tag{7-28}$$

To solve the governing Equations (7-21) to (7-28), a solution strategy was suggested as shown in Figure 7-7. In this algorithm, the principal tensile strain is assumed and then the principal compression strain is evaluated to satisfy the equilibrium Equation (7-27). A fast convergence was achieved using the secant method.

7.4.3 Model verification

For illustration purpose, the model was used to evaluate the response of a beam-column joint as shown in Figure 7-8. The joint had dimensions of 600 x 600 mm, 250 mm wide, with 12 # 20 longitudinal steel bars and subjected to an applied normal stress of 0.15 f_c'. The concrete compressive and steel yield strengths were 30, 400 MPa, respectively. To clarify the contribution of ties in the response of beam-column joints, the same joint was assumed to have hoops that comply with the CSA A23.3 (1994), Clause 21.4.4.1. Thus, two-legged 15 mm diameter hoops spaced 140 mm were used. The response of the joint was then evaluated using the model proposed in Section 7.3. The ties increased the joint strength by 75% and significantly improved the joint ductility, as

shown in Figure 7-9.

The model is used to predict the shear response of joint T-S1. The experimental response of the joint was discussed in Chapters 2 and 3. Satisfactory agreement between the experimental and the analytical results was obtained, as shown in Figure 7-10. The model slightly underestimated the joint strength. The ultimate experimental joint strength occurred at shear deformation that is less than the predicted response due to the bond deterioration of the beam bars after joint cracking.

7.5 MODELING OF FRP-STRENGTHENED JOINTS

In spite of the progress in the use of the FRP materials for strengthening shear deficient structural members, the lack of accurate analytical model is a major obstacle in the application of FRP materials for strengthening real structures. To the knowledge of the author, there are no rational analytical models that can predict the response of the FRP shear rehabilitated concrete members. Thus, an analytical model, that is capable of predicting the response of these members, is developed in this section. The MCFT is adopted where the FRP sheets were discretized as distributed ties instead of the steel ties.

7.5.1 FRP-shear strengthened concrete model

When modeling beam-column joints strengthened with FRP composites, the effect of the composite jacket is first identified. In general, the composite jacket contributes to the joint strength in two ways. The first is to confine the concrete core with the associated increase in the concrete strength, $f_c^{'}$ and ductility. The second is to provide shear reinforcement to the joint panel. The composite sheets with anchored ends can be

idealized as distributed ties in the joint panel. Each of these ties has a cross sectional area of t_j x t_j and spaced t_j where t_j is the composite jacket thickness. This discretization is implemented in the MCFT, and the response of concrete panels with externally bonded FRP sheets is evaluated.

The problem is represented by three sets of equations. These are:

a) Constitutive Equations:

This set of equations represents the constitutive relationships of the concrete and the composite sheet materials. The concrete constitutive relationship in compression will be considered as discussed in Section 6.2.3. The principal compressive concrete stress is given as:

$$f_2 = \frac{f_{2\max} x r}{r - 1 + x^r} \qquad , x \leq 1.0 \tag{7-29a}$$

$$f_2 = f_{2\max} + E_g(\varepsilon_2 - \varepsilon'_{cc}) \quad , x > 1.0 \tag{7-29b}$$

where E_g is the tangent stiffness of the stress-strain relationship of the concrete, and f_{2max} is the maximum concrete strength as estimated by Equation (7-6) where f'_{cc} in Equation (7-6) is the confined concrete strength as estimated by the FRP-confined concrete model.

The elastic constitutive relation of the composite FRP material is written as:

$$f_{frp} = E_j \, \varepsilon_j \tag{7-30}$$

where f_{frp} is the tensile stress in the composite materials that is corresponding to a tensile strain of ε_j and E_j is the modulus of elasticity of the FRP materials.

b) Compatibility Equations:

As outlined earlier in Section 7.3.1b, this set of equations relates the average axial and shear strains through Mohr's circle of strains. It is implicitly assumed that the angle of inclination of principal concrete stress is taken equal to the angle of principal strain and the angle of the crack inclination. Equations (7-13) to (7-16) are implemented in this set.

c) Equilibrium equations:

The equilibrium of stresses can be derived from Mohr's circle of stresses as described in Section 7.3.1c. The shear resistance of the joint panel is evaluated as:

$$V_j = \frac{A_{frp}\, f_{frp} + f_1\, b_v\, d_v}{\tan\theta} \tag{7-31}$$

where A_{frp} is the cross sectional area of the composite jacket.

The equilibrium of stresses as given by Mohr's circle, gives:

$$Error = (\cot\theta + \tan\theta)\frac{V_j}{b_v d_v} - f_1 - f_2 = 0 \tag{7-32}$$

The axial load resistance of the section is given as (Collins and Mitchell, 1990):

$$N = A_{sx} f_{sx} - V_j \cot\theta + f_1 b_v d_v \tag{7-33}$$

The solution strategy as summarized in Figure 7-4 is adopted herein. In this algorithm, a value of the shear strain, γ was assumed and then the axial strains, ε_x and ε_y were evaluated.

7.5.2 Illustration example

For illustration purpose, joint T-S1 is assumed to be rehabilitated using two layers

of MBrace CF 130 carbon sheets or using three layers of Tyfo SEH-51A glass fibre sheets. The predicted behaviour of the rehabilitated joint is shown in Figure 7-11 and Figure 7-12. In these figures, the effect of FRP sheets as shear reinforcement, without including its effect on concrete strength and ductility, was evaluated. The combined effect of the FRP sheets, as a confining jacket and shear reinforcement, was also evaluated. It is obvious that the FRP significantly improve the joint ductility and strength as compared to the control joint.

7.6 SUMMARY

In this chapter, analytical models to predict the shear behaviour of beam-column joints with ties, without ties or rehabilitated with FRP sheets were introduced. The model for joints with steel ties was based on the MCFT. The confined concrete model of Mander et al. (1988) and post-ultimate behaviour of the concrete were introduced in the model. The model for joints without ties was based on strut mechanism. In this model, the joint shear force was resisted by the horizontal component of the compression strut force. The dimensions and inclination of the strut was assumed fixed to the failure of the strut. To model the FRP strengthened joint, the FRP sheets were discretized as distributed ties and the MFCT was adopted. The FRP-confined concrete model, developed in Chapter 6, was implemented in this model. The FRP sheets significantly improved the shear strength and ductility of FRP strengthened joints.

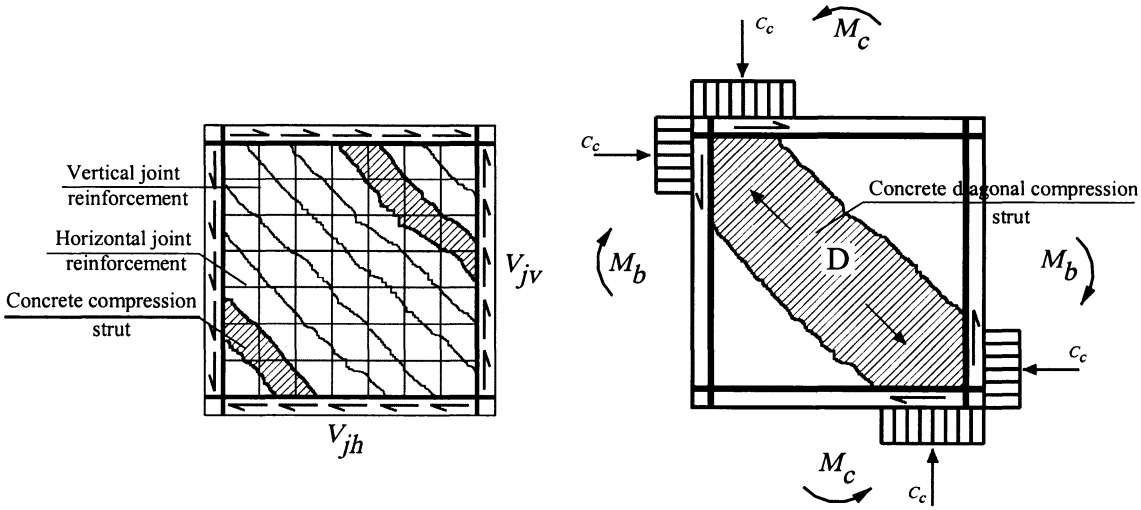

(a) Truss mechanism (b) Strut mechanism

Figure 7-1 Shear transfer mechanisms in concrete frame joints:

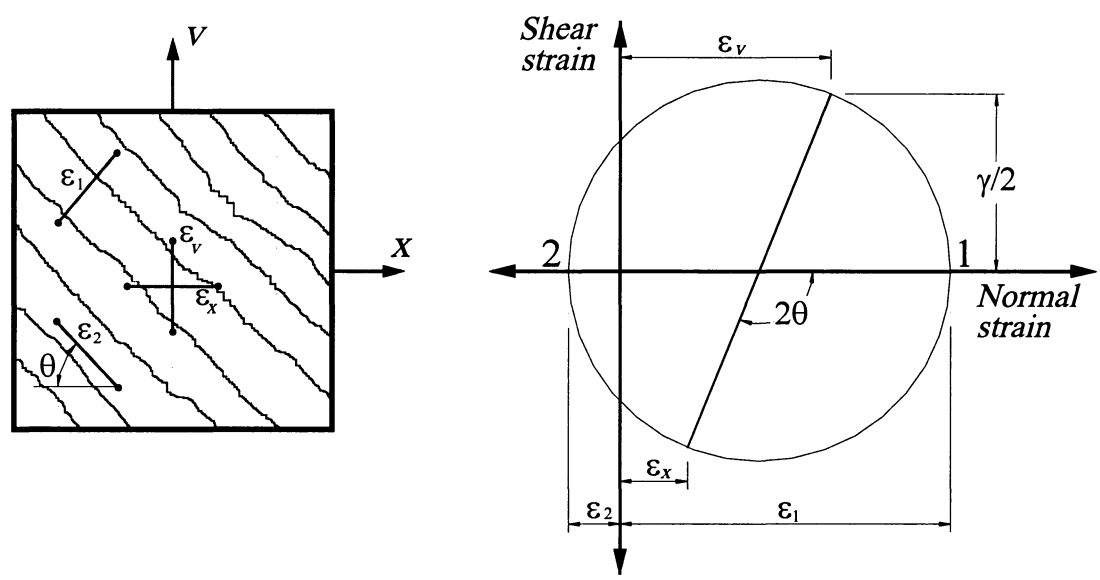

Figure 7-2 Compatibility conditions for cracked concrete element (Vecchio and Collins, 1986)

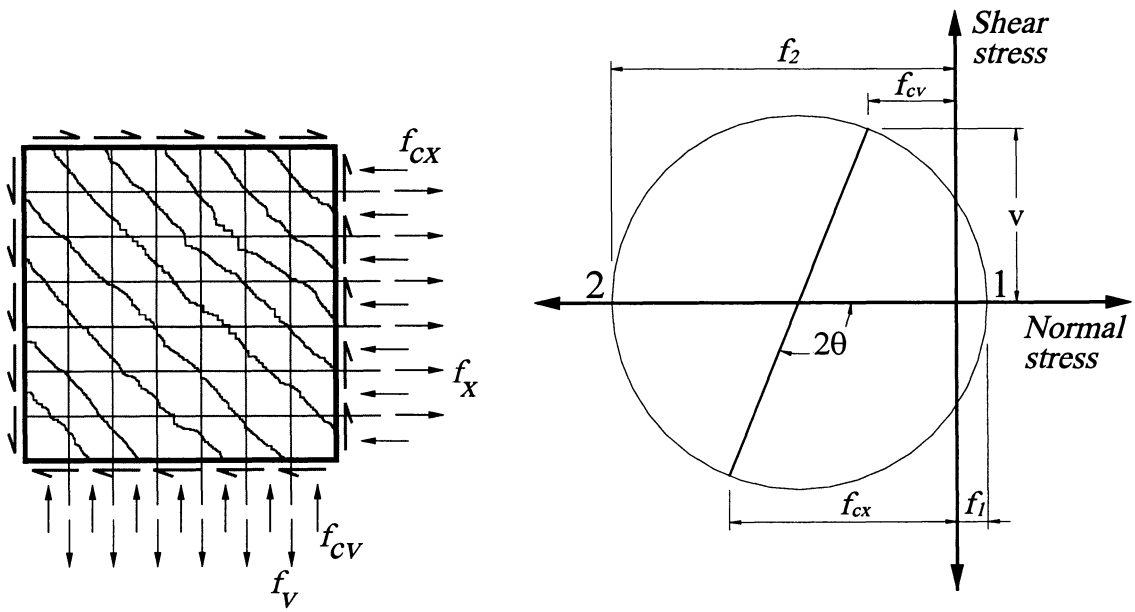

Figure 7-3 Equilibrium conditions for cracked concrete element (Vecchio and Collins, 1986)

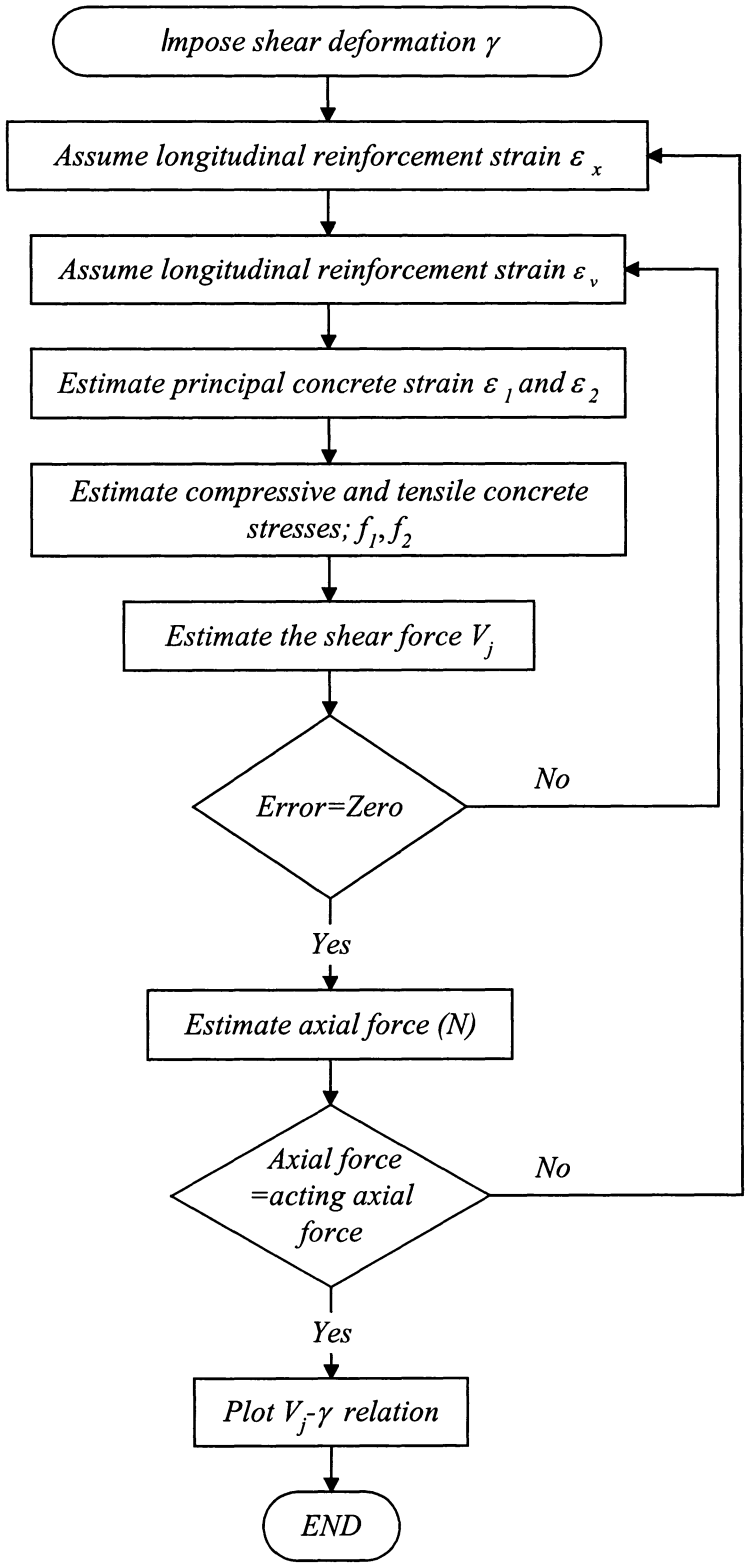

Figure 7-4 Solution algorithm for determining the shear force-strain relationship

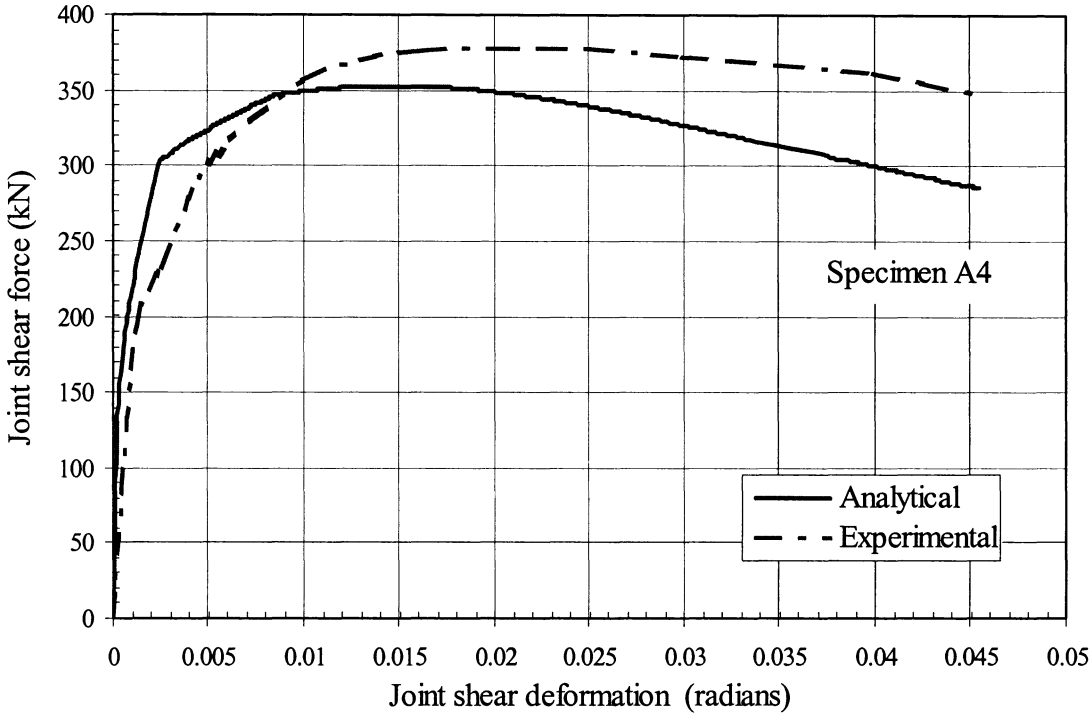

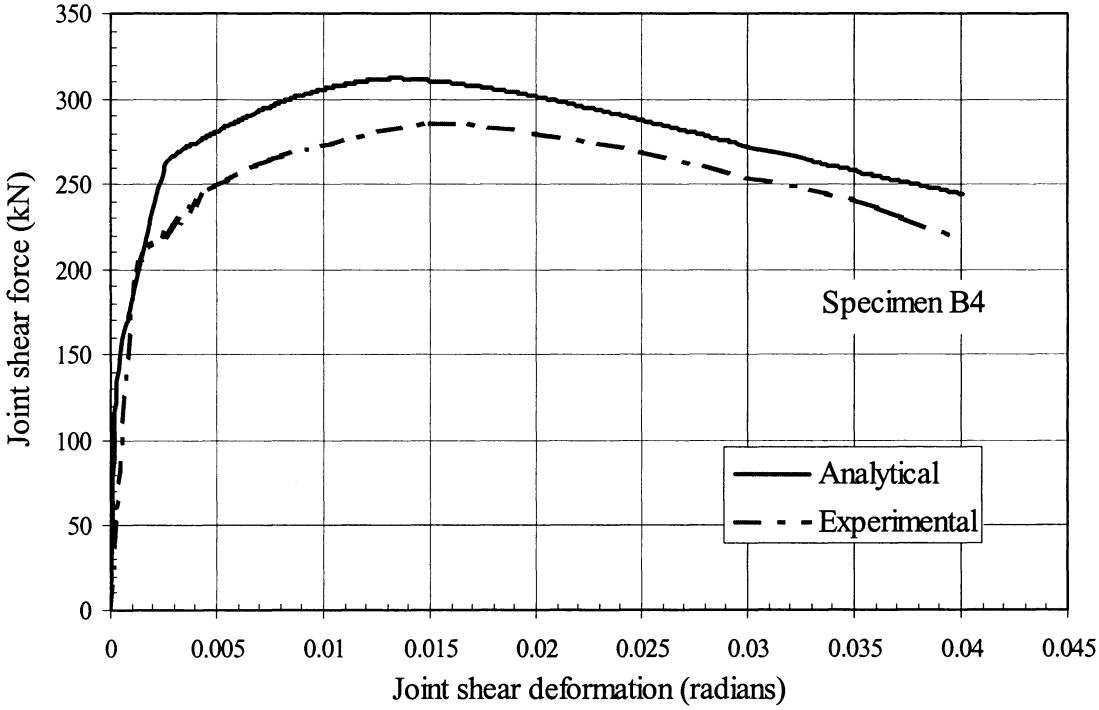

Figure 7-5 Experimental behaviour of beam-column joints (Fuji and Morita, 1991) compared to the analytical predicted behaviour

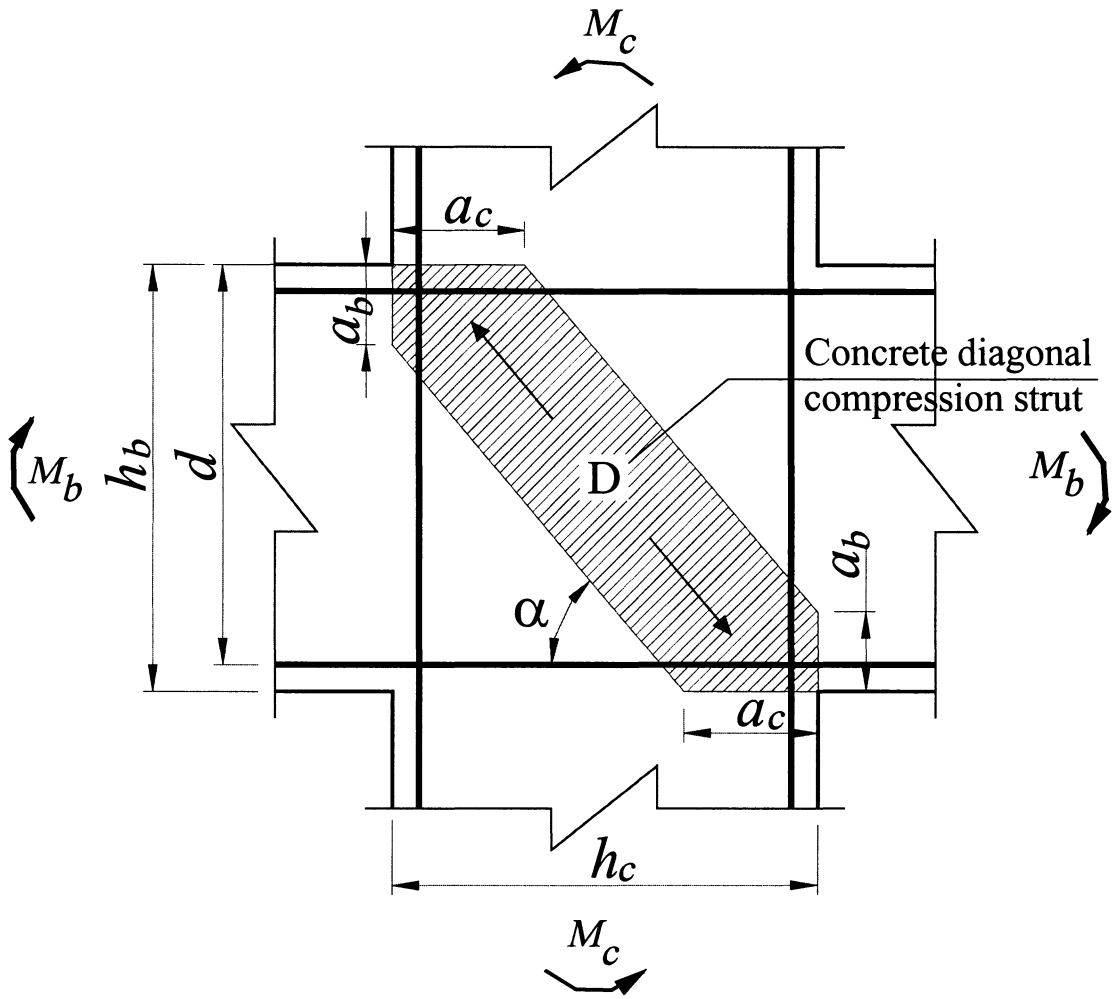

Figure 7-6 Diagonal compression strut oriented between the compression zones in the beams and the columns

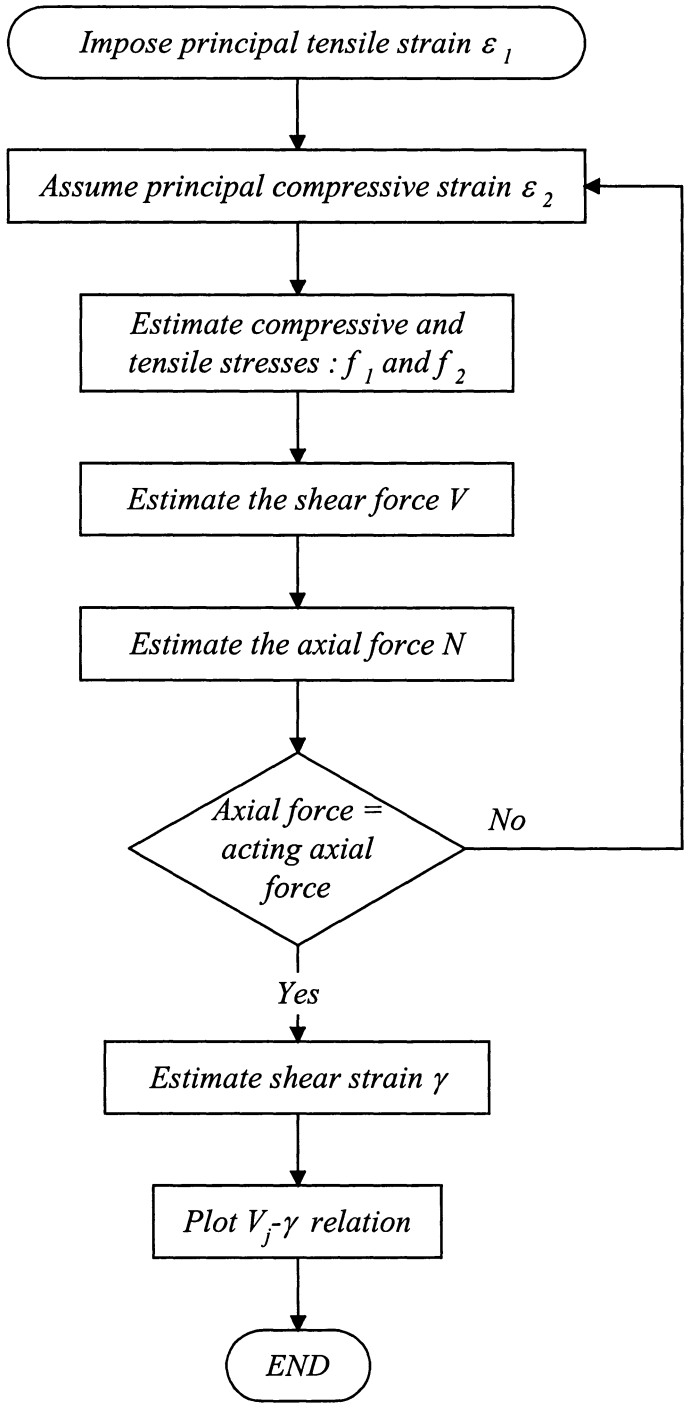

Figure 7-7 Solution strategy for the Fixed Angle Softened Strut Model

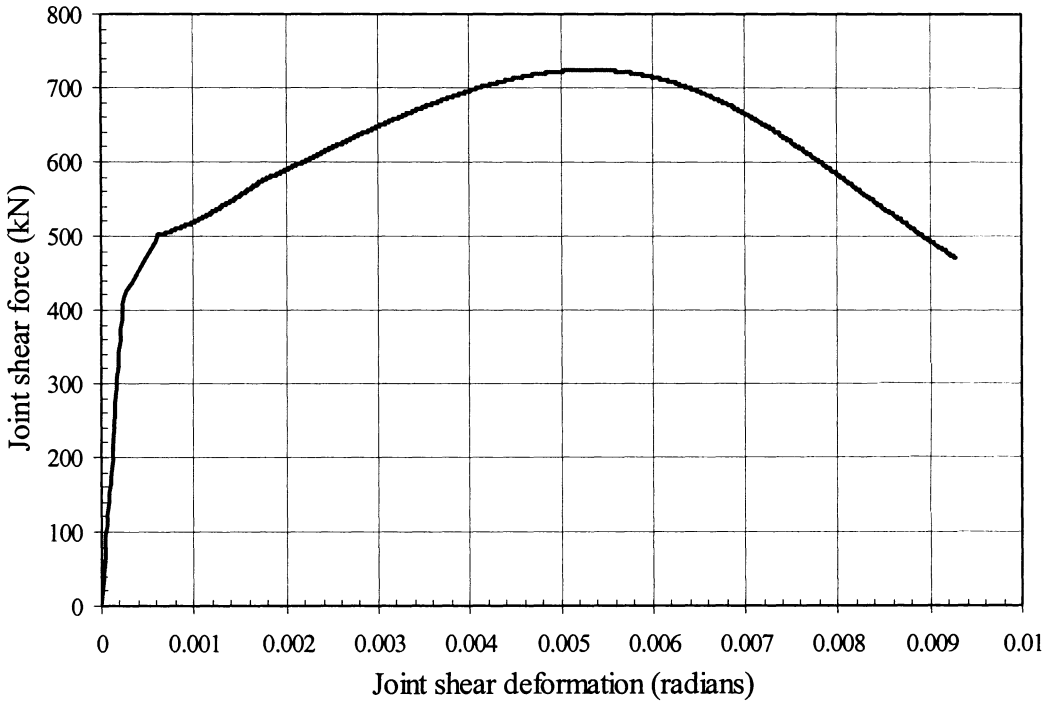

Figure 7-8 Joint shear force - deformation of a frame joint without ties

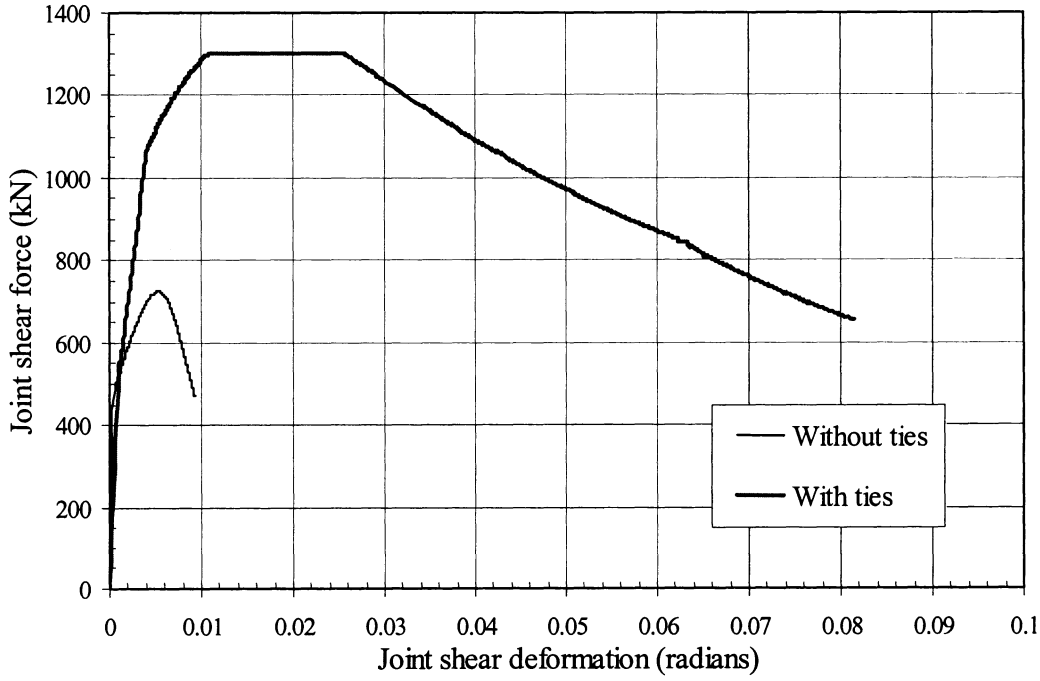

Figure 7-9 Comparison between the behaviour of a frame joint with and without joint ties

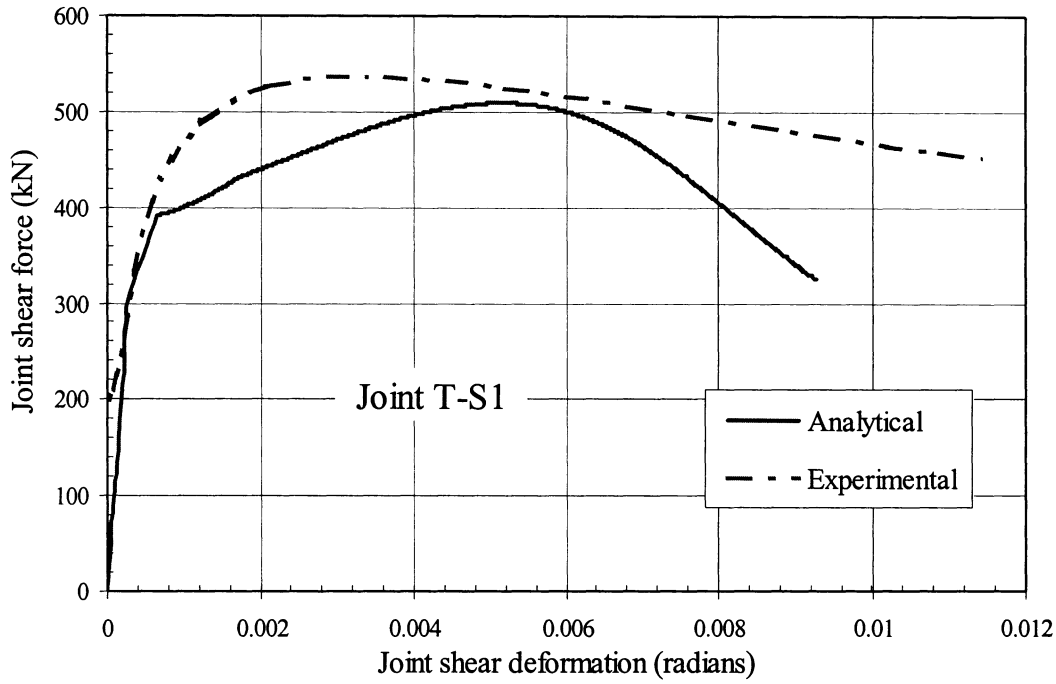

Figure 7-10 Predicted behaviour of joint T-S1

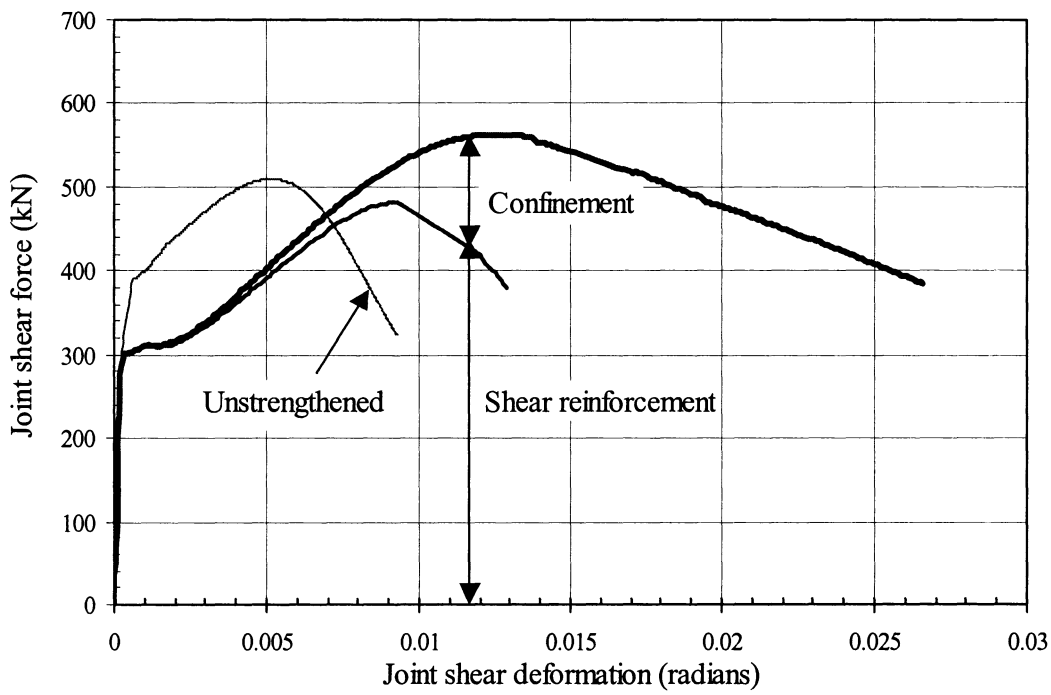

Figure 7-11 Predicted behaviour of joint T-S1 after strengthening with two CFRP sheets

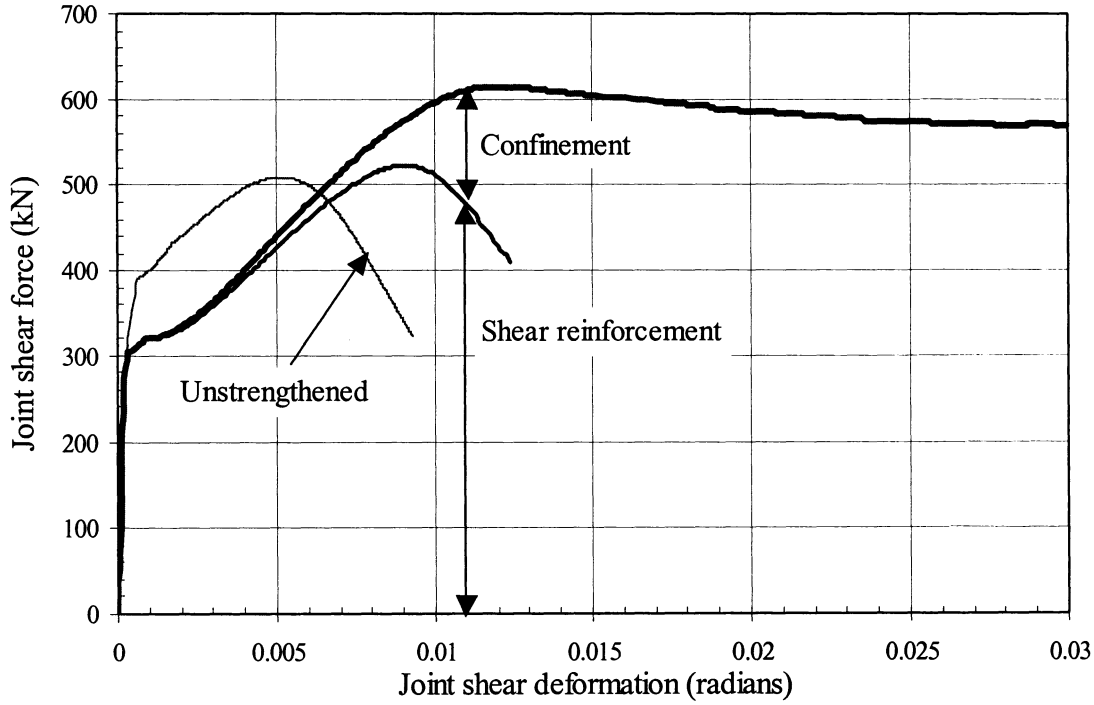

Figure 7-12 Predicted behaviour of joint T-S1 after strengthening with three GFRP sheets

This page is intentionally left blank

Chapter 8

BEAM-COLUMN JOINT MODEL

8.1 INTRODUCTION

Several models for predicting the nonlinear static and dynamic structural response have been developed. Taucer et al. (1991) classified these models into three categories: Global models, Discrete finite element models, and Microscopic finite element models. The first type is useful in the preliminary study of the structural response. For instance, a multi-storey frame could be represented as a series of lumped masses at each floor level, each with lateral degrees of freedom that has the hysteretic characteristics of the interstorey shear-lateral drift response. In discrete finite element models, or the *macroscopic models*, the structure is modeled as an assembly of interconnected elements that describe the hysteretic behaviour of reinforced concrete members. Finite element models require discretization of the element or the whole structure by a large number of elements. Thus, this approach is time consuming, needs a powerful computational system and is simply impractical to model a complete structure.

The term "*macromodeling*" refers to the process of reducing the complex behaviour of a member or connection to "equivalent" models. The concept behind macromodeling is to capture the overall behaviour of the member, subassembly or structure using "reduced" elements and "composite" action. Since the inelastic behaviour of reinforced concrete structures is mostly concentrated at known locations in an element,

such as the element ends, a macromodel approach can be used with remarkable reliability. Macromodels are computationally efficient and offer a great deal of flexibility in modeling. Since it is possible to account for a variety of behaviour patterns (strength degradation, pinching effect, etc.) in an equivalent sense, such an approach is one of the most viable alternatives in the analysis of large structural systems. Macromodel-based nonlinear analysis of RC structures relies on a set of empirical force-deformation relationships to simulate the hysteretic inelastic action in RC section. These empirical relationships are popularly referred to as *hysteretic rules*. The load-deformation rules that govern loading, unloading and reloading behaviour are derived from observed behaviour in laboratory testing. Numerous models that reproduce a range of force-deformation behaviour can be found in the literature, with considerations of strength deterioration, stiffness degradation and pinching becoming rather commonplace in structural modeling. The basic objective in developing a member model for nonlinear analysis is to adequately characterize the varying stiffness properties of the element during a cyclic loading event. Member models may be derived using stiffness or flexibility formulations.

In this chapter, the response of nine beam-column subassemblies is analytically predicted. The specimens are selected to represent the joints built according to older codes, joints that comply with the current code provisions and joints rehabilitated using FRP sheets and steel elements. The adopted kinematic models for flexural beam and column elements and for the beam-column joint are described. The analytical prediction and experimental measurements of the response of the selected specimens are compared and the effectiveness of the models is evaluated.

8.2 COMPUTATIONAL TOOL

PC-ANSR is a nonlinear structural analysis program that operates on personal computers. It is based on ANSR-1 program (Mondkar and Powell, 1975). The program was developed by Maison (1992) at the University of California, at Berkeley. The program is written in a FORTRAN 77 language. It contains six basic elements, 3D linear and nonlinear truss elements, 2D linear and nonlinear beam elements, nonlinear gap element and nonlinear brace element. Three new elements, concrete spring element, steel spring element and shear spring element, were recently added to the program (Youssef, 2000). The theory and solution procedure used are based on finite element displacement formulation, with the nodal displacements as degrees of freedom. The structure mass is assumed to be lumped at the nodes, so that the mass matrix is diagonal. Loads are applied at the nodes only. Static loads are applied in an incremental manner with allowance for a combination of static load patterns to be applied. Dynamic loads may be either in the form of ground excitation or nodal dynamic forces. The program can perform static, dynamic or static followed by dynamic analyses. Different iteration types, including Newton-Raphson or constant stiffness iterations, may be performed. For dynamic analysis, Newmark's β-γ-δ integration method is used.

Performing a displacement-controlled analysis is necessary for the seismic analysis of structures in the inelastic range. The main objective of this analysis is to predict the ductility capacity of the building. Since PC-ANSR performs only load-controlled analysis, modification of the program is necessary. A relatively accurate procedure is conducted to perform the displacement-control analysis. As shown in Figure

8-1, two elastic springs are connected in series to the point at which the displacement is applied. To impose a certain displacement "u" on the structure, an equivalent force "*P*" is applied at the connection between the two springs. The value of the force *P* equals "K_2 *u*", where K_2 is the smaller stiffness of the two springs. The ratio of the equivalent stiffness of the two springs and the stiffness of structure is an important parameter that affects the accuracy of the approach. A reasonable ratio between the stiffness of the structure K_{st} and the equivalent stiffness of the two springs is 1 to 1000 (Elmorsi, 1998). The hysteretic behaviour of the structure can be established as the relationship between the force in the spring of bigger stiffness and the recorded displacement.

8.3 KINEMATIC MODELS

In this study, the concept of macromodeling is adopted. The flexural elements are modeled as elastic beam-column element with inelastic concrete and steel springs at their ends to capture the inelastic flexural behaviour. The beam-column joint is represented by four pin-connected rigid elements, which are diagonally connected by two inelastic shear springs.

8.3.1 Flexural elements

Nonlinear modeling of concrete flexural elements received much attention since the mid of 1960's. Various types of elements were proposed. These include global elements, fibre elements where the member is divided into longitudinal axial fibres of infinitesimal cross-sectional area, and multi-springs elements. To capture the nonlinear response, several approaches may be adopted, such as lumped plasticity, distributed

plasticity or fibre formulation. A successful element should represent the characteristics of concrete structural elements hysteretic behaviour such as pinching, stiffness degradation and strength softening.

A multi-spring model of concrete flexural element was proposed (Lai et al., 1984). The member is represented as an elastic beam-column element with five zero-length inelastic springs at member ends as shown in Figure 8-2. Each of the four exterior springs represents the stiffness of the effective reinforcing bars and the surrounding concrete in compression. The spring at the centre represents the effective concrete in the central region of the section. The capacity of the exterior concrete springs was based on the balanced condition, whereas the spacing between the exterior springs was determined from the condition that the inelastic springs at yielding must produce the same yielding moment of the original section at the balanced condition.

Further refinement of this model was implemented (Jiang and Saiidi, 1990). The five concrete springs and four steel springs were replaced with four composite springs. The model was able to predict the stiffness degradation but was lacking strength softening.

The Lai's model was used to model unidirectional flexural members (Youssef and Ghobarah, 1999). The inelastic springs were reduced to three steel springs and three concrete springs. The properties of the concrete springs were determined using the acting axial load instead of the balanced condition. The spacing between exterior springs was determined such that the inelastic springs produce the same ultimate moment of the original section.

In this study, Lai's model is adopted to represent the flexural concrete beam and column members. The flexural element is represented by an elastic beam-column element with three steel and three concrete springs at each end. The response of the steel springs is determined as described in Section 6.4. Thus, the steel spring represents the interaction between the steel and the surrounding concrete. The hysteretic response developed by Youssef and Ghobarah (1999), as shown in Figure 8-3, is adopted. The monotonic response of the spring is represented by an initial elastic stiffness K_s to the steel yield force P_{sy}, then a post-yield stiffness rK_s to the steel ultimate force P_{su}. To represent the post-slip failure behaviour of the steel spring, the steel force P_s corresponding to steel displacement d_s is given as (Youssef and Ghobarah, 1999):

$$P_s = P_{su}[R_{so} + \frac{1 - R_{so}}{1 + \alpha_s (d_s - d_{su})^2}] \tag{8-1}$$

where d_{su} is the steel spring displacement that corresponds to the ultimate steel force

R_{so} is the ratio between the residual steel force and ultimate steel force

α_s is the softening factor

The effective area of the exterior concrete spring, A_{ce} is determined as the compression zone at ultimate moment. The effective area of the central spring, A_{ci} equals:

$$A_{ci} = A_g - 2A_{ce} - \sum A_{st} \tag{8-2}$$

where A_g is the gross cross-sectional area

$\sum A_{st}$ is the sum of steel bars cross-sectional areas

The yield force of the concrete spring, P_{cy} that corresponds to concrete ultimate

strength, equals:

$$P_{cy} = 0.85 k_h A_c f_c^{'} \tag{8-3}$$

where $A_c = A_{ce}$ for exterior spring

$= A_{ci}$ for interior spring

k_h is the confinement coefficient and equals $\frac{f_{cc}^{'}}{f_c^{'}}$

The plastic deformation of the effective concrete element is postulated to represent the accumulated concrete crushing behaviour over the member length. The concrete spring yield displacement, d_{cy} that corresponds to the yield spring force is determined as the integration of the strain at ultimate condition over the member length. The hysteretic response of the concrete springs (Youssef, 2000), as shown in Figure 8-4, is adopted. The monotonic response of the concrete spring in compression is represented by a parabola to the spring yield force. The post yield response is represented by a straight line of slope Z. The spacing between exterior springs, d_{sp} is determined such that the inelastic springs produce the same yield moment of the original section.

8.3.2 Beam-column joints

The beam-column joint is one of the critical elements in moment resisting frames. In traditional analysis of reinforced concrete frames, beam-column joints are assumed rigid. Post-earthquake field surveys emphasized the need to include the deformation of beam-column joints of existing structures. The joint deformation is governed by shear deformation and bond-slip behaviour of the beam bars. A successful joint model should be able to represent these two causes of deformations and different failure modes such as

joint shear failure, concrete crushing and bond-slip.

In this study, the kinematic joint model proposed by Youssef and Ghobarah (2001) is adopted. In this model, the joint core is represented by four rigid pin-connected elements. Two diagonal shear springs connect the corners of the joint core. During the analysis, the joint shear force–shear deformation is predicted as discussed in Chapter 7. The force in each of the diagonal springs, F can be calculated from simple equilibrium (Youssef and Ghobarah, 2001) as:

$$F = \frac{V_j}{2\cos\phi} \tag{8-4}$$

where V_j is the joint shear force

ϕ is the spring inclination

The deformation of the spring can be estimated from the joint shear rotation using simple geometry rules (Youssef and Ghobarah, 2001). The hysteretic response of the shear springs is shown in Figure 8-5.

8.4 APPLICATIONS

To illustrate the use of the proposed concrete, steel and shear models, and to verify the applicability of the adopted kinematic model to represent various types of RC frame joints, nine examples were analyzed. These examples were selected to cover the current-code designed joints (one case), the deficient existing joints (four cases) and the FRP-rehabilitated joints (four cases). The kinematic model that is used to represent the beam-column subassemblies is shown in Figure 8-6.

8.4.1 Current-code designed joint

As the behaviour of the current seismic codes designed joints are not of interest in this study, only one specimen was analyzed. The specimen J2 (Ghobarah et al., 1997) represented an exterior joint that was designed according to the current Canadian concrete design code (CSA A23.3-94, 1994). The beam was 610 mm high and 610 mm wide, whereas the column was 510 mm high and 610 mm wide. The specimen was tested in a test set-up similar to the one used in the current study. A quasi-static load was applied at the beam tip with a moment span of 1120 mm. A constant axial load of 505 kN was applied to the column. The beam was reinforced with 7 # 15 bars as top and bottom reinforcement which were hooked in the joint zone. The joint zone was reinforced with # 10 steel ties spaced 96 mm. The plastic hinge zones in the column above and below the joint were adequately confined with # 10 steel ties spaced 96 mm, as shown in Figure 8-7.

The unconfined concrete strength of the specimen, as tested, was 22.0 MPa. The analytical confined concrete behaviour was predicted using Mander's model, as explained in Section 6.2.2, and is shown in Figure 8-8a. The ultimate concrete strength in the beam and column was 29.74 and 35.69 MPa, respectively. The difference in concrete strength is due to the different confinement conditions provided by steel ties in the column and the beam. The joint shear behaviour is shown in Figure 8-8b. No degradation of joint shear strength was expected to occur. The seven beam top or bottom bars were represented by one exterior steel spring whereas the four middle bars were represented by another spring. The four exterior column steel bars were represented by a

single steel spring and so the four intermediate bars. The response of the column and beam steel bars are shown in Figure 8-8c to e. Fracture of the bars was expected to occur before anchorage-slip. This is due to the proper anchorage conditions of the steel bars. The exterior beam bars; top and bottom bars; reached larger displacement than the displacement of the column bars. This is because the bar displacement is the integration of the strain along the bar length which corresponds to the stress of the bar. Whereas the force in the column bars varies between a maximum value at the bar tip and zero at the bar end, the force in the exterior beam bars varies between a maximum value at the bar tip and a smaller value at the hook. Table 8-1 lists all the calculated parameters of steel and concrete springs.

The experimental and the analytical response of the specimen are shown in Figure 8-9. The peak recorded joint response was 400 kN. Minor cracks were observed in the joint zone. Flexural hinging failure mode of the beam occurred. High shear at the flexural hinge caused rapid deterioration and disintegration of the concrete in the hinge zone. The analytical prediction agrees fairly well with the experimental results. Although, the model slightly overestimated the ultimate specimen strength, the model predicted the stiffness degradation and strength deterioration satisfactorily.

8.4.2 Pre-seismic code designed joints

To verify the ability of the model to predict the response of deficient existing joints, four specimens were analyzed. Three specimens were experimentally tested in this study; T-B10, T-S1 and T-SB3 and the last one is specimen J1 (Ghobarah et al., 1996).

8.4.2.1 Joint T-B10

The beam bottom bars of the specimen were anchored 150 mm into the joint zone whereas adequate amount of steel ties were installed in the joint zone. Thus, the joint has anchorage strength deficiency of the beam bottom bars. The specimen reinforcement details and experimental behaviour were described in Chapters 2 and 4, respectively.

The analytical concrete stress-strain relationships for the specimen elements as predicted by the concrete material models are shown in Figure 8-10a. The difference between the concrete behaviour in beam, column and joint is due to the different confinement conditions. The joint shear response is shown in Figure 8-10b. The degradation of the joint shear strength is due to the degradation of concrete compression stress due to the coexisting principle tensile strain. The two beam top or bottom bars were represented by a single steel spring. The three exterior column bars were represented by a single steel spring and so the two middle bars. The response of the column and beam steel bars are shown in Figure 8-10c to f. Although the short embedment length of the beam bottom bars, yielding of the bars occurred which coincides with the experimental measurements. Following the yield onset, degradation of the force in the steel bars was predicted due to the failure of the steel-to-concrete bond strength, which is known as bond-slip failure mode. Table 8-2a and b list all the parameters of steel and concrete springs. Due to the different behaviour of the top and bottom beam steel springs, the location of these springs with respect to the beam centre line was different.

Comparison between the joint experimental and analytical beam-tip load-displacement is shown in Figure 8-11. The model agrees well with the experimental

results. Bond-slip failure mode was predicted in the positive loading direction while the negative joint strength was preserved.

8.4.2.2 Joint T-S1

The specimen represented an exterior beam-column joint with deficient joint shear strength. No ties were installed in the joint zone. The beam bars were bent in the joint zone to improve the anchorage condition. The specimen reinforcement details and experimental behaviour were described in Chapters 2 and 3, respectively.

The analytical concrete stress-strain response of the joint elements, as predicted by the concrete material models, are shown in Figure 8-12a. The joint concrete behaviour in compression was predicted using the Popovics's model for unconfined concrete whereas the concrete behaviour of the beam and column was predicted using the Mander's model. The joint shear response is shown in Figure 8-12b. The response of the column and beam steel bars are shown in Figure 8-12c to f. No anchorage failure of the steel beam bars is expected to occur. Table 8-3 lists all the calculated parameters for the steel and concrete springs.

Comparison between the specimen experimental and analytical beam-tip load-displacement is shown in Figure 8-13. Satisfactory agreement between the experimental and the analytical results was demonstrated.

8.4.2.3 Joint T-SB3

The specimen represented an exterior beam-column joint with deficient joint shear strength and anchorage strength of beam bars. No ties were installed in the joint

zone. The beam top bars were hooked in the joint zone to improve the anchorage condition whereas the beam bottom bars were anchored 150 mm into the joint zone. The specimen reinforcement details and experimental behaviour were described in Chapters 2 and 5, respectively.

The analytical concrete stress-strain response for the specimen elements, as predicted by the concrete material models, are shown in Figure 8-14a. The joint shear response is shown in Figure 8-14b. The response of the column and beam steel bars are shown in Figure 8-14c to f. Bond-slip failure of the beam bottom bars was predicted slightly before the onset of yielding. Table 8-4 lists all the calculated parameters of steel and concrete springs.

Comparison between the specimen experimental and analytical beam-tip load-displacement is shown in Figure 8-15. Although the model predicted the strength softening and stiffness degradation fairly well, the model overestimated the specimen ultimate strength. This was due to the absence of ties in the joint zone which resulted in inadequate confinement in the embedment zone of beam bars. Therefore, the bars tensile strength would degrade just after the developing of bond cracks, which was not accounted for in the adopted concrete-to-steel bond law. In other words, the adopted bond law is only valid for well-confined concrete elements.

8.4.2.4 Specimen J1

The specimen represents an exterior beam-column joint with deficient joint shear strength (Ghobarah et al., 1996). Four ties of 10 mm diameter, which represent 50% of

the required shear reinforcement, were installed in the joint zone. The beam bars were bent into the joint zone to improve the anchorage condition. The specimen had the same concrete dimensions as specimen J2. The specimen reinforcement details are shown in Figure 8-16.

The analytical concrete stress-strain response for the specimen elements, as predicted by the concrete material models, are shown in Figure 8-17a. The joint shear response is shown in Figure 8-17b. As opposite to specimen J2, degradation of the joint shear strength occurred. The response of the column and beam steel bars are shown in Figure 8-17c to e. No bond-slip failure of the steel bars is expected to occur. Table 8-5 lists all the calculated parameters of steel and concrete springs.

Comparison between the specimen experimental and analytical beam-tip load-displacement relationships is shown in Figure 8-18. The model agrees well with the experimental results. The analysis overestimated the specimen strength because the adopted steel-to-concrete bond laws are valid for well-confined anchorage zones as discussed earlier.

8.4.3 FRP-rehabilitated specimens

Four joints were analyzed to verify the validity of the model to predict the response of FRP-rehabilitated joints. Two of the joints were tested in this study; T-S4R and T-SB7; and the others were tested by other authors; T2R (Ghobarah and Said, 2002) and Specimen # 3 (Clyde and Pantelides, 2002).

8.4.3.1 Joint T-S4R

This joint represented a full-scale exterior frame joint that was deficient in joint shear strength. The specimen was strengthened using three CFRP sheets wrapped around the joint zone. The specimen reinforcement details were described in Chapter 2, whereas the specimen experimental response was discussed in Chapter 3.

The analytical concrete stress-strain response for the specimen elements, as predicted by the concrete material models, are shown in Figure 8-19 a and b. The monotonic response of the concrete in the joint zone showed no degradation until failure of the CFRP jacket. The joint shear response is shown in Figure 8-19c. Contrary to the joints reinforced with steel ties; such as joint T-B10; or joints without ties; such as joint T-S1, the joint showed an increasing shear resistance to the failure of the composite jacket. This was due to the confinement effect provided by the jacket and the subsequent increase in concrete strength. The response of the column and beam steel bars are shown in Figure 8-19d to f. Table 8-6 lists all the calculated parameters of steel and concrete springs.

Comparison between the specimen experimental and analytical hysteretic response is shown in Figure 8-20. The model agrees in general features with the experimental results. However, the model could not predict the specimen strength at failure because of the unexpected fracture of one of the beam top bars and the subsequent twisting of the beam section.

8.4.3.2 Joint T-2R

The joint represented an exterior beam-column joint that was deficient in joint shear strength (Ghobarah and Said, 2002). No ties were installed in the joint zone. The specimen had the same concrete dimensions and reinforcement details as joint T-S4R. GFRP jacket was used to improve the joint shear strength. The jacket was composed of two bi-directional GFRP sheets mounted on the joint zone and another composite layer covers 300 mm of the column above and below the joint. The ends of the composite sheets were anchored using two side steel plates and four steel tie rods drilled through the joint.

The analytical concrete stress-strain response of the specimen elements, as predicted by the concrete material models, are shown in Figure 8-21a and b. The joint shear response is shown in Figure 8-21c. The response of the column and beam steel bars are shown in Figure 8-21d to f. Table 8-7 lists all the parameters of steel and concrete springs.

Reasonable agreement between the experimental and analytical response was achieved, as shown in Figure 8-22. High shear at flexural beam hinge caused rapid deterioration and disintegration of the concrete in the hinge zone, which was not included in the model.

8.4.3.3 Joint T-SB7

The specimen represented full-scale exterior frame joint that has joint shear strength and beam bars anchorage strength deficiencies. The joint shear strength was

improved using GFRP jacket whereas a steel bridle was welded to the beam bottom bars to improve their anchorage conditions. The dimensions and reinforcement details of this joint were described in Chapter 2, whereas details of the rehabilitation scheme and the experimental response of the joint were discussed in Chapter 5.

The analytical concrete stress-strain response of the specimen elements, as predicted by the concrete material models, are shown in Figure 8-23a and b. As compared to joint T-S4R, the concrete strength in the joint zone showed a more gradual strength increase as a result of the low stiffness of the GFRP jacket as compared to the CFRP jacket. The monotonic response of the concrete in the joint zone showed no degradation until failure of the GFRP jacket. The joint shear response is shown in Figure 8-23c. A slight decrease of joint shear strength followed by a strength recovery was noted. The response of the column and beam steel bars are shown in Figure 8-23d to f. Table 8-8 lists all the calculated parameters of steel and concrete springs.

Comparison between the specimen experimental and analytical response is shown in Figure 8-24. Excellent agreement between the experimental and analytical results in terms of strength and stiffness was achieved. However, the model underestimated the pinching in the loading cyclic and overestimated the unloading stiffness. It is worth mentioning that there is as yet no rational model for predicting the unloading stiffness in inelastic concrete elements.

8.4.3.4 Specimen # 3

A half-scale reinforced concrete exterior beam-column joint was constructed with

deficient joint shear strength (Clyde and Pantelides, 2002). The beam was reinforced using 4 # 9 (28 mm diameter) hooked bars as top and bottom reinforcement. No ties were installed in the joint zone. The dimensions and reinforcement details of the specimen are shown in Figure 8-25. To simulate the column gravity load, a constant axial stress of $0.1 f_c^{'}$ was applied to the column. To improve the joint shear resistance, four CFRP sheets were wrapped around the joint zone at an angle of ± 51° to the column axis. The column and beam regions near the joint were wrapped with CFRP sheets for confinement as shown in Figure 8-26. A quasi-static cyclic load was applied to the beam tip to simulate the seismic actions.

The analytical concrete stress-strain response of the specimen elements, as predicted by the concrete material models, are shown in Figure 8-27a and b. The monotonic response of the concrete in the joint zone showed no strength degradation until failure of the CFRP jacket. The joint shear response is shown in Figure 8-27c. The response of the column and beam steel bars are shown in Figure 8-27d to f. Table 8-9 lists all the parameters of steel and concrete springs.

Comparison between the specimen experimental and analytical lateral drift-lateral load is shown in Figure 8-28. Good agreement between the analytical and experimental response is shown. The model was capable of predicting the specimen ultimate strength, post-ultimate strength and stiffness degradation. However, pinching of the analyzed joint was underestimated. This was because the hysteretic model of the steel springs did not account for the degradation of unloading and reloading stiffness.

8.5 SUMMARY

In this chapter, a kinematic beam-column joint model was adopted with some refinements include the estimate of the model parameters. The proposed materials and shear models discussed in Chapters 6 and 7 were used to estimate the parameters of the model components. Nine exterior beam-column joints were selected to cover the current code designed, pre-seismic code design and FRP-rehabilitated joints. Satisfactory agreement was found between the analytical prediction and the experimental measurements for the analyzed joints. The adopted steel-to-concrete bond laws proved to overestimate the behaviour of steel bars in unconfined anchorage zones. The model successfully predicted the joints ultimate strength, strength deterioration and stiffness degradation.

Table 8-1 Model parameters of specimen J2

	Parameter	Beam	Upper column	Lower column
Exterior Steel Spring	d_{su} (mm)	36.000	15.554	15.554
	P_{sy} (kN)	688.11	371.71	371.71
	K_s (kN/mm)	1791.01	1032.53	1032.53
	r	0.0070	0.0124	0.0124
	R_{so}	----	----	----
	α_s	----	----	----
Central steel Spring	d_{su} (mm)	11.500	15.554	15.554
	P_{sy} (kN)	165.00	371.71	371.71
	K_s (kN/mm)	529.84	1032.53	1032.53
	r	0.0160	0.0124	0.0124
	R_{so}	----	----	----
	α_s	----	----	----
Exterior concrete spring	P_{cy} (kN)	790.51	1131.57	1131.57
	d_{cy} (mm)	0.402	0.652	0.828
	K_h	1.35	1.62	1.62
	Z	28.07	26.17	26.17
Central concrete spring	P_{cy} (kN)	5317.42	3509.54	3509.54
	d_{cy} (mm)	1E-06	0.481	0.610
	K_h	1.35	1.62	1.62
	Z	28.01	26.17	26.17
Distance between exterior springs (mm)		522.30	473.89	473.89

Table 8-2a Parameters of steel springs in beam and columns of specimen T-B10

Parameter	Beam		Column	
	Bottom steel spring	Top steel spring	Exterior steel spring	Central steel spring
d_{su} (mm)	2.798	21.441	14.255	15.960
P_{sy} (kN)	310.60	300.00	500.00	210.00
K_s (kN/mm)	409.93	857.14	1067.85	494.04
r	0.0076	0.0100	0.0103	0.0125
R_{so}	0.369	---	0.540	----
α_s	0.195	---	0.209	----

Table 8-2b Parameters of concrete springs in beam and columns of specimen T-B10

Parameter	Top concrete spring	Central concrete spring	Bottom concrete spring	Exterior concrete spring	Central concrete spring
P_{cy} (kN)	396.47	2143.78	396.47	1000.37	837.33
d_{cy} (mm)	0.244	0.002	0.027	0.874	0.052
K_h	1.12	1.12	1.12	1.20	1.20
Z	37.40	37.40	37.40	24.41	24.41
Location* of exterior springs	-128.70, 139.82			-140.82, 140.82	

* With respect to the members axis.

Table 8-3 Model parameters of joint T-S1

Parameter	Beam		Column	
	Exterior steel spring	Central steel spring	Exterior steel spring	Central steel spring
d_{su} (mm)	23.745	NA	9.102	12.940
P_{sy} (kN)	620.00	NA	478.18	170.13
K_s (kN/mm)	1080.52	NA	683.11	401.25
r	0.0129	NA	0.0189	0.0184
R_{so}	----	NA	0.489	----
α_s	----	NA	0.135	----
Parameter	Exterior concrete spring	Central concrete spring	Exterior concrete spring	Central concrete spring
P_{cy} (kN)	554.10	2011.30	1077.06	1112.17
d_{cy} (mm)	0.577	0.010	0.898	0.052
K_h	1.16	1.16	1.13	1.13
Z	26.01	26.01	28.78	28.78
Distance between exterior springs (mm)	283.55		290.04	

Table 8-4 Model parameter of specimen T-SB3

Parameter	Beam		Column	
	Exterior steel spring	Central steel spring	Exterior steel spring	Central steel spring
d_{su} (mm)	3.129	25.317	9.766	16.441
P_{sy} (kN)	568.56	642.12	460.19	175.40
K_s (kN/mm)	495.39	1008.83	794.80	404.04
r	0.0028	0.0125	0.0170	0.0121
R_{so}	0.333	---	0.488	0.567
α_s	0.130	---	0.134	0.132
Parameter	Exterior concrete spring	Central concrete spring	Exterior concrete spring	Central concrete spring
P_{cy} (kN)	484.97	1568.64	932.19	679.39
d_{cy} (mm)	1.032	0.0001	0.932	0.023
K_h	1.12	1.12	1.12	1.12
Z	53.09	53.09	37.40	37.40
Distance between exterior springs (mm)	264.75		288.35	

Table 8-5 Model parameters of specimen J1

	Parameter	Beam	Upper column	Lower column
Exterior Steel Spring	d_{su} (mm)	320.240	18.951	18.951
	P_{sy} (kN)	658.11	384.63	384.63
	K_s (kN/mm)	17129.93	1046.05	1046.05
	r	0.0102	0.0090	0.0090
	R_{so}	----	0.457	0.457
	α_s	----	0.102	0.102
Central steel Spring	d_{su} (mm)	16.118	18.951	18.951
	P_{sy} (kN)	216.71	384.63	384.63
	K_s (kN/mm)	742.66	1046.05	1046.05
	r	0.0090	0.0090	0.0090
	R_{so}	----	0.457	0.457
	α_s	----	0.102	0.102
Exterior concrete spring	P_{cy} (kN)	825.97	1158.59	1158.59
	d_{cy} (mm)	0.386	0.592	0.592
	K_h	1.17	1.12	1.12
	Z	21.54	37.15	37.15
Central concrete spring	P_{cy} (kN)	5748.19	3875.34	3875.34
	d_{cy} (mm)	1E-05	0.945	0.945
	K_h	1.17	1.12	1.12
	Z	21.54	37.15	37.15
Distance between exterior springs (mm)		517.70	469.45	469.45

Table 8-6 Model parameters of specimen T-S4R

Parameter	Beam		Column	
	Exterior steel spring	Central steel spring	Exterior steel spring	Central steel spring
d_{su} (mm)	25.296	NA	13.517	12.294
P_{sy} (kN)	620.00	NA	489.31	176.48
K_s (kN/mm)	1080.52	NA	815.51	542.36
r	0.0138	NA	0.0144	0.0135
R_{so}	----	NA	0.532	----
α_s	----	NA	0.200	----
Parameter	Exterior concrete spring	Central concrete spring	Exterior concrete spring	Central concrete spring
P_{cy} (kN)	558.24	1953.05	780.10	311.05
d_{cy} (mm)	0.561	0.010	5.595	2.770
K_h	1.20	1.20	1.16	1.16
Z	18.63	18.63	25.21	25.21
Distance between exterior springs (mm)	284.04		289.88	

Table 8-7 Model parameters of Specimen T2R

Parameter	Beam		Column	
	Exterior steel spring	Central steel spring	Exterior steel spring	Central steel spring
d_{su} (mm)	22.986	NA	11.964	12.813
P_{sy} (kN)	649.54	NA	468.19	181.56
K_s (kN/mm)	1312.46	NA	916.94	626.93
R	0.0104	NA	0.0144	0.0103
R_{so}	----	NA	0.515	----
α_s	----	NA	0.173	----
Parameter	Exterior concrete spring	Central concrete spring	Exterior concrete spring	Central concrete spring
P_{cy} (kN)	485.74	1567.10	930.51	682.76
d_{cy} (mm)	0.518	1.040	0.921	0.024
K_h	1.16	1.16	1.13	1.13
Z	28.50	28.50	38.45	38.45
Distance between exterior springs (mm)	269.42		285.35	

Table 8-8 Model parameters of specimen T-SB7

Parameter	Beam		Column	
	Exterior steel spring	Central steel spring	Exterior steel spring	Central steel spring
d_{su} (mm)	20.210	NA	7.940	16.440
P_{sy} (kN)	637.95	NA	456.68	175.40
K_s (kN/mm)	839.40	NA	746.70	404.04
r	0.0144	NA	0.0121	0.0121
R_{so}	0.638	NA	0.457	0.567
α_s	0.010	NA	0.102	0.102
Parameter	Exterior concrete spring	Central concrete spring	Exterior concrete spring	Central concrete spring
P_{cy} (kN)	386.78	1093.86	780.10	311.05
d_{cy} (mm)	0.186	0.010	5.595	2.770
K_h	1.20	1.20	1.16	1.16
Z	18.63	18.63	25.21	25.21
Distance between exterior springs (mm)	280.10		276.33	

Table 8-9 Model parameters of specimen # 3

Parameter	Beam		Column	
	Exterior steel spring	Central steel spring	Exterior steel spring	Central steel spring
d_{su} (mm)	40.010	NA	10.703	10.703
P_{sy} (kN)	1374.24	NA	551.60	382.26
K_s (kN/mm)	2192.81	NA	1374.53	748.80
r	0.0064	NA	0.0130	0.0140
R_{so}	0.694	NA	0.530	0.506
α_s	0.007	NA	0.255	0.205
Parameter	Exterior concrete spring	Central concrete spring	Exterior concrete spring	Central concrete spring
P_{cy} (kN)	946.88	2546.13	1496.49	2107.49
d_{cy} (mm)	0.489	0.006	0.833	0.251
K_h	1.05	1.05	1.05	1.05
Z	86.07	86.07	102.53	102.53
Distance between exterior springs (mm)	262.91		382.89	

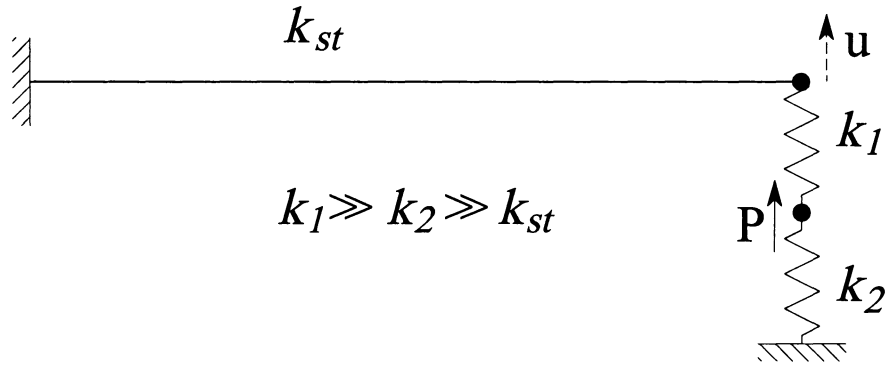

Figure 8-1 Displacement-controlled loading scheme

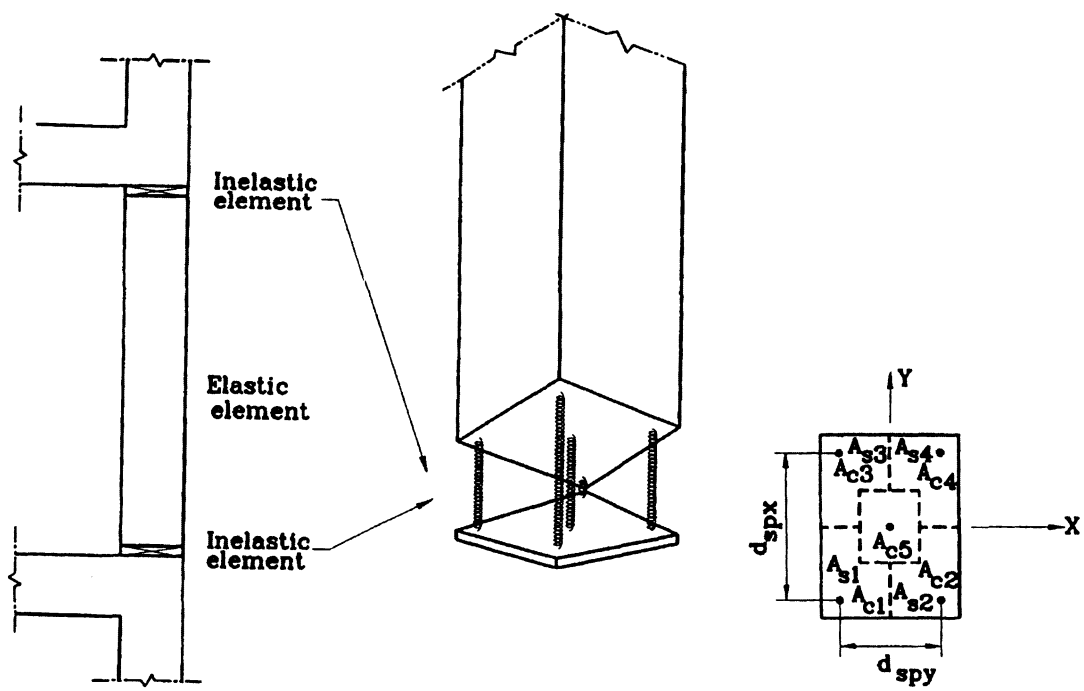

Figure 8-2 Multi-spring model to represent flexural members (Lai et al., 1984)

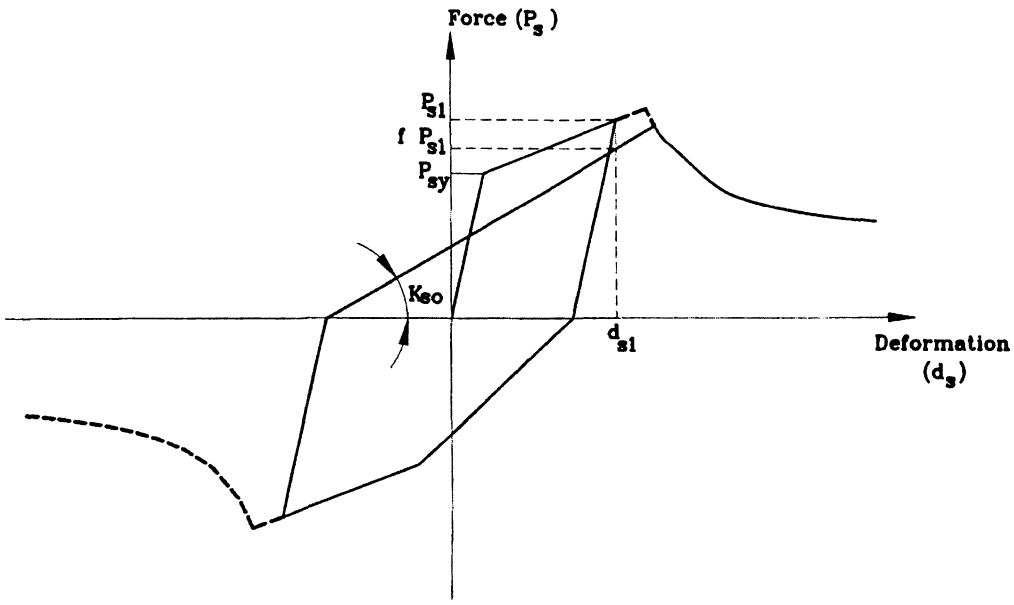

Figure 8-3 Hysteretic model for steel spring (Youssef and Ghobarah, 1999)

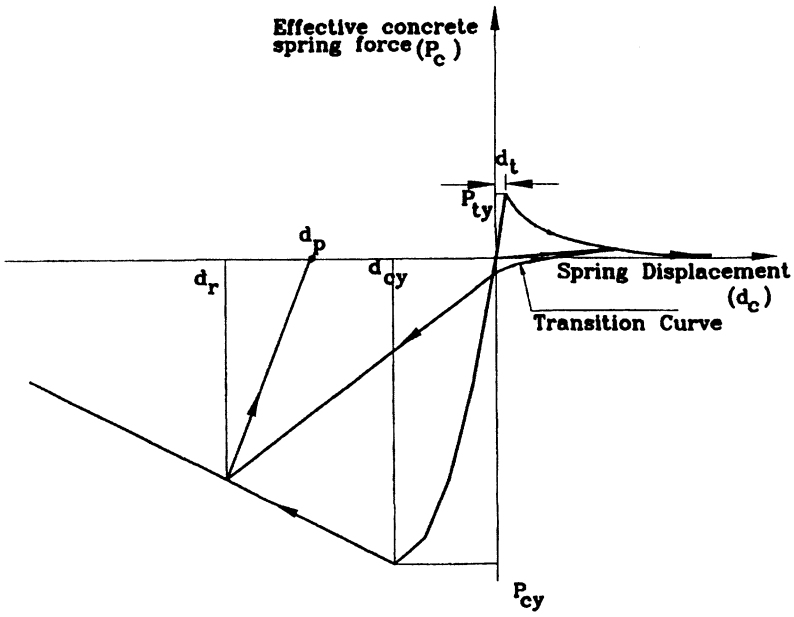

Figure 8-4 Hysteretic response for concrete spring (Youssef, 2000)

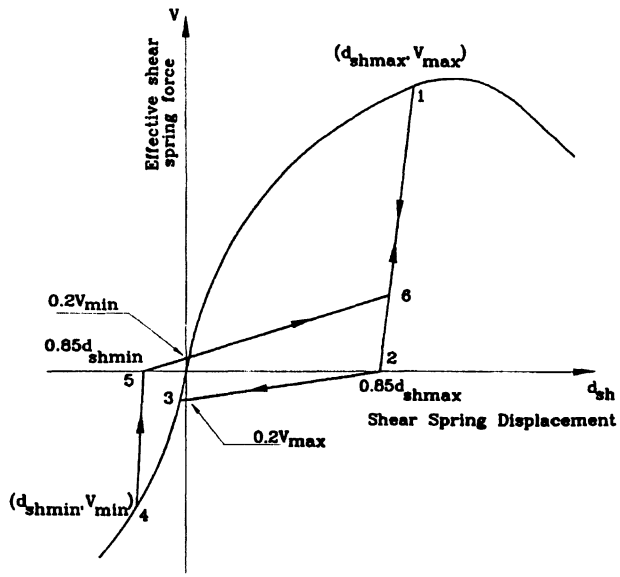

Figure 8-5 Hysteretic response for shear spring (Youssef and Ghobarah, 2001)

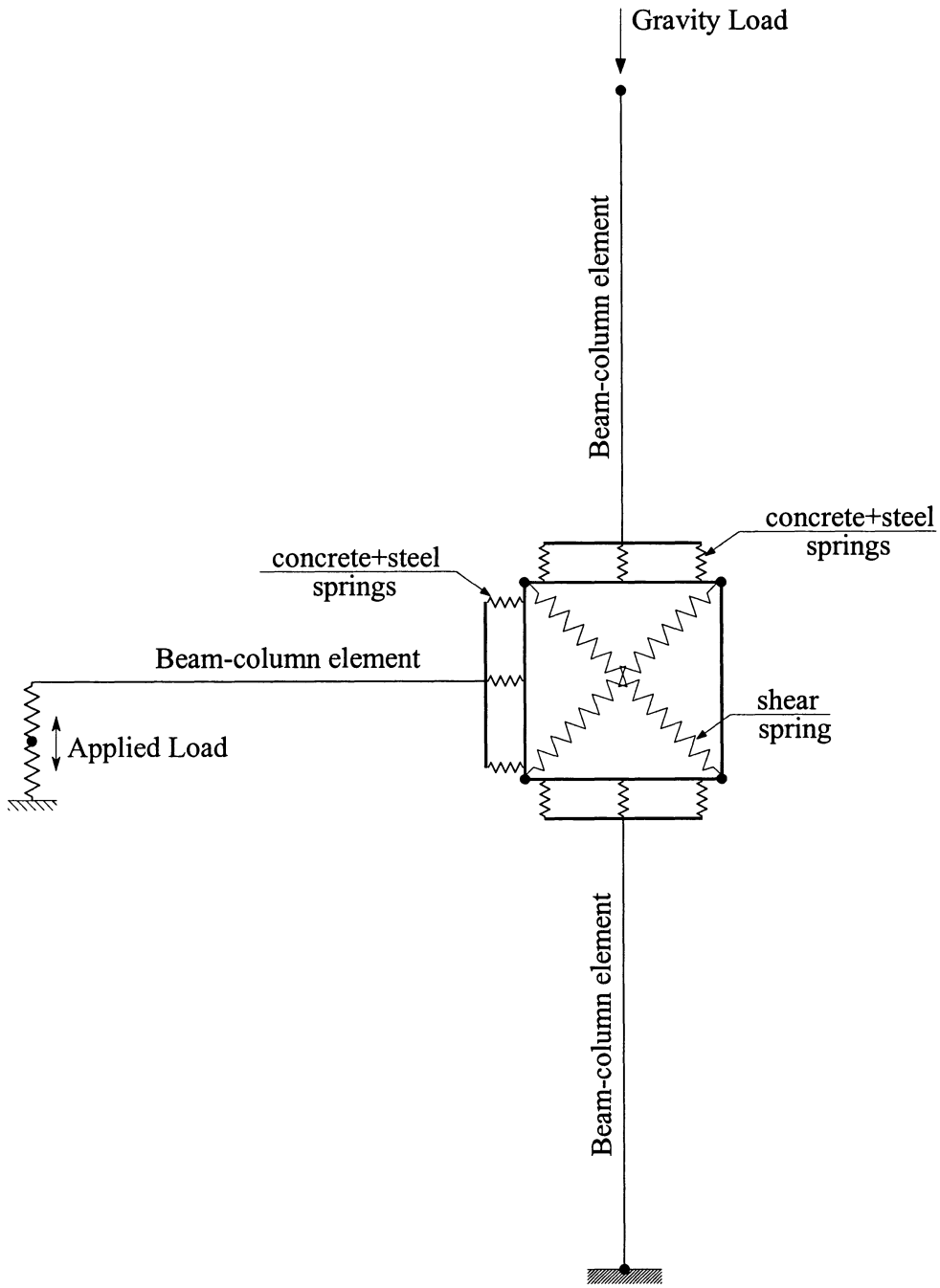

Figure 8-6 Kinematic beam-column model

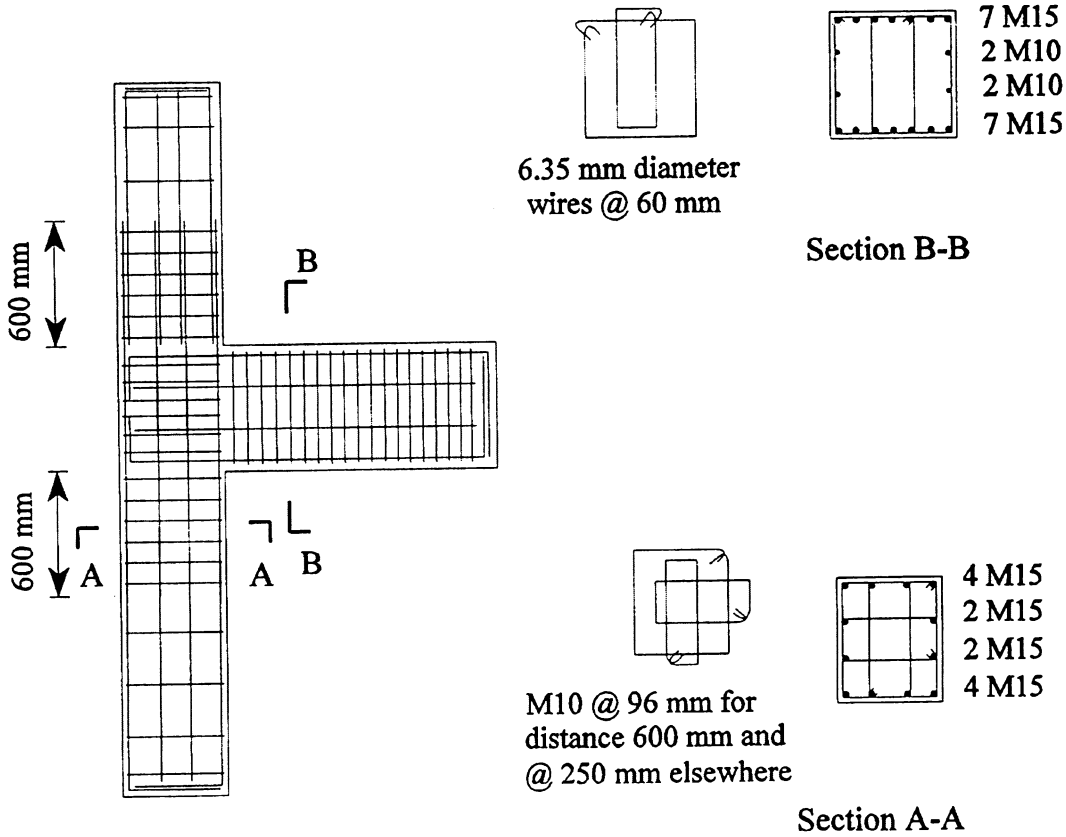

Figure 8-7 Reinforcement details of specimen J2 (Ghobarah et al., 1997)

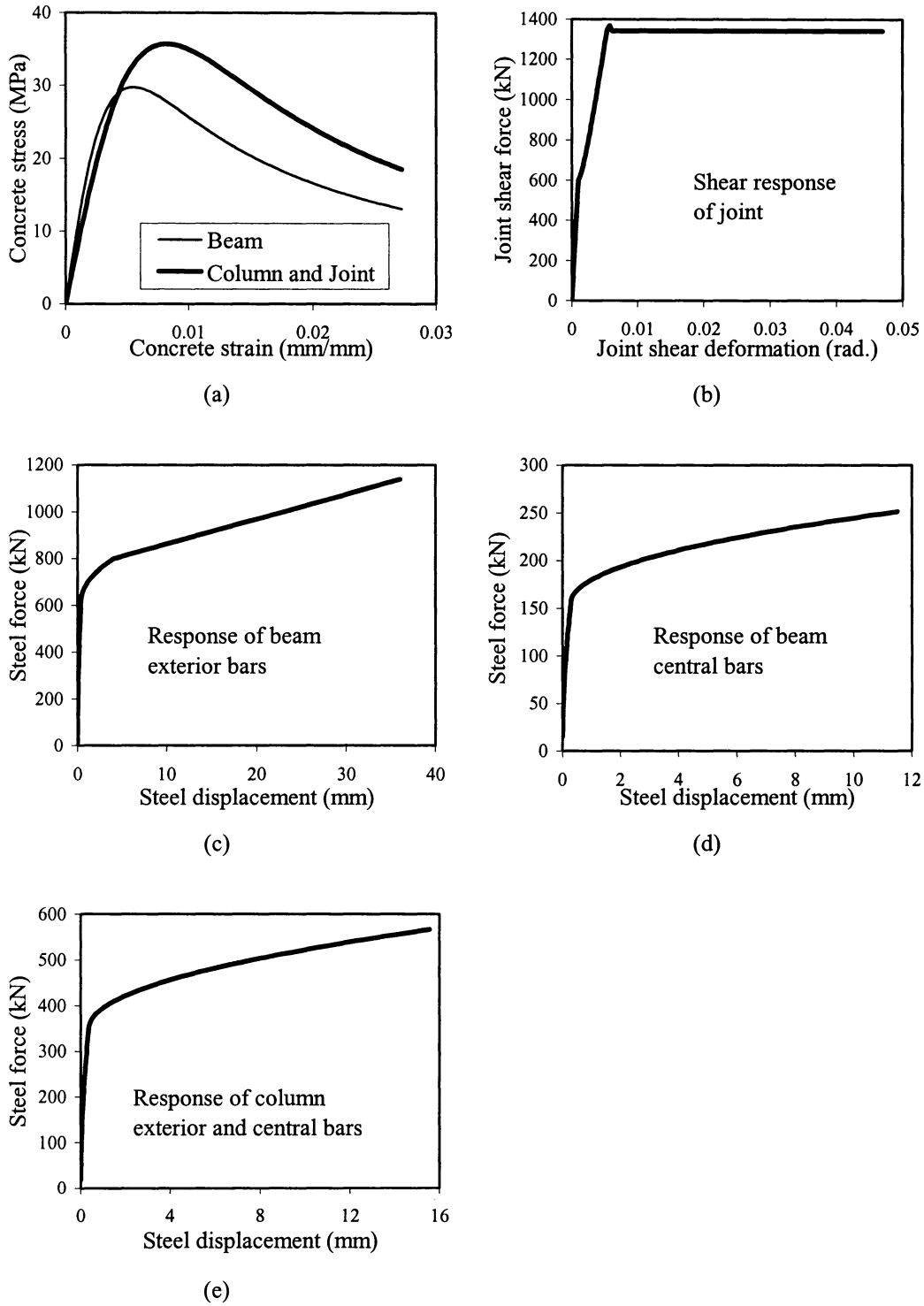

Figure 8-8 Analytical prediction of model elements of specimen J2

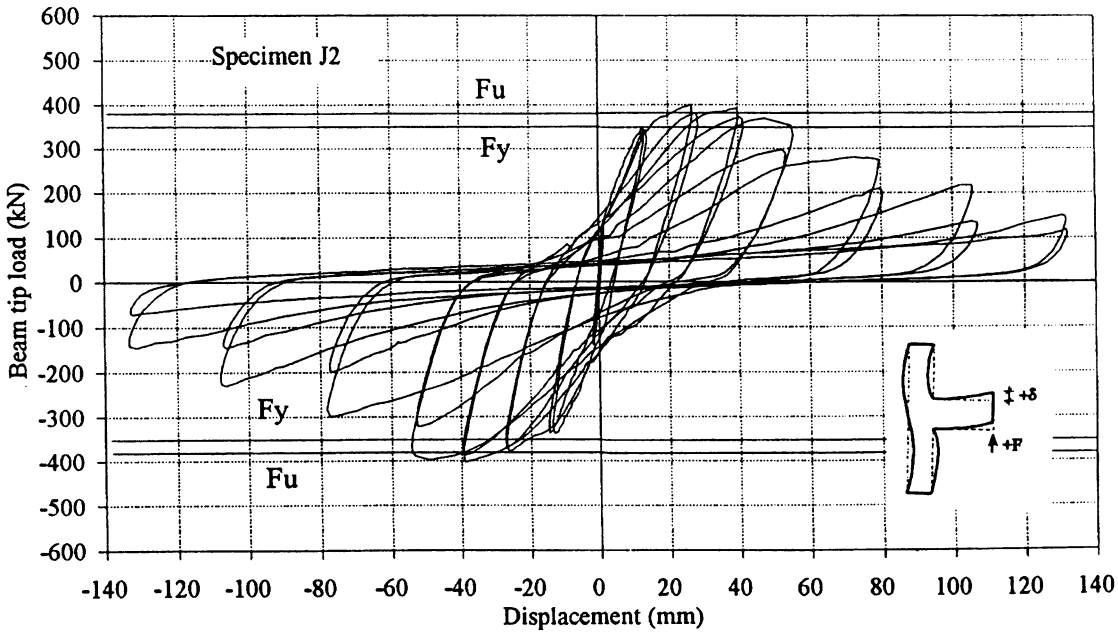

(a) Experimental response (Ghobarah et al., 1997)

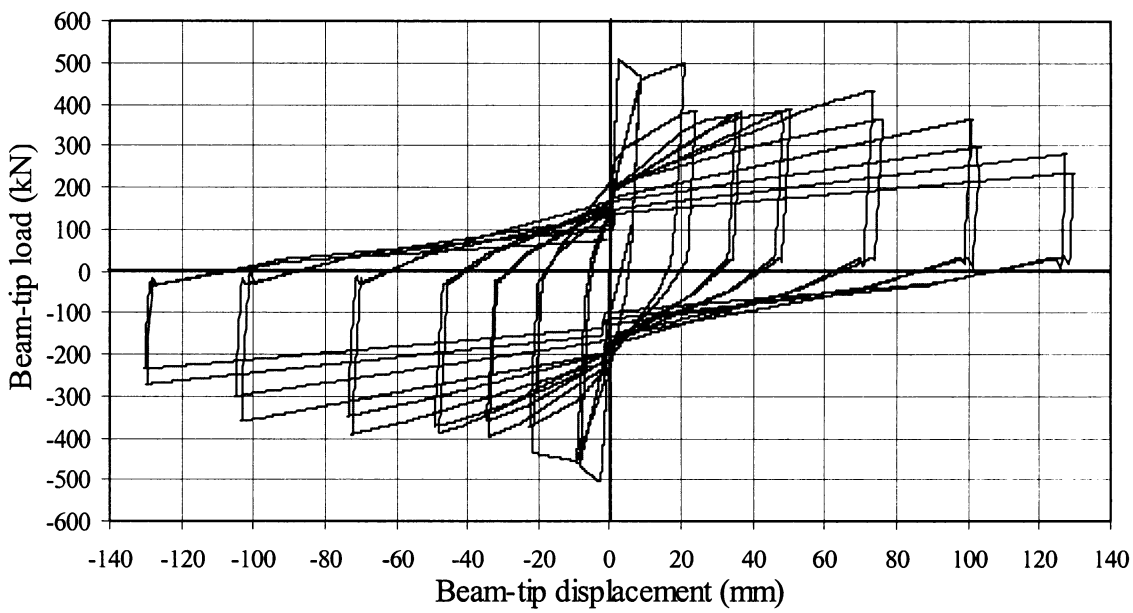

(b) Analytical response

Figure 8-9 Experimental measurement and analytical response of specimen J2

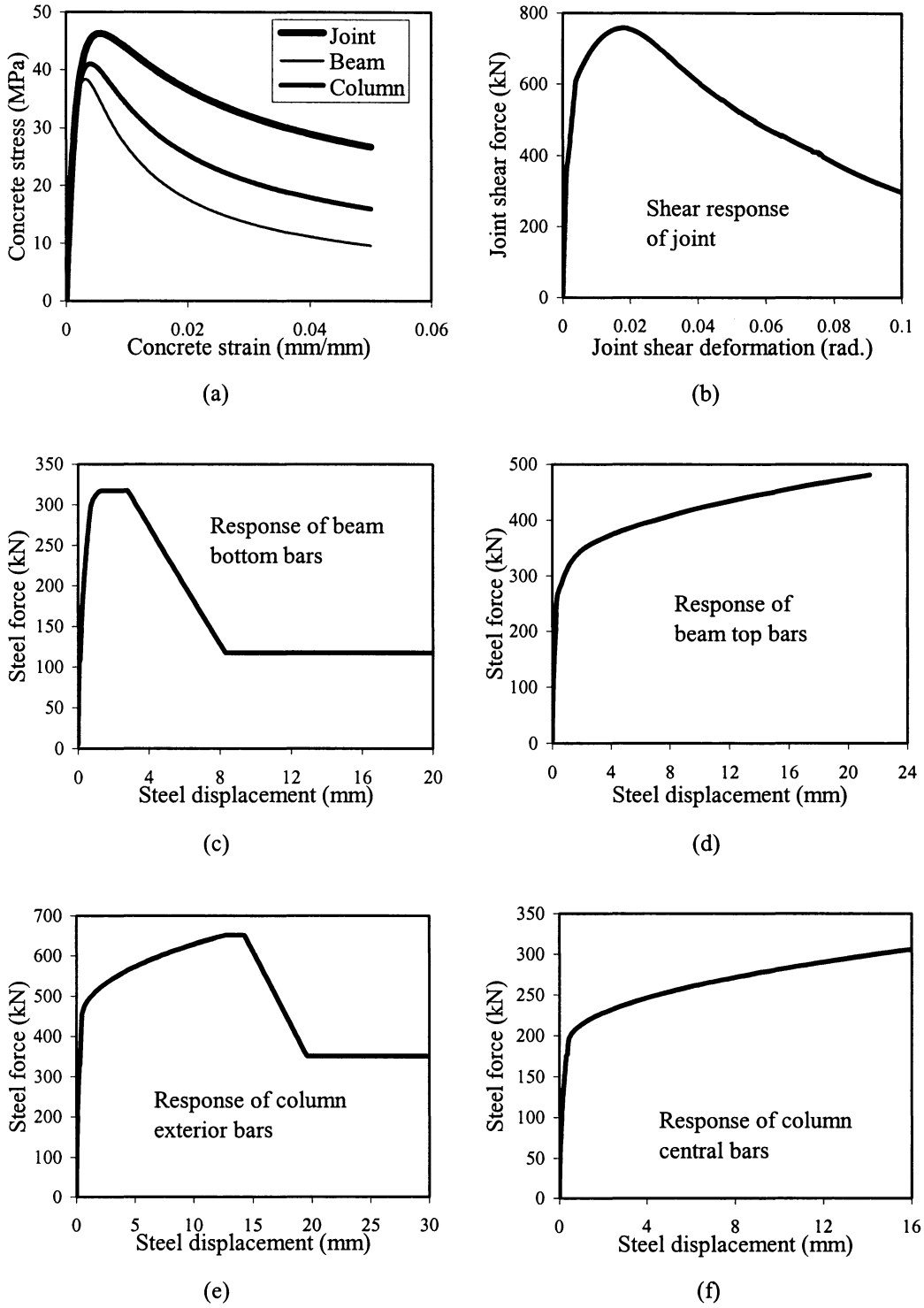

Figure 8-10 Analytical prediction of model elements of joint T-B10

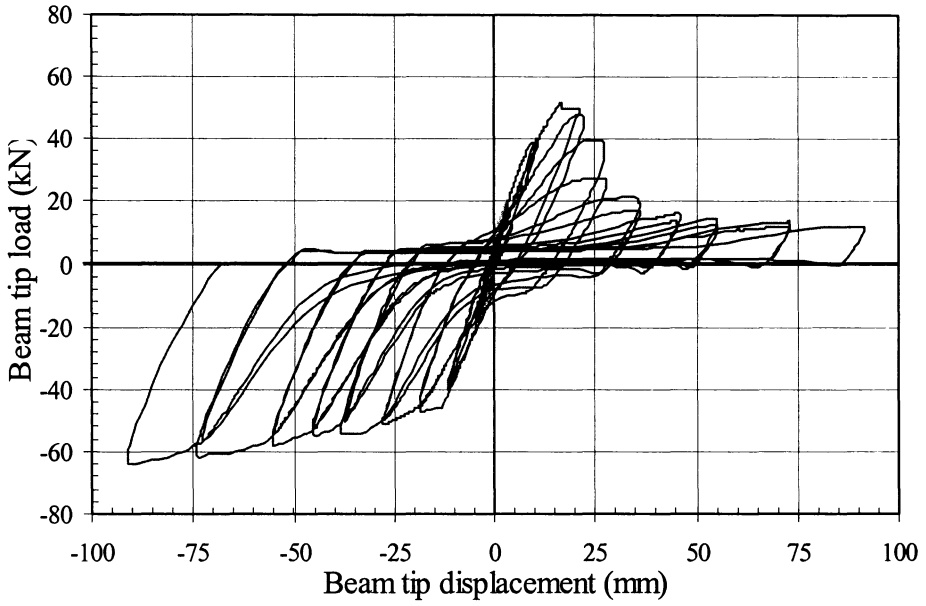

(a) Experimental response

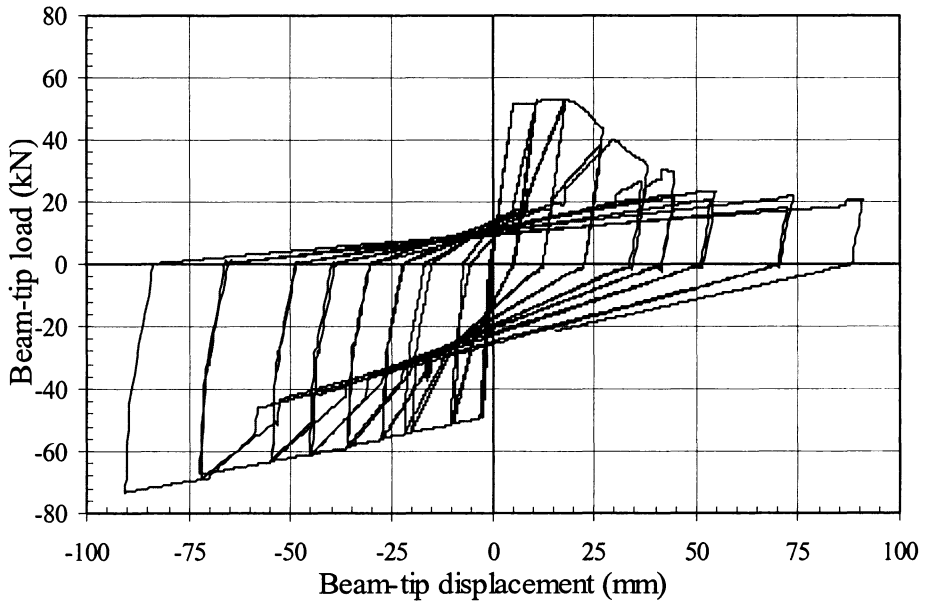

(b) Analytical response

Figure 8-11 Experimental measurements and analytical response of joint T-B10

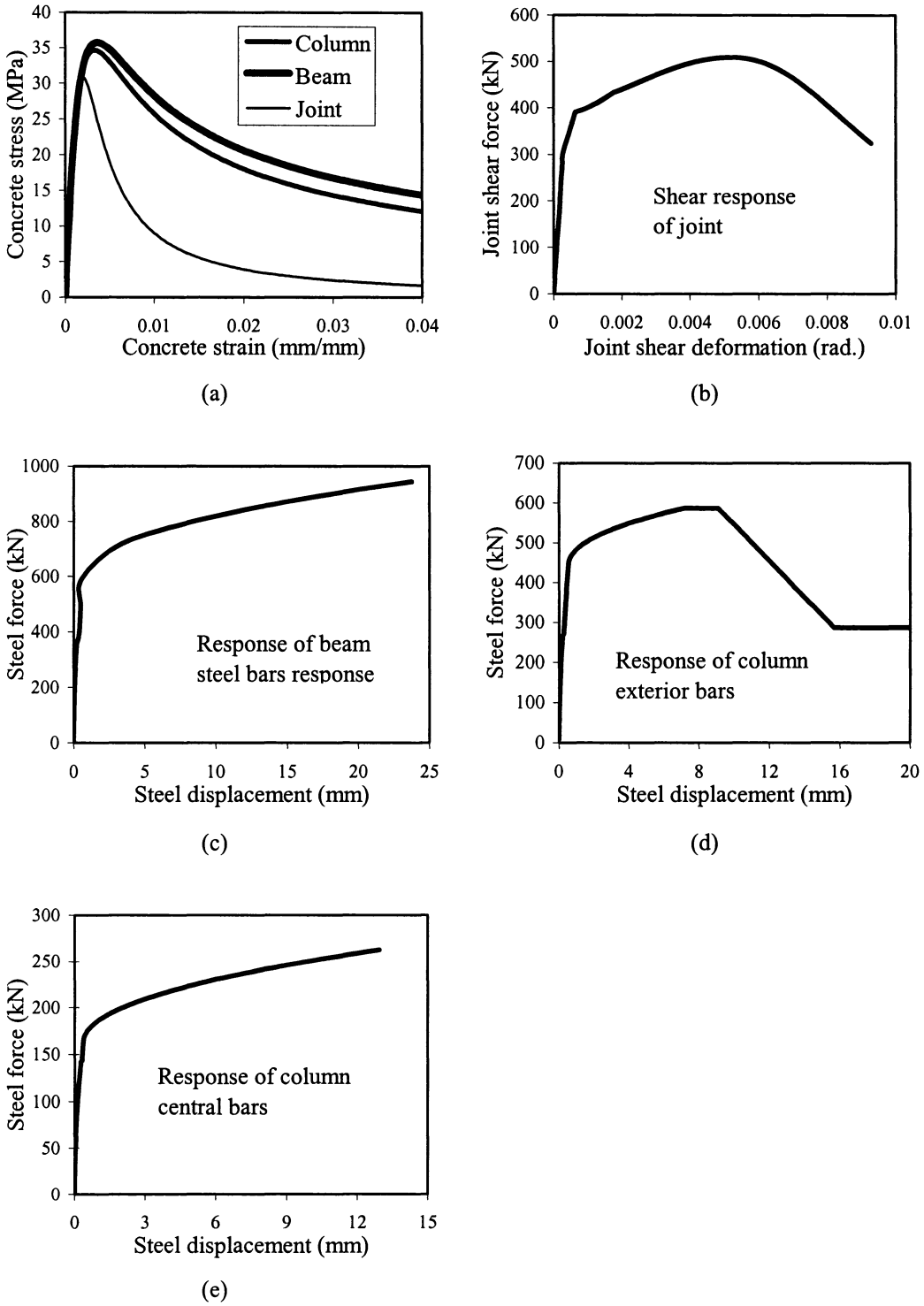

Figure 8-12 Analytical prediction of model elements of joint T-S1

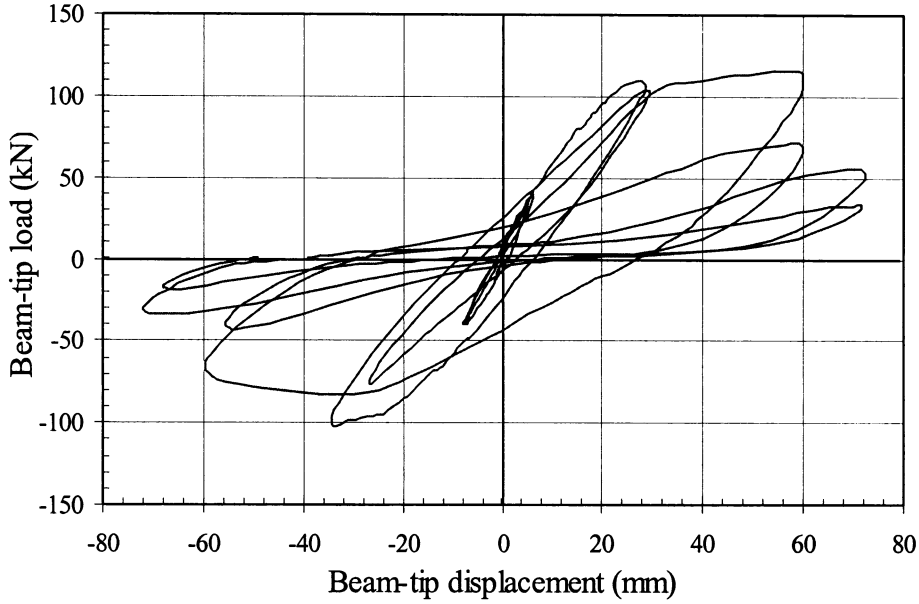

(a) Experimental response

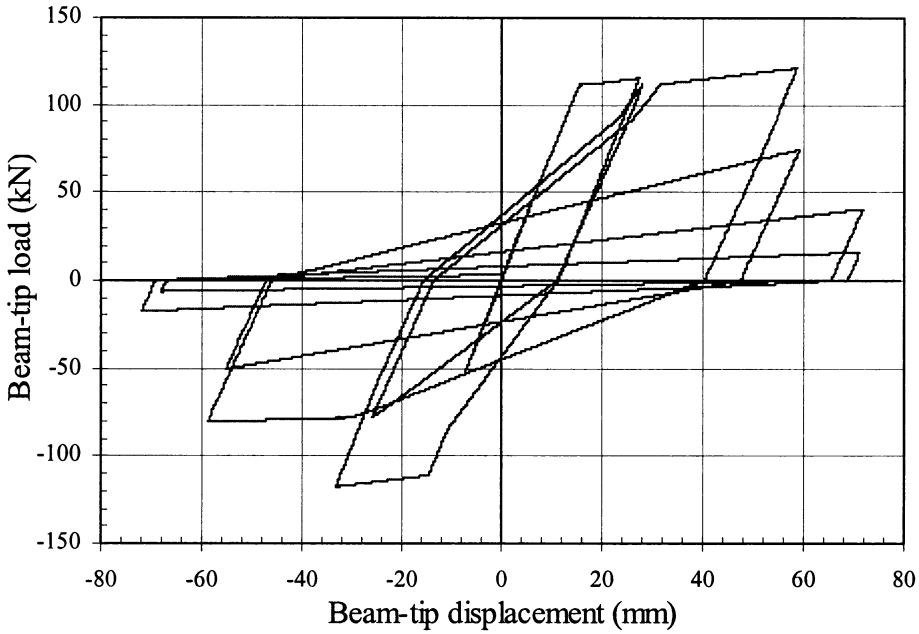

(b) Analytical response

Figure 8-13 Experimental measurements and analytical response of joint T-S1

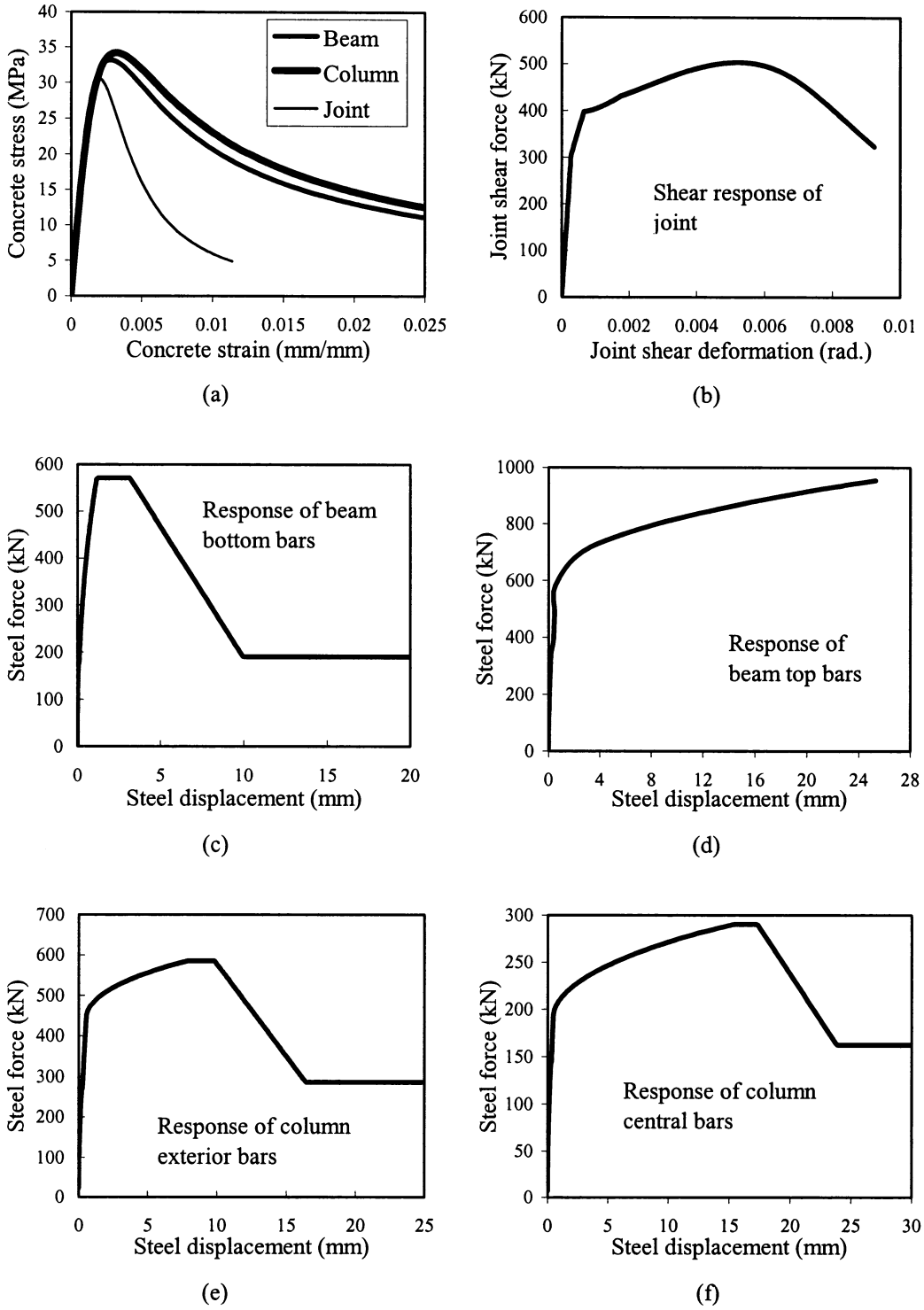

Figure 8-14 Analytical prediction of model elements of joint T-SB3

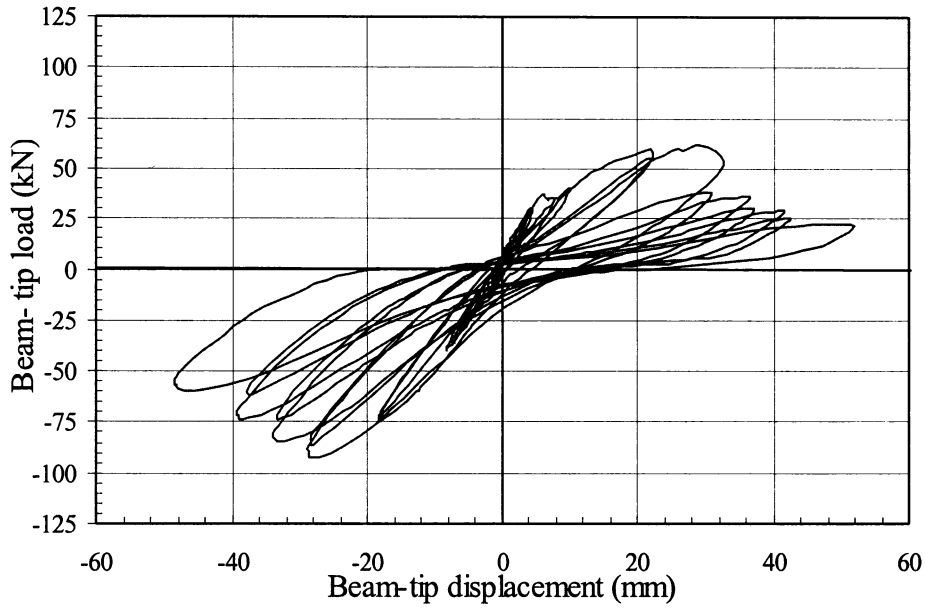

(a) Experimental response

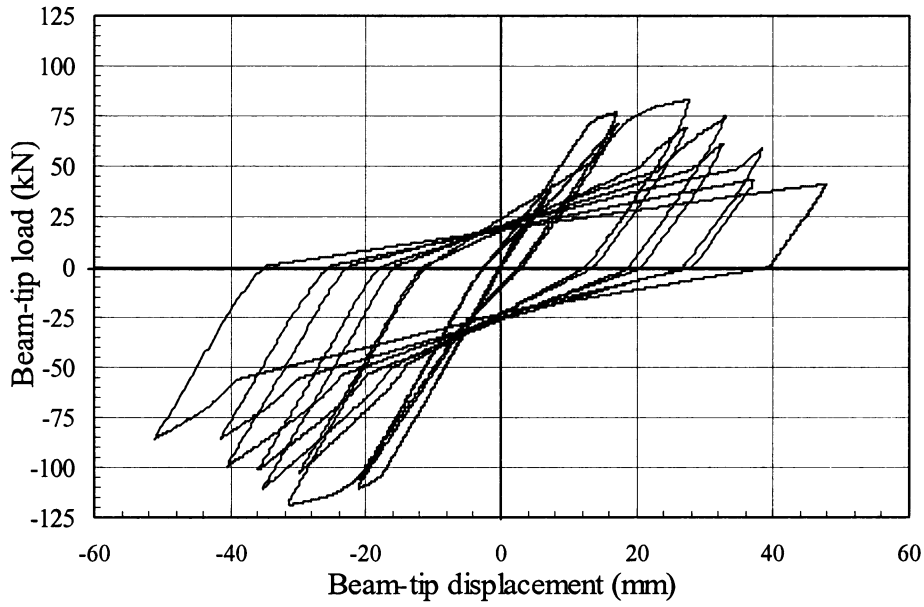

(b) Analytical response

Figure 8-15 Experimental measurements and analytical response of joint T-SB3

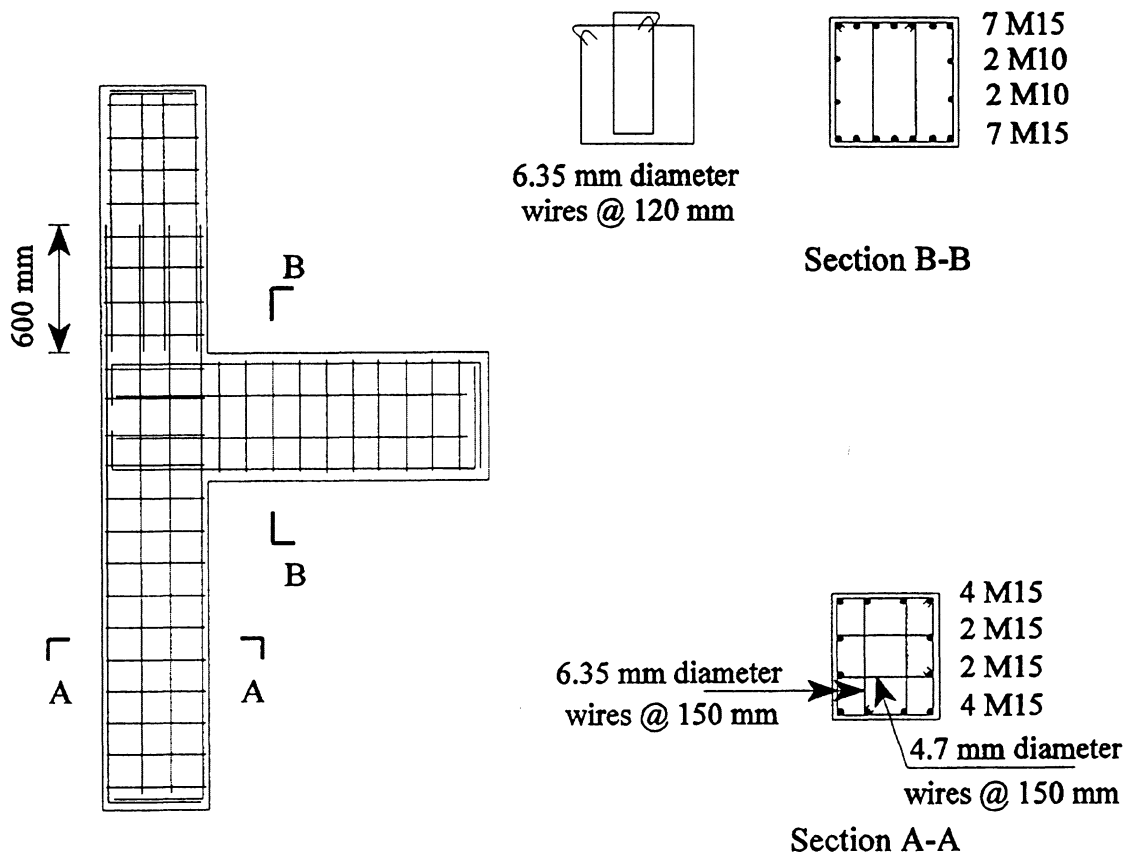

Figure 8-16 Reinforcement details of specimen J1 (Ghobarah et al., 1996)

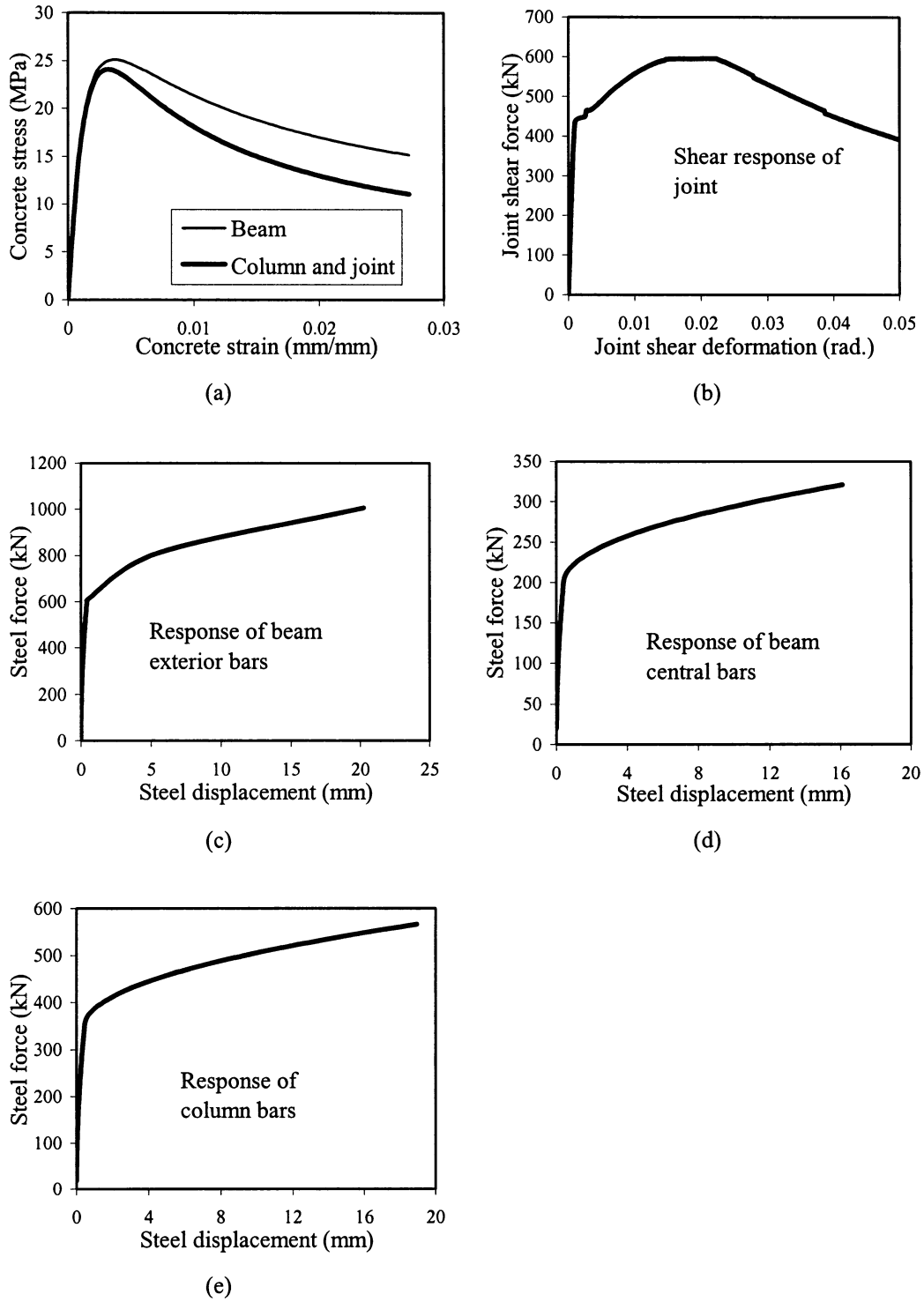

Figure 8-17 Analytical prediction of model elements of specimen J1

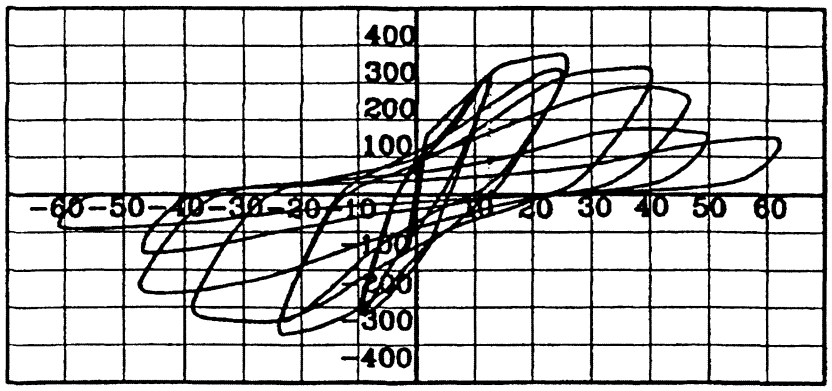

(a) Experimental response (Ghobarah et al., 1996)

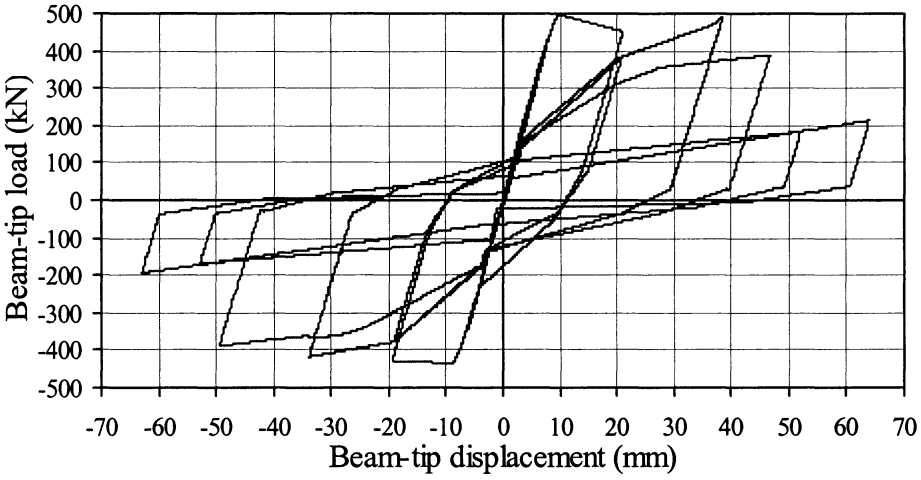

(b) Analytical response

Figure 8-18 Experimental measurements and analytical response of specimen J1

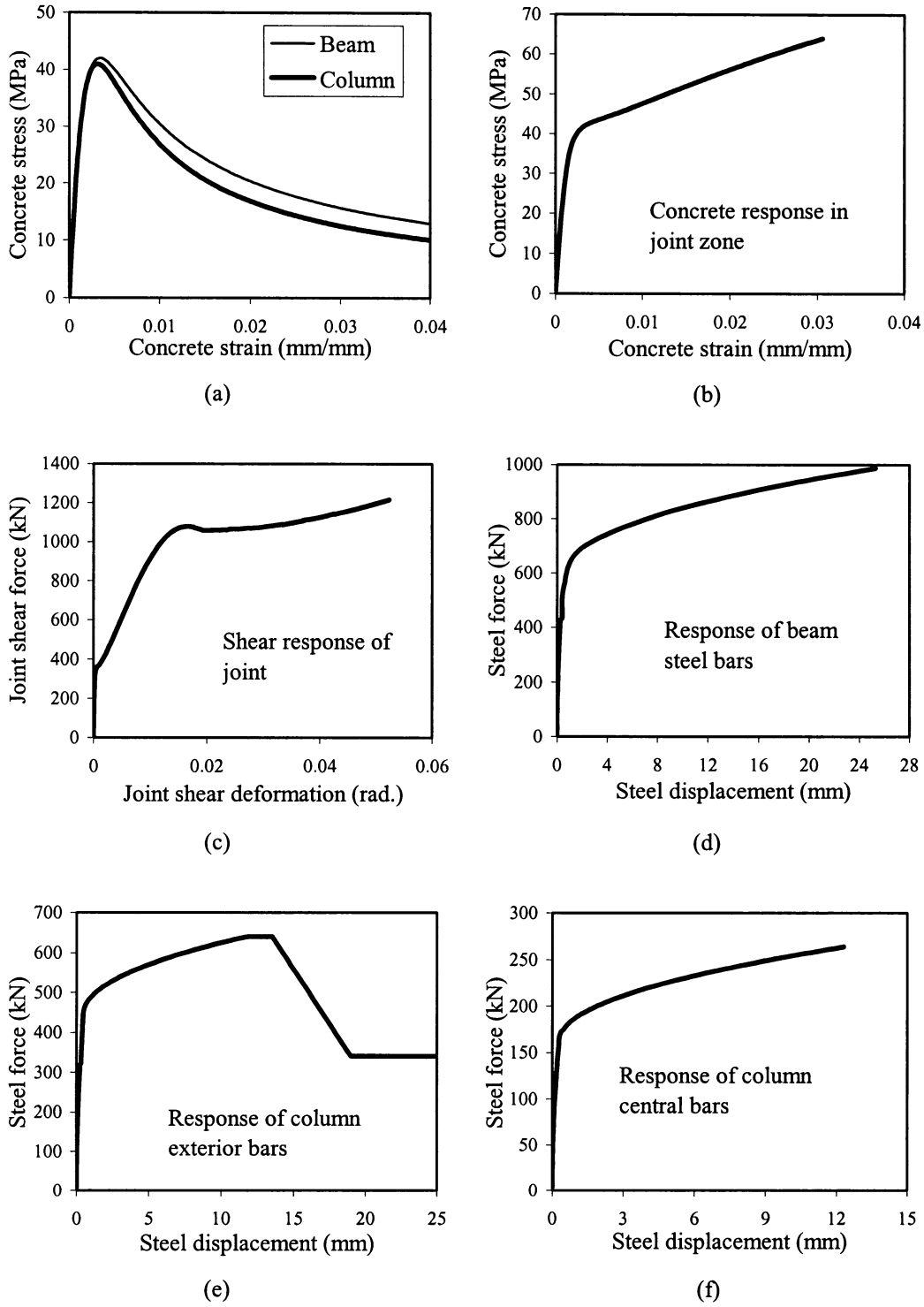

Figure 8-19 Analytical prediction of model elements of joint T-S4R

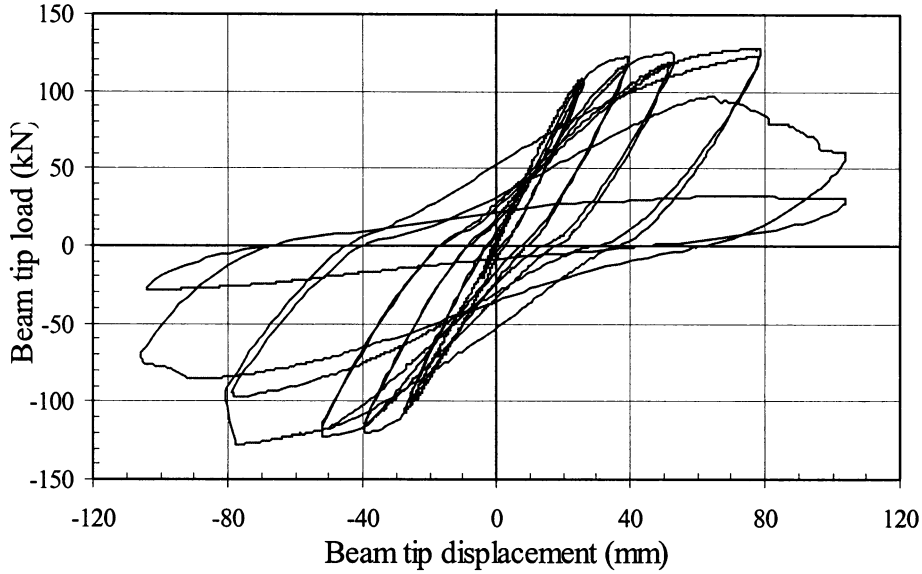

(a) Experimental response

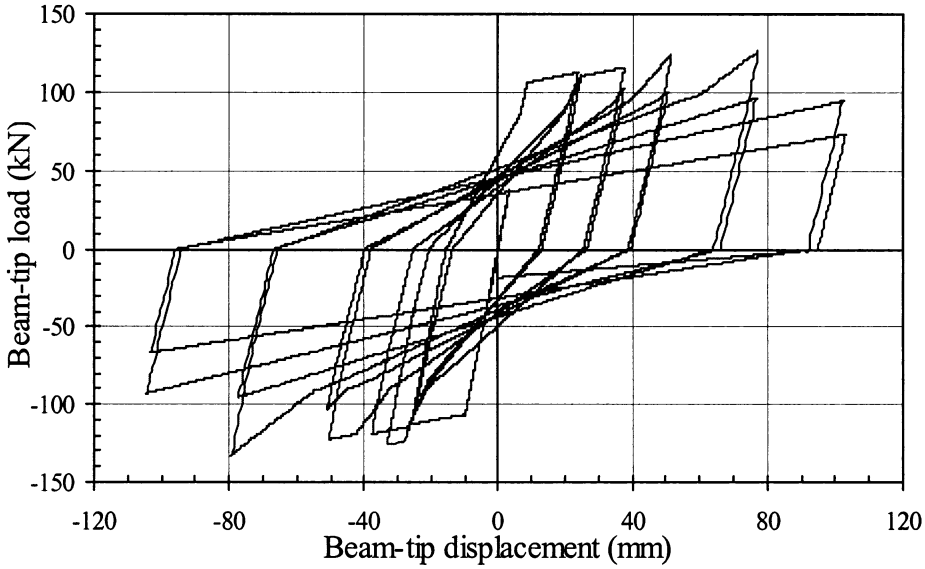

(b) Analytical response

Figure 8-20 Experimental measurements and analytical response of joint T-S4R

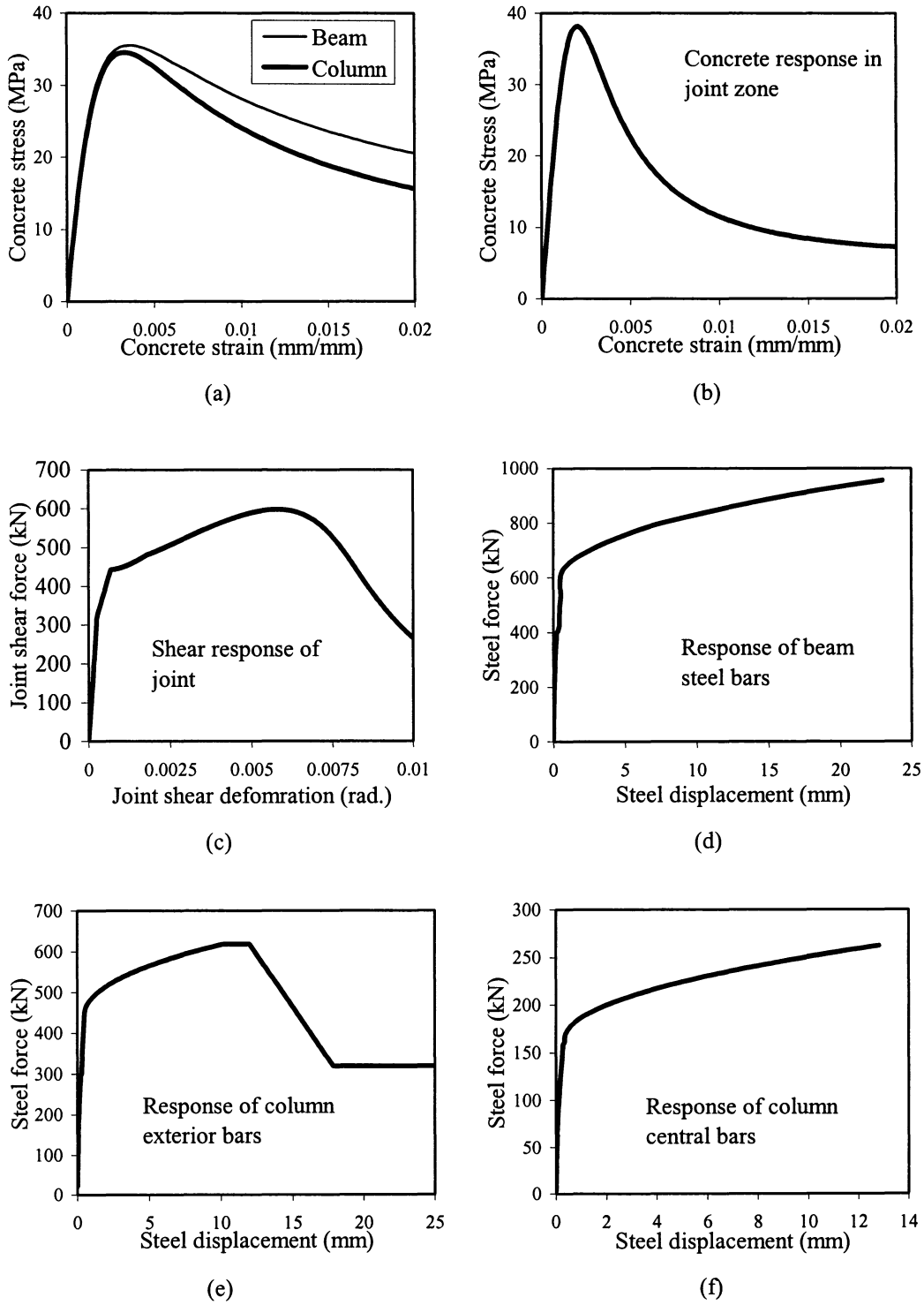

Figure 8-21 Analytical prediction of model elements for specimen T2R

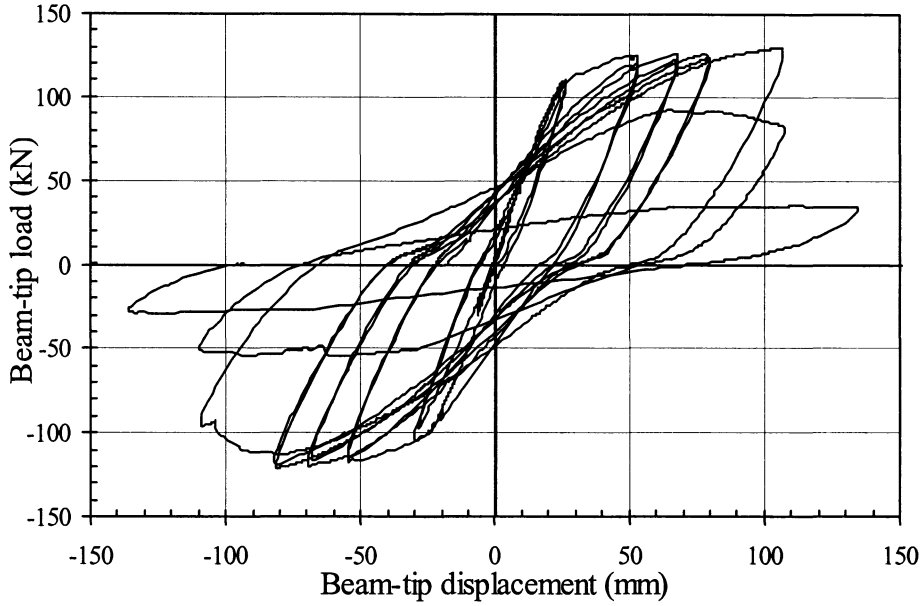

(a) Experimental response (Ghobarah and Said, 2002)

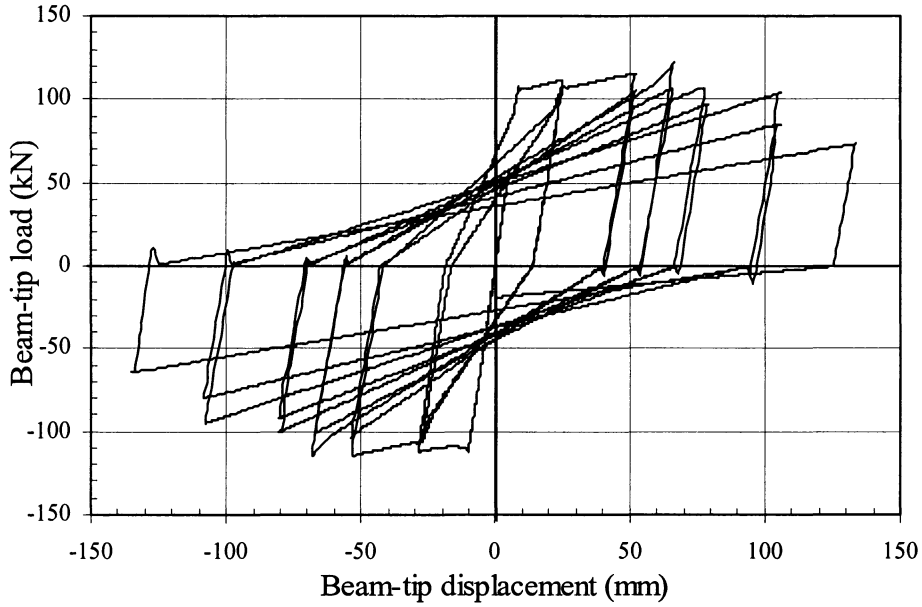

(b) Analytical response

Figure 8-22 Experimental measurements and analytical response for specimen T2R

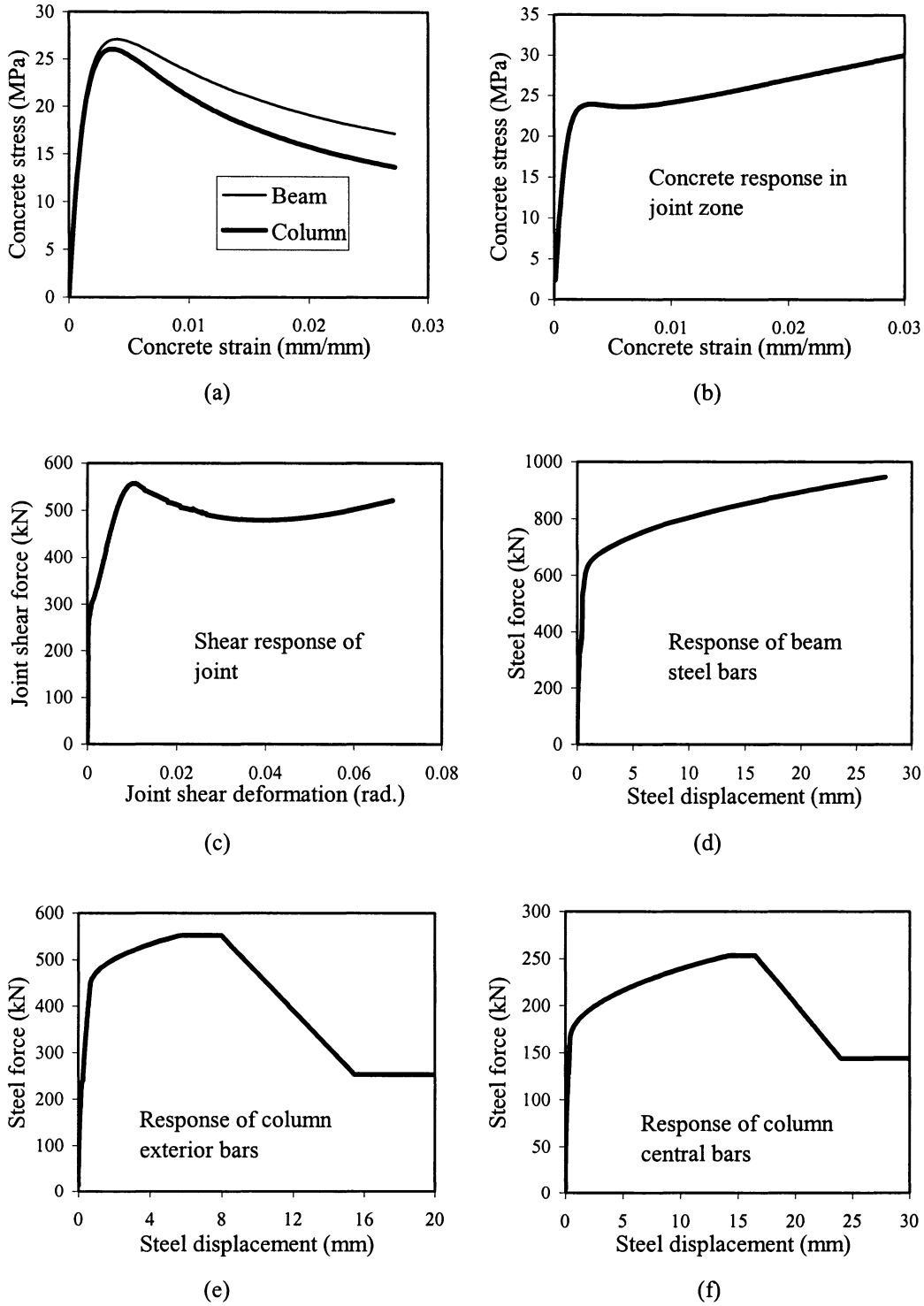

Figure 8-23 Analytical prediction of model elements for joint T-SB7

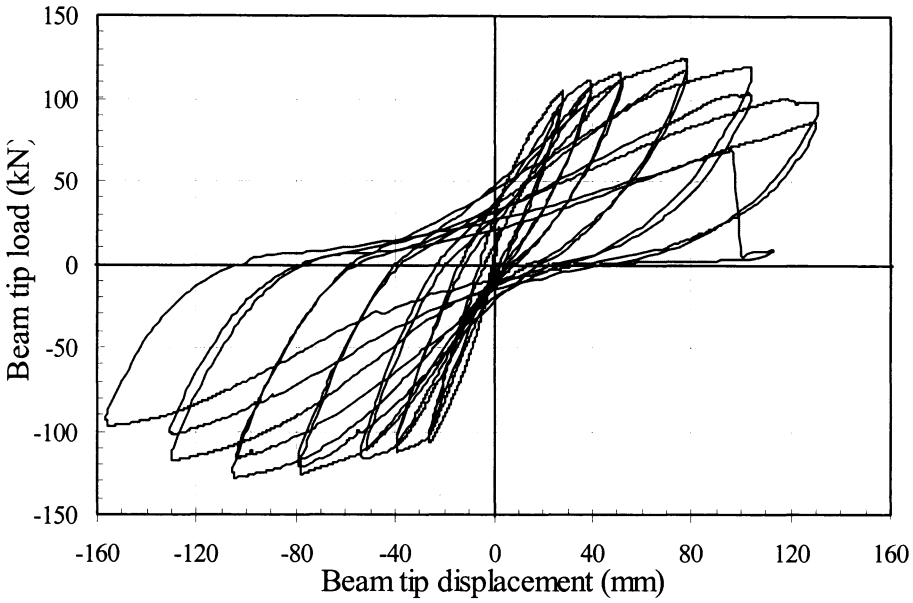

(a) Experimental response

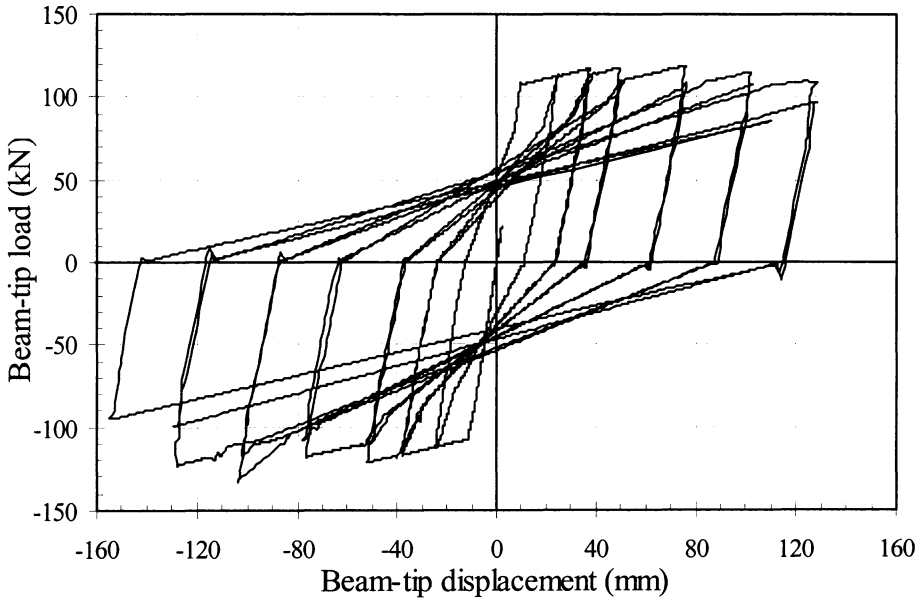

(b) Analytical response

Figure 8-24 Experimental measurements and analytical response of joint T-SB7

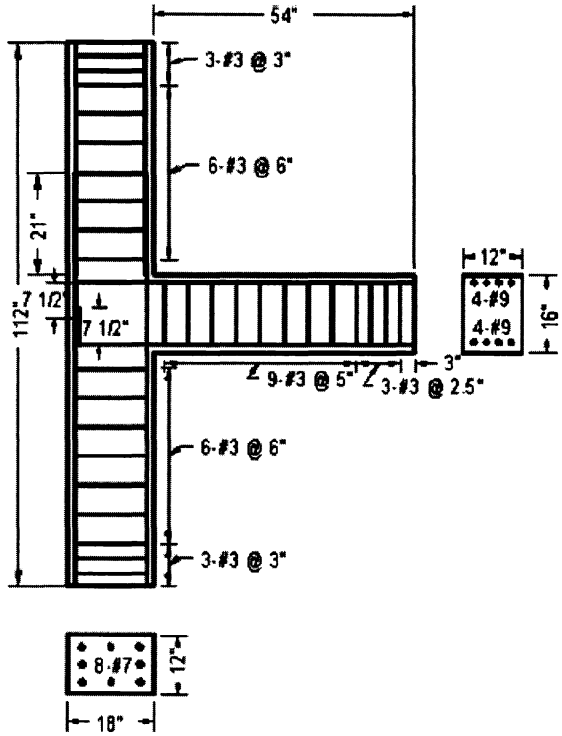

Figure 8-25 Dimensions and reinforcement details of specimen # 3 (Clyde and Pantelides, 2002)

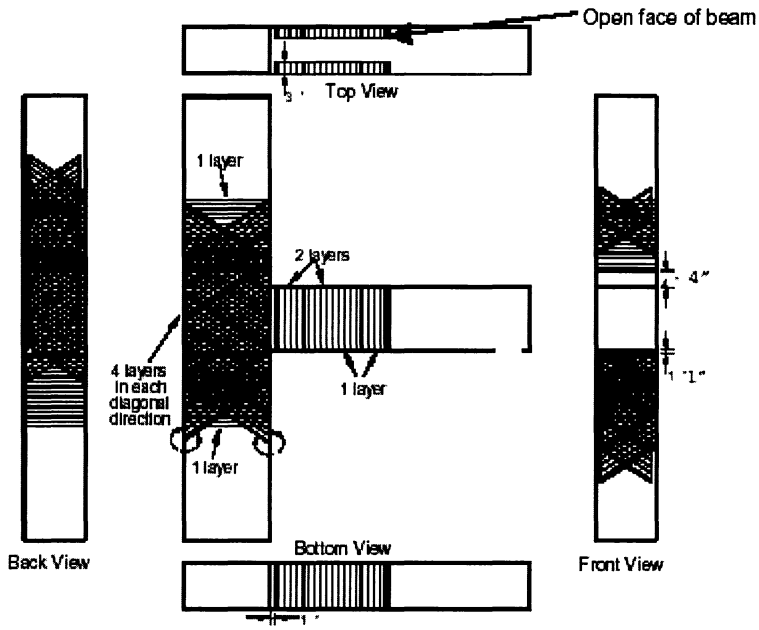

Figure 8-26 Rehabilitation scheme of specimen # 3 (Clyde and Pantelides, 2002)

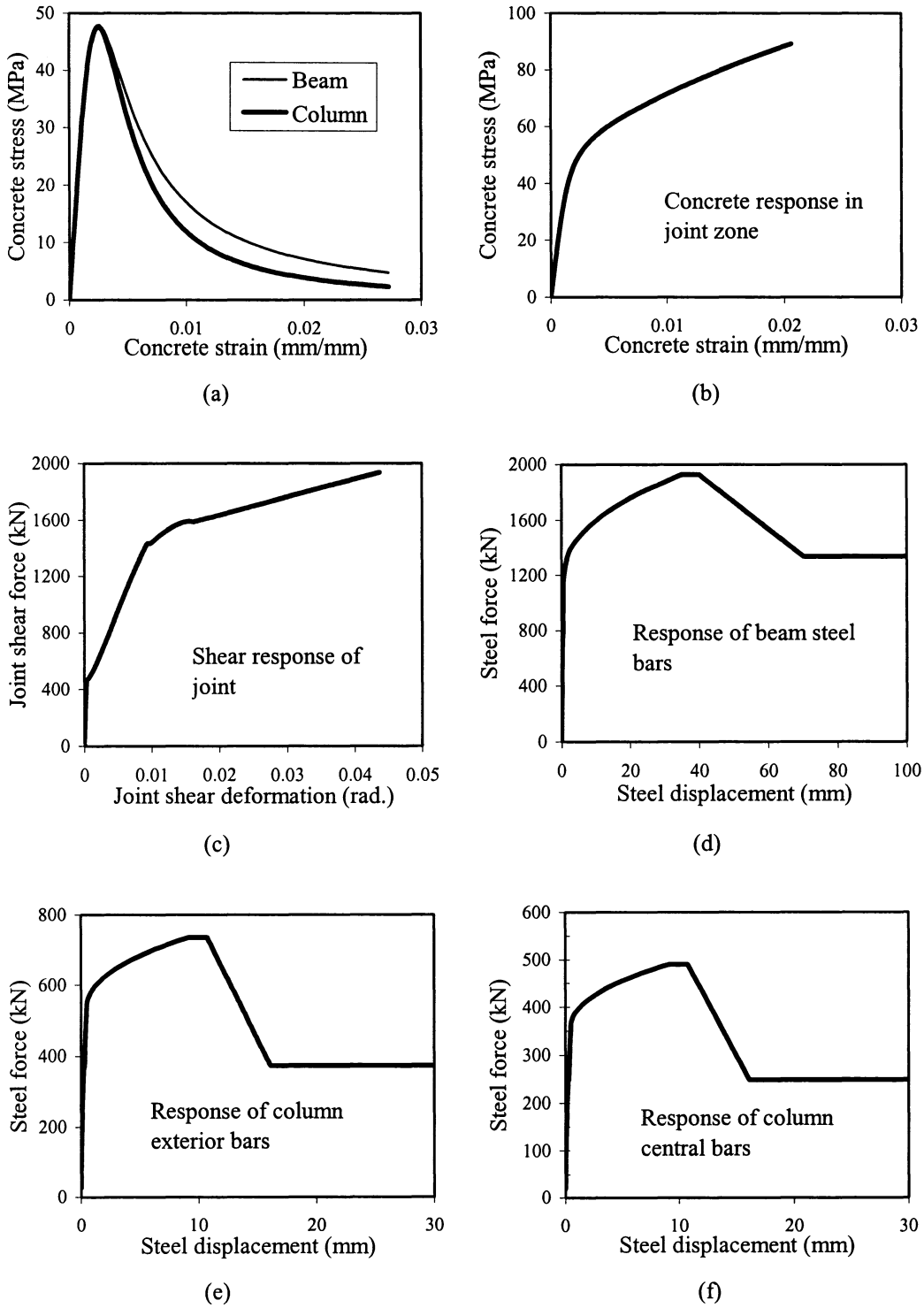

Figure 8-27 Analytical prediction of model elements of specimen # 3

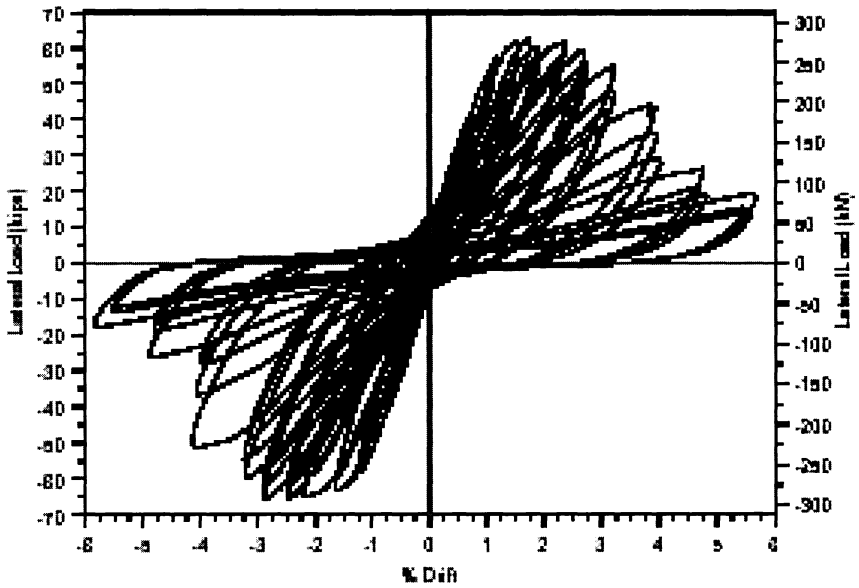

(a) Experimental response (Clyde and Pantelides, 2002)

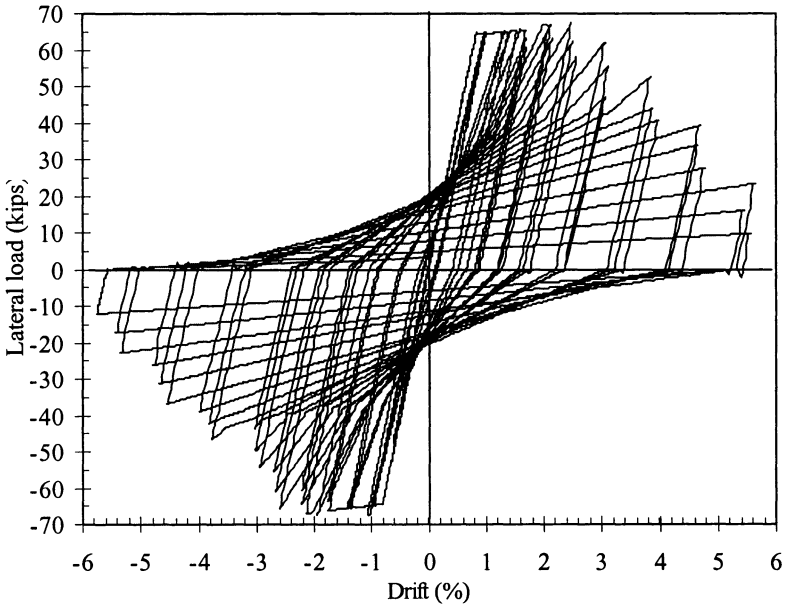

(b) Analytical response

Figure 8-28 Experimental measurements and analytical response of specimen # 3

This page is intentionally left blank

Chapter 9

CONCLUSIONS AND RECOMMENDATIONS

9.1 SUMMARY

The objectives of this research were to experimentally and analytically evaluate the response of pre-seismic code designed beam-column joints and investigate feasible rehabilitation schemes for strengthening these deficient RC frame elements. Novel rehabilitation techniques were developed using FRP composites and steel elements to strengthen the joint shear resistance and beam bars anchorage-slip. New shear models were proposed to predict the hysteretic response of joints without steel ties, with steel ties or with FRP sheets.

The experimental phase of this study included testing of twelve full-scale exterior beam-column subassemblies. The specimens were divided into three groups, *shear-deficient joints, bond-deficient joints* and *shear/bond-deficient joints*. One specimen of each group was tested as control specimen and the others were rehabilitated before testing. FRP jacket was applied to the joint zone to strengthen the joint shear resistance. To account for the anchorage deterioration of beam reinforcement bars, externally bonded FRP sheets were applied to the beam bottom face, steel plates were used to tie the existing beam bars or new steel reinforcement were installed. The test results showed significant improvement in the hysteretic response of the rehabilitated specimens. Design guidelines were proposed for the rehabilitation schemes.

A simple but sufficiently accurate FRP-confined concrete model was developed. The model considers the lateral compatibility between the concrete section and the FRP jacket. Two shear models were proposed. The compression softened strut mechanism was used to predict the shear response of concrete frame joint without steel ties. The MCFT was adopted to predict the shear response of concrete joints with externally bonded FRP sheets.

To verify the validity of the proposed material and shear models, a modified version of the computer program PC-ANSR (Youssef, 2000) was used to analyze several beam-column subassemblies. Satisfactory agreement between the experimental and analytical responses was obtained.

9.2 CONCLUSIONS

From the experimental and the analytical investigations, the following conclusions were arrived at:

1- Concrete frame joint with no shear reinforcement in the joint zone experiences uncontrolled diagonal shear cracks which results in a brittle joint shear failure.

2- Concrete frame joint with inadequate anchorage length of beam bars shows brittle bond-slip failure, regardless of the confinement condition in the anchorage zone. However, providing adequate confinement to the anchorage zone resists the developed bond cracks and hence yield strength may be achieved before strength deterioration occurs.

3- Concrete frame joint with no shear reinforcement and inadequate anchorage

length of beam bars experiences combined joint shear failure and bond-slip failure modes. Severe strength deterioration, stiffness degradation, low ductility and low energy dissipation capability occur.

4- Concrete frame joint without adequate steel ties in the joint zone is unable to provide proper anchorage to the beam reinforcement even though the bars are bent into the joint zone. Confining the anchorage zone with FRP sheets is a feasible technique to improve the bond conditions of these bars.

5- Rehabilitation of shear strength-deficient joint using FRP jacket provides confinement and additional shear reinforcement to the joint and hence maintains the concrete integrity and significantly improves the joint strength and ductility.

6- FRP sheets used for strengthening joint shear resistance are more effective if they are mounted in the hoop direction of the column rather than in a direction parallel to the column axis.

7- Anchoring the FRP sheets is crucial. Both steel and FRP anchors are effective in eliminating the debonding of the composite sheets at their free edges.

8- In designing the rehabilitation scheme, attention must be paid to the expected change in the beam, column and joint strength and mode of failure. To satisfy the *"weak beam-strong column"* concept, strengthening of the beam near the joint should be avoided whereas confining the column potential plastic hinge region is advantageous.

9- FRP sheets attached to the beam bottom face can successfully replace the action of the ineffective beam reinforcement and significantly improve the joint strength,

ductility, and energy dissipation capability. Instead of the brittle bond-slip failure mode, beam hinging occurs.

10- Adequate anchorage must be provided to the composite sheets to prevent the debonding of the composite sheets from the beam-column interface. External steel tie rods are effective in eliminating the sheets debonding whereas expansion anchors could not sustain high level of cyclic loads.

11- Rehabilitation the anchorage strength of beam bars using steel plates and tie rods welded to the bars significantly improves the anchorage of these bars, restores the full joint strength and enhance the joint ductility and energy dissipation capability.

12- An efficient model was proposed to predict the behaviour of FRP-confined concrete elements under monotonic loading. The model takes into consideration the deformation compatibility between the FRP sheets and the concrete element. The model accuracy was assessed and it was found to be sufficiently capable of predicting the monotonic response of GFRP- and CFRP-confined concrete elements.

13- A new shear model was proposed to predict the behaviour of shear-dominant concrete elements, such as beam-column joints, rehabilitated using externally bonded FRP sheets. The model adopts the principles of the Modified Compression Field Theory, and thus the equilibrium and compatibility conditions are satisfied. The role of the FRP sheets in improving the concrete strength by confinement and providing the concrete shear element with additional shear reinforcement mechanism are considered. The model is rational and successful in

predicting the joint shear response.

14- A simple shear model was proposed to predict the behaviour of beam-column joints without shear reinforcement. The model assumes a major inclined concrete compression strut to resist the developed shear force. The joint failure occurs when principal compression strain of 0.0035 is exceeded in the diagonal strut.

15- A macro-model representing the beam-column subassembly was adopted. The developed concrete and shear models were used to predict the monotonic response of different model elements. The model was then validated using available experimental results from this study and from studies by several independent researchers and showed satisfactory accuracy in predicting the joint strength, strength deterioration and stiffness degradation.

Finally, it should be noted that the presented analyses and conclusions were based on a limited number of tests. To establish general conclusions on the behaviour of as-built and rehabilitated beam-column joints, a more comprehensive testing program is needed.

9.3 RECOMMENDATIONS FOR FUTURE RESEARCH

Further research is needed in the following areas:

1- This study had focused on the behaviour of exterior beam-column joint. Analytical and experimental investigations are needed to study the behaviour of interior beam-column joints with slabs and transverse beams.

2- A parametric study is needed to evaluate the effect of different elements of the rehabilitation systems, such as the number of composite sheets, the inclinations of the main fibres and type of anchorage.

3- In the adopted macro model, the shear deformation in the beams and columns are assumed to remain elastic. A shear-interface spring can be implemented into the macro-model to represent the nonlinear shear deformation in the beam and column.

4- Further refinements of the adopted hysteretic models may be introduced to better represent the unloading and reloading stiffness and to adequately model the pinching of the hysteretic response.

5- A new shear model was developed to predict the shear behaviour of FRP-rehabilitated joints. Experimental program for testing concrete elements with FRP sheets under combined shear and axial stresses is essential to evaluate the proposed model.

6- Assessing the behaviour of existing reinforced concrete buildings before and after rehabilitation.

7- A FRP model was proposed to predict the flexural behaviour of externally bonded FRP sheets under cyclic loading. The model may be implemented into structural analysis software to evaluate concrete elements strengthened with FRP sheets.

APPENDIX A

DESIGN OF REHABILITATION SCHEMES

This section contains design guidelines for the rehabilitation systems proposed to strengthen the joint shear resistance and beam bars anchorage strength.

A.1 DESIGN OF FRP-SHEAR STRENGTHENING JACKET

The developed shear force in the joint is calculated as (park and Paulay, 1975; and CSA A23.3, 1994):

$$V_j = 1.25 A_s f_y - V_{col} \tag{A-1}$$

Where V_j is the developed joint shear force

V_{col} is the shear force in the column

A_s is the beam longitudinal reinforcement

f_y is the steel yield strength

The total shear resistance of the joint consists of the concrete resistance V_c, the resistance of the steel ties V_s, and the resistance provided by the composite sheets V_{frp}, or:

$$V_j = V_c + V_s + V_{frp} \tag{A-2}$$

The concrete shear resistance can be estimated using ACI-ASCE (1976) provision, as:

$$V_c = 0.3\sqrt{f_c^{'}(1+0.3 f_{col})}\, b_j d_j \tag{A-3}$$

where f_{col} is the axial stress applied to the column

b_j is the joint effective width

d_j is the joint effective depth.

The resistance of existing ties in the joint can be estimated using the traditional 45° truss model as (ACI-ASCE, 1976):

$$V_s = \frac{A_{st} f_y d_j}{s} \tag{A-4}$$

where A_{st} is the area of a single steel tie in joint zone

s is the spacing of steel ties in joint zone

Thus, the contribution of FRP sheets in resisting joint shear V_{frp}, is estimated as:

$$V_{frp} = V_j - V_c - V_s \tag{A-5}$$

Using the conventional truss model, the area of FRP sheets A_{frp} required to resist shear force of V_{frp} is:

$$A_{frp} = \frac{V_{frp}}{\varepsilon_{frp} E_{frp}} \tag{A-6}$$

where ε_{frp} is the effective strain of the FRP sheets

E_{frp} is the modulus of elasticity of FRP sheet

Although the ultimate strain of FRP sheet under coupon tests may exceed 10 times the yield strain of steel bars, several experimental investigations showed that the FRP can only reach a fraction of this strain. The Canadian standards (CSA S806-02, 2002) limit the FRP effective strain to be less than a strain of 0.004. From the experimental findings of this study, the effective FRP strain would range from 1/4 to 1/3 of the ultimate FRP strain.

For the rehabilitated specimen T-S4R, The ultimate capacity of the beam section

was estimated to be 196.41 kN.m. Column shear force is obtained by dividing the ultimate moment capacity by the shear span, so V_{col} is estimated to be 80.17 kN. Equation (A-1) gives the total joint shear V_j to be 635.33 kN. Equation (A-3) gives V_c of 277.80 kN, whereas due to the absence of shear reinforcement in the joint, V_s is zero. From equation (A-5), the required shear resistance contributed by the fibre, V_{frp}, is 357.53 kN. Thus the required thickness of CFRP jacket, assuming the effective CFRP strain of ¼ of the ultimate strain, is 0.96 mm. Thus, three layers of CFRP would be sufficient.

A.2 DESIGN OF FLEXURAL STRENGTHENING SCHEMES

Several rehabilitation schemes were proposed to account for the expected deterioration in flexural strength due to the loss of anchorage of beam bars. These systems include using FRP sheets attached to the beam bottom face, steel bridle that is welded to the existing bars, and installing new reinforcement bars.

A.2.1 FRP sheets

The composite sheets are used to replace the inadequately anchored bottom steel bars of the beam. In the design process, composite sheets are provided to develop the same ultimate flexural moment of the reinforced concrete beam section. This moment limit is imposed on the flexural strengthening system to avoid creating a beam that is stronger than the column.

The beam ultimate moment is estimated according to the provisions of CSA A23.3 (1994). In the design procedure, three assumptions are made:

(1) Strain compatibility between different materials is maintained.

(2) Ultimate concrete strain in compression is taken as 0.0035.

(3) Contribution of the existing beam bars to beam flexural strength is ignored.

The tensile force developed in the fibre sheets can be estimated as:

$$T_{frp} = \varepsilon_{frp} E_{frp} A_{frp} \tag{A-7}$$

where ε_{frp} is the strain developed in the FRP sheets, which should be less than the ultimate strain, E_{frp} is the modulus of elasticity of the FRP; and A_{frp} is the area of the FRP sheets.

The depth of the concrete compression block "a_c" can be estimated from the moment equilibrium equation, knowing the target sectional moment capacity, M_r:

$$M_r = \alpha_1 f_c^{'} a_c b(t - a_c / 2) + A_{s'} \varepsilon_{s'} E_s (t - d^{'}) \tag{A-8}$$

where α_1 is the equivalent compression block reduction factor, and equals:

$$\alpha_1 = 0.85\text{-}0.0015 f_c^{'} \geq 0.67$$

b and t are the beam width and height

$d^{'}$ is the concrete cover above the compression steel reinforcement

$A_{s'}$ is the area of the compression steel

E_s is the modulus of elasticity of the steel

$\varepsilon_{s'}$ is the strain in the compression steel

From the equilibrium of forces:

$$T_{frp} = C_c + C_{s'} \tag{A-9}$$

From Equation (A-8), the depth of compression zone can be estimated, and from

Equation (A-9), the required tension force in the FRP sheets is estimated. By substituting in Equation (A-7), the number of FRP sheets can be estimated.

A.2.2 Design of steel bridle

A steel bridle was used to tie the existing steel bars. For each bar, two fillet weld lines were used to transfer the bar force to the steel plate. The size of the weld line may be selected to be equal to the radius of the reinforcement bar; which is the maximum practical weld size. The weld shear resistance V_r should equal to the bar tensile force and is taken as the lesser of (CISC, 1995):

$$V_r = 0.67\phi_w X_u A_w \quad \text{or} \quad V_r = 0.67\phi f_y A_m \tag{A-10}$$

where ϕ and ϕ_w are the resistance factor for the steel bar and the weld materials, respectively.

A_m and A_w are the steel and weld effective area, respectively.

X_u is the ultimate weld strength.

Under cyclic loading, it is expected that the weld strength would reduce and may experience brittle failure mode. To avoid this and due to the absence of design provisions that consider the effect of cyclic loading on the strength of welded connection, it is recommended to consider only a fraction of the ultimate weld strength in the previous equation. In Specimen T-SB7, when taking the ultimate weld strength of ¼ of the value proposed by the Canadian Standards (CISC, 1995), Equation (A-10) gave a weld length of 188mm. So, a weld length of 200 mm was used.

The tensile forces are then transmitted to the welded steel plate, which was designed to have a larger cross sectional area than the total area of the steel bars. Four

external steel tie rods were welded to the steel plate. The rods were designed to transfer the tensile forces to the bearing plate. Thus, the diameter of rod used in the retrofit was selected to provide tensile strength that is equal to the ultimate tensile strength of the beam bars. Similar length of weld was used to connect the tie rods to the steel plate. The tensile forces developed in the tie rods were then transmitted to the joint concrete by bearing against the column backside. The area of the bearing plate should be selected to result in a bearing stress that is less than the allowable bearing stress suggested by the CSA A23.3 (1994) Clause 10.8.1.

A.2.3 Design of Additional flexural reinforcement

The philosophy of this system was to replace the action of the inadequately anchored bars with new reinforcement. Section analysis was performed to estimate the required reinforcement. The existing reinforcement bars were assumed ineffective when performing this analysis. Steel dowels are installed to confine the new reinforcement. New concrete is poured to cover the new reinforcement. Thus, the beam depth in the retrofit zone is increased. However, caution must be paid to avoid strong beam-weak column condition.

The critical issue in this scheme is the shear strength along the interface between the old and newly poured concrete. It is necessary for the success of this scheme to eliminate the delamination of new concrete and to insure that the shear forces can be transmitted safely along the interface surface. Limited research is available on the shear transfer between old and new concrete. Moreover, no research is available on the shear strength along the interface surface between old and new concrete under cyclic loading.

In general, the shear strength along the interface surface is shared between two sources, cohesion between old and new concrete, and steel dowels that are installed normal to the interface surface. The cohesion along the interface surface was ignored and hence, steel dowels were designed to carry the total shear forces along the interface surface. No bond-enhancing chemicals were used along the interface surface as it was suggested that it has minor effect on improving the bond along the interface surface (Silfwerbrand and Paulsson, 1998; and Menn, 1992)

The shear force V_{sf} that must be transmitted along that surface equals the tensile forces in the steel tie rods

$$V_{sf} = A_{sf}\, f_y \tag{A-11}$$

where A_{sf} is the effective cross sectional area of the rods

f_y is the yield strength of the steel rods

No Standards are available for estimating the strength of these dowels. However, the Canadian Standards estimate the resistance of shear connectors in the composite concrete slab-steel girder section as (CISC, 1995):

$$V_r = 0.5\phi\, A_{sc} \sqrt{f_c^{'} E_c} \quad \leq f_y\, \phi\, A_{sc} \tag{A-12}$$

where ϕ is the resistance factor and equals 0.8

A_{sc} is the connector cross sectional area

f_y is the yield stress of the connector

For joint T-SB8, Two-legs 10 mm diameter steel ties were used as shear connectors. Substituting in the Equations (A-11) and (A-12), V_{sf} would equal 409.0 kN

and V_r, for each branch of the ties, equals 32.0 kN. Thus, seven ties are sufficient to resist the shear forces along the interface surface.

Although, the dowels of joint T-SB8 were assumed to work in shear, they failed by pulling out a cone of the old concrete, which indicates that the dowels were working in tension. For rough interface surface, diagonal compression stresses are created due to the aggregate interlocking. This caused tensile stresses in the dowels in addition to the tensile stresses caused by the beam shear force. Adequate embedment length of the dowel into the old concrete is required to develop full dowel tensile strength and hence avoid this brittle failure mode. It is also possible to replace the shear dowels with equivalent steel plates welded to the existing and new reinforcement bars (El-Amoury et al., 2003).

APPENDIX B

BOND-SLIP COMPUTER PROGRAM

In this Appendix, a Fortran 77 program "BOND1" is listed. The program predicts the monotonic behaviour of embedded steel bars in concrete joints. The model predicts the bond-slip failure and the bar fracture failure modes.

The listing of the program is as follows:

```
C*********************************************************************
      PROGRAM BOND1
C*********************************************************************
C     BILINEAR STESS-STRAIN CURVE FOR STEEL REINFORCEMENT
C*********************************************************************
      IMPLICIT DOUBLE PRECISION (A-H,O-Z)
C*********************************************************************
      DIMENSION Uavg(1000), Fs(1000), S(1000), Se(1000), Ps(1000)
      DIMENSION Le(1000), Lsh(1000)
      DOUBLE PRECISION Ld, Fy, Es, Lt, L1, Le, Lsh, L2, Fs
C     OPEN OUTPUT FILE
      OPEN(20, FILE= 'S33L-COL-EXT-BARS.OUT')
      NOU=20
C     CONSTANTS
      PI=355./113.
C     *********     INPUT VARIABLES    **********
      Fy=585.0
      Fu=1.6*Fy
      Es=200000.0
      STRAINy=Fy/Es
      STRAINu=75*STRAINy
      Esu=(Fu-Fy)/(STRAINu-STRAINy)
      Fc=26.3
      PHIp=14
      Nb=2
      Ld=440*PI*PHIp*PHIp/4*Fy/(3*PHIp*400*SQRT(Fc))
      Lt=16.07*PHIp
      S1=SQRT(30/Fc)
      TAW1=(20-PHIp/4)*SQRT(Fc/30)
      S2=3*S1
```

```
      S3=10*S1
      TAW2=TAW1
      TAW3=TAW1/3
      Ue=Fy*PHIp/(4*Ld)
      WRITE(NOU,1010)PHIp, Ld, Lt, Fy, Es, Fc, S1, S2, S3, TAW1, TAW2, TAW3,
*      Ue
      WRITE(NOU,1020)
C     ************** STAGE I: LOAD CONTROL TO YIELD ****************
      N=Fy/8
      DO 100 I=1,N
      Fs(I)=I*Fy/N
      Le(I)=Fs(I)*PHIp/(4*Ue)
      IF (Le(I).LE.Lt)THEN
      S(I)=0.5*Fs(I)/Es*Le(I)
      Ps(I)=Nb*Fs(I)*PI*PHIp*PHIp/4/1000
      IF (Fs(I).GT.Fu)THEN
      WRITE(NOU,*)'BAR FAILURE'
      ENDIF
      WRITE(NOU,1030) I, Se(I), S(I), Fs(I), Ps(I), Le(I)
      ELSE
      L=I
      GO TO 150
      ENDIF
100   CONTINUE
      GO TO 300
C     ************            SLIP BEFORE YIELDING     **************
C     *****  SLIP OCCURS: (1) LOAD CONTROL TO THE S1          ********
150   DO 200 I=L,500
      Fs(I)=Fs(I-1)+0.01*Fy
      IF (Fs(I).GT.Fy)THEN
      GO TO 180
      ENDIF
      Uavg(I)=Fs(I)*PHIp/(4*Lt)
      Se(I)=S1*((Uavg(I)/TAW1)**2.5)
      IF (Se(I).LE.S1)THEN
      S(I)=Se(I)+0.5*Fs(I)/Es*Lt
      ELSE
C     CHANGE TO DISPLACEMENT CONTROL
      M =I
      GO TO 210
      ENDIF
      Fs(I)=4*Uavg(I)*Lt/PHIp
      Ps(I)=Nb*Fs(I)*PI*PHIp*PHIp/4/1000
```

```
      S(I)=Se(I)+0.5*Fs(I)/Es*Lt
      Le(I)=Lt
      GO TO 190
C     ------------------ IF Fs(I) .GT. Fy ------------------
C     **************** SLIP AFTER YIELD ********************
180   IF (Fs(I).GT.Fy)THEN
      Lsh(I)=(Fs(I)-Fy)*PHIp/(4*TAW3)
      Le(I)=Lt-Lsh(I)
      Uavg(I)=Fy*PHIp/(4*Le(I))
      IF (Uavg(I).GT.TAW1)THEN
      WRITE(NOU,*)'ULTIMATE STRENGTH IS ACHIEVED'
      J=I
      GO TO 500
      ELSE
      Se(I)=S1*((Uavg(I)/TAW1)**2.5)
      S(I)=Se(I)+0.5*STRAINy*Le(I)+(STRAINy+0.5*(Fs(I)-Fy)/Esu)
*     Lsh(I)
      Ps(I)=Nb*Fs(I)*PI*PHIp*PHIp/4/1000
      ENDIF
      ENDIF
190   IF(Fs(I).GT.Fu)THEN
      WRITE(NOU,*)'BAR FAILURE'
      ENDIF
      WRITE(NOU,1030) I, Se(I), S(I), Fs(I), Ps(I), Le(I)
200   CONTINUE
C
C     --- SLIP BEFORE YIELD: (2) DISPLACEMENT CONTROL TILL FAILURE --
C           ****************          YIELDING    ******************
210   DO 250 I=M,500
      Se(I)=Se(I-1)+0.1*S1
      IF (Se(I).LE.S2)THEN
      Uavg(I)=TAW1
      ELSEIF (Se(I).LE.S3)THEN
      Uavg(I)=TAW2-(Se(I)-S2)/(S3-S2)*(TAW2-TAW3)
      ELSE
      Uavg(I)=TAW3
      ENDIF
      Fs(I)=4*Uavg(I)*Lt/PHIp
      Ps(I)=Nb*Fs(I)*PI*PHIp*PHIp/4/1000
      S(I)=Se(I)+0.5*Fs(I)/Es*Lt
      Le(I)=Lt
      IF(Fs(I).GT.Fu)THEN
      WRITE(NOU,*)'BAR FAILURE'
```

```
      ENDIF
      WRITE(NOU,1030) I, Se(I), S(I), Fs(I), Ps(I), Le(I)
250   CONTINUE
      GO TO 1000
C     ************ STAGE II :LOAD CONTROL TO SLIP < S1 ***************
300   DO 400 I=1,500
      Fs(I)=(1.+REAL(I)/100)*Fy
      Le(I)=Fy*PHIp/(4*Ue)
      Lsh(I)=(Fs(I)-Fy)*PHIp/(4*TAW3)
      IF ((Le(I)+Lsh(I)).LE.Lt)THEN
      S(I)=0.5*STRAINy*Le(I)+(STRAINy+0.5*(Fs(I)-Fy)/Esu)*Lsh(I)
      ELSE
      Le(I)=Lt-Lsh(I)
      Uavg(I)=Fy*PHIp/(4*Le(I))
      Se(I)=S1*((Uavg(I)/TAW1)**2.5)
      IF (Se(I).LT.S1)THEN
      S(I)=Se(I)+0.5*STRAINy*Le(I)+(STRAINy+0.5*(Fs(I)-Fy)/Esu)*Lsh(I)
      ELSE
      J=I
      GO TO 500
      ENDIF
      ENDIF
      Ps(I)=Nb*Fs(I)*PI*PHIp*PHIp/4/1000
      IF (Fs(I).GT.Fu)THEN
      WRITE(NOU,*)'BAR FAILURE'
      ENDIF
      WRITE(NOU,1030) I, Se(I), S(I), Fs(I), Ps(I), Le(I)
400   CONTINUE
C     ** STAGE III: SLIP OCCURRENCE (DISPLACEMENT CONTROL GT. S1)**
C     ********************     SLIP AFTER YIELD ************************
500   DO 600 I=J,500
      Se(I)=Se(I-1)+0.1*S1
      IF(Se(I).LE.S1)THEN
      Uavg(I)=TAW1*((Se(I)/S1)**0.4)
      ENDIF
      IF (Se(I).GT.S1.AND.Se(I).LE.S2) THEN
      Uavg(I)=TAW1
      END IF
      IF (Se(I).GT.S2.AND.Se(I).LE.S3) THEN
      Uavg(I)=TAW3+(TAW1-TAW3)*(S3-Se(I))/(S3-S2)
      ENDIF
      IF (Se(I).GT.S3)THEN
      Uavg(I)=TAW3
```

```
      ENDIF
      Le(I)=Fy*PHIp/(4*Uavg(I))
      Lsh(I)=Lt-Le(I)
      Fs(I)=4*Uavg(I)*Le(I)/PHIp+4*TAW3*Lsh(I)/PHIp
      IF (Fs(I).GT.Fs(I-1))THEN
      S(I)=Se(I)+0.5*STRAINy*Le(I)+(STRAINy+0.5*(Fs(I)-Fy)/Esu)*Lsh(I)
      Ps(I)=Nb*Fs(I)*PI*PHIp*PHIp/4/1000
      ELSE
      Ful=Fs(I-1)
      L1=Le(I-1)
      L2=Lsh(I-1)
      J=I
      GO TO 700
      WRITE(NOU,*)'UNLOADING'
      ENDIF
      IF (Fs(I).GT.Fu)THEN
      WRITE(NOU,*)'BAR FAILURE'
      ENDIF
      WRITE(NOU,1030) I, Se(I), S(I), Fs(I), Ps(I), Le(I)
600   CONTINUE
      GO TO 1000
C     ***************** UNLOADING PART  ******************
700   DO 800 I=J,500
      Se(I)=Se(I-1)+0.1*S1
C
      IF(Se(I).LE.S1)THEN
      Uavg(I)=TAW1*((Se(I)/S1)**0.4)
      ENDIF
      IF (Se(I).GT.S1.AND.Se(I).LE.S2) THEN
      Uavg(I)=TAW1
      END IF
      IF (Se(I).GT.S2.AND.Se(I).LE.S3) THEN
      Uavg(I)=TAW3+(TAW1-TAW3)*(S3-Se(I))/(S3-S2)
      ENDIF
      IF (Se(I).GT.S3)THEN
      Uavg(I)=TAW3
      ENDIF
      Fs(I)=4*Uavg(I)*L1/PHIp+4*TAW3*L2/PHIp
      S(I)=Se(I)+0.5*(4*Uavg(I)*L1/PHIp)/Es*L1+(STRAINy+0.5*(Ful-Fy)/
      *Esu-0.5*((Ful-Fs(I))+(Fy-4*Uavg(I)*L1/PHIp))/Es)*L2
      Ps(I)=Nb*Fs(I)*PI*PHIp*PHIp/4/1000
      IF (Fs(I).GT.Fu)THEN
      WRITE(NOU,*)'BAR FAILURE'
```

```
      ENDIF
      WRITE(NOU,1030) I, Se(I), S(I), Fs(I), Ps(I)
800   CONTINUE
1000  CONTINUE
C
1010  FORMAT('PROBLEM PROPERTIES',/,
    * 5X,35HSTEEL BAR DIAMETER(mm)............=,F10.2,/,
    * 5X,35HBAR DEVELOPEMENT LENGTH(mm).......=,F10.4,/,
    * 5X,35HBAR TOTAL LENGTH(mm)..............=,F10.2,/,
    * 5X,35HSTEEL YIELD STRESS(MPa)...........=,F10.2,/,
    * 5X,35HSTEEL MODULUS OF ELASTICITY(MPa)..=,F10.2,/,
    * 5X,35HCONCRETE ULTIMATE STRENGTH(MPa)...=,F10.2,/,
    * 5X,35HSLIP VALUE "S1"(mm)...............=,F10.3,/,
    * 5X,35HSLIP VALUE "S2"(mm)...............=,F10.3,/,
    * 5X,35HSLIP VALUE "S3"(mm)...............=,F10.3,/,
    * 5X,35HMAX. BOND STRESS"TAW1"(MPa).......=,F10.3,/,
    * 5X,35HMAX. BOND STRESS"TAW2"(MPa).......=,F10.3,/,
    * 5X,35HMAX. BOND STRESS"TAW3"(MPa).......=,F10.3,/,
    * 5X,35HELASTIC BOND STRESS"TAW3"(MPa)....=,F10.3,/)
1020  FORMAT('OUTPUT VALUES FOR STEEL STRESS - SLIP
      RELATIONSHIP',/,
    * 6X,'INCREMENT',6X, 'END SLIP(mm)', 6X,'LEAD SLIP (mm)', 6X,
    *' STEEL STRESS (MPa)',6X,'STEEL FORCE (kN)',6X,'ELASTIC LENGTH')
1030  FORMAT(I10, 6X, F8.4, 6X, F10.4, 10X, F10.4, 10X, F10.4, 10X,
      *F10.4, 10X, F10.4)
C
      END
```

REFERENCES

ACI-ASCE, 1976, "Recommendations for Design of Beam-Column Joints in Monolithic Reinforced Concrete Structures", Committee report 352, American Concrete Institute, Detroit, Michigan, 19 pages.

ACI-ASCE, 1997, "Recommendations for Design of Beam-Column Joints in Monolithic Reinforced Concrete Structures", Committee report 352R-91, American Concrete Institute, Detroit, Michigan, 21 pages.

ACI 318-63, 1968, "Building Code Requirements for Reinforced Concrete", American Concrete Institute, Detroit, Michigan.

ACI, 1992, "State-of-The-Art Report on Bond under Cyclic Loads", Committee report 408, American Concrete Institute, Detroit, Michigan, 32 pages.

Alcocer, S.M., and Jirsa, J.O., 1991, "Reinforced Concrete Frame Connections Rehabilitated by Jacketing", PMFSEL Report 91-1, Department of Civil Engineering, The University of Texas at Austin, Texas, 221 pages.

Alcocer, S.M., and Jirsa, J.O., 1993, "Strength of Reinforced Concrete Frame Connections Rehabilitated by Jacketing", ACI Structural Journal, Vol. 90, No. 3, pp. 249-261.

Aliswat, J.M., and Saatcioglu, M., 1992, "Reinforcement Anchorage Slip under Monotonic Loading", Journal of Structural Engineering, ASCE, Vol. 118, No. 9, pp. 2421-2438.

Antonopoulos, C.P., and Triantafillou, T.C., 2003, "Experimental Investigation of FRP-Strengthened RC Beam-Column Joints", Journal of Composites for Construction, Vol. 7, No. 1, pp. 39-49.

Assa, B., Nishiyama, M., and Watanabe, F., 2001, "New Approach for Modeling Confined Concrete: II – Rectangular Columns", Journal of Structural Engineering, ASCE, Vol. 127, No. 7, pp.751-757.

ASTM-A370-02, 2003, "Standard Test Methods for Definitions for Mechanical Testing of Steel Products", ASTM International, Vol. 01.04, pp. 174-224.

ASTM-C39-96, 2002, "Standard Test Method for Compressive Strength of Cylindrical Concrete Specimens", ASTM International, Vol. 04.02, pp. 17-21.

ASTM-C469-94, 2002, "Standard Test Method for Static Modulus and Poisson's Ratio of Concrete in Compression", ASTM International, Vol. 04.02, pp. 242-245.

ASTM-C496-96, 2002, "Standard Test Method for Splitting Tensile Strength of Cylindrical Concrete Specimens", ASTM International, Vol. 04.02, pp. 268-271.

ASTM-D3039-95, 2002, "Standard Test Method for Tensile Properties of Polymer Matrix Composite Materials", ASTM International, Vol. 15.03, pp. 99-109.

Baglin, P.S., and Scott, R.H., 2000, "Finite Element Modeling of Reinforced Concrete Beam-Column Connections", ACI Structural Journal, Vol. 97, No. 6, pp. 886-894.

Beckingsale, C.W., Park, R., and Paulay, T., 1980, "Post Elastic Behaviour of Reinforced Concrete Beam-Column Joints", Research report 80-20, University of Canterbury, Christchurch, New Zealand.

Bentz, E.C., 2000, "Sectional Analysis of Reinforced Concrete Members", Ph.D. dissertation, Department of Civil Engineering, University of Toronto, Canada, 184 pages.

Beres, A., El-Borgi, S., White, R.N., and Gergely, P., 1992a, "Experimental Results of Repaired and Retrofitted Beam-Column Joint Tests in Lightly Reinforced Concrete Frame Buildings", NCEER technical report No. 92-25, State University of New York, Buffalo, NY.

Beres, A., White, R.N., and Gergely, P., 1992b, "Seismic Performance of Interior and Exterior Beam-to-Column Reinforced Concrete Frame Buildings, Detailed Experimental Results", Technical report No. 92-06, Department of Structural Engineering, Cornell University, Ithaca, NY.

Bhide, S.B., and Collins, M.P., 1989, "Influence of Axial Tension on the Shear Capacity of Reinforced Concrete Members", ACI Structural Journal, Vol. 86, No. 5, pp. 571-581.

Biddah, A.M.S., 1997, "Seismic Behaviour of Existing and Rehabilitated Reinforced Concrete Frame Connections", Ph.D. dissertation, McMaster University, Hamilton, Ontario, Canada, 326 pages.

Biddah, A, and Ghobarah, A., 1998, "Inelastic Shear Deformation Modeling in Existing and Rehabilitated Concrete Frames", Proceedings of the Sixth U.S. National Conference on Earthquake Engineering, Earthquake Engineering Research Institute, Oakland, CA.

Blume, J.A., Newmark, N.M., and Corning, L.H., 1961, "Design of Multi-Story Concrete Buildings for Earthquake Motions", Portland Cement Association, Skokie, Illinois.

CEB-FIP, 1978, "Model Code for Concrete Structures. CEB-FIP International Recommendation", third edition, Paris, France, 348 pages.

Cervenka Consulting, 1992, "SBETA Program Documentation", Prague.

Chajes, M.J., Finch, W.W., Januszka, T.F., and Thomson, T.A., 1996, "Bond and Force Transfer of Composite Material Plates Bonded to Concrete", ACI Structural Journal, Vol. 93, No. 2, pp.208-217.

Chen, W.F., 1982, " Plasticity in Reinforced Concrete", McGraw-Hill, New York.

Ciampi, V., Eligehausen, R., Bertero, V.V., and Popov, E.P., 1982, " Analytical Model for Concrete Anchorages of Reinforcing Bars Under Generalized Excitations", Report No. UCB/EERC-82-0023, Earthquake Engineering Research Center, University of California, Berkeley, CA, 103 pages.

CISC, 1995, "Handbook of Steel Construction", Canadian Institute of Steel Construction, Willowdale, Ontario, Canada.

Clyde, C., and Pantelides, C.P., 2002, "Seismic Evaluation and Rehabilitation of R/C Exterior Building Joints", Proceedings of the Seventh U.S. National Conference of Earthquake Engineering, 7NCEE, Earthquake Engineering Research Institute, Oakland, CA.

Cole, C. and Belarbi, A., 2001, "Confinement Characteristics of Rectangular FRP-Jacketed RC Columns", Proceedings of the Fifth Symposium on Fiber Reinforced Polymer for Reinforced Concrete Structures (FRPRCS-5), Cambridge, UK, pp. 823-832.

Collins, M.P., and Mitchell, D., 1987, "Prestressed Concrete Basics", Canadian Prestressed Concrete Institute, Ottawa, Ontario, Canada.

Collins, M.P., and Mitchell, D., 1990, "Prestressed Concrete Structures", Prentice Hall Inc., Englewood Cliffs, N.J.

Collins, M.P., Mitchell, D., Adebar, P., and Vecchio, F.J., 1996, "A General Shear Design Method", ACI Structural Journal, Vol. 93, No. 1, pp. 36-45.

Corazao, M. and, Durrani, A.J., 1989, "Repair and Strengthening of Beam-to-Column Connections Subjected to Earthquake Loading", NCEER technical report No. 89-13, State University of New York, Buffalo, NY.

CSA A23.3, 1994, "Design of Concrete Structures", Canadian Standards Association, Rexdale, Ontario, Canada, 220 pages.

CSA S806-02, 2002, "Design and Construction of Building Components with Fibre-Reinforced Polymers", Canadian Standards Association, Rexdale, Ontario, Canada.

El-Amoury, T., Arafa, A., and Ghobarah, A., 2003, "Strengthening of Seismically Vulnerable Beam-Column Joints", Proceeding of Response of Structures to Extreme Loading Conference, Elsevier, UK, Paper No. 17.

Eligehausen, F., Popov, E.P., and Bertero, V.V., 1983, " Local Bond Stress-Slip Relationships of Deformed Bars under Generalized Excitations", Earthquake Engineering Research Center, Report No. UCB/EERC-83/23, University of California, Berkeley, CA.

Elmorsi, M., 1998, "Analytical Modeling of Reinforced Concrete Beam-Column Connections for Seismic Loading", Ph.D. dissertation, McMaster University, Hamilton, Ontario, Canada, 236 pages.

Estrada, J.I., 1990, "Use of Steel Elements to Strengthen a Reinforced Concrete Building", M. Sc. dissertation, University of Texas at Austin, Texas, 65 pages.

Fam, A.Z., and Rizkalla, S.H., 2001, "Confinement Model for Axially Loaded Concrete Confined by Circular Fibre-Reinforced Polymer Tubes", ACI Structural Journal, Vol. 98, pp. 451-461.

Filippou, F.C., Popov, E.P., and Bertero, V.V., 1983, "Effects of Bond Deterioration on Hysteretic Behaviour of Reinforced Concrete Joints", Earthquake Engineering Research Center, Report No. UCB/EERC-83/19, University of California, Berkeley, CA.

Fuji, S., and Morita, S., 1991, "Comparison Between Interior and Exterior Beam-Column Joint Behaviour", ACI-SP123, Design of Beam-Column Joints for Seismic Resistance, pp. 145-165.

Fyfe Company LLC., 2000, Tyfo® BC Composite, Material Online data Sheet, *www.fyfeco.com*, downloaded in July, 2000.

Galal, K.E.M., 2002, "Modeling and Rehabilitation of Non-Ductile Spatial RC Columns", Ph.D. dissertation, McMaster University, Ontario, Canada, 289 pages.

Gergely, J., Pantelides, C.P., and Reaveley, L.D., 2000, "Shear Strengthening of RC T-Joints Using CFRP Composites", Journal of Composites for Construction, Vol. 4, No. 2, pp. 56-64.

Ghobarah, A., Aziz, T. S., and Biddah, A., 1996, "Seismic Rehabilitation of Reinforced Concrete Beam-Column Connections", Earthquake Spectra, Vol. 12, No. 4, pp. 761-780.

Ghobarah, A., Aziz, T.S., and Biddah, A., 1997, "Rehabilitation of Reinforced Concrete Frame Connections Using Corrugated Steel Jacketing", ACI Structural Journal, Vol. 4, No.3, pp. 283-294.

Ghobarah, A., and Biddah, A., 1999, "Dynamic Analysis of Reinforced Concrete Frames Including Joint Shear Deformation", Engineering Structures, Vol. 21, pp. 971-987.

Ghobarah, A., and Said, A., 2001, "Seismic Rehabilitation of Beam-Column Joints Using FRP Laminates", Journal of Earthquake Engineering, Vol. 5, No. 1, pp. 113-129.

Ghobarah, A., and Said, A., 2002, "Shear Strengthening of Beam-Column Joints", Engineering Structures, Vol. 24, No.7, pp. 881-888.

Ghobarah, A., and Youssef, M., 1999, "Response of an Existing RC Building Including Concrete Crushing and Bond Slip Effects", Proceedings of the Eighth Canadian Conference on Earthquake Engineering, Vancouver, B.C., pp. 427-432.

Ghusn, G.E., and Saiidi, M., 1986, "A Simple Hysteretic Element for Biaxial Bending of R/C Columns and Implementation in NEABS-86", Report No. NCEER 81-1, Civil Engineering Department, University of Nevada, Reno, Nevada.

Gupta, A., and Krawinkler, H., 1998, "Effect of Stiffness Degradation on Deformation Demands for SDOF and MDOF Structures", Proceedings of the Sixth U.S. National Conference on Earthquake Engineering, Earthquake Engineering Research Institute, Oakland, CA.

Hakuto, S., 1995, "Retrofitting of Reinforced Concrete Moment Resisting Frames", Ph.D. dissertation, Department of Civil Engineering, University of Canterbury, Christchurch, New Zealand, 390 pages.

Hanson, N.M. and Conner, H.W., 1967, "Seismic Resistance of Reinforced Concrete Beam-Column Joints", Journal of the Structural Division, ASCE, Vol. 93, pp. 533-560.

Hosotani, M., Kawashima, K., and Hoshikuma, J., 1997, "A Model for Confinement Effect for Concrete Cylinders Confined by Carbon Fibre Sheets", Proceedings of the Workshop on Earthquake Engineering Frontiers in Transportation Facilities, NCEER-97-0005, National Center for Earthquake Engineering Research, Buffalo, NY, pp. 405-430.

Howie, I., and Karbhari, V.M., 1995, "Effect of Tow Sheet Composite Wrap Architecture on Strengthening of Concrete due to Confinement: I-Experimental Studies", Journal of Reinforced Plastics and Composites, Vol. 14, No. 9, pp. 1008-1030.

Humar, J. 1980, "Effect of Stiffness Degradation on Seismic Response of Concrete Frames", Proceedings of the Seventh World Conference on Earthquake Engineering, Istanbul, Turkey, Vol.5, pp. 505-512.

Hwang, S.J., and Lee, H.J., 1999, "Analytical Model for Predicting Shear Strengths of Exterior Reinforced Concrete Beam-Column Joints for Seismic Resistance", ACI Structural Journal, Vol. 96, No. 5, pp. 846-857.

Hwang, S.J., and Lee, H.J., 2000, "Analytical Model for Predicting Shear Strengths of Interior Reinforced Concrete Beam-Column Joints for Seismic Resistance", ACI Structural Journal, Vol. 97, No. 1, pp. 35-44.

ICBO-AC178, 2001, "Acceptance Criteria for Inspection and Verification of Concrete and Reinforced and Unreinforced Masonry Strengthening Using Fibre-Reinforced Polymer (FRP) Composite Systems", ICBO Evaluation Service INC., Whittier, CA, 7 pages.

Ilki, A., kumbasar, N., and koc, V., 2002, "Effect of Shape of Cross-Section for CFRP Wrapped Concrete", Proceedings of the Twelfth European Conference of Earthquake Engineering, Paper No. 20, London, U.K.

Jiang, Y., and Saiidi, S., 1990, "Four Spring Element for Cyclic Response of R/C Columns", Journal of Structural Engineering, ASCE, Vol. 116, No. 4, pp. 1018-1029.

Kaku, T., and Asakusa, H., 1991, " Ductility Estimation of Exterior Beam-Column Subassemblages in RC Frames", ACI-SP 123, Design of Beam-Column joints for Seismic Resistance, pp. 167-185.

Kent, D.C., and Park, R., 1971, "Inelastic Behaviour of Reinforced Concrete Members with Cyclic Loading", Bulletin of the New Zealand Society for Earthquake Engineering, Vol. 4, No. 1, pp. 108-125.

Lai, S.S., Will, G.T., and Otani, S., 1984, "Model for Inelastic Biaxial Bending of Concrete Members", Journal of Structural Engineering, ASCE, Vol. 110, No. 11, pp. 2563-2584.

Li, K.N., Aoyama, H., and Otani, S., 1988, "Reinforced Concrete Columns under Varying Axial Load and Bi-Directional Lateral Load Reversals", Proceedings of Ninth World Conference on Earthquake engineering, Tokyo, Japan, Vol. VIII, pp.537-542.

Liu, A. and Park, R., 2001a, "Seismic Behaviour and Retrofit of Pre-1970's As-Built Exterior Beam-Column Joints Reinforced by Plain Round Bars", Bulletin of the New Zealand Society for Earthquake Engineering, Vol. 34, No. 1, pp. 68-81.

Liu, A. and Park, R., 2001b, "Seismic Behaviour of Existing Moment-Resisting Frames with Plain Round Reinforcing Bars Designed to Pre-1970s Codes", Proceedings of the Twelfth World Conference of Earthquake Engineering, 12WCEE, New Zealand Society for Earthquake Engineering, Auckland, New Zealand, Paper 1030.

Lowes, L.N., and Altoontash, A., 2002, "Modeling the Response of RC Building Beam-Column Joints Subjected to Earthquake Loading", Proceedings of the Seventh U.S. National Conference of Earthquake Engineering, 7NCEE, Earthquake Engineering Research Institute, Oakland, CA.

Lutz, L.A., and P. Gergely, 1967, "Mechanics of Bond and Slip of Deformed Reinforcement", ACI Journal of Structural Division, Vol. 64, pp. 711-721.

Ma, S.Y., Bertero, V.V., and Popov, E.P., 1976, "Experimental and Analytical Studies on the Hysteretic Behaviour of Reinforced Concrete Rectangular and T-Beams", Earthquake Engineering Research Center, Report No. UCB/EERC 76-2, University of California, Berkeley, CA.

Maison, B.F., 1992, "PCANSR: A Computer Program for Nonlinear Structural Analysis", University of California, Berkeley, CA.

Mander, J.B., Priestly, M.J.N., and Park, R., 1988, "Theoretical Stress-Strain Model for Confined Concrete", Journal of Structural Engineering, ASCE, Vol. 114, No. 8, pp. 1804-1826.

Marques, J.L.G., and Jirsa, J.O., 1975, " A Study of Hooked Bar Anchorages in Beam-Column Joints", ACI Structural Journal, Vol. 72, No. 5, pp. 198-209.

Master Builders Inc., 2000, MBrace™ Composite Strengthening System, Material Online Data sheet, ***www.masterbuilders.com***, downloaded in September, 2000.

Menn, C., 1992, "Bonding of Old and New Concrete for Monolithic Behaviour", Proceedings of the Third International Workshop on Bridge Rehabilitation, Darmstadt, Germany, John Wiley & Son.

Mirmiran, A., and Shahawy, M., 1997, "Dilation Characteristics of Confined Concrete", Journal of Mechanics of Cohesive-Frictional Materials, Vol. 2, pp. 237-249.

Mondkar, D.P., and Powell, G.H., 1975, "ANSR-1: General Purpose Program for Analysis of Linear Structural Response", Earthquake Engineering Research Center, Report No. UCB/EERC 75-37, University of California, Berkeley, CA.

Monti, G., Filippou, F., and Spacone, E., 1997, "Finite Element for Anchored Bars under Cyclic Load reversals", Journal of Structural Engineering, ASCE, Vol. 123, No. 5, pp. 614-623.

Nanni, A., and Bradford, N.M., 1995, "FRP Jacketed Concrete under Uniaxial Compression", Journal of Construction and Building Materials, Vol. 9, No. 2, pp. 115-124.

Otani, S., and Sozen, M., 1972, "Behaviour of Multistory Reinforced Concrete Frames during Earthquakes", Structural Research series, No. 392, University of Illinois, Urbana, Illinois.

Pantelides, C., Clyde, C., and Reaveley, L.D., 2000, "Rehabilitation of R/C Building Joints with FRP Composites", Proceedings of The Twelfth World Conference on Earthquake Engineering, 12WCEE, New Zealand Society for Earthquake Engineering, Auckland, New Zealand, Paper No. 2306.

Pantelides, C.P., Gergely, I., Reaveley, L.D., and Nuismer, R.J., 1997, "Rehabilitation of Cap Beam-Column Joints with Carbon Fibre Jackets", Proceedings of The Third International Symposium of Non-Metallic (FRP) Reinforcement for Concrete Structures (FRPRCS-3), Sapporo, Japan, Vol. 1, pp. 587-595.

Park, R., and Paulay, T., 1975, "Reinforced Concrete Structures", John Wiley & Sons, New York.

Park, R., 1994, "Recent Seismic Load Tests on Reinforced Concrete Structural Elements and Subassemblies at The University of Canterbury", Proceedings of the Tenth European Conference on Earthquake Engineering, Austrian Association for Earthquake Engineering, Vienna, Vol. 3, pp. 2351-2360.

Park, R., 2002, "A Summary of Results of Simulated Seismic Load Tests on Reinforced Concrete Beam-Column Joints, Beams and Columns with Substandard Reinforcing Details", Journal of Earthquake Engineering, Vol. 6, No. 2, pp. 147-174.

Paulay, T., and Priestley, M.J.N., 1992, "Seismic Design of Reinforced Concrete and Masonry Buildings", John Wiley & Sons, Inc., New York.

Pessiki, S.P; Conley, C.H.; Gergely, P., and White, R.N., 1990, "Seismic Behaviour of Lightly Reinforced Concrete Column and Beam-Column Joint Details", NCEER technical report 90-14, State University of New York, Buffalo, NY.

Popov, E.P., 1984, " Bond and Anchorage of Reinforcing Bars under Cyclic Loading", ACI Structural Journal, Vol. 81, No. 4, pp. 340-349.

Popovics, S., 1973, "A Numerical Approach to the Complete Stress-Strain Curve of Concrete", Cement and Concrete Research, Vol. 3, pp. 583-599.

Prota, A., Manfredi, G., and Cosenza, E., 2002, "Selective Seismic Strengthening of RC Frames with Composites", Proceedings of the Seventh U.S. National Conference on Earthquake Engineering, 7NCEE, Earthquake Engineering Research Institute, Oakland, CA.

Russo, G., Zingone, G., and Romano, F., 1990, "Analytical Solution for Bond-Slip of Reinforcing Bars in R.C. Joints", Journal of Structural Engineering, ASCE, Vol. 116, No. 2, pp. 336-355.

Saadatmanesh, H.; Ehsani, M.R., and Li, M.W., 1994, "Strength and Ductility of Concrete Columns Externally Reinforced with Fibre Composite Straps", ACI Structural Journal, Vol. 91, No. 4, pp. 434-447.

Said, A.M., 2000, "Seismic Rehabilitation of beam-Column Joints Using Advanced Composite Materials", M.Eng. Thesis, McMaster University, Canada, 172 pages.

Samaan, M.; Mirmiran, A., and Shahawy, M., 1998, "Model of Concrete Confined by Fibre Composites", Journal of Structural Engineering, ASCE, Vol. 124, No. 9, pp. 1025-1031.

Shiohara, H., 2001, "New Model for Shear Failure of RC Interior Beam-Column Connections", Journal of Structural Engineering, ASCE, Vol. 127, No. 2, pp. 152-160.

Silfwerbrand, J., and Paulsson, J., 1998, "Better Bonding of Bridge Deck Overlays", Concrete International, Vol. 20, No.10, pp. 56-61

Soroushian, P., Obaseki, K., Nahi, M., and Rojas, M., 1988, "Pullout Behaviour of Hooked Bars in Exterior Beam-Column Connections", ACI Structural Journal, Vol. 85, No.3, pp. 269-276.

Soroushian, P., and Choi, K.B., 1989, "Local Bond of Deformed Bars with Different Diameters in Confined Concrete", ACI Structural journal, Vol. 86, No. 2, pp. 217-222.

Soroushian, P., and Choi, K.B., 1991, "Analytical Evaluation of Straight Bar Anchorage Design in Exterior Joints", ACI Structural journal, Vol. 88, No. 2, pp. 161-168.

Soroushian, P., Choi, K.B., Park, G.H., and Aslani, F., 1991a, "Bond of Deformed Bars to Concrete: Effects of Confinement and Strength of Concrete", ACI Structural journal, Vol. 88, No. 3, pp. 227-232.

Soroushian, P., Obasaki, K., and Marihunte, S., 1991b, "Analytical Modeling of Bonded Bars under Cyclic Loads", Journal of Structural engineering, ASCE, Vol. 117, No. 1, pp. 48-60.

Speolstra, M.R., and Monti, G., 1999, "FRP-Confined Concrete Model", Journal of Composites for Construction, Vol. 3, No. 3, pp. 143-150.

Stevens, N.J., Uzumeri, S.M., and Collins, M.P., 1987, "Analytical Modeling of Reinforced Concrete Subjected to Monotonic and Reversed Loading", Report No 87-01, University of Toronto, Toronto, Canada.

Takeda, T., Sozen, M., and Nielsen, N.N., 1970, "Reinforced Concrete Response to Simulated Earthquakes", Journal of the structural Division, ASCE, Vol.96, No. 12, pp. 2557-2573.

Tamai, S. Shima, H., Izumo, J., and Okamura, H., 1988, "Average Stress-Strain Relationship in Post Yield Range of Steel Bar in Concrete", Concrete Library of JSCE, No. 11, pp. 117-129. (Translation from Proceedings of JSCE, No. 378/V-6, Feb 1987)

Taucer, F.F., Spacone, F.C., and Filippou, F.F., 1991, "A Fiber Beam-Column Element for Seismic Response Analysis of Reinforced Concrete Structures", Earthquake Engineering Research Center, Report No. UCB/EERC 91/17, University of California at Berkeley, CA.

Ueda, T., Lin, I., and Hawkins, N.M., 1986, "Beam Bar Anchorage in Exterior Column-Beam connections", ACI Structural Journal, Vol. 83, No. 3, pp. 412-422.

Ustuner, H., 1992, "An Analytical Study of the Mechanics of Bond Deterioration Caused by Yield Penetration", Master of Applied Science Dissertation, Department of Civil Engineering, University of Toronto, Ontario, Canada.

Uzumeri, S.M., and Seckin, M., 1974, "Behaviour of Reinforced Concrete Beam-Column Joints Subjected to Slow Load Reversals", Report No. 74-05, Department of Civil Engineering, University of Toronto, Canada, 72 pages.

Vecchio, F.J., and Collins, M.P., 1982, "Response of Reinforced Concrete to In-Plane Shear and Normal Stresses", Publication No. 82-03, Department of Civil Engineering, University of Toronto, Canada, 332 pages.

Vecchio, F.J., and Collins, M.P., 1986, " The Modified Compression Field Theory for Reinforced Concrete Elements Subjected to Shear", ACI Structural Journal, Vol. 83, No. 2, pp. 219-231.

Viwathanatepa, S., Popov, E.P., and Bertero, V.V., 1979, "Effects of Generalized Loadings on Bond of Reinforcing Bars Embedded in Confined Concrete Blocks", Earthquake Engineering Research Center, technical report UCB/EERC-79/22, University of California, Berkeley, CA.

Vollum, R.L., and Newman, J.B., 1999, "Strut and Tie Models for Analysis/Design of External Beam-Column Joints", Magazine of Concrete Research, Vol. 51, No. 6, pp. 415-425.

Wang, Y.C., and Restrepo, J.I., 2001, "Investigation of Concentrically Loaded Reinforced Concrete Columns Confined with Glass Fibre-Reinforced Polymer Jackets", ACI Structural Journal, Vol. 98, No. 3, pp. 377-385.

Youssef, M., 2000, "Modeling of Existing and Rehabilitated RC Buildings". Ph.D. dissertation, McMaster University, Canada, 143 pages.

Youssef, M., and Ghobarah, A., 1999, "Strength Deterioration due to Bond Slip and Concrete Crushing in Modeling of Reinforced Concrete Members", ACI Structural Journal, Vol. 96, No. 6, pp. 956-966.

Youssef, M., and Ghobarah, A., 2001, "Modeling of RC Beam-Column Joints and Structural Walls", Journal of Earthquake Engineering, Vol. 5, No. 1, pp. 93-111.